Real-time Dynamics of Quantum Impurity Systems in fermionic and bosonic Environments

Dissertation
zur Erlangung des Doktorgrades
der Naturwissenschaften
der Fakultät Physik an der
Technischen Universität Dortmund

vorgelegt von

Christian Kleine
aus Ahlen (Westf.)

Dezember 2015

Erster Gutachter	Prof. Dr. Frithjof B. Anders
Zweiter Gutachter	Prof. Dr. Joachim Stolze
Tag der mündlichen Prüfung	12.02.2016

Kontakt zum Autor christian.kleine@tu-dortmund.de

Contents

Table of abbreviations

ACR	asymmetric critical
ASC	asymmetric strong coupling
ASC′	asymmetric strong coupling prime
BEC	Bose-Einstein condensation
BF	Bose-Fermi
BFAM	Bose-Fermi Anderson model
BFCR	Bose-Fermi critical
BFCR*	Bose-Fermi critical star
BFKM	Bose-Fermi Kondo model
BF-NRG	Bose-Fermi numerical renormalisation group
BF-QIS	Bose-Fermi quantum impurity system
cK	charge-Kondo
CT-QMC	continuous-time quantum Monte Carlo
D	delocalised
DMFT	dynamical mean-field theory
DMRG	density matrix renormalisation group
DNA	deoxyribonucleic acid
DOF	degree of freedom
DOS	density of states
ED	exact diagonalisation
EDMFT	extended dynamical mean-field theory
FI	free impurity
FP	fixed point
KLM	Kondo lattice model
KM	Kondo model
L	localised
LM	local moment
LM′	local moment prime
MCKM	multi-channel Kondo model
NRG	numerical renormalisation group
pg	pseudo-gap
pg-DOS	pseudo-gap density of states

pg-KM	pseudo-gap Kondo model
ph	particle-hole
qc	quantum critical
QCP	quantum critical point
QCR	quantum critical region
QD	quantum dot
QDS	quantum dissipative system
QIS	quantum impurity system
QMC	quantum Monte Carlo
QPT	quantum phase transition
RG	renormalisation group
RKKY	Ruderman-Kittel-Kasuya-Yosida
SBM	spin-boson model
SC	strong coupling
SCR	symmetric critical
SCR′	symmetric critical prime
SIAM	single-impurity Anderson model
sK	spin-Kondo
SSC	symmetric strong coupling
SWT	Schrieffer-Wolff transformation
TCKM	two-channel Kondo model
TIKM	two-impurity Kondo model
TD-NRG	time-dependent numerical renormalisation group
VF	valence fluctuation

Introduction

In condensed matter physics we generally have to deal with a large number $O(10^{23})$ of interacting particles. Their interaction is described quantum-mechanically by a Hamiltonian, and their interplay may result in a collective behaviour, which can only be understood in a many-body picture. Examples for collective phenomena are superconductivity [1, 2], Bose-Einstein condensation (BEC) [3] and superfluidity [4].
In the BEC a large number of non-interacting bosonic particles undergo a phase transition at low temperatures contributing all to the same quantum ground state and, hence, expanding it on a macroscopic scale. Although ^{4}He atoms [5] are interacting, these bosonic particles show a BEC at a temperature $\sim$ 2 K, leading to a superfluid behaviour, namely a frictionless flow of the superfluid. Also the fermionic ^{3}He atoms [6] exhibit a superfluid phase at $\sim$ 3 mK. For fermionic atoms one has to distinguish whether the interaction, which leads to a formation of a spinless singlet bound pair, is strong or weak [7]. For a strong interaction the pairs are composite bosons. If the overlap between two pairs is smaller than the pair spacing (low density), the pairs can be understood as a gas of free bosonic particles and the gas undergoes a BEC below a critical temperature. Experiments confirmed the BEC in ultra-cold gases [8–11]. On the other hand, if the interaction is weak, the spatial extension of the formed pairs is greater than the pair spacing, leading to a large overlap between pairs. The ground state has the same structure as for a strong interaction but the analogy to a free bosonic bath fails. Nevertheless, a gas of these weakly-bounded pairs has a superfluid ground state. The superfluid phase vanishes above a critical temperature when the pairs break up. Certain metals, such as mercury [12, 13], show a resistanceless current at low temperatures indicating superconductivity. Bardeen, Cooper and Schrieffer [14] have explained the superconductivity by the binding of two electrons with opposite spin through a phonon-mediated attractive electron-electron interaction. Superconductivity may be viewed as a BEC of weakly-bounded Cooper pairs.

Beside of these collective phenomena which are connected to bulk phase transitions at a finite temperature, there are quantum phase transitions (QPTs) at zero temperature, where the transition is only driven by quantum fluctuations. They occur both for bulk materials, such as for heavy-fermion systems [15], and quantum impurity sys-

tems (QISs), where only a part of the material undergoes a QPT. A QIS consists of an impurity, described by a finite number of degrees of freedom (DOFs), which couple to an *infinite* bath with a macroscopically large number of non-interacting particles. For a QPT a non-thermal control parameter r is varied and the QPT occurs at the quantum critical point (QCP), which is associated with the critical parameter r_c. The QPT is only driven by quantum fluctuations and features a quantum critical region close to r_c for finite temperatures.

A possible realisation of a QIS is a non-magnetic host material (e.g. Cu, Ag and Au) with a small concentration of strongly correlated atoms (e.g. Mn or Fe), which are randomly distributed in the host material. In such correlated systems we have to take into account a finite Coulomb interaction U between pairs of valence electrons, e.g. in partially filled $3d$ or $4f$ shells in an atom. Anderson [16] has shown that a strong Coulomb interaction $U/\Gamma_0 > 1$, compared to the charge-fluctuation scale Γ_0, is crucial for the formation of localised magnetic moments. These moments are formed for the QISs stated above. Since the repulsive Coulomb interaction determines the physics, it is convenient to simplify the system to the single-impurity Anderson model (SIAM) [16]. The impurity is a spin-degenerate d level with the Coulomb repulsion U in presence of two electrons with opposite spin. The impurity is embedded in a bath of non-interacting fermionic particles, the conduction band. The hybridisation of the impurity with the conduction band enables the move of electrons from the impurity into the band and vice versa. The hybridisation competes with the Coulomb interaction on the establishment of the magnetic local moment. The SIAM has been thoroughly investigated on its equilibrium properties e.g. with Bethe ansatz technique [17, 18] and Wilson's numerical renormalisation group (NRG) [19, 20]. The hybridisation is affected by the scattering rate $\Gamma(\epsilon) \propto |\epsilon|^r$, which is given in a generalised pseudo-gap (pg) form [21] here. In metals the exponent is $r = 0$ and the non-zero hybridisation at the Fermi energy $\epsilon = 0$ features the Kondo screening of the impurity [22]. In insulators a finite bandgap at the Fermi energy prevents the Kondo screening because no electronic excitations are possible for low temperatures [23]. An infinitely narrow gap is associated with the limit $r \to \infty$. Dilute magnetic impurities in unconventional d- and p-wave superconductors [24, 25] can be described with the exponents $r = 1$ and $r = 2$. Furthermore, $r = 1$ features the physics in two-dimensional materials, such as in graphene sheets at the Dirac points [26, 27]. If we treat the generalised pg form the SIAM shows in the range $0 < r < 1/2$ a QPT between two stable fixed points (FPs) at zero temperature [25]. The two FPs are separated by a QCP at the critical Coulomb interaction U_c. For $U > U_c$ the impurity emerges a free magnetic local moment (LM) defining the LM FP. Whereas, for $U < U_c$ the local moment undergoes the Kondo screening leading to the symmetric strong coupling (SSC) FP: The impurity local moment is screened by the surrounding conduction band electron spins at low temperatures, due to resonant spin-flip scattering, forming collectively an spatial extended Kondo singlet state. As Kondo [22]

explained with a perturbative approach, these spin-flip processes between the impurity and the surrounding electron spins yield an additional logarithmic contribution to the electrical resistance. This contribution increases with decreasing temperature and, since in Matthiensen's rule [28] all contributions to the resistance are summed up, the increasing logarithmic contribution balances with the other decreasing contributions at a minimum in the resistance at a finite temperature, such as for impure gold [29] at 3.7 K. For $T \to 0$ the logarithmic contribution of the resistance diverges, which is artificial and originates from the shortcomings of the perturbative approach. Since the concentration of the impurity atoms is finite, the resistance increases to a finite value in the limit $T \to 0$.

QISs can also be useful to explain physics in lattices. For example, the Mott-insulator transition of a metal due to a strong Coulomb repulsion [30, 31] is correctly described by the dynamical mean-field theory (DMFT) [32–34]. Within the DMFT the lattice self-energy is approximated to be momentum-independent and the lattice is mapped onto an effective impurity model. This approximation becomes exact in the limit of an infinite number of next neighbours [35]. The local Coulomb interaction of one lattice site is treated non-perturbatively on the impurity and the correlations with the other lattice sites are mapped to a bath of non-interacting particles, which couple to the impurity. The properties of the impurity model are extracted from the Green's function of the lattice. In the impurity model a new self-energy is calculated and used in the lattice model again for each lattice site. This is repeated self-consistently until the self-energy is converged.

In other QISs the bath may consist of bosons, e.g. phonons or magnons, or is a mixture of bosonic and fermionic DOFs.

To describe quantum dissipation and decoherence in the limit of a two-state system, which interacts with its environment, the spin-boson model (SBM) [36, 37] is suitable to feature the essential physics. It has been applied to several effects: to friction in electron transfer and pair hopping in biomolecules [38–40], to the polarisation of an impurity spin [41–44], to quantum entanglement between a qubit and its environment [45] and to transport dynamics through quantum dots (QDs) [46–48]. A QD is a semi-conductor device and features discrete energy levels [49, 50]. The QD can be used to trap an electron or hole and may, in addition, be coupled to one or multiple leads to enable electron transport [47, 51]. Since a QD is a built object one may refer to it as an artificial atom which may be used as a qubit to realise a quantum computer [52, 53]. Since a gate voltage applied to a QD is never perfectly constant, one can either neglect this or model the fluctuations in the gate voltage as a bosonic DOF [54] and receive a Bose-Fermi quantum impurity system (BF-QIS). These BF-QISs [55–57] reveal new QPTs by an interplay of fermion-induced Kondo screening and boson-induced friction. The Bose-Fermi Anderson model (BFAM) is one example for a BF-QIS. It has been recently studied [56, 57] with the Bose-Fermi numerical renormalisation group (BF-NRG). Fur-

thermore, these BF-QISs can be used as effective impurity models within the DMFT. In this case, the bosonic DOFs on the impurity re-introduce fluctuations of the surrounding lattice f shell moments, which are neglected by the mean-field approach.

We have extended the BF-NRG [55] for BF-QISs to non-equilibrium using the time-dependent numerical renormalisation group (TD-NRG) [42]. Similar to experimental measurements [58] of the spin configuration in single-electron transistors by a sudden change in the gate voltage, we perform sudden quenches at $t = 0$ in local parameters, like the Coulomb repulsion, the level energy or the couplings to the fermionic and bosonic bath. Suitable models for such a system are the SIAM as well as the BFAM. If particle-hole (ph) symmetry is maintained, the level occupation $\langle n_{\mathrm{d}}(t)\rangle$ is constant over time and we will only present the real-time dynamics of the double occupancy $\langle D(t)\rangle$. Since both models, the SIAM and the BFAM, exhibit a rich phase diagram, we are able to present quenches within one phase and over QCPs into other phases. We will show that the local dynamics equilibrates for all regarded quenches onto a steady-state value. This value coincides with its thermal equilibrium value if the quench is within or into a strong coupling (SC) phase, otherwise the steady-state value deviates systematically from its thermal equilibrium value, since effective DOFs decouple from the system preventing the complete relaxation of the steady-state. In the former case we refer to thermalisation, since the thermal equilibrium value is reached, which itself is calculated independently by an equilibrium NRG calculation. Although it has been argued that the Wilson chain does not represent a thermal reservoir [59], we will show that thermalisation occurs.

This thesis is organised as follows: In Chap. 1 we introduce the models of interest. We start with the explanation of the Kondo effect as an example for a collective phenomenon. There, a screening of an impurity spin is achieved by the build-up of a collective mode comprising the spin DOFs of the impurity and of the conduction band. As basis for a fermionic QIS we reflect the QPT in the SIAM, and the QPT in the SBM as basis for a bosonic QIS. Then, we briefly introduce the Bose-Fermi Kondo model (BFKM) and the BFAM as simple models for BF-QISs.
In Chap. 2 we explain, in more general, what a QPT is and show how we can track its QCP. We discuss in detail the quantum criticality due to a pseudo-gap density of states (pg-DOS) in the SIAM and the BFAM. Wherein, we present the rich phase diagrams for both models and summarise the equilibrium properties of the stable FPs, as well as the unstable QCPs. A closer look on the quantum criticality in the Kondo model (KM) and the BFKM is given in App. A. At a QCP the static local response function may show an exponential behaviour revealing critical exponents. These exponents are probably connected via hyperscaling relations. A comprehensive overview of the critical exponents is given in App. B.
The numerical methods to calculate the equilibrium properties, as well as the local

real-time dynamics, are sketched in Chap. 3. We introduce Wilson's NRG and explain the modifications to incorporate additional bosonic DOFs revealing the BF-NRG. The chapter is completed with on overview of the TD-NRG.
In Chap. 4 we are interested in the local dynamics in the SIAM questioning thermalisation and leading time scales. To enable a QPT between a SSC and a LM phase, we use a pg coupling function $\Gamma(\epsilon) \propto |\epsilon|^r$. We will show that the local dynamics within or into the SSC phase thermalises nicely. Whereas, within or into the LM phase, a deviation between the steady-state value and its thermal equilibrium emerges due to a decoupling of an effective local moment from the system. We will enlighten a systematic dependence of this deviation on a crossover energy scale $T^\star$ tracking the build-up of the effective local moment, which combines local DOFs and DOFs of the whole conduction band. Furthermore, this crossover scale can be related to a spatial extension of the effective local moment using the Fermi velocity of the host: $\xi^\star = hv_\mathrm{F}/T^\star$. Since this spatial extension is described accurately with the NRG, we will compare our dynamics with recent data of a time-dependent Gutzwiller approach [60]. In contrast, this approach restricts the effective local moment formation only on the impurity site, leading to an overestimation of the Coulomb repulsion and hence to a strong oscillatory dynamics.
We have extended the SIAM to the BFAM through the coupling to an additional bosonic bath. We will analyse the real-time dynamics in the BFAM in Chap. 5. Using our novel approach, we will address the question how the bosonic bath influences the real-time dynamics in comparison to the purely fermionic model. For a strongly-coupled bosonic bath, which is characterised by its spectral function $J(\omega) \propto \omega^s$, the bosonic localised (L) phase emerges. The QCP separating the L phase from the SSC phase has critical exponents depending on the specific combination of the bath exponents (r, s) [57]. Three types of combinations can be distinguished: For a certain combination of the parameters (r, s), the critical exponents of the fermionic model are obtained, and therefore, the combination (r, s) is of the F type. While for another combination (r, s) the exponents of the bosonic model are observed, defining the B-type combinations. For a third mixed combination the critical exponents do not correspond to ones of these limiting models. We will show that for a F-type combination, the dynamics of the BFAM can completely be expressed by the dynamics of a SIAM with properly chosen parameters. In equilibrium the bosonic bath renormalises the Coulomb interaction $U > 0$ to smaller or even attractive values. For the B-type, this occurs at lower energy scales compared to the F-type. Hence, it slows down the dynamics at intermediate times compared to corresponding dynamics in the SIAM where the Coulomb interaction reveals its full influence directly from the beginning. Furthermore, we will show that the L phase and the LM phase are mirror images of each other with an effective charge moment or an effective local moment, respectively, decoupling from the system and hence preventing thermalisation of the local dynamics. The more spa-

tially extended the effective moment the stronger the steady-state value deviates from its thermal equilibrium value. Whereas, quenches within or into the SSC phase thermalise within the accuracy of the TD-NRG. We will present that this is also fulfilled for quenches starting from a ph symmetry broken initial configuration.
To conclude our investigations on BF-QISs, we will briefly discuss the real-time spin polarisation $\langle S_z(t)\rangle$ of an initially polarised spin in the BFKM in Chap. 6. We will enlighten that the decay of the polarisation is induced by the coupling to the fermionic bath and undergoes a friction-induced slowdown due to the bosonic coupling.
We summarise our results in Chap. 7.

Chapter 1

Models

The interest in quantum impurity systems (QISs) arose by a measured unexpected minimum in the electrical resistance at a low temperature for apparently pure metals, such as gold [29]. Further investigations revealed that the metal was not completely pure and contained a small concentration of magnetic impurities, such as iron or manganese atoms. These impurities are randomly distributed and well dispersed. Hence, we can effectively describe such a QIS by a Hamiltonian

$$H_{\mathrm{QIS}} = H_{\mathrm{imp}} + H_{\mathrm{bath}} + H_{\mathrm{coup}} \tag{1.1}$$

modelling one impurity in a surrounding bath continuum. The Hamiltonian H_{imp} describes the local impurity, e.g. represented by a spin-1/2 particle. The Hamiltonian H_{bath} refers to the bath which is in comparison *infinite* and consists of non-interacting particles, e.g. the conduction band electrons of a host metal. Consequently, the coupling term H_{coup} mediates the interaction between both subsystems.
Although the minimum in the electrical resistance has already been measured in the early 1930s, it took nearly 30 years until Kondo [18, 22] provided a physical explanation for this effect. We will explain the Kondo effect in Sec. 1.1. Kondo's perturbative ansatz revealed the existence of the minimum. Nevertheless, his ansatz fails in describing the low-temperature physics accurately. It took another 10 years until Wilson [19] developed his numerical renormalisation group (NRG) in 1975. This numerical approach captures the low-temperature physics accurately and will be presented in Sec. 3.1.
In the following we introduce the single-impurity Anderson model (SIAM) in Sec. 1.2 and the spin-boson model (SBM) in Sec. 1.3 as basic fermionic or rather bosonic QIS. Both exhibit a quantum phase transition (QPT) with respect to a variation in a non-thermal control parameter [61]. Furthermore, we combine bosonic and fermionic baths and present in Sec. 1.4 the Bose-Fermi Kondo model (BFKM) and the Bose-Fermi Anderson model (BFAM) as exemplary Bose-Fermi quantum impurity systems (BF-QISs).

1.1 The Kondo model

The temperature dependence of the electrical resistance in metals is expressed by the sum of different scattering contributions, known as Matthiensen's rule [28], here for low temperatures:

$$\rho(T) = \rho_0 + aT^2 + bT^5 \quad . \tag{1.2}$$

Electron scattering processes lead to a contribution proportional to T^2. Through the vibration of the lattice structure an additional electron-phonon contribution proportional to T^5 is gained. This electron-phonon interaction is present for temperatures below the Debye temperature. For higher temperatures all vibrational modes are aggregated and the contribution becomes linear in T.
In Fig. 1.1 a sketch shows the resistance for low temperatures in different cases. With decreasing temperature the electron-electron and the electron-phonon interaction vanish. Therefore, for a pure metal the resistance decreases down to a residual resistance ρ_0 [29]. This is represented by the blue curve. Some metals become superconducting (green curve) below a critical temperature T_c and the resistance vanishes at T_c to zero. On the other hand, for a metal which contains a small concentration of magnetic impurities, e.g. iron atoms in gold, the resistance increases again for temperatures $T < T_K$ below the Kondo temperature. This is called the Kondo effect (red curve). Several experimental measurements showed a linear dependence between the residual resistance and the concentration of the impurities in the host metal [62].

To gain some understanding in the physics of the Kondo effect, Kondo [22] made some simple assumptions: The concentration of the impurity atoms in the host material is small and the impurities are well distributed, hence, the system is represented by a single impurity atom interacting with an uncorrelated host metal. Kondo described the impurity atom by a spin-1/2 particle[1]. This impurity spin interacts with the local spin density of the surrounding electrons in the host metal on the impurity. Kondo showed that this interchange coupling tends to infinity in the limit $T \to 0$.
The Hamiltonian of this so-called Kondo model (KM) is given by

$$H_{\mathrm{KM}} = \sum_{k,\sigma} \epsilon_{k,\sigma} c^\dagger_{k,\sigma} c_{k,\sigma} + J\vec{S}\vec{s} \tag{1.3}$$

with

$$\vec{s} = \frac{1}{2N} \sum_{k,k'} \sum_{\alpha,\beta} c^\dagger_{k,\alpha} \vec{\sigma}_{\alpha,\beta} c_{k',\beta} \tag{1.4}$$

[1] In Kondo's explanation [18, 22] of the Kondo effect, he uses a spin-1/2 as impurity for the iron atoms, although it is more reasonable that iron atoms have a spin $S = 3/2$ [63].

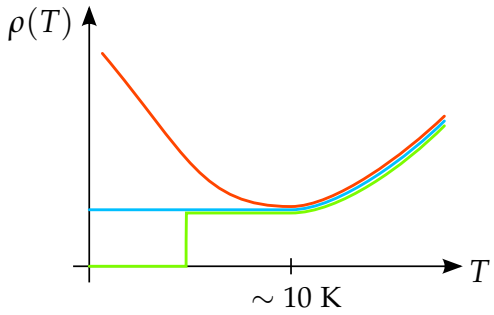

Figure 1.1: Electrical resistance $\rho(T)$ in dependence of the temperature T for a pure metal (blue curve), for a superconductor (green curve) and for a metal with a small concentration of randomly distributed impurities (red curve) which cause the Kondo effect. Taken from [64].

being the projection of the conduction band electron spins onto the place of the impurity. The operator $c^{\dagger}_{k,\sigma}$ creates an electron with spin σ and momentum k in the conduction band, which has the dispersion $\epsilon_{k,\sigma}$. The impurity spin $\vec{S}$ couples via the Kondo coupling J to the conduction band spin $\vec{s}$. N is the number of lattice places and $\vec{\sigma} = (\sigma_x, \sigma_y, \sigma_z)^T$ contains the Pauli matrices.

A ferromagnetic coupling $J < 0$ favours a parallel polarisation of the conduction band spins in the vicinity of the impurity. Whereas, an antiferromagnetic coupling $J > 0$ favours an antiparallel orientation of the spins and enables spin-flip scattering processes between two energy-degenerated states. Kondo treated this system with perturbation theory up to third order in the coupling J and revealed that through spin-flip scattering processes an additional contribution to the resistance in Eq. (1.2) proportional to $\ln(T)$ emerges [22]. Hence, the resistance shows a minimum at a finite temperature where the decreasing contributions of Eq. (1.2) and the increasing Kondo contribution balance. Since in the limit $T \to 0$ the logarithmic contribution diverges, the predicted behaviour of the resistance is artificial. The amount of impurities in the host metal is small and the resistance has to reach some finite value for $T \to 0$. This logarithmic singularity is also called the infra-red problem within quantum-field theories.
Consequently, there is a finite temperature below which the perturbative approach fails. This is the Kondo temperature

$$T_K \propto D e^{-\frac{1}{\rho J}} \tag{1.5}$$

with ρ being the density of states (DOS) of the conduction band and ρJ being the bare coupling constant. Kondo showed that the effective scattering rate becomes of the order $O(1)$ at this exponentially small temperature.
Over the time it turned out, that the Kondo temperature T_K represents a crossover temperature below which all physical quantities show universal behaviour. Below T_K

a Fermi-liquid phase is formed. The resistance and the impurity contribution to the magnetic susceptibility obey a scaling law proportional to $(T/T_K)^2$.

1.1.1 The poor man's scaling

In the late 1960s Anderson [65] has gained further insight in the Kondo problem with perturbative renormalisation group (RG) techniques. By his so-called *poor man's scaling* an effective low-energy model is generated by integrating out the high-energy contributions. His approach can also treat the more complex anisotropic KM which is described by the Hamiltonian

$$H_{\mathrm{AKM}} = \sum_{k,\sigma} \epsilon_{k,\sigma} c^\dagger_{k,\sigma} c_{k,\sigma} + J_z S_z s_z + \frac{1}{2} J_\perp \left(s^+ S^- + s^- S^+ \right) \quad . \tag{1.6}$$

Here, the interaction is split into a polarisation part J_z and a spin-flip component $J_\perp$. The anisotropic KM corresponds to the isotropic KM in Eq. (1.3) for $J = J_z = J_\perp$. The conduction band has a non-vanishing DOS at the Fermi energy. Although the high-energy part of the DOS may be rather complicated for real materials such as gold, the low-temperature physics is only driven by the DOS near the Fermi energy $\epsilon = 0$. Therefore, we can replace the real DOS by a simple assumption,

$$\rho(\epsilon) = \sum_k \delta(\epsilon - \epsilon_k) = \frac{1}{2D} \Theta(D - |\epsilon|) \quad , \tag{1.7}$$

namely a constant DOS in the range $[-D, D]$ with $2D$ being the bandwidth. This consequently alters slightly the high-energy physics but models the low-energy physics accurately.

The key idea in the perturbative RG is to generate an effective low-energy Hamiltonian and to map it onto a KM with effective parameters. This is reproduced iteratively until a FP is reached. If an effective Hamiltonian $H^\star$ stays constant under a RG step $\mathcal{R}$, we talk about a FP Hamiltonian $\mathcal{R}(H^\star) = H^\star$.
To generate the effective low-energy Hamiltonian, we divide the Hamiltonian H into a diagonal part H_D and an off-diagonal part V:

$$H = \underbrace{PHP + QHQ}_{=H_D} + \underbrace{PHQ + QHP}_{=V} \quad . \tag{1.8}$$

Here we use the projector P for the low-energy states and $Q = 1 - P$ for the high-energy states. The off-diagonal part V connects the high- and low-energy states. To

incorporate the virtual excitations of the high-energy part into an effective low-energy Hamiltonian we transform the Hamiltonian by a unitary transformation[2]

$$H' = \mathrm{e}^{S} H \mathrm{e}^{-S} = H + \sum_{n=1}^{\infty} \frac{1}{n!} [S, H]_n \tag{1.9}$$

$$= H_{\mathrm{D}} + V + [S, H_{\mathrm{D}}] + [S, V] + \sum_{n=2}^{\infty} \frac{1}{n!} [S, H]_n \quad . \tag{1.10}$$

Our aim is to eliminate the contributions of V in first order such that the low-energy part of H' contains the virtual excitations only in second order. This is a Schrieffer-Wolff transformation (SWT) [67] and the linear term vanishes for

$$[S, H_{\mathrm{D}}] = -V \quad . \tag{1.11}$$

Then, the transformed Hamiltonian reads

$$H' = H_{\mathrm{D}} + \frac{1}{2}[S, V] + \frac{1}{2}[S, [S, V]] + \sum_{n=3}^{\infty} \frac{1}{n!} [S, H]_n \quad . \tag{1.12}$$

We assume that the eigenstates and eigenenergies of the diagonal part are known,

$$H_{\mathrm{D}}|p\rangle = E_p|p\rangle \quad \text{and} \quad H_{\mathrm{D}}|q\rangle = E_q|q\rangle \quad , \tag{1.13}$$

with p labelling the low-energy part and q the high-energy part. This additionally leads to the projectors

$$P = \sum_p |p\rangle\langle p| \quad \text{and} \quad Q = \sum_q |q\rangle\langle q| \quad . \tag{1.14}$$

Here we have assumed that the interaction in H_{D} between the low- and high-energy part is small and that we can, therefore, build the projectors simply of the diagonal part H_{D} rather than of the full Hamiltonian H.

Hence, the matrix elements of the transformation are

$$S_{p,q} = \frac{V_{p,q}}{E_p - E_q} \tag{1.15}$$

and the second-order correction of the low-energy part is given by

$$\Delta H_{p,p'} = \langle p|P\frac{1}{2}[S, V]P|p'\rangle \tag{1.16}$$

$$= \frac{1}{2}\sum_q V_{p,q} V_{q,p'} \left(\frac{1}{E_p - E_q} + \frac{1}{E_{p'} - E_q} \right) \quad . \tag{1.17}$$

[2] We use theBaker-Campbell-Hausdorff formula [66] to calculate the transformation.

If we neglect the higher order corrections we gain the effective low-energy Hamiltonian $H' = PHP + \Delta H$. We do not go into the details of the derivation, which can be looked up in Ref. [65]. If we assume an infinitesimally small high-energy part, which is integrated out, and repeat the procedure iteratively, we can gain by this perturbative RG approach differential equations in the coupling constants. For the Hamiltonian in Eq. (1.6) one can derive two coupled differential equations

$$\frac{\mathrm{d}\tilde{J}_\perp}{\mathrm{d}\ln D} = -\tilde{J}_\perp \tilde{J}_z \quad \text{and} \quad \frac{\mathrm{d}\tilde{J}_z}{\mathrm{d}\ln D} = -\tilde{J}_\perp^2 \quad . \tag{1.18}$$

Here D is the effective bandwidth, an energy scale which divides the high-energy from the low-energy regime, and $\tilde{J} = J\rho$ is the dimensionless coupling strength. Combining both equations leads to the relation $\tilde{J}_z^2 - \tilde{J}_\perp^2 = \text{const}$ which means that the parameters $\tilde{J}_z$ and $\tilde{J}_\perp$ are connected by a hyperbolic curve in the parameter space $(\tilde{J}_z, \tilde{J}_\perp)$, as depicted in Fig. 1.2. Furthermore, the flow equations in Eq. (1.18) have two FPs. The trivial FP is given for $\tilde{J}_z^\star = \tilde{J}_\perp^\star = 0$. There, the spin is decoupled from the conduction band. This LM FP is unstable for any finite $\tilde{J}_z, \tilde{J}_\perp > 0$. The second FP is the stable SC FP. It is characterised by diverging couplings $\tilde{J}_z^\star, \tilde{J}_\perp^\star \to \infty$. In this FP the impurity spin forms a bond state with the spins of the conduction band electrons and is, hence, completely screened by the conduction band electrons.
The flow of the couplings $\tilde{J}_z$ and $\tilde{J}_\perp$ is sketched in Fig. 1.2. The flow is indicated by the incoming and outgoing arrows. In addition to the two FPs above, there are two lines of FPs. One line of stable FPs when the flow is stopped with $\tilde{J}_\perp^\star = 0$ for a ferromagnetic $\tilde{J}_z^\star < 0$ and one line of unstable FPs when the flow begins at $\tilde{J}_\perp^\star = 0$ for an antiferromagnetic $\tilde{J}_z^\star > 0$. In the former case the spins of the conduction band electrons in the vicinity of the impurity are polarised parallel to the impurity spin. If we switch on the spin-flip term with any finite $\tilde{J}_\perp > 0$ it does not affect the polarised spin state and, therefore, these FPs are stable. Whereas in the latter case for the antiferromagnetic $\tilde{J}_z > 0$ the spins of the conduction band electrons near the impurity are aligned antiparallel to the impurity spin. If we switch on any finite $\tilde{J}_\perp > 0$, the impurity spin and the conduction band spins interact via spin-flip scattering. Consequently these FPs are unstable.

For the isotropic Hamiltonian in Eq. (1.3), the differential equation is given by

$$\frac{\mathrm{d}\tilde{J}}{\mathrm{d}\ln D} = -\tilde{J}^2 \tag{1.19}$$

and via integration we gain

$$\tilde{J} = \frac{\tilde{J}_0 \ln(D/D_0)}{\tilde{J}_0 \ln(D/D_0) + 1} \quad . \tag{1.20}$$

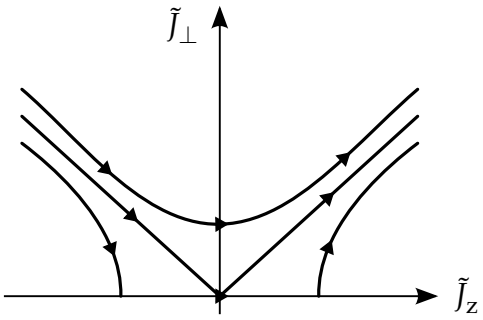

Figure 1.2: Flow of the coupling constants $\tilde{J}_z$ and $\tilde{J}_\perp$ with the SC FP in the upper right corner ($\tilde{J}_z, \tilde{J}_\perp \to \infty$). Taken from [65].

This solution breaks down when the denominator diverges for $D = T_K$. Therefore, we get the low-energy scale

$$T_K = D_0 e^{-\frac{1}{J_0}} \tag{1.21}$$

which is the original Kondo temperature, cf. Eq. (1.5). With Anderson's perturbative RG approach [65] different low-energy FPs have been revealed. Nevertheless, due to its perturbative nature the accurate description of the low-energy physics below T_K fails. This was first achieved by Wilson's NRG [19], which will be presented in detail in Sec. 3.1

1.1.2 Further Kondo models

Due to the great success of Wilson's NRG in investigating the physics at zero temperature, different classes of KMs have been derived and expansions to more complex impurities, like the SIAM in Sec. 1.2, have been done. In general, real magnetic impurities in metals have both orbital and spin DOFs and the resulting low-energy effective impurity models can be very complicated [18]. If the ground state is an orbital singlet, e.g. Mn atoms in metals, the effective impurity model can be described by the multichannel Kondo model (MCKM) [68]. Its Hamiltonian is extended from Eq. (1.3) with a spin of size S and a sum over n conduction bands. This MCKM shows for an antiferromagnetic coupling $J > 0$ a complete screening of the Kondo spin for $n = 2S$, as the standard KM, and hence behaves as a Fermi liquid.
In the case $n > 2S$, for example in the two-channel Kondo model (TCKM) [69, 70] the spin-1/2 couples to two bands and is overscreened in the zero-temperature limit. Both conduction bands try to screen the impurity spin at once, hence, a new net spin-1/2 is formed with a zero-temperature entropy $\ln(2)/2$, indicating a half-fermionic excitation, and the spin susceptibility shows a logarithmic divergence. The SC FP, which shows Fermi-liquid behaviour for a single channel, is unstable in this case. A new intermediate-coupling FP emerges and shows non-Fermi-liquid behaviour.

For $n < 2S$, the Kondo impurity is underscreened meaning that the coupled bands are unable to screen the full spin and a residual moment remains in the zero-temperature limit. One example for the case $1 = n < 2S$ is a single band with a spin-1 particle [71]. Interestingly, the spectrum of the zero-temperature FP corresponds to the one of a standard ferromagnetic spin-1/2 KM. In the limit $T \to 0$, this residual moment vanishes very slowly. The thermodynamic quantities show logarithmic corrections at low temperatures, instead of power-law corrections as for the completely screened case. Therefore, they are sometimes named singular Fermi liquids [72]. Nevertheless, the underscreened KM is a Fermi liquid.
Another nice feature appears for a spin-1 QD with two bands [73]. There, $n = 2S$ is fulfilled but the screening of the Kondo spin takes place in two steps. First the impurity spin is screened half at T_{K1} and then completely at a temperature $T_{\mathrm{K2}} < T_{\mathrm{K1}}$. Within the regime $T_{\mathrm{K2}} < T_{\mathrm{K}} < T_{\mathrm{K1}}$ the system shows the underscreened behaviour.

Furthermore, to derive new types of KMs, one can expand the impurity to two or more spins. The two-impurity Kondo model (TIKM) consists of two spin-1/2 particles at some distance R which couple to one conduction band [74, 75]. Both spins can interact indirectly with each other via the conduction band. This leads to the Ruderman-Kittel-Kasuya-Yosida (RKKY) interaction $\tilde{I}_{\mathrm{RKKY}}$ [76–79], which was already described by second-order perturbation theory in the 1950s. The RKKY interaction is dependent on the distance R of both spins. It can be antiferromagnetic and ferromagnetic in dependence of R and decreases with R^{-3} for large distances so that in the limit $R \to \infty$ both spins are decoupled from each other. Combined with a direct interaction between both spins, an effective interaction $\tilde{I}_{\mathrm{eff}}$ emerges due to the competition of the local Kondo exchange and the intersite RKKY interaction. For $\tilde{I}_{\mathrm{eff}} \to -\infty$ both spins form a spin-1 which interacts antiferromagnetically with two conduction band channels (even and odd parity). The coupling strengths $\tilde{J}_{e/o}(k)$ are in general energy dependent. For $\tilde{I}_{\mathrm{eff}} \to +\infty$ both spins form an intersite non-magnetic singlet and the Kondo effect is absent. It is argued that a QPT occurs between these two limits, the magnetic and the non-magnetic ground state [75, 80]. However, a QPT is only present if the coupling strengths are approximated by $\tilde{J}_{e/o}(k_{\mathrm{F}})$ at the Fermi momentum k_{F} for a constant DOS. If one considers the full energy-dependent coupling strengths, the QPT in the TIKM is replaced by a simple crossover [20].

1.2 The single-impurity Anderson model

A slightly more complex model is the single-impurity Anderson model (SIAM). It deals with a spin-degenerate energy level as impurity, which can carry zero to two electrons. This generalisation leads to new interesting physics such as charge fluctuations at the impurity. The SIAM was introduced and first investigated by Anderson [16] in the early

1960s. His investigation was a first attempt on the description of localised magnetic states in metals and makes use of a self-consistent Hartree-Fock calculation. There, the magnetic state in the d shell depends on the free electron DOS, the Coulomb repulsion U within the d shell and the s-d admixture matrix element.

The Hamiltonian of the single-impurity Anderson model (SIAM) is given by

$$H_{\mathrm{SIAM}} = H_{\mathrm{SIAM,imp}} + H_{\mathrm{SIAM,bath}} + H_{\mathrm{SIAM,coup}} \quad . \tag{1.22}$$

The impurity is coupled to a conduction band, which is given by

$$H_{\mathrm{SIAM,bath}} = \sum_{k,\sigma} \epsilon_k c^\dagger_{k,\sigma} c_{k,\sigma} \tag{1.23}$$

and consists of non-interacting electrons. The fermionic operator $c^\dagger_{k,\sigma}$ creates an electron with spin σ and momentum k in the conduction band. The energy dispersion of the conduction band is given by ϵ_k. The Hamiltonian of the impurity, which consists of the spin-degenerate d-shell energy level, is given by

$$H_{\mathrm{SIAM,imp}} = \sum_{\sigma} \epsilon_{\mathrm{d}} d^\dagger_\sigma d_\sigma + U d^\dagger_\uparrow d_\uparrow d^\dagger_\downarrow d_\downarrow \quad . \tag{1.24}$$

Here, $d^\dagger_\sigma$ creates an electron at the impurity with spin σ and the level energy ϵ_{d}. In presence of two electrons on the impurity site (in the d shell) an additional repulsive Coulomb energy U has to be paid. The coupling term, Anderson's s-d admixture,

$$H_{\mathrm{SIAM,coup}} = \sum_{k,\sigma} V_k \left(c^\dagger_{k,\sigma} d_\sigma + d^\dagger_\sigma c_{k,\sigma} \right) \quad , \tag{1.25}$$

enables the hopping of an electron with spin σ and the momentum k from the impurity into the bath and vice versa. The hybridisation and the energy-dependent DOS $\rho(\epsilon) = \sum_k \delta(\epsilon - \epsilon_k)$ of the conduction band enter the model only in combination in the scattering rate

$$\Gamma(\epsilon) = \pi \sum_k \delta(\epsilon - \epsilon_k) V_k^2 = \pi \rho(\epsilon) V_0^2(\epsilon) \quad , \tag{1.26}$$

if we assume a k-independent hybridisation $V_0(\epsilon)$. While for gapless Fermi systems the assumption of a constant DOS $\rho_0 = 1/(2D)$ and a constant hybridisation is a well-proved choice, some Fermi systems show a pg at the Fermi energy; e.g. for d superconductors [24, 81] or graphene sheets [27, 82] $\Gamma(\epsilon)$ is a complicated function of energy. Nevertheless, it has been realised [25, 83, 84] that for the low-energy physics only the spectrum close to the Fermi energy is relevant. Therefore, a power-law scattering rate

$$\Gamma(\epsilon) = \Gamma_0 \, (r+1) \left| \frac{\epsilon}{D} \right|^r \Theta(D - |\epsilon|) = \Gamma_0 \, \rho_r(\epsilon) \tag{1.27}$$

is a good assumption. The energy dependence is completely shifted into the pg-DOS

$$\rho(\epsilon) = \sum_k \delta(\epsilon - \epsilon_k) = \rho_0 \cdot \rho_r(\epsilon) = \frac{1}{2D} \cdot (r+1) \left|\frac{\epsilon}{D}\right|^r \Theta(D - |\epsilon|) \tag{1.28}$$

with the bath exponent r. $\Gamma_0 = \pi\rho_0 V_0^2$ is the charge-fluctuation scale. While $r = 0, 1, 2$ are prototypical experimental realisations [81], we take r as an arbitrary parameter. The use of a pg-DOS for impurity models was imposed in the 1990 by Withoff and Fradkin [21] who examined the pseudo-gap Kondo model (pg-KM) with a poor man's scaling approach.

While for the constant DOS the SIAM exhibits only the SC FP at zero temperature, the phase diagram becomes richer by the pg-DOS. Due to the pseudo-gap fewer DOFs are present near the Fermi energy with increasing $r > 0$. For simplicity we assume ph symmetry here. In the range $0 < r \leq 1/2$ the competition between the coupling to the bath according to Γ_0 and the Coulomb repulsion U leads to a QPT. If the charge-fluctuation scale Γ_0 is strong compared to the Coulomb repulsion U, the known Kondo screening of the impurity DOFs occurs. This classifies the SC FP, due to the pseudo-gap the impurity DOFs are only fractionally screened. In the opposite case, a strong Coulomb repulsion favours an unscreened local moment. The DOFs near the Fermi energy are too weak to screen the moment. This characterises the LM FP. A QPT between these two stable FPs emerges. Its unstable QCP is dependent on the ratio U/Γ_0 or in other words on a critical charge-fluctuation scale $\Gamma_c(U)$. For a bath exponent $1/2 < r$, the DOFs near the Fermi energy are in total too weakly coupled and the SC FP disappears.

Furthermore, as Fig. 1.3 illustrates, the phase boundary between the SC and LM phase is a line of QCPs depending on the bath exponent r. The presence or absence of ph symmetry additionally effects the properties of the FPs. This is discussed in detail in Sec. 2.3. Briefly, in the ph-symmetric case the critical coupling Γ_c diverges for $r \to (1/2)^-$ and only the LM FP remains for $r > 1/2$. Whereas, for ph asymmetry no divergence occurs since the SC FP becomes the stable asymmetric strong coupling (ASC) FP for $r > r^* \sim 0.375$ and the QPT between the ASC an the LM FP is present for all $r > r^*$.

Another possible realisation for the DOS is a hard gap [23]

$$\rho_{\mathrm{hg}}(\epsilon) = \frac{1}{2(D-\Delta)} \Theta(|\epsilon| - \Delta)\, \Theta(D - |\epsilon|) \tag{1.29}$$

with a bandgap width 2Δ. In presence of ph symmetry, the SIAM with the hard gap features only the LM FP. This is reasonable because no exications are possible within the gap and, hence, no screening of the impurity occurs. An infinitely small hard gap is equivalent to the pg-DOS in the limit $r \to \infty$. For ph asymmetry the

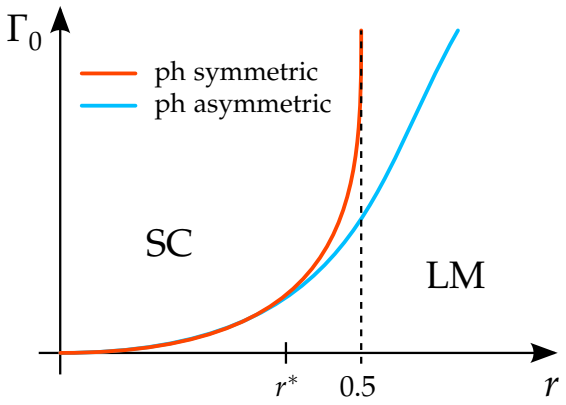

Figure 1.3: Sketch of the phase boundary Γ_c for a fixed U between the SC and LM phase in dependence of the bath exponent r for ph symmetry and asymmetry. After [87].

impurity DOFs are screened completely if $\Delta \ll T_K$. This refers to the ASC FP. Kondo screening is suppressed, if the bandgap is bigger than T_K, and an unscreened moment remains [23, 85, 86]. Anyway, in this thesis the hard-gapped DOS is not part of further investigations.

1.3 The spin-boson model

So far we discussed fermionic QISs with an impurity represented by either a spin or an energy level. This section deals with the SBM: A spin-1/2 impurity couples to a bath of non-interacting bosonic modes. The SBM arises naturally in the description of a quantum dissipative system (QDS), as it is done in Ref. [36]. For an arbitrary real system, which shows a potential $V(q)$ with two separate minima regarding a continuous DOF q, the SBM is sufficient to describe the essential physics. In Fig. 1.4 such a double-well potential in the two-state limit is shown. If we assume that the barrier V_B between both minima is large compared to the energy hierarchy $\hbar\omega_0 \sim \hbar\omega_- \sim \hbar\omega_+$ of both minima, the quantum motion is in either well separately semi-classical. Within each well the separation between the ground state and the first excited state is of the order $\hbar\omega_0$. If the bias ϵ between the two ground states of the wells is small compared to the ground state energies, $\epsilon \ll \hbar\omega_0$, the system is effectively restricted to the two-dimensional Hilbert space of the two ground states in the low-temperature limit $k_B T \ll \hbar\omega_0$. Furthermore, the model allows a tunnelling between both wells according to a typical matrix element Δ, as indicated by the dashed left-right arrow in Fig. 1.4. Under the assumption $V_B \gg \hbar\omega_0$ the tunnelling is exponentially small compared to ω_0 and an admixture of excited states of the system into the ground states may be neglected. Consequently, here we deal with a two-state system, which can be easily written with the help of the Pauli matrices $\vec{\sigma} = (\sigma_x, \sigma_y, \sigma_z)^T$.

It is adequate for most purposes that the coupling of the two-state system to its en-

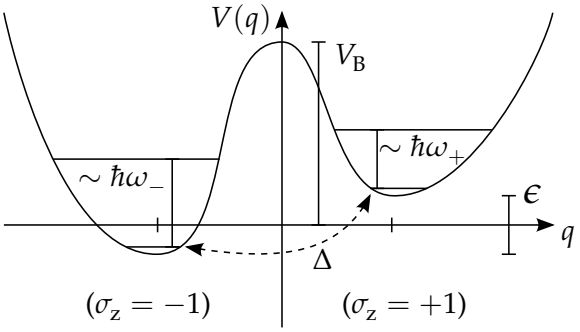

Figure 1.4: Sketch of a double-well potential to motivate the impurity of the SBM. Both ground states differ in the energy ϵ and a tunnelling according to Δ between both wells is possible. V_B is the barrier height separating both wells. The ground state of each well can be identified with a spin state: $\sigma_z = \pm 1$. After [36].

vironment is mediated through $\sigma_z V$ with V being some operator of the environment. Any interaction proportional to σ_y and σ_z, which have only off-diagonal elements in the basis of σ_z, has to be of the order of the exponentially small tunnelling amplitude [36]. This interaction is not necessarily unimportant in special cases but is neglected at this stage. Furthermore, the environment in such QDS can be described by a set of harmonic oscillators with a coupling linear in the oscillator elongation [88].
Hence, the full Hamiltonian of the spin-boson model (SBM) reads

$$H_{\mathrm{SBM}} = \frac{\epsilon}{2}\sigma_z - \frac{\Delta}{2}\sigma_x + \frac{1}{2}\sigma_z \left(\sum_q \lambda_q \left(\phi_q^\dagger + \phi_q \right) \right) + \sum_q \omega_q \phi_q^\dagger \phi_q \quad . \tag{1.30}$$

The first two terms describe the impurity. Through the energy splitting term the spin-up and spin-down state differ in energy by ϵ. The tunnelling between both spin states is mediated by the tunnelling amplitude Δ. The third term describes the friction due to the coupling of the z polarisation to the elongation $X_q = (\phi_q^\dagger + \phi_q)$ of each bosonic mode q of the environment. The last term, consequently, describes the environment of non-interacting bosonic modes with $\phi_q^\dagger$ creating an excitation with energy ω_q.

For a better understanding of the friction term we assume $\Delta = 0 = \epsilon$. Then, the Fock space of the SBM separates with respect to the σ_z basis into a spin-up and a spin-down subspace. For example in the spin-up subspace the elongations $\{X_q\}$ of the friction term can be incorporated into new free bosonic bath modes $\tilde{\phi}_q^\dagger = \phi_q^\dagger - \Theta_q$. These modes are displaced bosonic modes with $\Theta_q = \lambda_q/(2\omega_q)$ and they are shifted in the opposite direction in the opposite spin sub-space. This leads to an impurity entropy $S_{\mathrm{imp}} = \ln(2)$ because there are two possible ground states. Whereas, if the tunnelling amplitude is finite $\Delta > 0$ and we decouple the impurity from the bath, the ground state is a non-degenerated admixture of the spin-up and spin-down state.

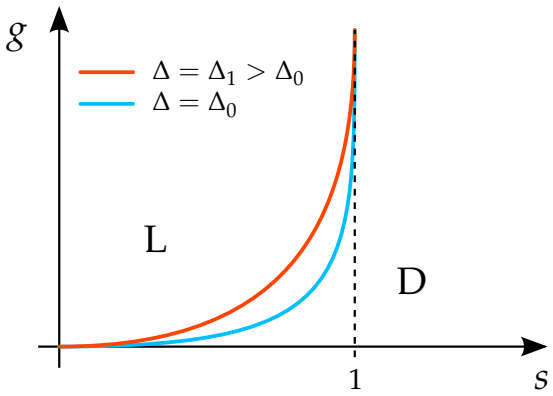

Figure 1.5: Schematic phase diagram of the SBM in the plane spanned by the coupling parameter g and the bath exponent s. With smaller tunnelling parameter Δ the phase boundary is shifted to smaller couplings. After [37].

The bosonic bath consists of independent bosonic modes with only positive frequencies. The bath can be completely described by its spectral bath function

$$J(\omega) = \pi \sum_q \lambda_q^2 \delta(\omega - \omega_q) \quad . \tag{1.31}$$

So far, the parameters λ_q are arbitrary and depend on the physical system of interest [89]. For the low-temperature physics, similarly to the fermionic bath, the spectral function can be replaced by an easier function which captures the essential low-energy physics. In the limit $T \to 0$, the physics is dominated by the low-frequency modes and, hence, for $\omega \to 0$ real systems show a dependence $J(\omega) \sim \omega^s$. This leads to the standard power-law form of the spectral function [36]

$$J(\omega) = 2\pi g {\omega_c}^{1-s} \omega^s \, \Theta(\omega)\Theta(\omega_c - \omega) \quad . \tag{1.32}$$

This form includes a hard high-frequency cut-off ω_c and a dimensionless parameter g, which determines the coupling strength between the impurity and the bath. The bosonic bath exponent s determines the type of the bath: For $0 < s < 1$ it is sub-ohmic [90], for $s = 1$ it is ohmic [36] and for $1 < s$ it is super-ohmic [91]. For example, the ohmic type can be mapped onto the anisotropic KM [92].

The SBM with $\epsilon = 0$, $\Delta > 0$ and $g > 0$ has two stable FPs within the sub-ohmic regime $0 < s < 1$: the localised (L) and the delocalised (D) FP. A QCP separates these two stable FPs at a critical $g_c(\Delta, s)$ and the phase boundary in dependence of the bath exponent s is depicted in Fig. 1.5. For the L FP, the tunnel amplitude Δ is renormalised to zero by the coupling to the bosonic bath. This corresponds to a spontaneous broken symmetry. The spin has to be either in the one or the other ground state with $|\langle S_z \rangle| > 0$ leading to a two-fold-degenerated ground state with impurity entropy $S_{\text{imp}} = \ln(2)$. Consequently, we are talking about localisation [37, 93]. The eigenenergies in the L FP

are also two-fold degenerated. Furthermore, under localisation an initially prepared impurity spin state, e.g. $\langle S_z \rangle = 1/2$, remains unchanged under time evolution. On the other hand, if a finite renormalised tunnelling amplitude Δ_{ren} remains, the ground state is a superposition of the spin-up and spin-down state with $|\langle S_z \rangle| = 0$ and the impurity entropy $S_{\text{imp}} = \ln(1)$ vanishes. Then, we are talking about the D FP.
In the ohmic case, $s = 1$, the SBM as well undergoes the QPT between the L and D phase. Here, the QPT is of the Kosterlitz-Thouless type, which is explained in Sec. 2.1. If we increase the bath exponent further to $1 < s$, the SBM is in the super-ohmic regime. There, no QPT occurs because for all g the bosonic bath couples too weakly to the impurity and a finite Δ_{ren} remains [93]. Consequently, the D FP is the only stable FP for the super-ohmic regime.

In the sub-ohmic regime ($0 < s < 1$) the SBM can be used to describe the physics of a small QD which is part of a mesoscopic ring and capacitively coupled to an external circuit with a dissipative impedance [94]. The external circuit is the source of the quantum fluctuations which drive the QPT. The bosonic bath models the quantum fluctuations of the electromagnetic field of the external circuit since it is never perfectly constant. In the context of quantum computation [52, 53, 95] the SBM is applicable to simple realisations of qubits: For example, the qubit is an electron spin confined in a QD [96]. Due to its interaction with the environment the qubit is perturbed and information is lost [97]. The interaction with the dissipative environment is expressed by the bosonic bath which models a collective vibrational mode built up by the surrounding electrons or nuclear spins.
Furthermore, electron transport properties through QDs under the influence of such an external noise show a competition of the tunnelling between the leads and the bosonic damping. This directly leads to BF-QISs which we will discuss next.

1.4 Bose-Fermi quantum impurity models

Since the pure fermionic and pure bosonic QISs show QPTs under certain conditions, it is an interesting question how combined Bose-Fermi quantum impurity systems (BF-QISs) are related to these QPTs. Here we introduce the Bose-Fermi Kondo model (BFKM) and the Bose-Fermi Anderson model (BFAM) and present their QPTs in Sec. 2.4.

In the simplest case, we combine the KM of Sec. 1.1 and the SBM of Sec. 1.3 because both consist of an impurity spin-1/2 particle. Hence, we derived the Bose-Fermi Kondo

model (BFKM). If we avoid a potential scattering term which breaks ph symmetry, the Hamiltonian of the BFKM reads

$$H_{\mathrm{BFKM}} = \vec{\xi}\vec{S} + J\vec{S}\vec{s} + \sum_{k,\sigma} \epsilon_{k,\sigma} c^{\dagger}_{k,\sigma} c_{k,\sigma} + S_z \left(\sum_q \lambda_q \left(\phi^{\dagger}_q + \phi_q \right) \right) + \sum_q \omega_q \phi^{\dagger}_q \phi_q \quad . \tag{1.33}$$

The first term can be interpreted as a local magnetic field $\vec{\xi} = (-\Delta, 0, \epsilon)^T$ applied to the impurity spin with the energy level splitting ϵ and the tunnelling amplitude Δ, both known from the SBM. The second term describes the Kondo coupling with the coupling strength J and with

$$\vec{s} = \frac{1}{2N} \sum_{\vec{k},\vec{k}'} \sum_{\alpha,\beta} c^{\dagger}_{\vec{k},\alpha} \vec{\sigma}_{\alpha,\beta} c_{\vec{k}',\beta} \tag{1.34}$$

being the local spin density of the fermionic bath. The fermionic bath is given with the dispersion $\epsilon_{k,\sigma}$ in the third term. The operator $c^{\dagger}_{k,\sigma}$ creates an electron with spin σ and momentum k. The fourth term is the known bosonic coupling term of the SBM. The impurity spin only couples with its z component to the bosonic bath while all its components couple to the fermionic bath. The last term represents the bosonic bath[3] with the operator $\phi^{\dagger}_q$ creating a bosonic excitation with energy ω_q. In the following we assume an antiferromagnetic Kondo coupling $J > 0$ which enables spin-flip scattering processes.

Under the restrictions that (i) we have no magnetic field $\vec{\xi} = 0$, (ii) the fermionic DOS is a real pg with $0 < r < 1/2$ and (iii) the bosonic spectral function is sub-ohmic with $1/2 \leq s < 1$, the BFKM yields two types of localisation which both destroy the Kondo screening of the impurity spin: Either by a free local moment due to weak couplings or by the formation of a partially unscreened local moment due to a strong bosonic coupling.
For a weak coupling $J < J_c(g = 0)$ to the fermionic and no coupling to the bosonic bath, the impurity spin remains a free local moment, indicating the LM FP, and no Kondo screening occurs. For any finite bosonic coupling $g > 0$ exists a line $J_c(g)$ (or $g_c(J)$) of QCPs separating the Kondo SC phase for $J > J_c$ from the L phase for $J < J_c$. In the L FP a partially unscreened effective local moment is formed due to the strongly coupled ($g > g_c$) bosonic bath. This effective moment decouples from the rest of the system and the Kondo screening is partially suppressed.

Thorough numerical investigations on the BFKM, as well as the development of the BF-NRG, have been done in Refs. [55, 100]. Within the extended dynamical mean-field

[3] We like to emphasise that the bath indeed has to be a continuum of bosonic DOFs. If only a small number of bosonic DOFs is present, as for models similar to the Anderson-Holstein model [98, 99], the bosonic DOFs can be incorporated into the first Wilson shell and the standard fermionic NRG can be used.

theory (EDMFT) [101, 102] the BFKM serves as effective impurity model. For a heavy-fermion QPT, the competition between the screening of the f-shell moments by the conduction band and their magnetic ordering by the RKKY interaction is relevant, as described by the Kondo lattice model (KLM) [103, 104]. In the EDMFT the lattice of the KLM is mapped onto a BFKM with the bosonic part representing the fluctuating effective magnetic field generated by the other f moments. Also in the modelling of QDs such a BF-QIS is important. Since a gate voltage applied to a QD is never perfectly constant, one can either neglect this or model the fluctuations in the gate voltage as bosonic DOFs [54].

While in the BFKM the impurity interacts only via spin-flip scattering with the conduction band, we want to enable charge scattering processes as well. Therefore, we use the SIAM and additionally couple the impurity to a bosonic bath. Hence, we get the so-called charge-coupled Bose-Fermi Anderson model (BFAM). The BFAM is used, similar to the BFKM, as effective impurity model within the EDMFT. Its Hamiltonian is given by

$$H_{\mathrm{BFAM}} = \sum_{\sigma} \epsilon_{\mathrm{d}} d_{\sigma}^{\dagger} d_{\sigma} + U d_{\uparrow}^{\dagger} d_{\uparrow} d_{\downarrow}^{\dagger} d_{\downarrow} \tag{1.35a}$$

$$+ \sum_{k,\sigma} V_k \left(c_{k,\sigma}^{\dagger} d_{\sigma} + d_{\sigma}^{\dagger} c_{k,\sigma} \right) + \sum_{k,\sigma} \epsilon_k c_{k,\sigma}^{\dagger} c_{k,\sigma} \tag{1.35b}$$

$$+ \left(\sum_{\sigma} d_{\sigma}^{\dagger} d_{\sigma} - 1 \right) \left(\sum_{q} \lambda_q \left(\phi_q^{\dagger} + \phi_q \right) \right) + \sum_{q} \omega_q \phi_q^{\dagger} \phi_q \quad . \tag{1.35c}$$

The impurity part in Eq. (1.35a) describes the spin-degenerate energy level with energy ϵ_{d}. The level can be either zero-occupied $|0\rangle$, single-occupied $|\uparrow\rangle$ or $|\downarrow\rangle$, or double-occupied $|\uparrow\downarrow\rangle$. In the last case an additional Coulomb repulsion U at the impurity has to be paid. While the single-occupied states carry spin and no charge, the zero-occupied and double-occupied state carry the charge $Q = \pm 1$, regarding half-filling, and are spinless. Consequently, the impurity has the symmetry $\mathrm{SU}(2)_{\mathrm{spin}} \times \mathrm{SU}(2)_{\mathrm{charge}}$.
The fermionic bath and its coupling term to the impurity are given in Eq. (1.35b). The Hamiltonian of the conduction band has the dispersion ϵ_k and the operator $c_{k,\sigma}^{\dagger}$ creates a fermion in the conduction band with energy ϵ_k and momentum k. The hybridisation of the impurity to the fermionic bath is mediated by V_k which will be assumed to be independent of k in the following.
The bosonic parts in Eq. (1.35c) comprise the bosonic bath with the operator $\phi_q^{\dagger}$ creating an excitation with energy ω_q in the bath and the bosonic coupling term. In contrast to the SBM, here the elongation $X_q = (\phi_q^{\dagger} + \phi_q)$ of mode q couples via λ_q to the impurity charge $(\sum_{\sigma} d_{\sigma}^{\dagger} d_{\sigma} - 1)$ with respect to half-filling. Therefore, only the charge-full impurity states are coupled to the bosonic bath whereas the spin-full impurity states are only indirectly effected over the fermionic bath. This coupling type features a localisation

in the sense that one of the charge states is favoured. Furthermore, one pronounced effect is a renormalisation of the Coulomb repulsion U and will be explained later in Sec. 5.2.1. Combined with the possibility of spin and charge fluctuations between the impurity and the conduction band the BFAM has a very rich phase diagram, which will be presented in more detail in Sec. 2.4.
Under the restrictions that (i) we have no magnetic field $\vec{\xi} = 0$, (ii) the fermionic DOS is a real pg with $0 < r < 1/2$ and (iii) the bosonic spectral function is sub-ohmic with $1/2 \leq s < 1$, the BFAM also yields two types of localisation which both destroy the Kondo screening of the impurity orbital. A positive U and weak couplings to the fermionic and bosonic bath favour a localisation in the spin sector by the local moment formation indicating the LM FP. Whereas, a strong coupling to the bosonic bath, induces an attractive Coulomb interaction and hence, a localisation in the charge sector revealing the L FP. Hence, both effects favour different outcomes and compete with each other depending on the specific choice of Γ_0 and g for fixed U.

Chapter 2

Quantum criticality

Quantum mechanical systems, such as quantum impurity systems (QISs), may undergo a zero-temperature phase transition upon the variation of a non-thermal control parameter [61]. The order is destroyed solely by quantum fluctuations which make the transition to a quantum phase transition (QPT). A QPT occurs through a competition of different ground state phases and can be classified into a first-order or a continuous transition. The value of the non-thermal control parameter, at which the QPT occurs, defines the quantum critical point (QCP). This transition point is typically characterised by a critical continuum of excitation energies and can lead to unconventional behaviour; e.g. non-trivial power laws or non-Fermi liquid physics. For QISs we deal with boundary transitions where the degrees of freedom (DOFs) of a small subsystem, mainly but not necessarily only the impurity DOFs, become critical. For example, the impurity contributions of the free energy become singular at the QCP.

A well-written overview of QPTs is given in Ref. [81] and provides the major input for this section. In the 1970s the QPTs in the anisotropic Kondo model (KM) [18, 105] were the first investigated ones. A decade later the dissipative spin-boson model (SBM) [36, 91] became of interest. While QPTs occur in Kondo-type models with a fermionic bath and in dissipative models with a bosonic bath, it has been shown that these two classes are not fundamentally different and can be investigated with the same methods. Throughout this thesis we will use the numerical renormalisation group (NRG) to investigate QPTs. Nevertheless, there are several publications using other methods, as perturbative renormalisation group (RG) [81], Bethe ansatz [72, 106, 107] and conformal field theory techniques [108–110].

2.1 Classification of quantum phase transitions

A QPT in a QIS can be continuous or discontinuous. The latter one is typically a first-order transition. The continuous QPT can be classified either by a transition with a

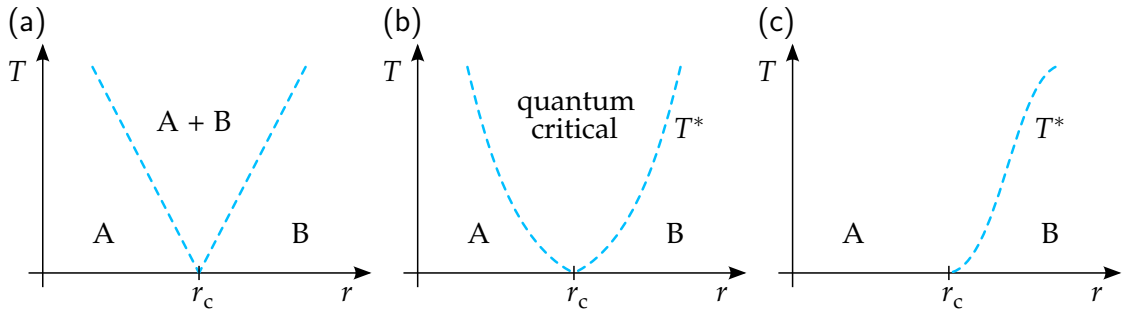

Figure 2.1: Classification of QPTs by their finite-temperature properties in dependence of the non-thermal control parameter r. A and B are stable phases. The transition is of (a) first order, (b) second order and (c) infinite order.

power-law behaviour, which is typical a second-order transition, or with an exponential behaviour. The latter type is an infinite-order transition, for example the Kosterlitz-Thouless QPT in the ohmic SBM. The order n of the QPT is defined by the n-th derivative of the impurity contribution to the ground state energy which shows a discontinuity with respect to a control parameter [81]. A sharp boundary transition for QISs only occurs at temperature $T = 0$. In Fig. 2.1 we summarise the different types of QPTs. A and B are stable phases, e.g. the SC and the LM phase of the SIAM of Sec. 1.2. Via the non-thermal control parameter r the system is driven through the phases. The critical parameter r_c marks the QCP at zero temperature.

A first-order transition is a simple level crossing in the ground state of the system and is depicted in Fig. 2.1(a). The stable phases A and B are two disconnected minima in the energy landscape of the system. At finite temperature near the QCP ($r \sim r_c$) the properties of the system are a thermodynamic mixture of the two phases.

For a second-order transition, as depicted in Fig. 2.1(b), a true quantum critical region (QCR) is present. At zero temperature a QCP exists at the critical parameter r_c with a RG level spectrum of an unstable FP. At finite temperature the QCR is controlled by this unstable FP and is bounded by the temperature

$$T^* \propto \left| \frac{r - r_c}{r_c} \right|^{\nu} \tag{2.1}$$

with the correlation-length exponent ν. For the pg versions of the KM and the SIAM, as well as, for the SBM the exponent ν depends on a continuous parameter, which is dependent on the low-energy power-law form of the bath's DOS, e.g. on the exponent s in $J(\omega)$. This parameter takes the role of a *dimension*. As a function of this dimension, the line of second-order transitions may terminate at a *lower-critical* dimension. As the lower-critical dimension is reached, ν diverges and the transition changes its type to the Kosterlitz-Thouless type. The pg models additionally feature an *upper-critical* dimension where the interacting critical FP changes to a non-interacting one and above

the upper-critical dimension the transition is of first order.
In Fig. 2.1(c) the infinite-order transition of the Kosterlitz-Thouless type is depicted. There exists no unstable FP at $T = 0$. The QCP at r_c belongs to the stable phase A. At finite temperature, the thermodynamic properties are separated by only one crossover line and the temperature T^* vanishes exponentially at the QCP.

2.2 Susceptibilities

To track the impurity QPT we need a thermodynamic property which shows a critical behaviour at the QCP. The thermodynamic property has to contain an impurity contribution, which consists of the local impurity contribution, as well as, the cross effects between the environment and the impurity, but without the pure effect of the environment itself. For this, we define the operation

$$\Delta(X) = \langle X \rangle - \langle X \rangle_{H_0} \tag{2.2}$$

which measures by $\langle X \rangle$ an observable X in presence of the impurity and the environment, and subtracts from it the effect $\langle X \rangle_{H_0}$ of this observable for a pure reference system H_0. The reference system H_0 is given by the same system without the impurity. For example, we can extract from the free energy $F = -T \ln Z$, with the partition function $Z = \mathrm{e}^{-\beta H}$, the impurity contribution $F_{\mathrm{imp}} = \Delta(F)$.

2.2.1 Total responses

We now apply bulk fields to the whole system to derive the impurity contribution of the total responses of the system. A total magnetic field Ξ and a total electrical potential Φ act on the full system via the additional Hamiltonian

$$H_{\mathrm{f}} = \Xi S_{z,\mathrm{tot}} + \Phi Q_{\mathrm{tot}} \tag{2.3}$$

with the total spin in z direction $S_{z,\mathrm{tot}} = S_{z,\mathrm{d}} + S_{z,\mathrm{bulk}}$, the total charge $Q_{\mathrm{tot}} = Q_{\mathrm{d}} + Q_{\mathrm{bulk}}$ and the definition of the charge $Q_{\mathrm{d}} = (\sum_\sigma d_\sigma^\dagger d_\sigma - 1)$ at the impurity with respect to half-filling.
Static response functions are defined as second derivative of a thermodynamic potential, e.g. of the free energy $F = -T \ln Z$. Therefore, the static impurity spin susceptibility $\chi_{\mathrm{s,imp}}$ and the static impurity charge susceptibility $\chi_{\mathrm{c,imp}}$ are given by

$$\chi_{\mathrm{s,imp}} = -\frac{\partial^2 F_{\mathrm{imp}}}{\partial \Xi^2} \quad \text{and} \quad \chi_{\mathrm{c,imp}} = -\frac{\partial^2 F_{\mathrm{imp}}}{\partial \Phi^2} \tag{2.4}$$

respectively. These impurity contributions show a discontinuity with respect to Ξ or Φ over the impurity QPT. If we perform the derivations above, we gain for the susceptibilities the expressions

$$T\chi_{\mathrm{s,imp}} = \Delta\left(\langle S^2_{\mathrm{z,tot}}(T)\rangle - \langle S_{\mathrm{z,tot}}(T)\rangle^2\right) \quad \text{and} \tag{2.5}$$

$$T\chi_{\mathrm{c,imp}} = \Delta\left(\langle Q^2_{\mathrm{tot}}(T)\rangle - \langle Q_{\mathrm{tot}}(T)\rangle^2\right) \quad , \tag{2.6}$$

which can be calculated numerically with the NRG. In the zero-temperature limit the susceptibilities diverge and the expressions in Eqs. (2.5) and (2.6) approach finite values:

$$\lim_{T\to 0} T\chi_{\mathrm{s,imp}}(T) = \mu^2_{\mathrm{eff}} \quad \text{and} \quad \lim_{T\to 0} T\chi_{\mathrm{c,imp}}(T) = 4Q^2_{\mathrm{eff}} \quad . \tag{2.7}$$

Here, μ^2_{eff} is the effective local moment and Q^2_{eff} the effective charge moment. For the pg models the effective local moment can be $0 \leq \mu^2_{\mathrm{eff}} \leq 1/4$, with the lower boundary of a completely screened effective local moment and the upper boundary of a free moment. The same boundaries hold for the effective charge moment Q^2_{eff}.

2.2.2 Local responses

So far we applied total fields to the system. Now we restrict ourselves on local fields

$$H_{\mathrm{lf}} = \xi S_{\mathrm{z,d}} + \phi Q_{\mathrm{d}} \tag{2.8}$$

which only act on the impurity. With the help of the local magnetic field ξ and the local electrical potential ϕ it is also possible to track the QCP. The local response functions, therefore, are given by

$$\chi_{\mathrm{s,loc}} = -\frac{\partial^2 F}{\partial \xi^2} \quad \text{and} \quad \chi_{\mathrm{c,loc}} = -\frac{\partial^2 F}{\partial \phi^2} \tag{2.9}$$

where we used the free energy F. Furthermore, the local magnetisation m_{loc} and the local charge q_{loc} are given by

$$m_{\mathrm{loc}} = \langle S_{\mathrm{z,d}}\rangle = -\frac{\partial F}{\partial \xi} \quad \text{and} \quad q_{\mathrm{loc}} = \langle Q_{\mathrm{d}}\rangle = -\frac{\partial F}{\partial \phi} \quad . \tag{2.10}$$

For completeness, the local static response functions depend on the local expectation values in the limits

$$\chi_{\mathrm{s,loc}} = -\lim_{\xi\to 0}\frac{m_{\mathrm{loc}}}{\xi} \quad \text{and} \quad \chi_{\mathrm{c,loc}} = -\lim_{\phi\to 0}\frac{q_{\mathrm{loc}}}{\phi} \quad . \tag{2.11}$$

For example, the quantities m_{loc} and q_{loc} turned out to be good order parameters to probe QPTs in the pg versions of the KM [111] and of the BFAM [56]. There, both quantities vanish continuously by a second-order transition as the QCP is reached for $r \to r_{\mathrm{c}}$.

2.3 Criticality in the SIAM

The first investigation on the SIAM with the NRG was done in the 1980s by Krishnamurthy, Wilkins and Wilson [112, 113] who calculated the FP spectrum and several static quantities. Historically, the SIAM was investigated for a constant DOS. The use of a pg-DOS for impurity models was proposed in 1990 by Withoff and Fradkin [21] who examined the pg KM via a *poor man's scaling* approach. In 1995 the pg KM was investigated with the NRG [114]. For the pg SIAM investigations with the NRG have been performed by several authors [25, 83, 115–117]. Ref. [25] is the most comprehensive review. In the following we omit the prefix pg.

2.3.1 Renormalisation group flow

The presentation of the RG flow follows Ref. [118]. The FP properties of the SIAM strongly depend on the presence or absence of ph symmetry. Here, we start with the description of the RG flow and summarise the characteristics of the FPs in Sec. 2.3.2.

For particle-hole symmetry

In Fig. 2.2 the RG flow is depicted in presence of ph symmetry. According to the exponent r the RG flow is divided into four regimes: (a) $r = 0$, (b) $0 < r < 1/2$, (c) $1/2 \leq r < 1$ and (d) $1 \leq r$. The plane is spanned by the bare parameters, the hybridisation strength Γ_0 and the level energy $\epsilon_{\mathrm{d}} = -U/2$, which incorporates the Coulomb repulsion. For given Γ_0 and U, the parameters renormalise in the direction of the arrows to a stable FP, which is marked by a filled circle. The unstable FPs are represented by unfilled circles.

For the metallic case $r = 0$, in Fig. 2.2(a), the flow for any finite hybridisation strength $\Gamma_0 > 0$ is towards the metallic Kondo-screened SC FP. With increasing Coulomb repulsion $U > 0$ the flow is stronger attracted by the unstable LM FP at first, then it reaches the stable SC FP. The LM FP corresponds to $\epsilon_{\mathrm{d}} = -\infty$ ($U = \infty$) and $\Gamma_0 = 0$ and consists of a free spin doublet ($|\uparrow\rangle$, $|\downarrow\rangle$). On the other hand, for an attractive Coulomb repulsion $U < 0$, on the right side of the graph, the flow is with increasing $|U|$ at first attracted towards the unstable local moment prime (LM′) FP and then to the stable SC FP. This LM′ FP at $\epsilon_{\mathrm{d}} = \infty$ ($U = -\infty$) and $\Gamma_0 = 0$ consists of a free charge doublet ($|0\rangle$, $|\uparrow\downarrow\rangle$).

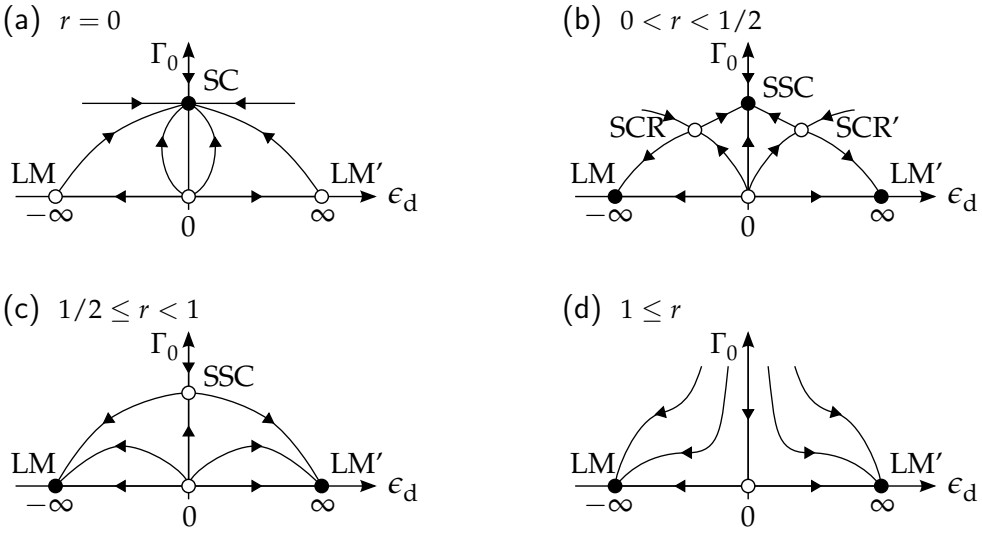

Figure 2.2: RG flow for the SIAM for ph symmetry with $\epsilon_d = -U/2$. The plane is spanned by the hybridisation strength Γ_0 and the level energy ϵ_d which incorparates the Coulomb repulsion U. The figure is subdivided into four regimes: (a) $r = 0$, (b) $0 < r < 1/2$, (c) $1/2 \leq r < 1$ and (d) $1 \leq r$. Filled circles are stable, unfilled circles are unstable FPs. The FPs are explained in the text. After [118].

For $0 < r < 1/2$, in Fig. 2.2(b), a small hybridisation strength and $U > 0$ ($U < 0$) lead to an unscreened impurity spin (charge). This is indicated by the flow towards the LM (or LM') FP. In this regime the LM and LM' FP are stable. Between the stable LM (or LM') FP and the stable SSC FP a new unstable symmetric critical (SCR) (or symmetric critical prime (SCR')) FP at finite $\Gamma_0, |\epsilon_d|$ emerges. It separates the flow towards the LM (or LM') and towards the SSC FP. The SSC FP differs from the SC FP of the previous regime by a fractional screening of the effective moments and a residual entropy, cf. Sec. 2.3.2. As $r \to 0$ the SCR FP merges with the LM FP with a diverging correlation-length exponent, as it is characteristic for a lower-critical dimension [118]. As $r \to 1/2$ the SCR FP merges with the SSC FP with the same characteristic.
Therefore, in the regime $1/2 \leq r < 1$, in Fig. 2.2(c), the critical FPs are gone. Furthermore, the SSC FP becomes unstable and divides the flow towards the LM and towards the LM' FP, which are still stable. In the limit $r \to 1$ this unstable SSC FP moves to $\Gamma_0 = 0$ and merges with the free impurity (FI) FP. Consequently, in the regime $1 \leq r$, in Fig. 2.2(d), no non-trivial FP is left.

For particle-hole asymmetry

While the fermionic DOS $\rho(\epsilon) \propto |\epsilon|^r$ is ph symmetric, the asymmetry has to be expressed by the impurity states: $0 \lesseqgtr U \neq -2\epsilon_d$. It is pointed out in Refs. [25, 118] that the critical properties of the SIAM are independent of the strength of the ph asymmetry. Therefore, we look at the SIAM with maximal ph asymmetry, i.e. $U = \infty$ (and $|\epsilon_d|$

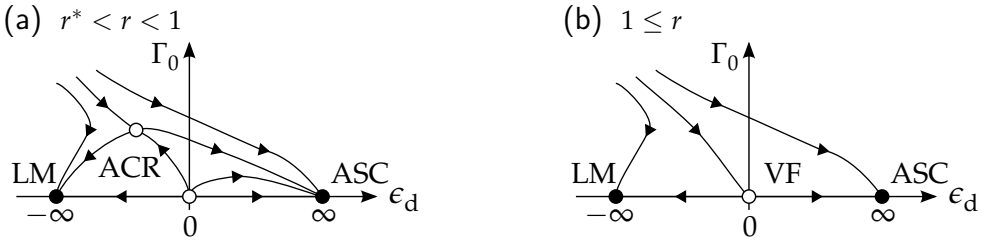

Figure 2.3: RG flow for the SIAM for maximal ph asymmetry with $U = \infty$ in the regime (a) $0.375 \simeq r^* < r < 1$ and (b) $1 \leq r$. Filled circles are stable, unfilled circles are unstable FPs. The FPs are explained in the text. After [118].

finite). In this case the double-occupied impurity state is excluded and the RG flow alters fundamentally.

According to the exponent r the RG flow is divided into four regimes: (a) $r = 0$, (b) $0 < r \leq r^*$, (c) $r^* < r < 1$ and (d) $1 \leq r$. At first, we explain the existence of the specific parameter r^*. For ph symmetry, $U > 0$ and $0 < r < 1/2$ there exists the SCR FP as stated above. If we break ph symmetry, the SCR FP remains stable with respect to the symmetry break for r close to 0. But it is unstable with respect to the symmetry break for r near $1/2$ and is replaced by a new asymmetric critical (ACR) FP. Therefore, there is a specific $r^* \sim 0.375$ above which the ACR FP is present due to ph asymmetry. For $r \to r^{*+}$ the ACR FP collapses with the SCR FP because the ph symmetry is dynamically restored.

In the case $r = 0$, the ph symmetry break has no effect on the FPs meaning that the SC FP is stable regarding ph asymmetry. Consequently, for $r = 0$ the RG flow is identical to the symmetric case in Fig. 2.2(a). As mentioned above the ph symmetry is dynamically restored in the regime $0 < r \leq r^*$ and the RG flow is identical to the symmetric case in Fig. 2.2(b). The ph-symmetry break leads to a different RG flow for $r^* < r$ as depicted in Fig. 2.3. At $\Gamma_0 = 0$, $\epsilon_d = 0$ the FI FP of the ph-symmetric case is now replaced by the valence fluctuation (VF) FP. The VF FP consists of three states since the double-occupied impurity state is excluded by the maximal ph asymmetry. For $\epsilon_d < 0$ the ground state is a spin doublet leading to the LM FP, whereas for $\epsilon_d > 0$ the zero-occupied singlet state remains in the zero-temperature limit. This can be interpreted as an ASC FP because no spin moment is left[4]. Between these two stable FPs a new unstable ACR FP emerges in the regime $r^* < r < 1$ at finite Γ_0, ϵ_d, cf. Fig. 2.3(a). It separates the flow towards the LM FP from the flow towards the ASC FP. For $1 \leq r$, in Fig. 2.3(b), the hybridisation Γ_0 is irrelevant and the transition is in leading order a level crossing at the VF point ($\Gamma_0 = 0$, $\epsilon_d = 0$). The ASC FP of the previous regime

[4] The maximal ph asymmetry can also be achieved by $\epsilon_d = -\infty$ and U finite which leads to the exclusion of the zero-occupied impurity state. Then, the double-occupied singlet state remains in the zero-temperature limit to which is referred as asymmetric strong coupling prime (ASC') FP. Nevertheless, both ways of achieving maximal ph asymmetry are interchangeable by a ph transformation.

FP	μ^2_{eff}	Q^2_{eff}	S_{imp}
SC	0	0	$\ln(1)$
LM	$1/4$	0	$\ln(2)$
LM′	0	$1/4$	$\ln(2)$
SSC	$r/8$	$r/8$	$2r\ln(2)$
FI	$1/8$	$1/8$	$\ln(4)$
ASC	0	0	$\ln(1)$
VF	$1/6$	$1/18$	$\ln(3)$

Table 2.1: Overview of the FP values for the SIAM in the zero-temperature limit with $\lim_{T\to 0}\mu^2_{\text{eff}}(T) =: \mu^2_{\text{eff}}$, $\lim_{T\to 0} Q^2_{\text{eff}}(T) =: Q^2_{\text{eff}}$ and $\lim_{T\to 0} S_{\text{imp}}(T) =: S_{\text{imp}}$.

merges with the VF FP for $r \to 1^-$. For ph symmetry $r \to 0^+$ is a lower-critical dimension and $r \to (1/2)^-$ an upper-critical dimension. For both limits the correlation-length exponent diverges. For ph asymmetry the upper-critical dimension is shifted to $r \to 1^-$.

2.3.2 Fixed point properties

To characterise and distinguish the different FPs we use the effective moments: the effective local moment $\mu^2_{\text{eff}}(T)$ and the effective charge moment $Q^2_{\text{eff}}(T)$, both introduced in Sec. 2.2.1. In Tab. 2.1 the FP values of the effective moments and the impurity entropy S_{imp} are collected in the zero-temperature limit $T \to 0$.
In the case of ph symmetry and $U > 0$, as mentioned above, exists the SCR FP separating the flow towards the LM FP and the flow towards the SSC FP for the bath exponent $0 < r = 0.4 < 1/2$. For a fixed coupling strength $\Gamma_0/D = 0.01$ the SCR FP emerges at a critical coupling strength $U_c/\Gamma_0 = 0.19387(0)$ for the NRG discretisation parameter $\Lambda = 2$. For an attractive Coulomb repulsion $U < 0$, the SCR′ at $-U_c/\Gamma_0$ separates the flow towards the LM′ FP and towards the SSC FP.

In Fig. 2.4 we present[5] for the SIAM the effective local moment in Fig. 2.4(a) and the effective charge moment in Fig. 2.4(b) for a Coulomb repulsion in the range $[-5U_c, 5U_c]$ in presence of ph symmetry, $\epsilon_d = -U/2$. For a Coulomb repulsion $U > U_c$ the system is in equilibrium in the LM phase, meaning that in the zero-temperature limit $T \to 0$ the effective moments reach their values of the LM FP. For $U \to {U_c}^+$ the FP values are only reached in the limit $T \to 0$. Otherwise, for e.g. $U/U_c = 5$, the FP values are already reached for a finite low temperature. In the LM FP the effective local moment is $\mu^2_{\text{eff}} := \lim_{T\to 0}\mu^2_{\text{eff}}(T) = 1/4$ and the effective charge moment $Q^2_{\text{eff}} := \lim_{T\to 0} Q^2_{\text{eff}}(T) = 0$; cf. Tab. 2.1. Consequently, the unstable SCR FP and, therefore $U_c(\Gamma_0)$, is defined by the effective moments being constant at low temperature without reaching one of

[5] We like to note that due to the even-odd oscillations the effective moments are averaged over splines which are produced separately for the even and for the odd iteration numbers.

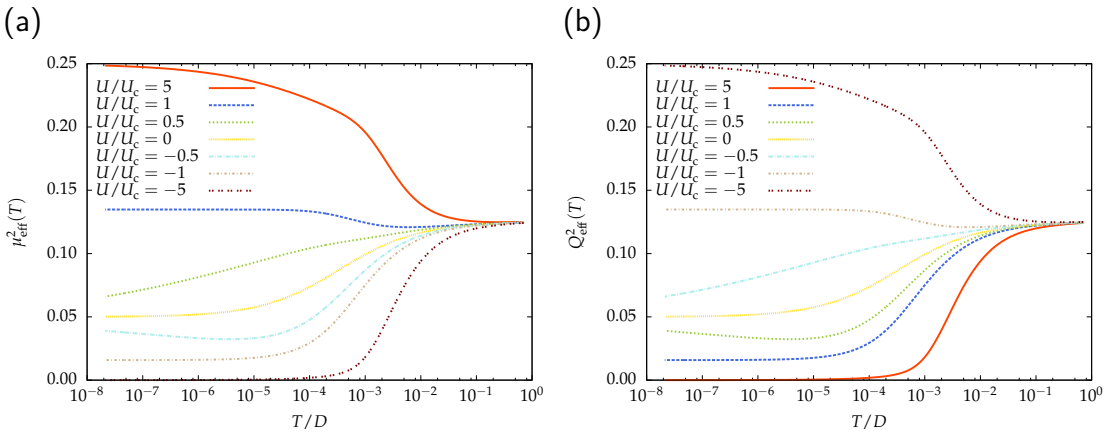

Figure 2.4: Effective local moment in (a) and effective charge moment in (b) for the SIAM with $\Gamma_0/D = 0.01$ and $r = 0.4$ in presence of ph symmetry, $\epsilon_d = -U/2$. The NRG parameters are $\Lambda = 2$, $N_S = 2000$, $N = 52$ and $N_z = 8$. The critical Coulomb repulsion is $U_c/\Gamma_0 = 0.19387(0)$.

the stable FPs. For this low-temperature FP at $U_c(\Gamma_0)$ both effective moments have r-dependent values which obviously are between the LM and SSC FP values. Decreasing the Coulomb repulsion further drives the system into the SSC phase in equilibrium. This means that for $-U_c < U < U_c$ the effective moments reach at least in the limit $T \to 0$ their SSC FP values: $\mu^2_{\rm eff} = r/8$ and $Q^2_{\rm eff} = r/8$. Similarly to the SCR FP, the SCR' FP at $-U_c(\Gamma_0)$ is defined by constant effective moments for low temperatures. Their values at the SCR' FP are r-dependent, as well, and are between the values of the SSC and the LM' FP. Anyway, the value of effective local moment $\mu^2_{\rm eff}$ in one critical FP, e.g. the SCR FP, is identical to the value of the effecive charge moment $Q^2_{\rm eff}$ in the other critical FP, e.g. the SCR' FP, and vice versa. To conclude this description, for a strong attractive Coulomb interaction $U < -U_c$ the system is driven in the LM' phase. There, the effective moments reach at least for $T \to 0$ the values of the LM' FP: $\mu^2_{\rm eff} = 0$ and $Q^2_{\rm eff} = 1/4$.

If we break ph symmetry with $-2\epsilon_d \neq U \gg 1$, the double-occupied impurity state is irrelevant in the zero-temperature limit. The impurity level energy ϵ_d is the control parameter which drives the system in equilibrium through the different phases. For the ph-asymmetric SIAM with $\Gamma_0/D = 0.01$, $U/\Gamma_0 = 100$ and $r^* < r = 0.4$ a QPT for $\epsilon_d < 0$ emerges. This unstable ACR FP at $\epsilon_{d,c}(U, \Gamma_0)$ separates the flow towards the LM FP and towards the ASC FP as long as $U > U_c(\Gamma_0)$.
In Fig. 2.5 for the ph asymmetric SIAM we present the effective local moment in Fig. 2.5(a) and the effective charge moment in Fig. 2.5(b) for a level energy in the range $[5\epsilon_{d,c}, -\epsilon_{d,c}]$. Starting with a strong negative $\epsilon_d < \epsilon_{d,c}$, e.g. $\epsilon_d/\epsilon_{d,c} = 5$ in Fig. 2.5, the system is driven in equilibrium in the LM phase. The LM FP has the same properties as in the ph symmetric case: $\mu^2_{\rm eff} = 1/4$ and $Q^2_{\rm eff} = 0$. Due to $U_c < U \gg 1$ and $\epsilon_d < 0$

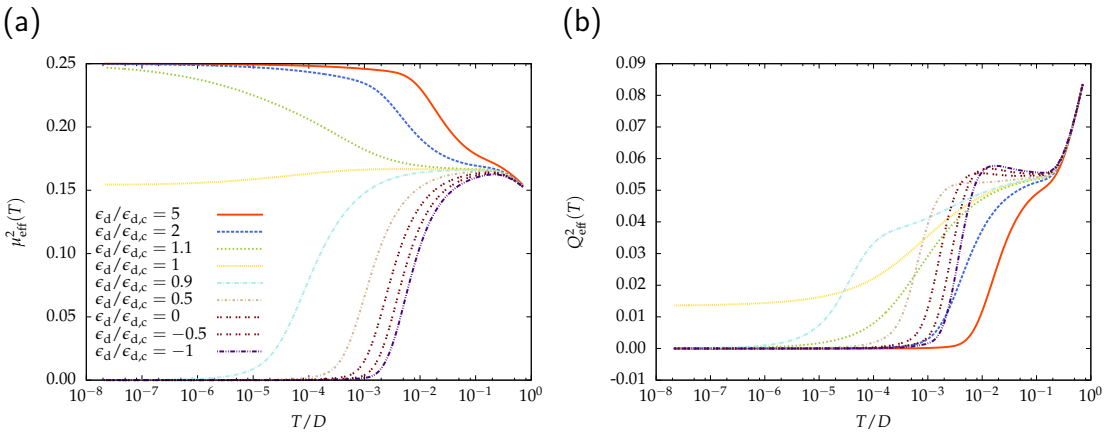

Figure 2.5: Effective local moment in (a) and effective charge moment in (b) for the SIAM with $\Gamma_0/D = 0.01$ and $r = 0.4$ for ph asymmetry $-2\epsilon_{\rm d} \neq U/\Gamma_0 = 100$. The NRG parameters are $\Lambda = 2$, $N_{\rm S} = 2000$, $N = 52$ and $N_{\rm z} = 8$. The critical level energy is $\epsilon_{\rm d,c}/\Gamma_0 = -0.6279(5)$.

the double-occupied and zero-occupied impurity states are suppressed by the RG and in the zero-temperature limit a spin doublet remains, as it is characteristic for the LM FP. The ACR FP, which separates the LM and the ASC FP, is defined by constant effective moments in the zero-temperature limit at $\epsilon_{\rm d,c}(U, \Gamma_0)$. The values of the effective moments in the ACR FP depend on r, similarly to the other unstable QCPs. For the effective local moment this value is between the values of the LM and ASC FP, whereas for the effective charge moment this is not the case. The effective charge moment is zero for both FPs but, anyway, at the ACR FP it is finite.

An increased level energy $\epsilon_{\rm d,c} < \epsilon_{\rm d}$ drives the system into the ASC FP in equilibrium. If we look at the effective local moment, with increasing $\epsilon_{\rm d}$ it renormalises faster, meaning that it reaches the ASC FP value at higher temperatures. We see the same effect in the effective charge moment. With increasing $\epsilon_{\rm d}$ the ASC FP value is reached at higher temperatures. Additionally, the effective charge moment forms a peak for this regime. This reflects that with increasing $\epsilon_{\rm d}$ and for a constant U the double-occupied and the single-occupied states are less stronger separated. This leads to a more pronounced influence of the double-occupied state at high temperatures which favours a build-up of the effective charge moment.

2.4 Criticality in the BFAM

The RG flow, as well as the FP properties, of the BFAM are summarised in Refs. [56, 57]. They provide the main input for this section. Since the KM can be derived from the SIAM by a SWT, the BFKM is a limiting model for the BFAM. Hence, we discuss only

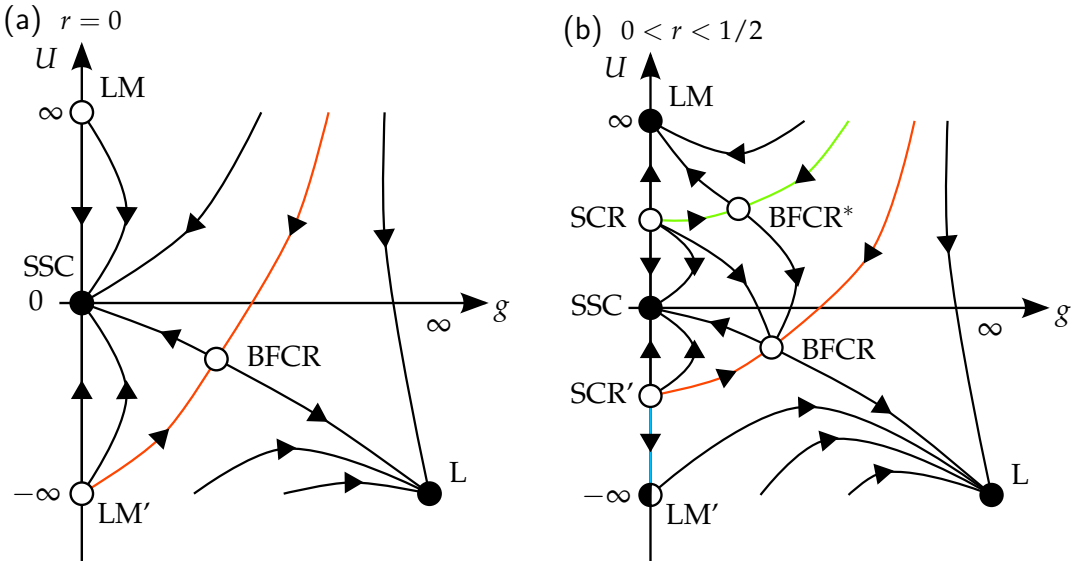

Figure 2.6: RG flow for the ph symmetric BFAM with a pg-DOS. The plane is spanned by the Coulomb repulsion U and bosonic coupling g. While the bosonic bath exponent is in the sub-ohmic range $0 < s < 1$, we distinguish by the fermionic bath exponent in (a) $r = 0$ and (b) $0 < r < 1/2$. A finite coupling $\Gamma_0 > 0$ to the conduction band is present. (Un)Filled circles are (un)stable FPs.

the more general BFAM here. We refer the reader to App. A.1 for the RG flow and the FP properties of the KM, and to App. A.2 for the critical properties of the BFKM.

2.4.1 Renormalisation group flow

The impurity is under all considerations constantly coupled to the conduction band with $\Gamma_0/D = 0.01$. Consequently, in the limiting SIAM (the BFAM for $g = 0$) features a QPT by varying over U. The unstable SCR FP of the QPT has a critical Coulomb repulsion $U_c(\Gamma_0) > 0$. For a negative U, the LM and SCR FPs have to be replaced by the primed FPs. In Fig. 2.6 we span the plane for the RG flow by the Coulomb repulsion U and the bosonic coupling g. Due to $\Gamma_0 > 0$, there is no limiting purely bosonic model. Nevertheless, the bosonic bath favours a stable L FP if the bosonic coupling g is large enough. Hence, there has to be at least one unstable Bose-Fermi critical (BFCR) FP which separates the stable FPs of the limiting SIAM from the stable L FP. In fact, the presented BFCR FP in Fig. 2.6 is dependent on the Coulomb repulsion U. Therefore, to be more precise, there is actually a line of BFCR FPs represented by the red line. Only one representative FP is drawn in Fig. 2.6 to add the RG flow arrows. For a constant fermionic DOS, in Fig. 2.6(a), the limiting SIAM favours only the stable SSC FP towards which the flow is directed. In presence of the bosonic coupling $g > 0$ a new unstable BFCR FP emerges at a critical coupling $g_c(U)$. It separates the flow towards the stable SSC FP for $g < g_c$ from the flow towards the stable L FP for $g_c < g$.

FP	μ^2_{eff}	Q^2_{eff}	S_{imp}	D_{eq}
SSC	$r/8$	$r/8$	$2r\ln(2)$	$1/4$
LM	$1/4$	0	$\ln(2)$	0
LM′	0	$1/4$	$\ln(2)$	$1/2$
L	0	$1/4$	$\ln(2)$	$1/2$

Table 2.2: Overview of the FP values of the BFAM in the zero-temperature limit with $\lim_{T\to 0}\mu^2_{\text{eff}}(T) =: \mu^2_{\text{eff}}$, $\lim_{T\to 0}Q^2_{\text{eff}}(T) =: Q^2_{\text{eff}}$, $\lim_{T\to 0}S_{\text{imp}}(T) =: S_{\text{imp}}$ and $\lim_{T\to 0}\langle D\rangle_{\text{eq}}(T) =: D_{\text{eq}}$.

For a pg-DOS with $0 < r < 1/2$, in Fig. 2.6(b), the LM and LM′ FP in the limiting SIAM become stable and in addition two unstable FPs emerge: the SCR FP at $U_{\text{c}}(\Gamma_0)$ and the SCR′ FP at $-U_{\text{c}}(\Gamma_0)$, respectively. The SCR FP separates the flow towards the SSC FP and towards the LM FP, as the SCR′ FP separates the flow towards the SSC FP and owards the LM′ FP. In presence of the bosonic bath, the flow is towards the L FP for $g > g_{\text{c}}$. The fermionic LM′ FP is only accessible for $g = 0$ (indicated by the blue line in Fig. 2.6(b)) because for $U \to -U_{\text{c}}^{+}$ the critical bosonic coupling $g_{\text{c}} \to 0$ vanishes. The energy spectrum of the LM′ and of the L FP are composed of purely fermionic and purely bosonic energies. Both FPs contain the fermionic energies of the LM′ FP of the SIAM. The LM′ FP additionally contains the energies of a free bosonic bath, while the L FP features the energies of the bosonic L FP of the SBM. Although both FPs differ in their energy spectrum, we claim that the L FP and the LM′ FP are alike for the BFAM in the sense that both FPs favour a build-up of an effective charge moment.
The LM and LM′ FP are stable for the pg-DOS in absence of the bosonic bath. With respect to any finite bosonic coupling $0 < g$, the LM′ becomes unstable and the flow is towards the L FP. Whereas, the LM FP remains stable for $0 < g < g^{\star}$ and the flow is towards the FP. At the critical coupling $g^{\star}(U)$ a second unstable Bose-Fermi critical star (BFCR*) FP emerges, separating the flow towards the LM FP and towards the SSC FP. In the range $g^{\star} < g < g_{\text{c}}$, in between the BFCR* and the BFCR FP, the flow is directed to the SSC FP. Otherwise, for $g > g_{\text{c}}$, the flow is towards the L FP. Furthermore, the SSC FP is stable and its energy spectrum contains the fermionic energies of the SSC FP of the SIAM and, additionally, the eigenenergies of a free bosonic bath.

2.4.2 Fixed point properties

Similarly to the SIAM in Sec. 2.3.2, we characterise the FPs by the effective moments: the effective local moment $\mu^2_{\text{eff}}(T)$ and the effective charge moment $Q^2_{\text{eff}}(T)$. In Tab. 2.2 the FP values of the effective moments, the impurity entropy and the equilibrium double occupancy are presented in the zero-temperature limit $T \to 0$. More information on the equilibrium double occupancy will be given in Sec. 5.2.2.

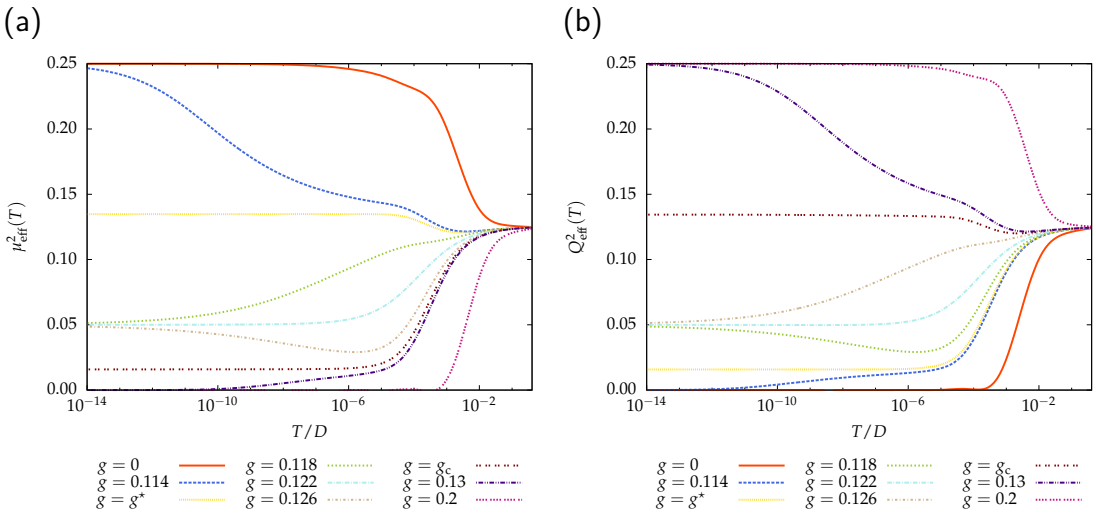

Figure 2.7: Effective local moment $\mu^2_{\mathrm{eff}}(T)$ in (a) and effective charge moment $Q^2_{\mathrm{eff}}(T)$ in (b) for the BFAM with bath exponents $r = 0.4$ and $s = 0.8$ without z-averaging. The model parameters are $\Gamma_0/D = 0.01$, $U/\Gamma_0 = 1$ and ph symmetry, $\epsilon_{\mathrm{d}} = -U/2$, is maintained. The FP values in the zero-temperature limit are stated in Tab. 2.2. The unstable FPs are at the couplings $g^\star = 0.11496(5)$ (BFCR* FP) and $g_{\mathrm{c}} = 0.12847(7)$ (BFCR FP). The NRG parameters are $\Lambda = 6$, $N_{\mathrm{S}} = 1000$, $N_{\mathrm{B}} = 10$, $N = 40$.

While we maintain ph symmetry and for a finite fermionic coupling $\Gamma_0 > 0$, the BFAM exhibits three stable and two unstable FPs for the bath exponents in the range $0 < r < 1/2$ and $1/2 < s < 1$. The LM FP and the SSC FP are known from the SIAM in Sec. 2.3.2. In the LM FP the impurity forms solely, or in correlation with the conduction band electrons, a full effective local moment with $\lim_{T\to 0} \mu^2_{\mathrm{eff}}(T) = 1/4$ and $\lim_{T\to 0} Q^2_{\mathrm{eff}}(T) = 0$. In the Kondo-screened SSC FP the impurity DOFs are partially screened by the conduction band electrons. This leads to $\lim_{T\to 0} \mu^2_{\mathrm{eff}}(T) = r/8$ and $\lim_{T\to 0} Q^2_{\mathrm{eff}}(T) = r/8$. In the L FP the impurity DOFs are controlled by the bosonic coupling and spin flips or charge fluctuations of the impurity with its environment are suppressed: The Kondo effect is forbidden. This Kondo destruction due to the localisation leads to the effective moments $\lim_{T\to 0} \mu^2_{\mathrm{eff}}(T) = 0$ and $\lim_{T\to 0} Q^2_{\mathrm{eff}}(T) = 1/4$.
In the following the repulsive Coulomb repulsion $U > U_{\mathrm{c}}$ is held constant. U_{c} is the critical Coulomb repulsion known by the SIAM. By varying over the bosonic coupling g we are able to drive the system in one of the stable FPs at low temperature.

In Fig. 2.7 we present the effective moments for a set of different bosonic couplings g: the effective local moment $\mu^2_{\mathrm{eff}}(T)$ in Fig. 2.7(a) and the effective charge moment $Q^2_{\mathrm{eff}}(T)$ in Fig. 2.7(b). The BFAM parameters are $U/\Gamma_0 = 1$, $\Gamma_0/D = 0.01$, $r = 0.4$, $s = 0.8$. The FP values are reached in the zero-temperature limit, i.e. $\mu^2_{\mathrm{eff}} = \lim_{T\to 0} \mu^2_{\mathrm{eff}}(T)$ and $Q^2_{\mathrm{eff}} = \lim_{T\to 0} Q^2_{\mathrm{eff}}(T)$. Due to the chosen parameters the limiting SIAM for $g = 0$ is in the LM FP for low temperatures. Therefore, the effective local moment μ^2_{eff} is built-up completely while the effective charge moment Q^2_{eff} is zero.

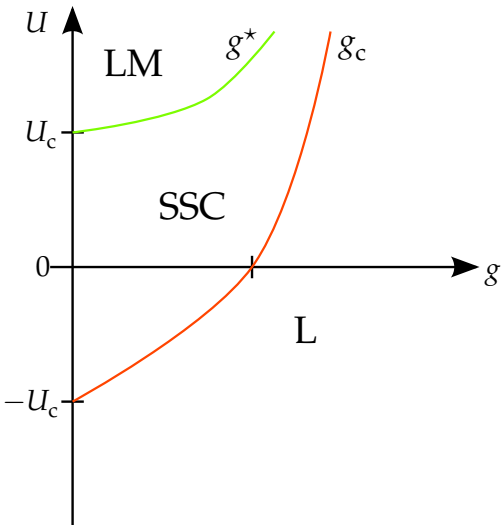

Figure 2.8: Schematic phase diagram of the BFAM in dependence of the Coulomb repulsion U (for a finite $\Gamma_0 > 0$) and the bosonic coupling g. The bath exponents are in the regimes $0 < r < 1/2$ and $1/2 < s < 1$. The critical $U_c(\Gamma_0)$ is known in the context of the SIAM ($g = 0$). The phase boundaries $g^\star$ and g_c separate the LM, the SSC and the L phase, respectively.

With increasing bosonic coupling $0 < g < g^\star$ up to the critical coupling $g^\star$, the LM FP stays stable. The phase boundary at $g^\star(U)$ corresponds to the unstable BFCR* FP at which both effective moments reach a constant FP value at low temperature. These values are r dependent and lay between the FP values of the LM and SSC FP. The bosonic exponent s alters the slope of $\mu^2_{\text{eff}}(T)$ and $Q^2_{\text{eff}}(T)$ but not the FP values.
Increasing the bosonic coupling further, $g^\star < g < g_c$, the SSC FP is reached at low temperature. The critical $g_c(U)$ marks the second phase boundary and corresponds to the unstable BFCR FP. Its FP values for the effective moments lay between the values of the SSC and the L FP. For a stronger bosonic coupling $g_c < g$, the system is in the L FP in equilibrium with a full built-up charge moment and a vanishing local moment.

According to the former description, we present a schematic phase diagram of the BFAM in Fig. 2.8. Here, ph symmetry is maintained, the fermionic coupling $\Gamma_0 > 0$ is finite and the bath exponents are in the ranges $0 < r < 1/2$ and $1/2 < s < 1$. Although there have been several publications about this model [56, 57] a full phase diagram has not been published yet. Furthermore, these investigations of the BFAM have only considered a repulsive Coulomb interaction $U > 0$. The phase boundaries start at the well-known phase boundary points of the SIAM [83, 119] for the same fermionic exponent r: U_c separates the LM and the SSC phase and $-U_c$ separates the SSC and LM' phase. For a finite bosonic coupling g, the phase boundary $g^\star$ is given for the former separation while the phase boundary g_c separates the SSC and L phases.

To conclude this section, we comment why we leave the LM' FP out of scope in the following. As mentioned in Sec. 2.4, the LM' FP is only accessible for $g = 0$. Neverthe-

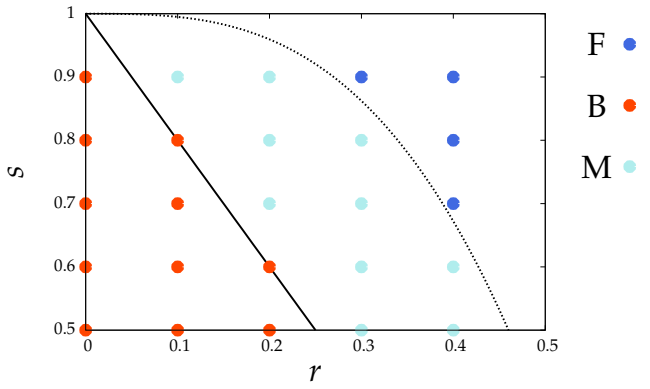

Figure 2.9: Exponent types in the BFAM in dependence of (r, s). Taken from [57].

less, the characteristics of the LM' and the L FP regarding the effective moments are identical, cf. Tab. 2.2. Both FPs favour a complete build-up of the charge moment at low temperature. Furthermore, for our analysis of the time-dependent dynamics for the BFAM we switch on the bosonic coupling g for times $t > 0$. Hence, the dynamics can not be driven by the LM' FP. Consequently, this FP is out of scope for the BFAM, whereas for the SIAM the LM' FP is of course relevant.

2.4.3 Critical exponents

In presence of a local magnetic field $H_{\mathrm{lf}} = \xi S_{\mathrm{z},d}$ we can measure the local magnetic susceptibility $\chi_{\mathrm{s,loc}}$, which has been introduced in Sec. 2.2.2. At a QCP, it shows an exponential behaviour

$$\chi_{\mathrm{s,loc}}(g = g_{\mathrm{c}}, T) \propto T^{-x} \tag{2.12}$$

with the exponent x. Since the BFCR FP of the BFAM is an interacting QCP the exponent x is connected to other critical exponents via hyperscaling relations [57]. For a detailed introduction to the critical exponents and their specific appearance for several models, we refer the reader to App. B.

The exponent x in the BFAM can be related to its fermionic $x_{\mathrm{F}}(r)$ counterpart of the SIAM, as well as to its bosonic $x_{\mathrm{B}}(s)$ counterpart of the SBM. Three types of quantum criticality in the BFAM can be distinguished [57] and are shown for different bath exponent combinations (r, s) in Fig. 2.9:

F For the fermionic type, the critical exponents are identical to those of the purely fermionic SIAM with the same r: $x(r, s) = x_{\mathrm{F}}(r)$.

B For the bosonic type, the critical exponents are identical to those of the purely bosonic SBM with the same s: $x(r, s) = x_{\mathrm{B}}(s)$.

M For the mixed type, the critical exponents satisfy $x(r,s) = x_{\mathrm{B}}$, but the order-parameter correlation-length exponent, cf. Sec. 2.1, lies between the values for the SBM and the SIAM: $\nu_{\mathrm{F}}^{-1}(r) < \nu^{-1}(r,s) < \nu_{\mathrm{B}}^{-1}(s)$.

Chapter 3

Numerical methods

The discovery of the Kondo effect in the early 1930s led to several approaches to explain it. The first approach which captures the low-temperature physics accurately has been done by Wilson in 1975. Wilson's numerical renormalisation group (NRG) [19] treats the Kondo model (KM) in a systematic and non-perturbative way. The prior perturbative approaches failed for the low-temperature physics due to infrared divergences at arbitrary small energies. The NRG proved to be suitable to solve other quantum impurity systems (QISs) as well, e.g. the symmetric [112] and asymmetric [113] single-impurity Anderson model (SIAM). We will introduce the NRG in Sec. 3.1.

Up to now, several extensions of the NRG have been developed. A very comprehensive overview is given in Ref. [20]. One extension is the bosonic NRG for bosonic environments, e.g. for the spin-boson model (SBM) [37, 90] or for more complex impurities, such as a DNA base pair in a bosonic environment [39, 40]. A hybrid NRG [120, 121] combines features of the NRG and density matrix renormalisation group (DMRG) to access long-time dynamics which is inaccessible for the NRG alone. Furthermore, the Bose-Fermi numerical renormalisation group (BF-NRG) [100] has been established to deal with a mixture of bosonic and fermionic baths. The relevant Bose-Fermi quantum impurity systems (BF-QISs) for the BF-NRG are the Bose-Fermi Kondo model (BFKM) [55, 100, 122] and the Bose-Fermi Anderson model (BFAM) [56, 57]. In Sec. 3.2 we will explain the additional modifications to the NRG to expand the NRG to BF-QISs.

With all these NRG variants equilibrium and dynamical properties of the QISs are accessible. To calculate real-time dynamics the time-dependent numerical renormalisation group (TD-NRG) has been developed [42, 123]. With this approach the real-time dynamics of the spin in the KM and the SBM has been investigated [123]. Recent improvements on pulsed dynamics [124] extended the possible applications of the TD-NRG. We will summarise the basic steps of the TD-NRG in Sec. 3.3.

3.1 The numerical renormalisation group

The discussion below follows primarily the presentation of the NRG in Ref. [20]. As exemplary impurity model, we use the SIAM of Sec. 1.2. Its Hamiltonian in Eq. (1.22) is given by

$$H_{\mathrm{SIAM}} = H_{\mathrm{SIAM,imp}} + H_{\mathrm{SIAM,bath}} + H_{\mathrm{SIAM,coup}} \tag{3.1}$$

with

$$H_{\mathrm{SIAM,imp}} = \sum_{\sigma} \epsilon_{\mathrm{d}} d_{\sigma}^{\dagger} d_{\sigma} + U d_{\uparrow}^{\dagger} d_{\uparrow} d_{\downarrow}^{\dagger} d_{\downarrow} \quad , \tag{3.2}$$

$$H_{\mathrm{SIAM,bath}} = \sum_{k,\sigma} \epsilon_k c_{k,\sigma}^{\dagger} c_{k,\sigma} \quad \text{and} \tag{3.3}$$

$$H_{\mathrm{SIAM,coup}} = \sum_{k,\sigma} V_k \left(c_{k,\sigma}^{\dagger} d_{\sigma} + d_{\sigma}^{\dagger} c_{k,\sigma} \right) \quad . \tag{3.4}$$

It is convenient to re-write the Hamiltonian of Eq. (3.1) in a continuum form [83]

$$H_{\mathrm{SIAM}} = H_{\mathrm{SIAM,imp}} + \sum_{\sigma} \int_{-D}^{D} \mathrm{d}\epsilon \; g(\epsilon) a_{\epsilon,\sigma}^{\dagger} a_{\epsilon,\sigma} + \sum_{\sigma} \int_{-D}^{D} \mathrm{d}\epsilon \; h(\epsilon) \left(d_{\sigma}^{\dagger} a_{\epsilon,\sigma} + a_{\epsilon,\sigma}^{\dagger} d_{\sigma} \right) \quad . \tag{3.5}$$

In this representation the operator[6] $a_{\epsilon,\sigma}^{\dagger}$ creates one fermion with energy ϵ and spin σ in the bath. The energy dispersion is expressed via $g(\epsilon)$ and the hybridisation by $h(\epsilon)$. Both functions are related to the scattering rate $\Gamma(\epsilon)$ via

$$\Gamma(\omega) = \pi h^2(\epsilon(\omega)) \frac{\mathrm{d}\epsilon(\omega)}{\mathrm{d}\omega} \tag{3.6}$$

with $\epsilon(\omega)$ being the inverse function of $g(\epsilon)$. It connects the continuum dispersion $g(\epsilon)$ and continuum hybridisation $h(\epsilon)$ to ϵ_k and V_k. The scattering rate $\Gamma(\epsilon)$ can be divided in many different ways according to Eq. (3.6) into $g(\epsilon)$ and $h(\epsilon)$.

For simplicity we make the assumption that the hybridisation $V_k = V_0$ is k independent and that we deal with a gapless Fermi system. Hence, the accurate low-energy physics can be obtained for a constant scattering rate $\Gamma(\epsilon) = \Gamma_0 \Theta(D - |\epsilon|)$ with $\Gamma_0 = \pi \rho_0 V_0^2$ and a constant conduction band DOS $\rho(\epsilon) = \rho_0 \Theta(D - |\epsilon|)$ with $\rho_0 = 1/(2D)$. For the constant DOS Eq. (3.6) is satisfied for $\epsilon(\omega) = \omega$ and $h^2(\epsilon) = \Gamma_0/\pi$, as shown in Ref. [112]. To handle an energy-dependent hybridisation, e.g. for a pg-DOS, one keeps the hybridisation $h^2(\epsilon)$ only in subintervals of the full band constant [83]. We will use the charge-fluctuation scale Γ_0 as physical energy unit for our results concerning the

[6] The fermionic operator $a_{\epsilon,\sigma}^{\dagger}$ fulfils the standard anticommutator relation $\{a_{\epsilon,\sigma}, a_{\epsilon',\sigma'}^{\dagger}\} = \delta(\epsilon - \epsilon')\delta_{\sigma,\sigma'}$.

SIAM and BFAM later. Nevertheless, for the following discussion of the NRG we use D as energy unit.

3.1.1 Logarithmic discretisation

The Hamiltonian in Eq. (3.5) reveals that the impurity is coupled to the whole energy continuum of the bath. This corresponds to a Hamiltonian matrix of infinite dimension and has to be restricted in some clever way. Wilson's proposal [19] to discretise the bath on a logarithmic mesh is the most efficient way to achieve a suitable energy hierarchy.

The discretisation points of the logarithmic mesh are

$$x_n^{\pm} = \pm D\Lambda^{-n} \quad , \qquad n = 0, 1, 2, 3, \ldots \tag{3.7}$$

with the discretisation parameter $\Lambda > 1$ and the index n counting the discretisation points. The interval width between two neighbouring discretisation points is

$$d_n = \left| x_n^{\pm} - x_{n+1}^{\pm} \right| = D\Lambda^{-n} \left(1 - \frac{1}{\Lambda} \right) \tag{3.8}$$

and shrinks logarithmically with increasing n. This produces a high resolution at energies close to the Fermi energy, which is relevant regarding the low-temperature physics.

In Fig. 3.1 the effect of the discretisation is sketched. In Fig. 3.1(a) the impurity couples to the whole energy continuum as described in Eq. (3.5). By introducing discretisation points and performing the following steps, the impurity couples only to one discrete energy for each subinterval, as depicted in Fig. 3.1(b) and as Eq. (3.14) will reveal.

So far, the energy continuum is only divided into subintervals. To achieve a discretised form of the Hamiltonian in Eq. (3.5) we introduce for each subinterval a new complete set of orthonormal functions [20]

$$\Psi_{n,p}^{\pm}(\epsilon) = \begin{cases} \frac{1}{\sqrt{d_n}} \mathrm{e}^{\pm i\omega_n p\epsilon} & \text{for } x_{n+1}^{\pm} < \pm\epsilon < x_n^{\pm} \quad , \\ 0 & \text{outside this interval} \quad , \end{cases} \tag{3.9}$$

with the frequency $\omega_n = 2\pi/d_n$ and the index $p \in \mathbb{Z}$. To expand the fermionic operator $a_{\epsilon,\sigma}^{\dagger}$ in this basis we have to distinguish between positive and negative energies, hence, we introduce two fermionic creation operators: $a_n^{\dagger}$ for the positive subinterval $[x_{n+1}^{+}, x_n^{+}]$ and $b_n^{\dagger}$ for the negative subinterval $[x_n^{-}, x_{n+1}^{-}]$. The conduction band operator reads in this basis

$$a_{\epsilon,\sigma}^{\dagger} = \sum_{n,p} \left(a_{n,p,\sigma}^{\dagger} \Psi_{n,p}^{+}(\epsilon) + b_{n,p,\sigma}^{\dagger} \Psi_{n,p}^{-}(\epsilon) \right) \quad . \tag{3.10}$$

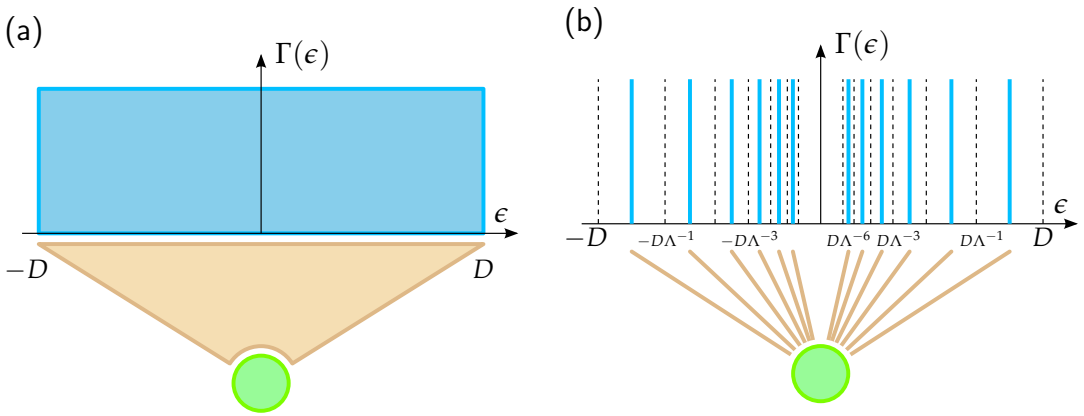

Figure 3.1: Discretisation of the conduction band with a constant DOS in the interval $[-D, D]$. In (a) the impurity couples via H_{coup} to the whole energy continuum. In (b) the continuum is divided into subintervals $[x_n^{\pm}, x_{n+1}^{\pm}]$. For each subinterval one discrete energy is used which couples to the impurity.

This corresponds to a Fourier transformation in each subinterval. We now take a closer look on the second part of H_{coup} in Eq. (3.5) and re-write it in this new basis:

$$\int_{-D}^{D} \mathrm{d}\epsilon\, h(\epsilon) a_{\epsilon,\sigma}^{\dagger} d_\sigma = d_\sigma \sum_{n,p} \left(a_{n,p,\sigma}^{\dagger} \int^{+,n} \mathrm{d}\epsilon\, h(\epsilon) \Psi_{n,p}^{+}(\epsilon) + b_{n,p,\sigma}^{\dagger} \int^{-,n} \mathrm{d}\epsilon\, h(\epsilon) \Psi_{n,p}^{-}(\epsilon) \right) \tag{3.11}$$

where we used the definitions

$$\int^{+,n} \mathrm{d}\epsilon = \int_{x_{n+1}^{+}}^{x_n^{+}} \mathrm{d}\epsilon \quad \text{and} \quad \int^{-,n} \mathrm{d}\epsilon = \int_{x_n^{-}}^{x_{n+1}^{-}} \mathrm{d}\epsilon \quad . \tag{3.12}$$

As expressed in Eq. (3.6), the energy dependence of the hybridisation function can be arbitrarily divided into $g(\epsilon)$ and $h(\epsilon)$. If we choose $h(\epsilon) = h$ to be constant[7], the integrals in Eq. (3.11) become

$$\int^{\pm,n} \mathrm{d}\epsilon\, h \Psi_{n,p}^{\pm}(\epsilon) = \sqrt{d_n} h \delta_{p,0} \tag{3.13}$$

and filter out the $p = 0$ component of the new basis. Therefore, the impurity couples only to the $p = 0$ component, or in other words, to one discrete energy value for the

[7] For a non-constant DOS, e.g. a pseudo-gap DOS or a bosonic power-law DOS, it is convenient to hold the hybridisation constant in each subinterval so that it is possible to perform the same steps and approximations. Bulla *et al.* [83] showed that it is a convenient choice to set the coupling strength $h_n^{\pm} = \frac{1}{d_n} \int^{\pm,n} \mathrm{d}\epsilon\, \frac{1}{\pi}\Gamma(\epsilon)$ to its mean value in the subinterval $[x_{n+1}^{\pm}, x_n^{\pm}]$. By this, the energy dependence is shifted into the dispersion $g(x_n) = x_n$ which exactly reproduces the energy dispersion at the discretisation points x_n, while for intermediate points $g(x) = x$ is not fulfilled.

whole subinterval $[x_n^{\pm}, x_{n+1}^{\pm}]$. It is possible to re-write the full Hamiltonian of Eq. (3.5) in this new basis. The main approximation of the NRG is that we neglect the $p \neq 0$ components because they do not couple to the impurity directly. The $p = 0$ and $p \neq 0$ components are still connected with each other in the free bath part H_{bath}. This connection will be neglected, as well. Hence, we do not need the index p any longer. The impact of this approximation is not obvious at this point. It can only be justified by the accuracy of the results, obtained for the $p = 0$ component, which are good and even good for large Λ. Furthermore, the $p = 0$ and $p \neq 0$ components couple to each other with a prefactor $(1 - 1/\Lambda)$, which vanishes in the continuum limit $\Lambda \to 1^+$ [20]. In this new basis the full Hamiltonian of Eq. (3.5) reads

$$\begin{aligned} H = H_{\text{imp}} &+ \sum_{n,\sigma} \left(\xi_n^+ a_{n,\sigma}^\dagger a_{n,\sigma} + \xi_n^- b_{n,\sigma}^\dagger b_{n,\sigma} \right) \\ &+ \frac{1}{\sqrt{\pi}} \sum_{n,\sigma} \left(d_\sigma^\dagger \left(\gamma_n^+ a_{n,\sigma} + \gamma_n^- b_{n,\sigma} \right) + \left(\gamma_n^+ a_{n,\sigma}^\dagger + \gamma_n^- b_{n,\sigma}^\dagger \right) d_\sigma \right) \end{aligned} \tag{3.14}$$

with the definitions

$$\gamma_n^{\pm} = \sqrt{\int^{\pm,n} \mathrm{d}\epsilon\, \Gamma(\epsilon)} \quad \text{and} \quad \xi_n^{\pm} = \frac{\int^{\pm,n} \mathrm{d}\epsilon\, \Gamma(\epsilon)\epsilon}{\int^{\pm,n} \mathrm{d}\epsilon\, \Gamma(\epsilon)} \quad . \tag{3.15}$$

More details on the derivation of Eq. (3.14) are given in Ref. [20].

3.1.2 Mapping onto a semi-infinite chain

The Hamiltonian in the discretised form in Eq. (3.14) has a star topology, namely the impurity couples to each discrete energy. Via a Householder transformation it is changed to a chain topology as depicted in Fig. 3.2. The unitary transformation maps the operators a_n and b_n to c_n. The Hamiltonian in Eq. (3.14) is transformed to

$$\begin{aligned} H = H_{\text{imp}} &+ \sqrt{\frac{\xi_0}{\pi}} \sum_{\sigma} \left(d_\sigma^\dagger c_{0,\sigma} + c_{0,\sigma}^\dagger d_\sigma \right) \\ &+ \sum_{n=0,\sigma}^{\infty} \left(\epsilon_n c_{n,\sigma}^\dagger c_{n,\sigma} + t_n \left(c_{n,\sigma}^\dagger c_{n+1,\sigma} + c_{n+1,\sigma}^\dagger c_{n,\sigma} \right) \right) \end{aligned} \tag{3.16}$$

with $\xi_0 = \int_{-D}^{D} \mathrm{d}\epsilon\, \Gamma(\epsilon)$. The operator $c_{n,\sigma}^\dagger$ creates an electron with spin σ on the n-th site of the so-called Wilson chain. The impurity (d operators, green in Fig. 3.2) only couples to the zeroth chain site (c_0 operators) with the coupling strength $\sqrt{\xi_0/\pi}$. A Wilson chain site couples to its next neighbour with the hopping term t_n and has the on-site energy ϵ_n which is zero for a ph symmetric bath.

In general, the chain parameters ϵ_n and t_n have to be calculated numerically which is explained in detail in Ref. [20]. For a few special cases analytical expressions for

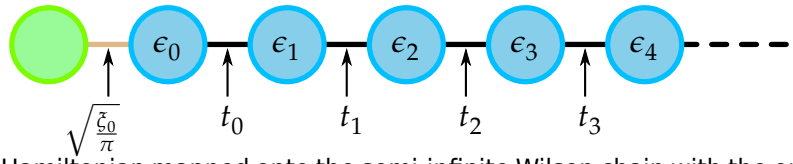

Figure 3.2: Hamiltonian mapped onto the semi-infinite Wilson chain with the on-site energies ϵ_n and the hopping terms t_n. The impurity only couples to the first chain site with the coupling strength $\sqrt{\xi_0/\pi}$.

the chain parameters have been gained. For example, for a constant DOS[8] Wilson has already derived the chain parameters in the context of the KM [19]. The on-site energy is $\epsilon_n = 0$ for all n, since the conduction band is ph symmetric, and the hopping term is

$$t_n = \frac{(1+1/\Lambda)(1-1/\Lambda^{n+1})}{2\sqrt{1-1/\Lambda^{2n+1}}\sqrt{1-1/\Lambda^{2n+3}}} D\Lambda^{-n/2} \quad . \tag{3.17}$$

In the limit $n \gg 1$, namely for long chains, the formula reduces to

$$t_n \to \frac{1}{2}\left(1+\frac{1}{\Lambda}\right) D\Lambda^{-n/2} \quad . \tag{3.18}$$

This reveals that the hopping terms fall off exponentially with increasing chain length which is a direct consequence of the used logarithmic mesh.
The coupling between the impurity and the zeroth Wilson chain site is simply given by $\sqrt{\xi_0/\pi} = V_0$ for a k-independent hybridisation. In general, this coupling is underestimated within the NRG due to the discretisation $\Lambda > 1$. To achieve the correct coupling in the continuum limit $\Lambda \to 1$ the coupling $V_0' = \sqrt{A_\Lambda} V_0$ is scaled by the correction factor A_Λ [112, 126]. For a constant DOS[9] this correction factor is given by

$$A_\Lambda = \frac{1}{2}\frac{\Lambda+1}{\Lambda-1}\ln\Lambda \quad . \tag{3.20}$$

Although this is a common procedure, in this thesis all results are calculated without this correction factor.

[8] Also for other DOSs analytical expressions have been derived, for example the hopping term t_n for a pg-DOS in Ref. [83]. In the case of a bosonic bath with the standard power-law coupling function $J(\omega)$, cf. Sec. 3.2, the on-site energy ϵ_n and the hopping term t_n have been calculated analytically in Ref. [125]. Due to the length of the formulas we only cite the references here.

[9] In the case of a pg-DOS with the exponent r the correction factor is

$$A_\Lambda(r) = \left(\frac{1-1/\Lambda^{2+r}}{2+r}\right)^{1+r}\left(\frac{1+r}{1-1/\Lambda^{1+r}}\right)^{2+r}\ln\Lambda \tag{3.19}$$

and has been derived in Ref. [25]. For a bosonic coupling function $J(\omega)$ an analytical form is not known.

3.1.3 Iterative diagonalisation

The chainlike Hamiltonian in Eq. (3.16) can be viewed as a sequence of Hamiltonians

$$H_N = \Lambda^{\frac{N-1}{2}} \left(H_{\text{imp}} + \sqrt{\frac{\xi_0}{\pi}} \sum_\sigma \left(d_\sigma^\dagger c_{0,\sigma} + c_{0,\sigma}^\dagger d_\sigma \right) + \sum_{n=0,\sigma}^{N} \epsilon_n c_{n,\sigma}^\dagger c_{n,\sigma} + \sum_{n=0,\sigma}^{N-1} t_n \left(c_{n,\sigma}^\dagger c_{n+1,\sigma} + c_{n+1,\sigma}^\dagger c_{n,\sigma} \right) \right) \tag{3.21}$$

with the finite chain length $N+1$ which approaches H in the limit

$$H = \lim_{N\to\infty} \Lambda^{-\frac{N-1}{2}} H_N \quad . \tag{3.22}$$

The scaling factor $\Lambda^{\frac{N-1}{2}}$ in Eq. (3.21) cancels the N dependence of the hopping term t_{N-1} between the last two chain sites. Therefore, the hopping term becomes of the order $O(1)$, which is useful for the discussion of FPs.

The RG concept of the NRG is expressed in the connection of two successive elements of the sequence, i.e.

$$H_{N+1} = \sqrt{\Lambda} H_N + \Lambda^{\frac{N}{2}} \sum_\sigma \left(\epsilon_{N+1} c_{N+1,\sigma}^\dagger c_{N+1,\sigma} + t_N \left(c_{N,\sigma}^\dagger c_{N+1,\sigma} + c_{N+1,\sigma}^\dagger c_{N,\sigma} \right) \right) \ , \tag{3.23}$$

which can be shortly written as $H_{N+1} = \mathcal{R}(H_N)$. The starting Hamiltonian for the RG is given by

$$H_0 = \Lambda^{-\frac{1}{2}} \left(H_{\text{imp}} + \sum_\sigma \epsilon_0 c_{0,\sigma}^\dagger c_{0,\sigma} + \sqrt{\frac{\xi_0}{\pi}} \sum_\sigma \left(d_\sigma^\dagger c_{0,\sigma} + c_{0,\sigma}^\dagger d_\sigma \right) \right) \tag{3.24}$$

which consists of the impurity coupled to a one-site Wilson chain. In Fig. 3.3 the RG procedure of the NRG is depicted: The innermost box is the starting Hamiltonian for the RG. In each NRG step one Wilson chain site is added to the chain and the enlarged chain is marked by the next-outer box. The RG step in Eq. (3.23) is independent of the specific impurity which only enters the starting Hamiltonian in Eq. (3.24).

To solve the Hamiltonian H in the limit of Eq. (3.22), we make use of the RG step in Eq. (3.23). Within the NRG we express the Hamiltonian H_N by its many-body eigenenergies and compare eigenenergies of different RG steps to classify the RG energy flow. Hence, the problem for a given N, can be written as

$$H_N |r\rangle_N = E_N(r) |r\rangle_N \quad , \qquad r = 1, ..., N_S \quad , \tag{3.25}$$

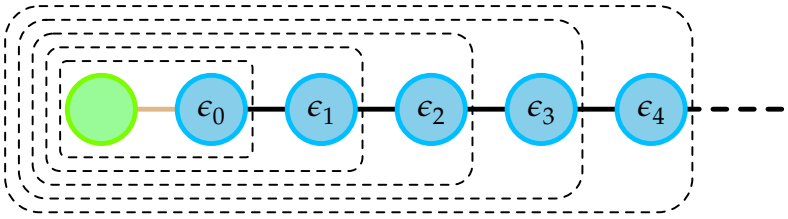

Figure 3.3: Subdivision of the impurity (green) and the semi-infinite Wilson chain (blue) into finite chains of length $N+1$ marked by the different boxes. Each box represents a Wilson shell. The innermost box marks the starting condition of the NRG and each next-outer box corresponds to a chain enlarged by one chain site.

with the eigenenergies $E_N(r)$ and the corresponding eigenstates $|r\rangle_N$. The Hamiltonian H_N has the dimension N_S. If we perform the RG step of Eq. (3.23), the basis of H_{N+1} is given by the product states

$$|r,s\rangle_{N+1} = |r\rangle_N \otimes |s(N+1)\rangle \tag{3.26}$$

with the eigenstates $|r\rangle_N$ of H_N and a suitable basis $|s(N+1)\rangle$ of the added Wilson chain site. For the fermionic bath the latter one may be $|0\rangle$, $|\uparrow\rangle$, $|\downarrow\rangle$ and $|\uparrow\downarrow\rangle$. Using the basis of Eq. (3.26) we can express the matrix elements of the Hamiltonian H_{N+1}:

$$H_{N+1}(r,s;r',s') = \langle r,s|H_{N+1}|r',s'\rangle \tag{3.27a}$$

$$\begin{aligned} &= \sqrt{\Lambda}E_N(r)\delta_{r,r'}\delta_{s,s'} + \Lambda^{\frac{N}{2}}\sum_\sigma \epsilon_{N+1}\langle s|c^\dagger_{N+1,\sigma}c_{N+1,\sigma}|s'\rangle\delta_{r,r'} \\ &\quad + \Lambda^{\frac{N}{2}}\sum_\sigma t_N\langle r,s|\left(c^\dagger_{N,\sigma}c_{N+1,\sigma} + c^\dagger_{N+1,\sigma}c_{N,\sigma}\right)|r',s'\rangle \quad . \end{aligned} \tag{3.27b}$$

The numerical diagonalisation of the matrix H_{N+1} in Eq. (3.27b) provides new eigenvalues $E_{N+1}(\omega)$ and eigenstates $|\omega\rangle_{N+1}$, which are related to the basis $|r,s\rangle_{N+1}$ via a unitary transformation

$$|\omega\rangle_{N+1} = \sum_{r,s} U(\omega;r,s)|r,s\rangle_{N+1} \quad . \tag{3.28}$$

By replacing the label ω by r we gain the eigenbasis of H_{N+1}.

Therefore, we achieved an iterative procedure to perform the limit in Eq. (3.22) by successively applying the former presented steps. Of course, the numerics has some limitations. Firstly, the number of eigenstates increases exponentially by adding new sites to the Wilson chain. With each chain site it increases by the dimension of the basis $|s(N+1)\rangle$. To keep the iterative procedure manageable[10] the new basis $|r\rangle_{N+1}$ has to be truncated: Only the N_S eigenstates with the lowest many-body eigenenergies are

[10] The restriction to a fixed number of states in each iteration guarantees that the computation time increases linearly with N. The truncation scheme is motivated in Sec. 3.1.4 and the number of kept states N_S highly depends on the model and has to be adjusted according to reliable results.

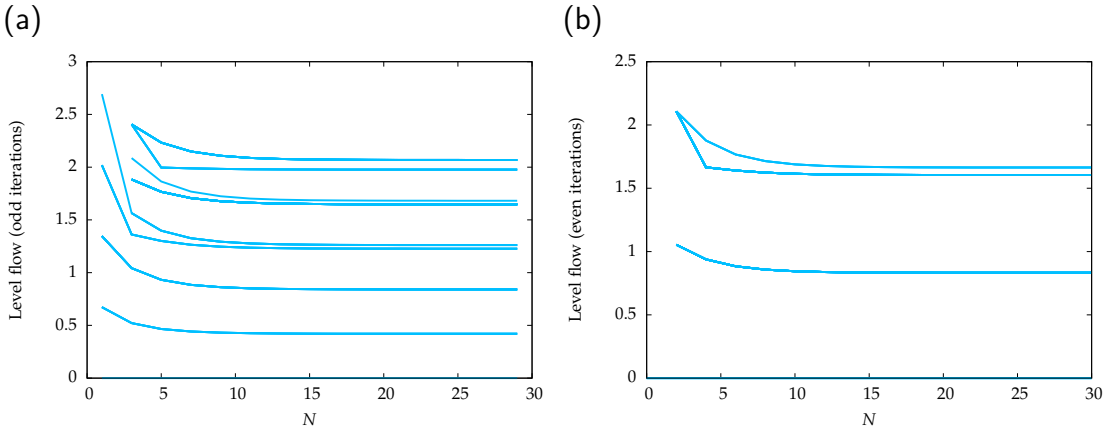

Figure 3.4: Flow diagram of the energy levels versus (a) odd and (b) even iteration numbers N for a free fermionic bath with the NRG parameter $\Lambda = \sqrt{2}$ and $N_S = 2000$ states kept in each iteration.

kept for the next RG step. Secondly, the limit in Eq. (3.22) is considered to be achieved if the flow of the eigenenergies $E_N(r)$ is converged into a FP spectrum. Due to the scaling factor $\Lambda^{\frac{N-1}{2}}$ in the RG step, cf. Eq. (3.23), the eigenenergies are of the order $O(1)$ for all iterations. A FP is reached if the Hamiltonian H^* is invariant under the RG step $\mathcal{R}(H^*) = H^*$.

For the free fermionic bath, the flow of the eigenenergies is shown in Fig. 3.4. The fermionic bath has only FPs under the RG transformation $\mathcal{R}^2$ because of the even-odd asymmetry: At an even iteration the number of electrons is even and they can form a singlet while for an odd iteration on electron is left over. Therefore, we show the eigenenergies at odd iterations in Fig. 3.4(a) and at even iterations in Fig. 3.4(b), respectively. With the chosen parameters $\Lambda = \sqrt{2}$ and $N_S = 2000$ the eigenenergies converge into the free bath FP after 15 iterations.

3.1.4 Calculation of impurity expectation values

With the help of the many-body eigenenergies, the NRG is capable to calculate thermodynamic expectation values of an operator O of the zeroth Wilson shell. In general, the expectation value is given by

$$\langle O \rangle = \frac{1}{Z} \mathrm{Tr} \left(\mathrm{e}^{-\beta H} O \right) \tag{3.29}$$

with the inverse temperature $\beta = 1/T$ and the partition function $Z = \mathrm{Tr} \left(\mathrm{e}^{-\beta H} \right)$. As described in the previous section the full Hamiltonian H is approximated by the dis-

cretised and truncated Hamiltonian H_N with the eigenstates $H_N|r\rangle_N = E_N(r)|r\rangle_N$, $r = 0, ..., N_S$, and the eigenenergies $E_N(r)$. Hence, the partition function is given by

$$Z_N = \sum_r \mathrm{e}^{-\beta_N E_N(r)} \quad \text{with} \tag{3.30}$$

$$\beta_N = \beta \Lambda^{-\frac{N-1}{2}} \quad . \tag{3.31}$$

The inverse temperature $\beta_N =: \overline{\beta} = O(1)$ is set to the order of one. Then, for a given temperature $\overline{T} = 1/\overline{\beta}$ the eigenenergies $E_N(r) \gg \Lambda^{-(N-1)/2}\beta$ are suppressed by the Boltzmann factor and do not contribute significantly to the expectation value[11]. This supports the argumentation why the truncation of high-energy states is a good approximation. By Eq. (3.31) and $\beta_N =: \overline{\beta} = O(1)$ a discretised temperature

$$T_N = \Lambda^{-\frac{N-1}{2}} \frac{1}{\overline{\beta}} \tag{3.32}$$

can be introduced. The temperature decreases exponentially with the iteration N. Finally, we can re-write Eq. (3.29) to

$$\langle O \rangle_N = \frac{1}{Z_N} \mathrm{Tr} \left(\mathrm{e}^{-\beta \Lambda^{-\frac{N-1}{2}} H_N} O \right) \tag{3.33}$$

$$= \frac{1}{Z_N} \sum_r \mathrm{e}^{-\beta_N E_N(r)} {}_N\langle r|O|r\rangle_N \quad . \tag{3.34}$$

This describes a sequence of expectation values $\langle O \rangle_N$ at decreasing temperatures T_N. Additionally, it is possible to re-write the calculation of the expectation value

$$\langle O \rangle = \frac{1}{Z} \mathrm{Tr} \left(\mathrm{e}^{-\beta H} O \right) = \mathrm{Tr} \left(\rho O \right) \tag{3.35}$$

with the density operator ρ, which is given in the discretised and truncated form by

$$\rho_N = \frac{1}{Z_N} \sum_r \mathrm{e}^{-\beta_N E_N(r)} |r\rangle_{NN}\langle r| \quad . \tag{3.36}$$

Performing the limit $N \to \infty$, the expectation value $\langle O \rangle_N \to \langle O \rangle$ reaches the low-temperature limit. In fact, generally it is sufficient to iterate until the expectation value has reached a FP value. To evaluate the expectation value for a finite temperature $T > 0$ the discretisation parameter Λ, the number of iterations N and the inverse temperature[12] $\overline{\beta}$ have to be chosen such that $T = T_N$ is fulfilled.

[11] To ensure that the full Hamiltonian H is well approximated by the discretised and truncated Hamiltonian H_N, it is important to keep enough N_S states at each iteration so that the condition $E_N(r) \gg \Lambda^{-(N-1)/2}\beta$ is still fulfilled.

[12] Normally, the inverse temperature $\overline{\beta} = 1$ is set to one.

3.1.5 Improvement: Oliveira's averaging

In Sec. 3.1.1 the discretisation of the bath continuum has been described. By the discretisation finite-size effects emerge within the NRG and, consequently, also for the derived methods, which are based on the NRG. These finite-size effects may cause the calculation of physical quantities, e.g. non-physical oscillations in the long-time dynamics for TD-NRG calculations. The greater the discretisation parameter Λ, the stronger are these non-physical effects.

To cure this problem Oliveira *et al.* [127–129] modified the logarithmic discretisation points of Eq. (3.7) by

$$x_n^{\pm} = \pm D\Lambda^{-(n+z)} \quad , \qquad n = 0, 1, 2, 3, \ldots \quad , \tag{3.37}$$

with $\Lambda > 1$ and $0 < z \leq 1$. Averaging over N_z different discretisations[13] of the bath for a fixed set of temperatures T_N is a successful way to avoid non-physical oscillations, e.g. in the impurity magnetic susceptibility of the KM.

This averaging is meant to re-introduce the continuum limit to some content and it is able to suppress oscillations introduced by the use of large Λ [129]. Nevertheless, it is not the same as the true continuum limit $\Lambda \to 1^+$.

3.2 The Bose-Fermi numerical renormalisation group

The first implementation of the NRG for a bath with bosonic DOFs was achieved by Bulla *et al.* [37, 90] in 2003. They examined the equilibrium properties of the SBM. The BF-NRG to investigate QIS with an environment consisting of bosonic and fermionic DOFs has been developed by Ingersent *et al.* [100] in 2005. They studied the BFKM [55, 100, 122] and the BFAM [56, 57]. The following discussion reflects primarily the presentation of the BF-NRG in Ref. [55] and is faithful to the bosonic bath description in Ref. [90]. In principle the BF-NRG works with the same steps as the NRG, hence, we only point out the additional steps which have to be done for the bosonic parts.

We explain the BF-NRG examplified for the BFAM whose Hamiltonian in Eq. (1.35) is given by

$$H_{\mathrm{BFAM}} = H_{\mathrm{SIAM}} + H_{\mathrm{B,bath}} + H_{\mathrm{B,coup}} \quad \text{with} \quad H_{\mathrm{B,bath}} = \sum_q \omega_q \phi_q^\dagger \phi_q \tag{3.38}$$

$$\text{and} \quad H_{\mathrm{B,coup}} = \left(\sum_\sigma d_\sigma^\dagger d_\sigma - 1 \right) \sum_q \lambda_q \left(\phi_q^\dagger + \phi_q \right) \quad . \tag{3.39}$$

[13] Typically, the z values are set to $z_i = i/N_z$ with $i = 1, \ldots, N_z$ and should be chosen in multiples of four to produce the best results [128].

The parameters λ_q and ω_q solely depend on the bosonic bath as stated in the context of the SBM in Sec. 1.3. They are determined by the bosonic spectral bath function

$$J(\omega) = 2\pi g \omega_c^{s-1} \omega^s \, \Theta(\omega)\Theta(\omega_c - \omega) \tag{3.40}$$

given in its power-law form. The bosonic bath consists only of positive energies with the high-energy cut-off ω_c, which may be used as energy unit.

Similarly to the NRG, the Hamiltonian in Eq. (3.38) can be re-written in the continuum form

$$\begin{aligned} H_{\mathrm{BFAM}} = H_{\mathrm{imp}} + \sum_\sigma \int_{-D}^{D} \mathrm{d}\epsilon \; g_{\mathrm{F}}(\epsilon) a^\dagger_{\epsilon,\sigma} a_{\epsilon,\sigma} + \sum_\sigma \int_{-D}^{D} \mathrm{d}\epsilon \; h_{\mathrm{F}}(\epsilon) \left(d^\dagger_\sigma a_{\epsilon,\sigma} + a^\dagger_{\epsilon,\sigma} d_\sigma \right) \\ + \int_0^{\omega_c} \mathrm{d}q \; g_{\mathrm{B}}(q) \phi^\dagger_q \phi_q + \left(\sum_\sigma d^\dagger_\sigma d_\sigma - 1 \right) \int_0^{\omega_c} \mathrm{d}q \; h_{\mathrm{B}}(q) \left(\phi^\dagger_q + \phi_q \right) \quad . \end{aligned} \tag{3.41}$$

The fermionic parts are the same as in Eq. (3.5). The function $g_{\mathrm{F/B}}(x)$ for the energy dispersion and $h_{\mathrm{F/B}}(x)$ for the coupling function[14] are related to each other via

$$\Gamma(x) = \pi h^2_{\mathrm{F}}(\epsilon_{\mathrm{F}}(x)) \frac{\mathrm{d}\epsilon_{\mathrm{F}}(x)}{\mathrm{d}x} \quad \text{, for fermionic relation, and} \tag{3.42}$$

$$J(x) = \pi h^2_{\mathrm{B}}(\epsilon_{\mathrm{B}}(x)) \frac{\mathrm{d}\epsilon_{\mathrm{B}}(x)}{\mathrm{d}x} \quad \text{, for bosonic relation,} \tag{3.43}$$

with $\epsilon_{\mathrm{F/B}}(x)$ being the inverse function of $g_{\mathrm{F/B}}(x)$. While Eq. (3.42) for the fermionic relation is identical to Eq. (3.6), the relation in Eq. (3.43) describes the bosonic case regarding the spectral function $J(x)$.

3.2.1 Discretisation and mapping

The spectral function $J(\omega)$ is discretised on a logarithmic mesh with the discretisation points

$$x_m = \omega_c \Lambda^{-m} \quad , \qquad m = 0, 1, 2, 3, \ldots \quad , \tag{3.44}$$

with the discretisation parameter $\Lambda > 1$ and the index m counting the discretisation points. In contrast to the fermionic discretisation in Sec. 3.1.1, we have here only positive energies. Since we discretise in the fermionic and the bosonic case with the same discretisation points, we imply in the following that the fermionic bandwidth and the bosonic cut-off are equal: $\omega_c / D = 1$. This is a rather strong assumption because in the

[14] The coupling function $h_{\mathrm{F/B}}(x)$ is called hybridisation function in the fermionic case and coupling function in the bosonic case.

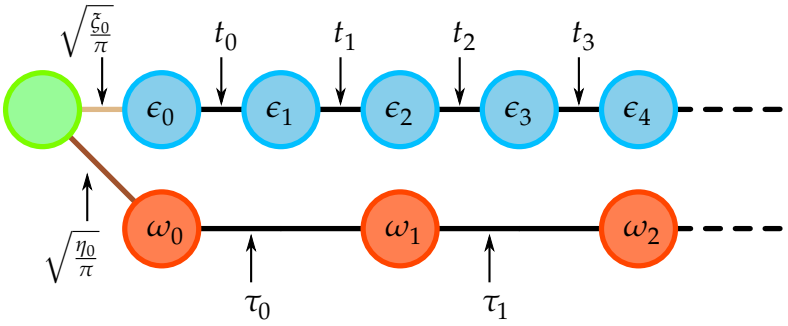

Figure 3.5: Hamiltonian mapped onto two semi-infinite Wilson chains. The fermionic Wilson chain (blue) has the on-site energies ϵ_n and the hopping terms t_n. The bosonic Wilson chain (red) has the on-site energies ω_m and the hopping terms τ_m. The impurity only couples to the first site of each chain with the coupling strength $\sqrt{\xi_0/\pi}$ for the fermionic chain and $\sqrt{\eta_0/\pi}$ for the bosonic chain.

context of the Anderson-Holstein model [99, 130] the phonon frequency is typically a small fraction of the bandwidth, i.e. $\omega_c/D = 0.01$. Nevertheless, instead of only one phonon, we deal here with a full continuum of bosonic DOFs. Hence, the specific choice of $\omega_c/D = 1$ does not influence the low-temperature physics.

Similarly to the standard NRG, the fermionic and the bosonic baths are mapped separately onto two semi-infinite chains, as depicted in Fig. 3.5. The Wilson chain sites for both chain types couple only to their next neighbour with the hopping term t_n for the fermionic and with τ_m for the bosonic type. The fermionic on-site energy ϵ_n is zero for all n in the case of a ph symmetric bath, whereas the bosonic on-site energy ω_m is finite due to the purely positive spectral function. Since the fermionic bath contains positive and negative energies, the fermionic hopping term $t_n \propto D\Lambda^{-(n/2)}$ scales exponentially with the index $n/2$, while the bosonic hopping term[15] $\tau_m \propto \omega_c\Lambda^{-m}$ scales with the index m. Hence, the bosonic hopping term τ_m falls off twice as fast as the fermionic hopping term t_n if we increase both indices by one. If we bind the bosonic index m to the fermionic index n via $m = \lfloor n/2 \rfloor$, both Wilson chains obey to the same energy hierarchy. The bosonic sites are assigned to the even-numbered fermionic sites as depicted in Fig. 3.5.

[15] A full analytical derivation of the on-site energy ω_m and the hopping term τ_m for the standard parametrisation of $J(x)$ in Eq. (3.40) can be looked up in Ref. [125].

3.2.2 Iterative diagonalisation

For the RG transformation $H_N = \mathcal{R}(H_{N-1})$, we have to distinguish if N is an even or an odd number due to the different scaling of the hopping terms. Two successive elements of the sequence H_N are connected by

$$H_N = \sqrt{\Lambda} H_{N-1} \tag{3.45a}$$

$$+ \Lambda^{\frac{N-1}{2}} \sum_\sigma \left(\epsilon_N c^\dagger_{N,\sigma} c_{N,\sigma} + t_{N-1} \left(c^\dagger_{N-1,\sigma} c_{N,\sigma} + c^\dagger_{N,\sigma} c_{N-1,\sigma} \right) \right) \tag{3.45b}$$

$$+ \Lambda^{\frac{N-1}{2}} \begin{cases} \left(\omega_M q^\dagger_M q_M + \tau_{M-1} \left(q^\dagger_{M-1} q_M + q^\dagger_M q_{M-1} \right) \right) & \text{for } N \text{ even} \quad , \\ 0 & \text{for } N \text{ odd} \quad . \end{cases} \tag{3.45c}$$

The starting Hamiltonian for the RG is given by

$$\begin{aligned} H_0 = \Lambda^{-\frac{1}{2}} \Bigg(& H_{\text{imp}} + \sum_\sigma \epsilon_0 c^\dagger_{0,\sigma} c_{0,\sigma} + \sqrt{\frac{\xi_0}{\pi}} \sum_\sigma \left(d^\dagger_\sigma c_{0,\sigma} + c^\dagger_{0,\sigma} d_\sigma \right) \\ & + \omega_0 q^\dagger_0 q_0 + \sqrt{\frac{\eta_0}{\pi}} \left(\sum_\sigma d^\dagger_\sigma d_\sigma - 1 \right) \left(q^\dagger_0 + q_0 \right) \Bigg) \quad , \end{aligned} \tag{3.46}$$

with the local couplings $\xi_0 = \int_{-D}^{D} \mathrm{d}\epsilon \; \Gamma(\epsilon)$ and $\eta_0 = \int_0^{\omega_c} \mathrm{d}x \; J(x)$. The operator $c^\dagger_{n,\sigma}$ creates an electron with spin σ on the n-th site of the fermionic Wilson chain, the operator $d^\dagger_\sigma$ creates an electron with spin σ on the impurity and the operator $q^\dagger_m$ creates an excitation on the m-th site of the bosonic Wilson chain.

For the RG step $N \to N+1$ the product basis of H_{N+1} contains a suitable basis $\{|s(N+1)\rangle\}$ of the added Wilson chain site(s). For an odd iteration number N only a fermionic site is added and $\{|s(N+1)\rangle\} = \{|F\rangle\}$ containing the fermionic occupation eigenstates $\{|F\rangle\} = \{|0\rangle, |\uparrow\rangle, |\downarrow\rangle, |\uparrow\downarrow\rangle\}$. For an even iteration number N a fermionic and a bosonic site are added which determine the suitable eigenstates $|s(N+1)\rangle = |F\rangle \otimes |B\rangle$ as a direct product of the fermionic basis $\{|F\rangle\}$ and the bosonic occupation basis[16] $\{|B\rangle\}$. In general, the bosonic occupation basis $q^\dagger_m q_m |n_m\rangle = n_m |n_m\rangle$, with the occupation number n_m of the m-th chain site, is infinite. For the numerics we have to restrict it to a finite number N_B of states: $n_m = 0, 1, ..., N_\text{B}$ and consequently $\{|B\rangle\} = \{|0\rangle, |1\rangle, ..., |N_\text{B}\rangle\}$. Then, we have a well-defined basis for H_{N+1} and can diagonalise the matrix of H_{N+1} to provide new eigenenergies $E_{N+1}(r)$ with the eigenstates $|r\rangle_{N+1}$ and proceed with the next RG step. With the eigenenergies $E_N(r)$ and eigenstates $|r\rangle_{N+1}$ we have all information needed to calculate impurity expectation values

[16] Within this thesis we only use the bosonic occupation basis, which has already been used in several publications [37, 39, 55, 90, 100]. Of course, other bases are also possible, e.g. consisting of coherent states [131] or displaced oscillator states [90]. The latter one has been used in the context of the SBM which was treated with a starlike NRG where the impurity couples to all representative energies directly.

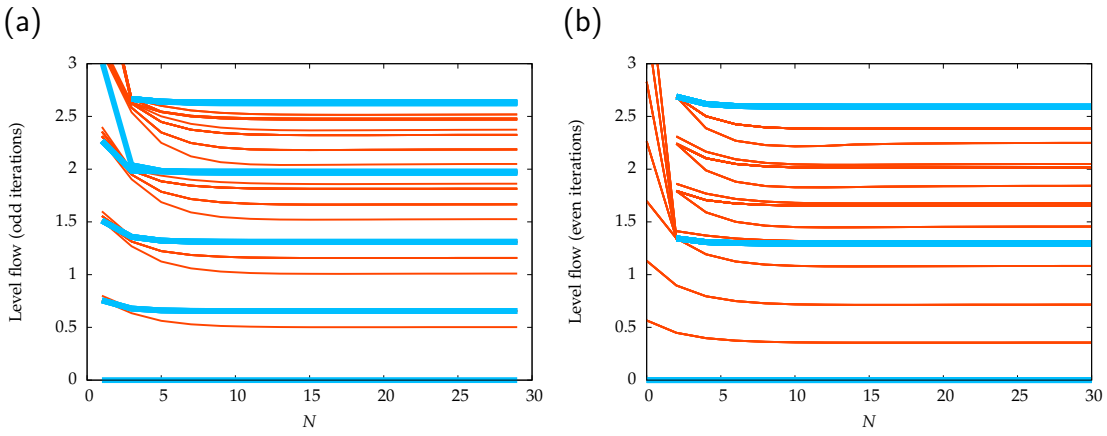

Figure 3.6: Flow diagram of the energy levels versus (a) odd and (b) even iteration numbers N. The energy levels of the system consisting of a free fermionic and bosonic bath are coloured in red. Additionally, the energy levels of a free fermionic bath are coloured in blue. The NRG parameters are $\Lambda = 2$, $s = 0.5$, $N_\mathrm{B} = 8$ and $N_\mathrm{S} = 1000$.

as described in Sec. 3.1.4. Through the iterative diagonalisation a flow of the eigenenergies $E_N(r)$ is generated, which can be used to characterise a specific FP. In Fig. 3.6 the flow of eigenenergies, called level flow, is shown in red colour for a system consisting of a free fermionic and a free bosonic bath. It is distinguished between even and odd iterations due to the even-odd oscillations of the fermionic bath, cf. the discussion at the end of Sec. 3.1.3. After a few iterations ($N \sim 15$) the levels converge and classify the so-called free baths FP. Its level structure is simply a linear combination of the level structures of the free fermionic bath FP, which are coloured in blue, and the free bosonic bath FP. This is easy to see for the even iterations in Fig. 3.6(b). The lowest red curve is the eigenenergy e_1^B. The second and third lowest red curves are integral multiples, $2e_1^\mathrm{B}$ and $3e_1^\mathrm{B}$, of this eigenenergy. The lowest blue curve, which is greater than zero, is the lowest fermionic eigenenergy e_1^F, which was calculated separately with the standard NRG. The next higher red eigenenergies are linear combinations of the two lowest bosonic and the second lowest fermionic eigenenergies: $E_N = k \cdot e_1^\mathrm{B} + l \cdot e_1^\mathrm{F}$. The level structure of the combined system for the even FP, therefore, consists of these eigenenergies: 0, e_1^B, $2e_1^\mathrm{B}$, $3e_1^\mathrm{B}$, e_1^F, $4e_1^\mathrm{B}$, $e_1^\mathrm{F} + e_1^\mathrm{B}$, $5e_1^\mathrm{B}$, $e_1^\mathrm{F} + 2e_1^\mathrm{B}$, $6e_1^\mathrm{B}$, $e_1^\mathrm{F} + 3e_1^\mathrm{B}$ and e_2^F.

3.3 The time-dependent numerical renormalisation group

F. B. Anders and A. Schiller [42, 123] developed the time-dependent numerical renormalisation group (TD-NRG) in 2005 to investigate real-time dynamics of QISs. The basic idea for the calculation of real-time dynamics is that a complete basis set is needed because the discarded high-energy states of the NRG are relevant for the dynamics at

short times. In the past decade the TD-NRG has been used for the investigations of several models: the KM [42, 132], the SIAM [117, 123], the SBM [43] and with this thesis of BF-QISs. Furthermore, the TD-NRG is a powerful tool for complex effects, as the build-up of Kondo correlations [133], steady-state currents through nano devices [134] or complex electron dynamics of molecule compounds [39, 40]. Recent improvements on pulsed dynamics [124] extended the possible applications of the TD-NRG.

At the time $t = 0$ a sudden quench disturbs the Hamiltonian locally, in the zeroth Wilson shell. We can express this time-dependent Hamiltonian

$$H(t) = H^{\mathrm{I}}\Theta(-t) + H^{\mathrm{F}}\Theta(t) \tag{3.47}$$

by two time-independent parts H^{I} before and H^{F} after the quench. The time evolution $O(t) = \mathrm{Tr}\,(\rho(t)O)$ of a local operator O depends on the time-dependent density operator $\rho(t)$. For the initial system according to H^{I} the NRG provides the eigenenergies and eigenstates in equilibrium. Hence, the initial density operator is given by

$$\rho^{\mathrm{I}} = \frac{\mathrm{e}^{-\beta H^{\mathrm{I}}}}{\mathrm{Tr}\left(\mathrm{e}^{-\beta H^{\mathrm{I}}}\right)} \quad . \tag{3.48}$$

After switching to the time-independent Hamiltonian H^{F} the density operator evolves in time

$$\rho(t) = \mathrm{e}^{-itH^{\mathrm{F}}}\,\rho^{\mathrm{I}}\,\mathrm{e}^{itH^{\mathrm{F}}} \tag{3.49}$$

with respect to H^{F} for $t \geq 0$. To calculate $\rho(t)$ we need the eigenenergies and eigenstates of H^{F}, which are provided by the NRG, and additionally overlap matrices to rotate the initial density operator ρ^{I} into the basis of H^{F}.

3.3.1 Complete basis set

For an accurate description of the time evolution all energy scales are relevant, hence, a complete basis set is needed. In the NRG high-energy eigenstates are discarded at each iteration. For the TD-NRG these discarded states, as well as the transformation matrices, have to be stored on the hard drive. While for the NRG the Wilson chain is extended iteratively until a finite chain length $N+1$ is reached, we deal directly with the full Wilson chain of length $N+1$ for the TD-NRG. In analogy to the NRG we can say that at the beginning all hopping terms t_n are set to zero and the impurity couples only to the zeroth Wilson chain site. With each iteration step the next hopping term t_n is set to its NRG value and the impurity couples to an enlarged chain until the Wilson chain has its full length. This leads to a subdivision of the full Wilson chain as depicted in Fig. 3.7. The full Wilson chain consists of (i) the already built-up chain H_L

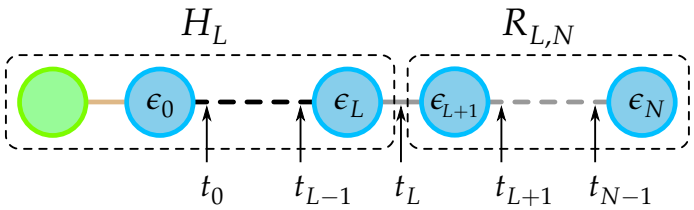

Figure 3.7: The Wilson chain of length $N+1$ is divided into two subchains: The subchain H_L of length $L+1$ and the environment subchain $R_{L,N}$ with switched-off couplings $t_n = 0$ for $L \leq n < N$ in gray.

with the length $L+1 (\leq N+1)$ and $t_n > 0$ for $n < L$ and (ii) the remaining chain $R_{L,N}$ with $t_n = 0$ for $L \leq n < N$, which will be called environment in the following. The Hamiltonian H_L always acts on the Fock space of the full Wilson chain

$$H_L|r, \alpha_{L+1}, ..., \alpha_N\rangle = E_L(r)|r_L, \alpha_{L+1}, ..., \alpha_N\rangle \tag{3.50}$$

with the product state

$$|r, \alpha_{L+1}, ..., \alpha_N\rangle = |r_L\rangle \otimes |\alpha_{L+1}\rangle \otimes \cdots \otimes |\alpha_N\rangle \tag{3.51}$$

consisting of the eigenstates $|r_L\rangle$ of H_L, with the eigenenergies $E_L(r)$, as well as the configurations $\{|\alpha_n\rangle\}$ of the n-th site, $L < n \leq N$, which do not couple to the subchain H_L. Hence, the environment causes an extra degeneracy d^{N-L} for each eigenenergy $E_L(r)$ with d being the number of distinct configurations of one chain site and $(N-L)$ being the length of the environment chain. In the following we use $|r, e; L\rangle$ as a diminutive of $|r_L, \alpha_{L+1}, ..., \alpha_N\rangle$ with $e = \{\alpha_{L+1}, ..., \alpha_N\}$ labelling the environment variables.
If we perform one iteration step by switching on the hopping term t_{L+1}, the new eigenstates

$$|r', e', L+1\rangle = \sum_{r, \alpha_{L+1}} U(r', \{r, \alpha_{L+1}\})|\{r, \alpha_{L+1}\}, e'; L\rangle \tag{3.52}$$

of the enlarged Hamiltonian H_{L+1} can be obtained by a unitary transformation as mentioned in the context of Eq. (3.28). Here, $e' = \{\alpha_{L+2}, ..., \alpha_N\}$ labels the remaining environment variables.
Within the NRG only N_S states with the lowest many-body eigenenergies are kept at each iteration to hold the computational effort manageable. Therefore, there is a first iteration $L_{\min}$ at which the complete set of states

$$\{|r, e; L_{\min}\rangle\} = \{|r, e; L_{\min}\rangle_{\text{kp}}\} + \{|r, e; L_{\min}\rangle_{\text{dis}}\} \tag{3.53}$$

is divided into a set of N_S states which are kept (kp) for the next iteration step and a set of discarded (dis) states which are now stored on the hard drive. If we consider

all eigenstates of the last iteration ($L = N$) also as discarded, then, all discarded states form a complete basis set with the completeness relation

$$\sum_{L=L_{\min}}^{N} \sum_{r,e} |r,e;L\rangle_{\text{dis}\ \text{dis}}\langle r,e;L| = 1 \tag{3.54}$$

which can obviously be divided $1 = 1_{\text{L}}^{-} + 1_{\text{L}}^{+}$ into two complementary parts

$$1_{\text{L}}^{-} = \sum_{L'=L_{\min}}^{L} \sum_{r,e} |r,e;L'\rangle_{\text{dis}\ \text{dis}}\langle r,e;L'| \quad \text{and} \tag{3.55}$$

$$1_{\text{L}}^{+} = \sum_{L'=L+1}^{N} \sum_{r,e} |r,e;L'\rangle_{\text{dis}\ \text{dis}}\langle r,e;L'| \quad . \tag{3.56}$$

The projector 1_{L}^{+} projects on all retained states at iteration L, spanning the retained subspace of $H_{\text{L}+1}$ with $L < N$. It can, therefore, be expressed by the kept states:

$$1_{\text{L}}^{+} = \sum_{r,e} |r,e;L\rangle_{\text{kp}\ \text{kp}}\langle r,e;L| \quad . \tag{3.57}$$

3.3.2 Time evolution of a local operator

The time evolution of a local operator O is given by

$$O(t) = \text{Tr}\,(\rho(t)O) = \sum_{L=L_{\min}}^{N} \sum_{r,e} {}_{\text{dis}}\langle r,e;L|\rho(t)O|r,e;L\rangle_{\text{dis}} \tag{3.58}$$

with the trace expressed in the complete basis set. By inserting the completeness relation between the density operator and the local operator and by following the discussion in Ref. [42], the time evolution becomes

$$O(t) = \sum_{L=L_{\min}}^{N} \sum_{r,r'}^{\text{trun}} \sum_{e,e'} {}_{\text{dis}}\langle r,e;L|\rho(t)|r',e';L\rangle_{\text{dis}\ \text{dis}}\langle r',e';L|O|r,e;L\rangle_{\text{dis}} \quad . \tag{3.59}$$

The restricted sum $\sum_{r,r'}^{\text{trun}}$ requires that at least one of the two states r, r' is discarded at iteration L. At the beginning of this section we claimed that O is a local operator. This is not necessarily the case, we only have to require that the operator O acts on states which are still available. This is the case for $L \leq L_{\min}$, so that the operator O may act on the impurity alone or also in its vicinity. This is a rather weak requirement since a lot of operators fulfil it.

Due to this locality, the operator O is independent of the DOFs of the environment and, hence,

$$ {}_{\text{dis}}\langle r', e'; L|O|r, e; L\rangle_{\text{dis}} = \delta_{e',e} O^L_{r',r} \quad . \tag{3.60} $$

If we further use the NRG basis set, generated for the final Hamiltonian H^{F}, and the standard NRG approximation $H^{\text{F}}|r, e; L\rangle = E_L(r)|r, e; L\rangle$, the density operator can be expressed by

$$ {}_{\text{dis}}\langle r, e; L|\rho(t)|r', e'; L\rangle_{\text{dis}} = \mathrm{e}^{it(E_L(r')-E_L(r))}\rho^{\text{red}}_{r,r'}(L) \quad , \tag{3.61} $$

where we defined the reduced density matrix

$$ \rho^{\text{red}}_{r,r'}(L) = \sum_e {}_{\text{dis}}\langle r, e; L|\rho^{\text{I}}|r', e; L\rangle_{\text{dis}} \quad . \tag{3.62} $$

Combining all this leads to the centrepiece of the TD-NRG, the time evolution formula

$$ O(t) = \sum_{L=L_{\text{min}}}^{N} \sum_{r,r'}^{\text{trun}} \mathrm{e}^{it(E_L(r')-E_L(r))} O^L_{r',r}\rho^{\text{red}}_{r,r'}(L) \quad . \tag{3.63} $$

To make some comments to this formula: Firstly, no restrictions on the initial density operator ρ^{I} were needed for the derivation. Secondly, all energy scales are indeed taken into account because all states of the finite Fock space are retained. And thirdly, it becomes exact in the limit $t \to 0^+$. One significant approximation through the derivation is $H^{\text{F}}|r, e; L\rangle = E_L(r)|r, e; L\rangle$, to which Wilson [19] has already shown in the context of the NRG that the associated error in the thermodynamic quantities is small and perturbative due to the separation of the energy scales by the logarithmic discretisation. Nevertheless, the discretisation of the bath limits the low-energy resolution and, therefore, Eq. (3.63) may become inaccurate for times $t \gg 1/T_N$, with the temperature $T_N \propto D\Lambda^{-(N-1)/2}$ representing the energy scale of the last Wilson chain site N. Anyway, the NRG can reach arbitrary low energy scales and, therefore, the TD-NRG arbitrary long times. At the same time, a continuous spectrum is vital for a complete relaxation in the system. This constitutes a fundamental error source for any solution and we mention two methods to reduce this error in Sec. 3.3.5.

3.3.3 Reduced density matrix

So far we only defined the reduced density matrix in Eq. (3.62), now we explain how to compute it. In the basis of the initial Hamiltonian H^{I} the density operator ρ^{I} is simply given by its thermal representation as in Eq. (3.48), but for Eq. (3.61) we used the eigenstates of the final Hamiltonian H^{F} to construct the reduced density matrix.

Therefore, we need transformation matrices which relate between these two basis sets. To distinguish between these two basis sets, we use the superscript I or F for the corresponding eigenstates. The reduced density matrix ρ^{I} in the basis of the initial Hamiltonian H^{I} is given by

$$\rho^{\mathrm{red,I}}_{r,r'}(L) = \sum_{e} {}^{\mathrm{I}}_{\mathrm{dis}}\langle r, e; L|\rho^{\mathrm{I}}|r', e; L\rangle^{\mathrm{I}}_{\mathrm{dis}} \quad . \tag{3.64}$$

For the complete basis of H^{I} we can write a completeness relation $\mathcal{I} = \mathcal{I}^{-}_{\mathrm{L}} + \mathcal{I}^{+}_{\mathrm{L}}$, similarly to Eq. (3.54), with

$$\mathcal{I}^{-}_{\mathrm{L}} = \sum_{L'=L_{\min}}^{L-1} \sum_{r,e} |r, e; L'\rangle^{\mathrm{I}}_{\mathrm{dis}} \, {}^{\mathrm{I}}_{\mathrm{dis}}\langle r, e; L'| \quad \text{and} \tag{3.65}$$

$$\mathcal{I}^{+}_{\mathrm{L}} = \sum_{q,e} |q, e; L\rangle^{\mathrm{I}}_{\mathrm{dis}} \, {}^{\mathrm{I}}_{\mathrm{dis}}\langle q, e; L| \tag{3.66}$$

where we used the calligraphic $\mathcal{I}$, instead of 1 in Eq. (3.54), to emphasise the basis of the initial Hamiltonian H^{I}. If we now insert $\mathcal{I}$ before and after the density operator, in Eq. (3.62), which was defined in the final basis set, the reduced density matrix decomposes into four contributions

$$\rho^{\mathrm{red}}_{r,r'}(L) = \rho^{++}_{r,r'}(L) + \rho^{+-}_{r,r'}(L) + \rho^{-+}_{r,r'}(L) + \rho^{--}_{r,r'}(L) \tag{3.67}$$

with the definition

$$\rho^{\mathrm{pp'}}_{r,r'}(L) = \sum_{e} {}^{\mathrm{F}}_{\mathrm{dis}}\langle r, e; L|\mathcal{I}^{p}_{\mathrm{L}}\rho^{\mathrm{I}}\mathcal{I}^{p'}_{\mathrm{L}}|r', e; L\rangle^{\mathrm{F}}_{\mathrm{dis}} \tag{3.68}$$

and $p, p' = \pm$. Only the contribution $\rho^{++}_{r,r'}(L)$ can be directly related to the initial density matrix:

$$\rho^{++}_{r,r'}(L) = \sum_{e} {}^{\mathrm{F}}_{\mathrm{dis}}\langle r, e; L|\mathcal{I}^{+}_{\mathrm{L}}\rho^{\mathrm{I}}\mathcal{I}^{+}_{\mathrm{L}}|r', e; L\rangle^{\mathrm{F}}_{\mathrm{dis}} \tag{3.69}$$

$$= \sum_{e} \sum_{q',q} \sum_{e',e} {}_{\mathrm{dis}}\langle r, e; L|q', e'; L\rangle^{\mathrm{I}}_{\mathrm{dis}} \, {}^{\mathrm{I}}_{\mathrm{dis}}\langle q', e'; L|\rho^{\mathrm{I}}|q, e; L\rangle^{\mathrm{I}}_{\mathrm{dis}} \, {}^{\mathrm{I}}_{\mathrm{dis}}\langle q, e; L|r', e; L\rangle_{\mathrm{dis}} \tag{3.70}$$

and leads to the transformation matrix

$$S_{q,r'}(L) = {}^{\mathrm{I}}_{\mathrm{dis}}\langle q, e; L|r', e; L\rangle^{\mathrm{F}}_{\mathrm{dis}} \quad . \tag{3.71}$$

It is independent in the environmental DOFs and, therefore, the index e is omitted. The matrix $S(L)$ is the wanted transformation matrix[17] at iteration L which transforms the

[17] We like to mention that the transformation matrix $S(L)$ is generally not unitary because the basis is reduced in each iteration step. Therefore, $S^*(L)S(L) \neq 1$ and/or $S(L)S^*(L) \neq 1$.

basis states from H^{I} to H^{F} and vice versa. A systematic way to compute the transformation matrices is explained in detail in the appendix of Ref. [42].

The other contributions to $\rho^{\mathrm{red}}_{r,r'}(L)$ in Eq. (3.67) describe how low- and high-energy states of the initial Hamiltonian H^{I} are coupled. For the NRG we deal with an initial density operator ρ^{I} which is in thermal equilibrium at low temperature. Hence, there are no significant contributions from high-energy states and the terms $\rho^{+-}_{r,r'}(L)$, $\rho^{-+}_{r,r'}(L)$ and $\rho^{--}_{r,r'}(L)$ may be neglected. If we start with an initial configuration far away from thermal equilibrium these contributions have to be taken into account, as it is discussed and has been done by Nghiem and Costi for periodic switching in Ref. [124].

With the transformation matrix $S(L)$ we simply obtain via rotation

$$\rho^{++}_{r,r'}(L) = \sum_{q',q} S^{*}_{q',r}(L)\ \rho^{\mathrm{I}}_{q',q}(L)\ S_{q,r'}(L) \tag{3.72}$$

out of the initial density matrix $\rho^{\mathrm{I}}_{q',q}(L) = {}^{\mathrm{I}}_{\mathrm{dis}}\langle q', e'; L|\rho^{\mathrm{I}}|q, e; L\rangle^{\mathrm{I}}_{\mathrm{dis}}$.

To set up a recurrence relation with respect to L for the reduced density matrix, we compute the reduced density matrix for the last iteration N. It is easy to write down the reduced density matrix

$$\rho^{\mathrm{red,I}}_{r,r'}(N) = \delta_{r,r'}\frac{1}{Z^{\mathrm{I}}}\mathrm{e}^{-\beta E^{\mathrm{I}}_{N}(r)} \tag{3.73}$$

with the initial partition function $Z^{\mathrm{I}} = \sum_r \mathrm{e}^{-\beta E^{\mathrm{I}}_N(r)}$ and the initial eigenenergies $E^{\mathrm{I}}_N(r)$. For an arbitrary $L < N$, we can split the sum over the environment $e = \{\alpha_{L+1}, e'\}$ into a part of the next chain site α_{L+1} and the rest environment $R_{L+2,N}$ with e' encoding the remaining labels $\alpha_{L+2}, ..., \alpha_N$. Substituting $\mathcal{I}^{+}_{\mathrm{L+1}}\rho^{\mathrm{I}}\mathcal{I}^{+}_{\mathrm{L+1}}$ for ρ^{I} in Eq. (3.64) leads to the recurrence relation

$$\rho^{\mathrm{red,I}}_{r,r'}(L) = \sum_{\alpha_{L+1}}\sum_{q',q}^{\mathrm{kept}} P_{q',r}[\alpha_{L+1}]P^{*}_{q,r'}[\alpha_{L+1}]\rho^{\mathrm{red,I}}_{q',q}(L+1) \tag{3.74}$$

with the definition

$$P_{q',r}[\alpha_{L+1}] = {}^{\mathrm{I}}_{\mathrm{dis}}\langle r, e; L|q', e'; L+1\rangle^{\mathrm{I}}_{\mathrm{dis}} \tag{3.75}$$

for the overlap matrix elements. The overlap matrices connect two successive NRG steps of the initial Hamiltonian H^{I}. The sum over q' and q in Eq. (3.74) is restricted to the states which are kept at iteration $L+1$. Furthermore, for $L = N-1$ the sum runs over all states of the last NRG iteration. If the state r or r' is discarded at iteration L, the reduced density matrix $\rho^{\mathrm{red,I}}_{r,r'}(L)$ vanishes because of the orthogonality of the basis set.

3.3.4 TD-NRG algorithm

The TD-NRG algorithm consists of two parts: (i) the forward iterations of the Hamiltonians H^{I} and H^{F} and (ii) the backward iteration according to the recurrence relation in Eq. (3.74).

In order to evaluate the time dependence of an operator O at a desired temperature T, one first has to adjust the discretisation parameter Λ and the number of iteration N such that $T \simeq T_N$ is fulfilled. Then, the forward iteration starts:

(i) Two normal NRG runs for both Hamiltonians H^{I} and H^{F} are performed,

(ii) the transformation matrices $S(L)$ of Eq. (3.71) are calculated at each NRG step and

(iii) the discarded states $\{|r, e; L\rangle_{\mathrm{dis}}\}$, the transformation matrices $S(L)$ and the overlap transformations $P[\alpha_{L+1}]$ are stored on the hard drive.

After this has been done the backward iteration starts and reads in the stored data. Then,

(i) the reduced density matrix of Eq. (3.73) at the last Wilson chain site is calculated with the initial eigenenergies,

(ii) the matrices $P[\alpha_{L+1}]$ are used to perform one backward step and calculate $\rho^{\mathrm{red,I}}(L)$ out of $\rho^{\mathrm{red,I}}(L+1)$ via Eq. (3.74),

(iii) the reduced density operator $\rho^{\mathrm{red,I}}(L)$ is transformed via Eq. (3.69) with the help of $S(L)$ into the basis of the final Hamiltonian H^{F} and

(iv) with the use of the time evolution formula in Eq. (3.63) the expectation values $\langle O(t_i)\rangle_L$ for all points in time t_i are computed at each backward iteration step L.

These steps are repeated until iteration $L = L_{\mathrm{min}}$ is reached, where no discarded states are left. Finally, we calculate the expectation value $\langle O(t_i)\rangle = \sum_L \langle O(t_i)\rangle_L$ at time t_i by a sum over all contributions of the iterations.

3.3.5 Improvements: Oliveira's averaging and damping

For the real-time dynamics of impurity expectation values strong non-physical oscillations may appear due to the discretisation of the bath(s). In the context of the NRG we introduced Oliveira's averaging in Sec. 3.1.5 to cure these non-physical effects by averaging over different discretisations.

Another way to smooth these oscillations is to explicitly damp them down. In the original implementation of the TD-NRG [42] each phase factor in Eq. (3.63) is Lorentz-broadened,

$$e^{it(E_L(r)-E_L(s))} \longrightarrow e^{it(E_L(r)-E_L(s))-\Gamma_L t} \quad , \tag{3.76}$$

with a damping factor $\Gamma_L = \alpha\varepsilon_L$. It is energy dependent on the energy scale $\varepsilon_L = D\Lambda^{-(L-1)/2}(1+1/\Lambda)/2$ at iteration L. The factor α is of the order $O(1)$ if $E_L(r) - E_L(s) \neq 0$, otherwise it is set to zero. Such a broadening smoothes the discretisation-related oscillations in the same spirit as the broadening of the NRG Lehmann representation of equilibrium spectral functions [20, 135–137].
However, such a broadening could wrongly damp out oscillatory contributions at long times. In order to avoid any prejudice, we usually set $\alpha = 0$ in this thesis and use Oliveira's averaging instead to minimise discretisation-related oscillations. Therefore, usually all our data contains some finite-size related noise at very long times.

Chapter 4

Real-time dynamics in gapless Fermi systems

In this chapter we focus on the real-time dynamics in gapless Fermi systems, which contain a small concentration of magnetic impurities embedded in a non-magnetic metallic host. Since the concentration is small and the impurities are randomly distributed, the interaction between each other can be neglected, and we model this system by a single impurity in a conduction band: The impurity is a localised orbital and hybridises to the conduction band enabling charge scattering between the impurity and the band. For an energy-dependent scattering rate $\Gamma(\epsilon) \propto |\epsilon|^r$ this single-impurity Anderson model (SIAM), cf. Sec. 2.3, features a quantum critical point (QCP) separating the local moment (LM) phase with an unscreened spin moment from a symmetric strong coupling (SSC) phase with a fractionally screened spin moment.

We investigate the local real-time dynamics upon equilibration and thermalisation for interaction quenches and hybridisation quenches by using the time-dependent numerical renormalisation group (TD-NRG). We find that, in all cases we looked at, the system equilibrates after quenching on a steady-state value, even for quenches across the QCP. For quenches within or into the LM phase no thermalisation occurs and the deviation from the thermal equilibrium systematically depends on the distance to the QCP. Furthermore, our numerical data agrees nicely with results of a perturbation-theory calculation, which becomes exact at short times. In a comparison of our results with previously published dynamics calculated with a time-dependent Gutzwiller variational approach, we see clear discrepancies which are related to restrictions in the wave-function ansatz of the Gutzwiller theory. Whereas, in the numerical renormalisation group (NRG) the formation of a spatially extended effective local moment in the unscreened phase is accurately described.

We like to note that this chapter is an abridged version of our publication in Ref. [117]. We start with an introduction and explain the physical picture of the decoupling effective local moment in Sec. 4.1. Then, we briefly portray the equilibrium properties of

the SIAM in Sec. 4.2 with a special focus on the equilibrium double occupancy, since a more general discussion has been done in Sec. 2.3.
For interaction quenches in Sec. 4.3 we study the real-time double occupancy in presence of particle-hole (ph) symmetry within the SSC phase, as well as for quenches from the SSC over the QCP into the LM phase. We supplement our investigations with results beyond ph symmetry.
For the second investigated type, the hybridisation quenches in Sec. 4.4, we focus on quenches within the LM phase and augment our numerics with perturbation theory results which show a perfect agreement. Furthermore, we discuss the energy flow from the impurity into the bath and explain the differences in our results compared to similar investigations with a time-dependent Gutzwiller ansatz. We summarise our results in Sec. 4.5.

4.1 Introduction

Elzerman *et al.* [58] have used gate-voltage pulses for a single-shot readout of the spin configuration in a single-electron transistor in a finite magnetic field. A suitable model for such a setup is given by the SIAM [16]. The metallic SIAM has a rather simple phase diagram [20, 112, 113] and it can be viewed as a special case of a more general class of models [25, 81, 83, 84]. For those, the coupling function $\Gamma(\epsilon) \propto |\epsilon|^r$ between the impurity and the non-interacting metallic host contains a real pseudo-gap (pg). The metallic case is equivalent to $r = 0$, and for $0 < r < 1/2$ the system exhibits [25, 83, 114, 115] a critical coupling strength Γ_c governing the transition between a LM phase for a weak coupling and a SSC phase for a large coupling to the metallic host. The SIAM has been extensively investigated in the context of Kondo impurities in unconventional superconductors [25, 81, 83, 84, 114, 115] or in the context of defects in graphene sheets [119, 138]. Some of the low-energy properties have been worked out in detail [118, 139, 140] and it has been shown that the universality class of the FPs changes with the coupling function exponent r. We are interested in the influence of these different ground states for the different phases on the real-time dynamics of a system driven out of equilibrium by a quantum quench.

The non-equilibrium dynamics in the metallic SIAM has been investigated [123] with the TD-NRG [42, 123, 124]. However, the dynamics with a real pseudo-gap for quenches within one phase and across the QCP has only recently been addressed by a time-dependent Gutzwiller ansatz [60]. With this non-equilibrium extension [60, 141, 142] of the well-established variational Gutzwiller technique [143, 144] it has been demonstrated [60] that the pg coupling function yields non-trivial dynamics as a consequence of the diverse low-energy FPs. In the LM phase an effective local moment decouples from the impurity. The properties of this spin DOF have a strong influence on the

formation of the steady state, as well as on thermalisation. We will show that an over-simplified picture for the description of the local moment is used in the Gutzwiller ansatz. For all quenches we will find a well-defined steady state at long times. The deviation of the steady-state value from the thermal equilibrium measures the degree of thermalisation. We will find thermalisation for quenches within or into the SSC phase, within the numerical accuracy of the TD-NRG [42, 123, 124]. Interestingly, we will show that thermalisation also occurs for quenches out of the SSC phase across the QCP (but only very close to the QCP). For even stronger quenches, the deviation between the steady state and the thermal state increases continuously with increasing distance to the critical coupling.

4.1.1 Physical picture

In the SSC phase, the Kondo temperature T_K governs the excitations around the SSC FP. T_K vanishes at the QCP and increases with increasing coupling to the conduction band. In analogy, in the LM phase one can define a crossover scale $T^\star$ which takes the role similar to T_K in the SSC phase and characterises the excitations around the LM FP. $T^\star$ decreases with increasing coupling and also vanishes at the QCP. To these crossover energy scales there are associated length scales $\xi^\star = v_F/T^\star$ and $\xi_K = v_F/T_K$ with v_F being the average Fermi velocity of the conduction band. These length scales can be interpreted as spatial extension of the decoupled local moment in the LM phase or of the Kondo singlet in the SSC phase. The larger the local Coulomb repulsion U the larger the crossover scale $T^\star$ becomes and the more closely to the impurity the local moment is formed. Hence, an ansatz for the ground state which restricts the local moment formation only on the impurity site, as used in the Gutzwiller approach [60, 141–143], significantly overestimates the critical Coulomb repulsion U_c. In such an approach the local moment formation can only occur at a much larger local Coulomb repulsion U or a much lower coupling Γ compared to accurate NRG calculations. This also leads to differences in the real-time dynamics: For quenches into the LM phase close to the QCP the decoupling effective LM is extended and a local observable explores still a large phase space of itinerant states. Hence, these quenches also thermalise. If we increase $U \gg U_c$, we reduce the size of the local moment such that it is more localised to the impurity. This leads to an increasing non-decaying fraction [145–147] of the expectation value. Hence, the steady-state value deviates significantly from the thermal equilibrium value. For the local double occupancy we will show an increasing deviation between the steady-state value and the thermal equilibrium value the more strongly the effective local moment is localised. On the other hand, for the energy flow into the conduction band, which is indicated by the hybridisation energy, we will find thermalisation even for quenches within the LM phase, although it has been questioned that the TD-NRG might not be suitable to describe the energy flow [59].

4.2 Equilibrium properties

Throughout this chapter we use the ph-symmetric coupling function [21, 25, 81, 83, 84, 114, 115]

$$\Gamma(\epsilon) = \Gamma_0 (r+1) \left| \frac{\epsilon}{D} \right|^r \Theta(D - |\epsilon|) \tag{4.1}$$

with the cut-off D defining the effective bandwidth. The parameter Γ_0 serves as energy scale of the problem and turns into the standard charge-fluctuation scale for a constant DOS. The normalisation factor $(r+1)$ ensures that the integral over the coupling function,

$$\pi V_0^2 = \int \mathrm{d}\epsilon \, \Gamma(\epsilon) = 2\Gamma_0 D \quad , \tag{4.2}$$

remains independent of the bath exponent $r \geq 0$. While $r = 0$ and $r = 1$ are the prototypically experimental realisations, we take r as an arbitrary parameter of the model. Unless otherwise stated, we focus on the ph symmetric case with $\Delta\epsilon = 2\epsilon_\mathrm{d} + U = 0$. As described in Sec. 2.3, the phase diagram of the SIAM is very rich and reveals a QCP between the SSC and LM phase. In equilibrium, the SSC FP can be reached in two ways: choosing the charge-fluctuation scale $\Gamma_0 > \Gamma_\mathrm{c}(U)$ for fixed U or by setting $U < U_\mathrm{c}(\Gamma_0)$ for fixed Γ_0. We show these phase boundaries in Fig. 4.1 for the ph symmetric SIAM. We observe a strong influence of the bandwidth D on the critical U_c and Γ_c. Furthermore, our Γ_c agrees excellently with Fig. 5 in Ref. [25]. Since we systematically eliminate the high-energy degrees in the RG procedure, a finite U only matters once the effective bandwidth $D \to D_\mathrm{eff}$ has reached the order U. At those energies, the system starts to detect the differences between the local double-occupied state and the local moment states. Then, the effective coupling to the remaining conduction band is given by $\Gamma(U)$ which decreases with increasing r or increasing D. Consequently, U_c has to decrease in these cases as well.

In Ref. [60] the ground state of the SIAM for a finite hybridisation has been approximated by a Gutzwiller wave-function ansatz. For $r = 0$ the quasi-particle renormalisation factor $Z \propto T_\mathrm{K}^\mathrm{Gutz} \propto \exp(-\pi U/16\Gamma_0)$ is a smooth function of the Coulomb interaction U and has been interpreted as effective Kondo temperature within the Gutzwiller approach [143]. We like to note that the exponent of $T_\mathrm{K}^\mathrm{Gutz}$ differs by a factor 2 from the standard Kondo temperature such that the exponential decay is underestimated [148]. Furthermore, an incorrect Kondo scale is found for the wide-band limit as it has been pointed out in Ref. [148]. The Gutzwiller aproach features a QCP at a finite critical U_c for all $r > 0$. The Gutzwiller prediction for $U_\mathrm{c}/\Gamma_0 = 16(r+1)/(\pi r)$ has been added to Fig. 4.1 as an analytical curve for large bandwidths. Since for $r > 1/2$ the SIAM only features the stable LM FP for all $U > 0$, the validity of the Gutzwiller approach is

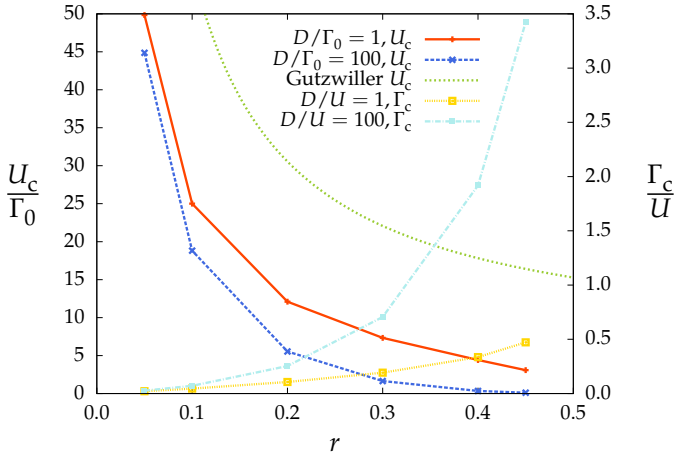

Figure 4.1: Phase diagram for different bath exponents r and bandwidths D. For comparison the analytical form of the Gutzwiller ansatz (cf. Ref. [60]) is added. Taken from [117].

restricted to $r < 1/2$. In comparison with the accurate NRG phase boundaries which are presented in Fig. 4.2, it becomes apparent that the renormalisation effects are underestimated by the Gutzwiller ansatz and, hence, there is an overestimation of the critical U_c. These limitations are also affect the real-time dynamics of the time-dependent Gutzwiller approach [60], as we will show by comparision with our TD-NRG calculations later.

Since we investigate the real-time dynamics of the double occupancy $\langle D(t)\rangle$ throughout this chapter, we first look at the equilibrium double occupancy $\langle D\rangle_{\text{eq}}$ versus U/Γ_0 for fixed $D/\Gamma_0 = 100$ in Fig. 4.2. The NRG results depicted in Fig. 4.2(a) demonstrate that $\langle D\rangle_{\text{eq}}$ is continuous across the QCP at U_c. This continuity of local observables across the QCP has already been identified by Gonzalez-Buxton and Ingersent more than 15 years ago, cf. Fig. 8 in Ref. [25]. In Fig. 4.2(b) we show the equilibrium double occupancy calculated with the Gutzwiller approach for the same coupling function $\Gamma(\epsilon)$. The double occupancy clearly differs from the NRG results. Within the Gutzwiller ansatz, the double occupancy vanishes at the QCP, i.e. $\langle D(U_c)\rangle_{\text{eq}} = 0$, and remains zero for $U > U_c$. Consequently, the physical properties of the Gutzwiller approach deviate significantly from the true ground state, as obtained by the NRG. Apparently, the Gutzwiller wave function ansatz cannot be applied in the LM phase close to the QCP since it misses the spatial extension of the effective local moment.

We will focus on the non-equilibrium dynamics of the ph symmetric SIAM close to and across the QCP. There are two different ways to drive the system across the QCP for $0 < r < 1/2$: For a fixed value of U we can switch the hybridisation strength Γ_0, which will be called hybridisation quench in the following, or for a fixed Γ_0 we can change U which defines the interaction quench.

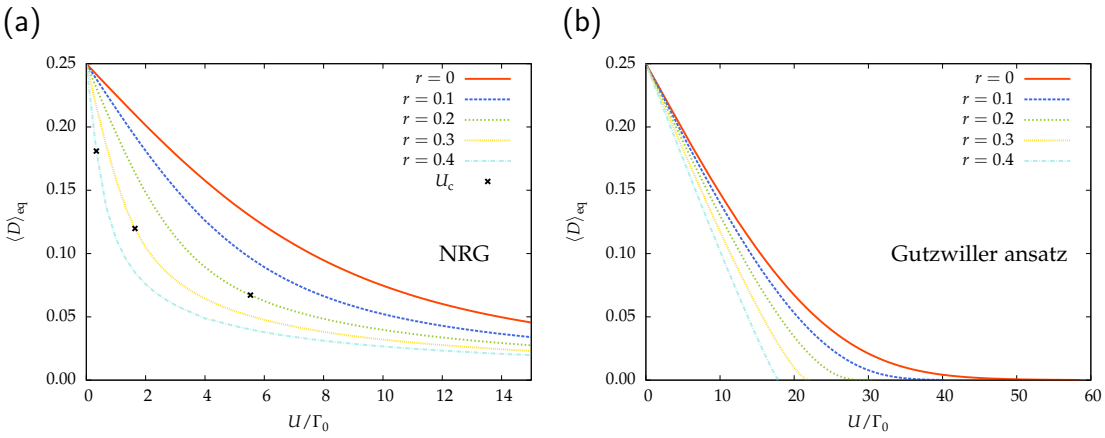

Figure 4.2: Equilibrium expectation value of the double occupancy $\langle D \rangle_{eq}$ versus U for different bath exponents r and a bandwidth $D/\Gamma_0 = 100$ calculated (a) with the equilibrium NRG and (b) with the equilibrium Gutzwiller ansatz [60, 142]. Taken from [117].

4.3 Interaction quenches

For an interaction quench, we switch the Coulomb repulsion from its initial value U_i for times $t < 0$ to the value U_f for $t \geq 0$. In order to maintain ph symmetry at all times, i.e. $U(t) + 2\epsilon_d(t) = 0$, we enforce also a switching in the d-level energy: $-2\epsilon_d(t) = \Theta(-t)U_i + \Theta(t)U_f$. The hybridisation strength $\Gamma(t) = \Gamma_i = \Gamma_f = \Gamma_0$ is kept constant and is used as unit of energy. Short, intermediate, and long times will correspond to $t\Gamma_0 \ll 1$, $t\Gamma_0 \sim 1$ and $t\Gamma_0 \gg 1$.
We prepare the system initially in the uncorrelated state by setting $U_i = \epsilon_{d,i} = 0$. Since the impurity is coupled to the conduction band, the system approaches the SSC FP for $T \to 0$. Therefore, the initial double occupancy is given by the uncorrelated value $\langle D \rangle_{eq} = 1/4$. In the LM FP, the double-occupied and the zero-occupied state on the impurity remain unoccupied, and $\langle D \rangle_{eq} = 0$.

4.3.1 Quenches within the SSC phase

If we switch on the Coulomb repulsion at $t = 0$, the system remains either in the SSC phase for $U_f < U_c$ or is driven by the equilibrium properties of the LM phase for $U_f > U_c$. Since we maintain ph symmetry, the level occupancy $\langle n_d(t) \rangle = 1$ remains at half-filling for all times and is unaffected by the quench. Hence, we focus on the dynamics of the double occupancy $\langle D(t) \rangle$. For a good energy separation between the bandwidth D and the charge-fluctuation scale Γ_0, we use $1 \ll 10 \leq D/\Gamma_0 \leq 100$.

We present the time-dependent double occupancy $\langle D(t) \rangle$ for quenches within the SSC phase ($U_f < U_c$) for multiple bandwidths D and $r = 0.4$ in Fig. 4.3. All curves start

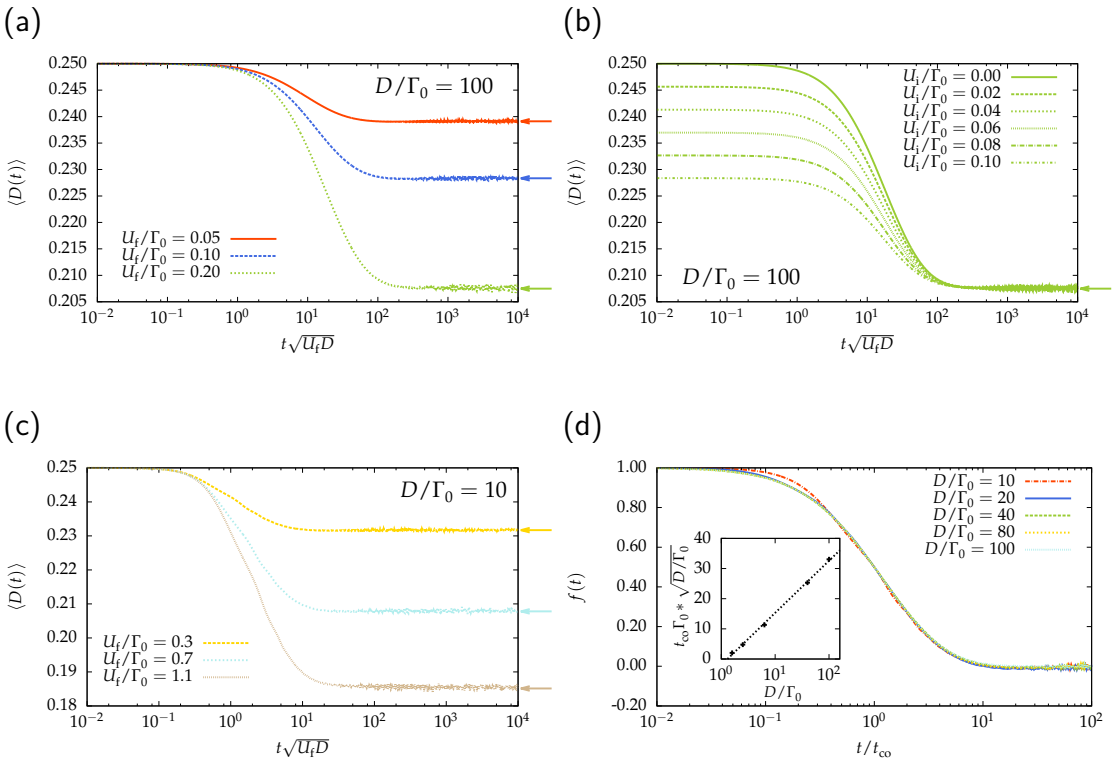

Figure 4.3: Time-dependent double occupancy $\langle D(t)\rangle$ for quenches within the SSC phase for $D/\Gamma_0 = 100$ for different final Coulomb repulsions $U_f/\Gamma_0 = 0.05, 0.1, 0.2 < U_c/\Gamma_0 \simeq 0.34$ in (a) and for different initial values U_i with fixed $U_f/\Gamma_0 = 0.2$ in (b). In (c): $\langle D(t)\rangle$ is shown for a smaller bandwidth $D/\Gamma_0 = 10$ with Coulomb repulsion $U_f/\Gamma_0 = 0.3, 0.7, 1.1 < U_c/\Gamma_0 \simeq 1.51$. In (d): $\langle D(t)\rangle$ for a set of different bandwidths with fixed $U_f/\Gamma_0 = 0.2$ versus the crossover time scale t_{co} with the dependence of t_{co} on D given in the inset. After [117].

at the non-interacting value $\langle D(t=0)\rangle = 1/4$ and reduce to smaller values since the Coulomb repulsion suppresses the charge fluctuations and the double occupancy. Quenches within the SSC phase equilibrate for long times to a steady-state value. The corresponding equilibrium value of the quenched system, which is obtained from an independent NRG calculation and is indicated in the figure by an arrow, agrees perfectly with the steady-state value. Hence, we conclude that $\langle D(t)\rangle$ thermalises for long times. This thermalisation is independent of the initial value U_i as shown in Fig. 4.3(b). We have plotted $\langle D(t)\rangle$ versus $t\sqrt{U_f D}$ in Figs. 4.3(a) to 4.3(c) to emphasise the quadratic decrease[18] $\langle D(t)\rangle = 0.25(1 - \alpha(t/t_{short})^2)$ with the short-time time scale $1/t_{short}^2 \propto U_f$. It stems from a linear contribution of $U_f n_\uparrow n_\downarrow$ in a perturbative expansion of the time-dependent density operator after the interaction quench [149].

[18] In our publication [117, Fig. 3] we plotted for the same quenches as in Figs. 4.3(a) to 4.3(c) $\langle D(t)\rangle$ versus tU_f. However, the perturbatively gained quadratic decrease in $\langle D(t)\rangle$ for short times seams more reasonable and should also hold for the dynamics which we presented in [117, Fig. 3]. Therefore, here in Figs. 4.3(a) to 4.3(c) we show $\langle D(t)\rangle$ versus $t\sqrt{U_f D}$.

The double occupancy does not expose any oscillations, which is in contrast to the predictions made by the time-dependent Gutzwiller approach, cf. Fig. 2 in Ref. [60]. Nevertheless, the this approach reveals the thermalisation of $\langle D(t)\rangle$ for those type of quenches [60] which is a non-trivial result.

In order to compare the dynamics independently of the long-time steady-state value $\langle D(\infty)\rangle$, we define the function

$$f(t) = \frac{\langle D(t)\rangle - \langle D(\infty)\rangle}{\langle D(0)\rangle - \langle D(\infty)\rangle} \quad . \tag{4.3}$$

It starts at $f(0) = 1$ and approaches $f(\infty) = 0$ at infinitely long times independent of the parameters. The data of Fig. 4.3(a) and Fig. 4.3(c) collapses for different Coulomb repulsion U_f, since the bandwidth $D = const$ is unaltered. There is still a weak dependence on U_f (about 2%) but it is negligible compared to the dependence of $f(t)$ on the ratio D/Γ_0. To eliminate further the dependence on D/Γ_0, we define a crossover time scale t_co, which fulfils the condition $f(t_\mathrm{co}) = 1/2$. Plotting $f(t)$ versus the dimensionless time scale t/t_co maps all data for different ratios D/Γ_0 onto one unique curve, as depicted in Fig. 4.3(d). Only the curve for $D/\Gamma_0 = 10$ deviates slightly from the others since the separation of energy scales is rather small. Furthermore, the dependence of t_co on D/Γ_0 is illustrated in the inset in Fig. 4.3(d). By fitting the numerical data we find that

$$t_\mathrm{co} \propto \frac{1}{\Gamma_0}\sqrt{\frac{D}{\Gamma_0}} \quad . \tag{4.4}$$

Since the U_f dependence enters primarily via $\langle D(\infty)\rangle$, the remaining real-time dynamics is governed by the time scale t_co, depending on D and Γ_0, and universality in the dynamics $f(t/t_\mathrm{co})$ has been found.

Now, we investigate the influence of the exponent $r = 0, 0.1, 0.2, 0, 3$ on the dynamics for quenches within the SSC phase. Again, we find universality for each exponent, expressed by $f_r(t/t_\mathrm{co})$. In Fig. 4.4(a) we present the different universal functions for different r. With decreasing r the universal curve emerges a dip at short times, after which it increases again to the steady-state value. The occurrence time of the dip correlates to the inverse temperature of the maximum in the effective local moment $\mu^2_\mathrm{eff}(T)$. In the inset of Fig. 4.4(a) $\mu^2_\mathrm{eff}(T)$ is depicted for $r = 0.2, 0.4$ and reveals a maximum for the small $r = 0.2$ while for $r = 0.4$ $\mu^2_\mathrm{eff}(T)$ decreases continuously. Consequently, the dynamics for $r = 0.4$ does not reveal this dip. We show the r dependence of the

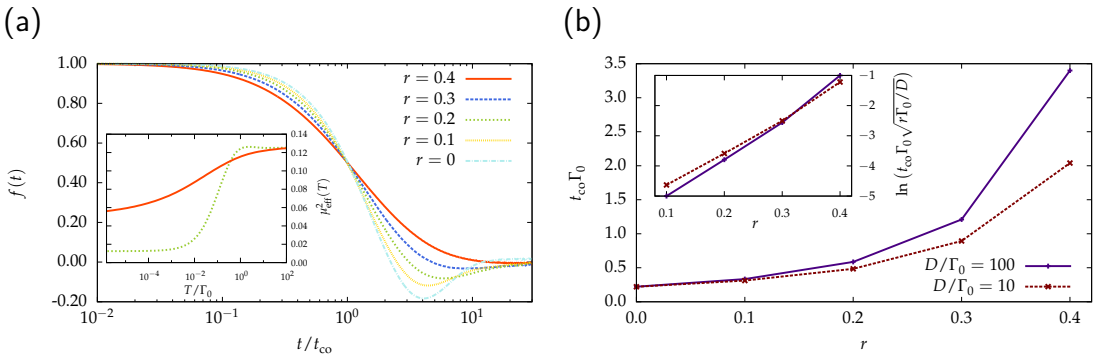

Figure 4.4: In (a): The universal $f_r(t)$ versus t/t_{co} for different exponents $r = 0, 0.1, 0.2, 0.3, 0.4$. In the inset of (a) the temperature-dependent equilibrium effective local moment $\mu^2_{eff}(T)$ is depicted for H^F, $D/\Gamma_0 = 100$, and $r = 0.2, 0.4$. In (b): The dependence of $t_{co}\Gamma_0$ on the exponent r with a linear relation of $\ln(t_{co}\Gamma_0\sqrt{r\Gamma_0/D})$ vs r in the inset. After [117].

universality time scale t_{co} in Fig. 4.4(b). If we scale t_{co} with $\sqrt{r}$ for $r \geq 0.1$, we find an exponential dependence of the crossover time scale t_{co} on r:

$$t_{co} \propto \frac{e^{m(D)r}}{\sqrt{r}}\sqrt{\frac{D}{\Gamma_0}} \tag{4.5}$$

with a bandwidth-dependent exponent $m(D)$, obtained for the data in Fig. 4.4(a). We like to note, that the phenomenological estimate (4.5) for the time scale does not interpolate to $r \to 0$ and, therefore, is only valid for $0.1 \leq r < 1/2$. The inset in Fig. 4.4(b) reveals the linear dependence of $\ln(t_{co}\Gamma_0\sqrt{r\Gamma_0/D})$ on r.

4.3.2 Quenches across the QCP

In the following we start from the SSC FP ($U_i = \epsilon_{d,i} = 0$) at $t = 0$ and quench over the QCP into the LM phase by setting $U_f > U_c$. The equilibrium properties of H^F, which govern the real-time dynamics, describe an effective local moment, which decouples from the conduction band leading to an effectively free conduction band. This effective local moment is composed of contributions of the local impurity spin, as well as of the conduction band electron spins. Hence, also in the LM phase a finite double occupancy $\langle D \rangle_{eq}$ is possible.

In Fig. 4.5 we show NRG calculations for the effective local moment for a set of Coulomb repulsions $U_c/\Gamma_0 \simeq 0.3392 < U_f/\Gamma_0 = 0.4, 0.6, 1, 4$ for $r = 0.4$. As the Kondo temperature T_K determines the low-energy crossover to the SSC FP, we can define a similar characteristic temperature $T^\star$, which fulfils

$$\mu^2_{eff}(T^\star) = 0.21 \tag{4.6}$$

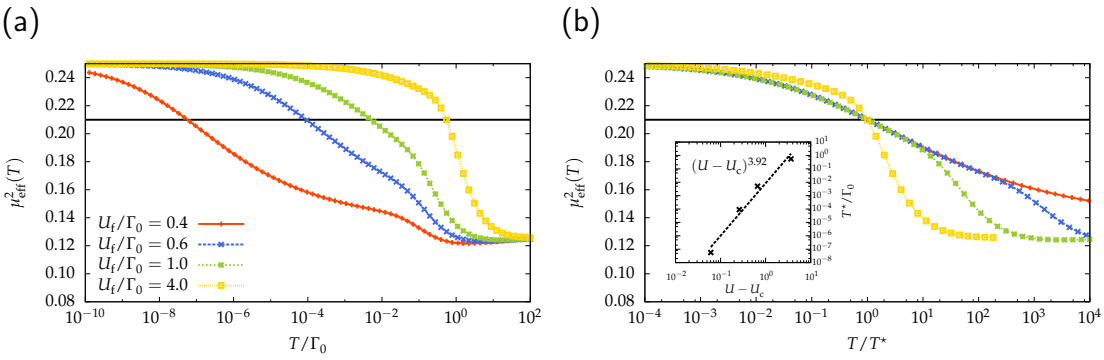

Figure 4.5: Effective local moment $\mu^2_{\rm eff}(T)$ of the impurity spin for different Coulomb repulsions $U_{\rm c}/\Gamma_0 \simeq 0.3392 < U_{\rm f}/\Gamma_0 = 0.4, 0.6, 1, 4$ with $D/\Gamma_0 = 100$ in (a). In (b) scaled data of (a) versus $T/T^\star$ with the inset showing the correlation-length exponent of $T^\star$. After [117].

and tracks the crossover near the QCP to the LM FP. We added the condition of Eq. (4.6) in Fig. 4.5(a) as horizontal line. To reveal the universality of $T^\star$ we plot the data of Fig. 4.5(a) in Fig. 4.5(b) versus $T/T^\star$. We note that $T^\star$ vanishes at the QCP and we show its dependence $T^\star \propto (U - U_{\rm c})^{\nu(r)}$ on the distance to the QCP with the correlation-length exponent $\nu(r = 0.4) = 3.92$ in the inset of Fig. 4.5(b). If U is close to $U_{\rm c}$, all energy scales contribute to the local moment formation in the LM phase. Similarly to the spatial extension of the Kondo cloud by $\xi_{\rm K} = v_{\rm F}/T_{\rm K}$ in the SSC phase [133, 150–154], with the Fermi velocity $v_{\rm F}$, we can interpret $\xi^\star = v_{\rm F}/T^\star$ as spatial extension of the local moment decoupling from the conduction band. Hence, in the limit $U \to U_{\rm c}$ the spatial extension of the local moment diverges. On the other side, the spatial extension of the local moment decreases with increasing U and, hence, the decoupled spin DOFs become more strongly localised to the impurity. In consequence, the thermalisation for this quenches is increasingly suppressed with increasing $U_{\rm f}$.

In Fig. 4.6 we present $\langle D(t) \rangle$ for quenches over the QCP with $U_{\rm c}(D/\Gamma_0 = 100)/\Gamma_0 \simeq 0.3392 < U_{\rm f}/\Gamma_0 = 0.4, 0.6, 1, 4$ at the temperature $T/\Gamma_0 \sim 10^{-10}$. Since $T < T^\star$ the real-time dynamics is temperature-independent and only governed by the overlap of the initial ground state with the eigenstates of the final Hamiltonian. To reveal the short-time dynamics we plot $\langle D(t) \rangle$ versus the dimensionless time $tU_{\rm f}$ in Fig. 4.6(a). For these quenches across the QCP into the LM phase, we find coinciding short-time dynamics which are proportional to $1/U_{\rm f}$. Probably the Coulomb repulsion $U_{\rm f}/\Gamma_0$ is too strong for a perturbative statement of the short-time dynamics, as is has been done in Fig. 4.3. For the two smallest interactions, $U_{\rm f}/\Gamma_0 = 0.4, 0.6$, we the steady-state value is very close to the thermal equilibrium value, which is indicated by an arrow in the figure. Consequently, we consider both quenches as thermalised. For a strong interaction, $U_{\rm f}/\Gamma_0 = 4$, we observe a damped oscillatory behaviour with a frequency proportional to $U_{\rm f}$. The long-time steady-state value strongly deviates from its thermal equilibrium

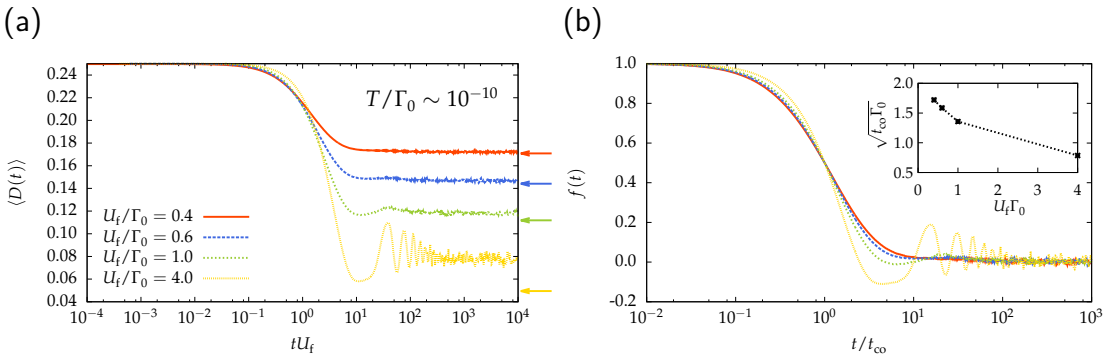

Figure 4.6: Double occupancy $\langle D(t)\rangle$ for quenches from the SSC FP ($U_i = 0$) over the QCP into the LM phase for different Coulomb repulsions $U_c/\Gamma_0 \simeq 0.3392 < U_f/\Gamma_0 = 0.4, 0.6, 1, 4$ with $D/\Gamma_0 = 100$. In (a): $\langle D(t)\rangle$ versus tU_f at $T/\Gamma_0 \sim 10^{-10}$. Thermal expectation values as arrows at the right side of the graph. In (b): The data of (a) scaled via Eq. (4.3) to $f(t)$ versus t/t_{co}. In the inset the dependence of t_{co} on U_f is shown. Taken from [117].

value revealing non-thermalisation. Plotting the data of Fig. 4.6(a) via Eq. (4.3) as $f(t)$ versus t/t_{co} in Fig. 4.6(b), we can extract the dependence of U_f on the crossover time scale, as depicted in the inset in Fig. 4.6(b). In equilibrium we have shown for the double occupancy $\langle D\rangle_{eq}$ a continuous decrease with increasing U even across the QCP. Whereas, the outcome for the dynamics for quenches across the QCP in Fig. 4.6(a) and for quenches within the SSC phase in Sec. 4.3.1 is significantly different. In both cases, the double occupancy equilibrates to a steady state but thermalises only in the SSC phase. For quenches within the SSC phase the characteristic time scale t_{co} depends in leading order on Γ_0/D and shows universal behaviour, whereas for quenches across the QCP the real-time dynamics is governed by $1/U_f$.

To investigate the connection between the spatial extension of the effective local moment and the degree of thermalisation, we take a look at the difference between the long-time steady-state value

$$D^\infty = \lim_{T\to\infty} \frac{1}{T}\int_0^T \mathrm{d}t\, \langle D(t)\rangle \tag{4.7}$$

and the thermal equilibrium value $\langle D\rangle_{eq}$. The deviation $\Delta D = D^\infty - \langle D\rangle_{eq}$ for a set of different U_f for the bandwidth $D/\Gamma_0 = 100$, as in Fig. 4.6, are depicted in red versus $T^\star/\Gamma_0$ in Fig. 4.7. Close to the QCP the deviation is less than 3% which is of the order of discretisation-related errors of the TD-NRG. For increasing U_f the deviation increases. We supplement data for fixed $U_f/\Gamma_0 = 1$ and a variation of D in blue to Fig. 4.7. The deviation ΔD follows the same trend and agrees within the numerical error with the data for fixed D/Γ_0 when approaching the QCP. ΔD systematically increases with increasing $T^\star$, either by increasing U_f or increasing D/Γ_0. This supports the picture

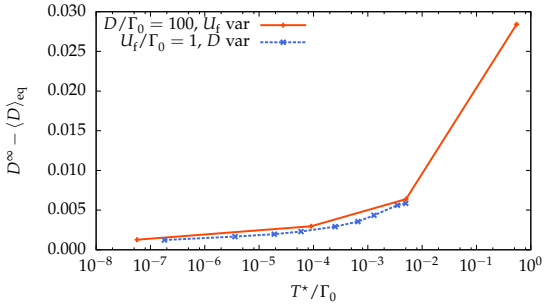

Figure 4.7: Difference between the long-time steady-state value D^∞ and the thermodynamic equilibrium value $\langle D \rangle_{eq}$ as function of $T^\star$ either for fixed D/Γ_0 and a variation of U_f or for fixed U_f/Γ_0 and a variation of D. Taken from [117].

of an increasingly localised effective moment and leads to an increasing non-decaying fraction of the local double occupancy, which prevents the thermalisation of the local expectation value.
The same type of quenches has been analysed with the time-dependent Gutzwiller approach in Fig. 3 of Ref. [60]. There the double occupancy $\langle D(t) \rangle$ strongly oscillates and never reaches a steady-state value at long times. This is in strong contrast to our results which reveal a steady state for long time for these quenches. Since the Gutzwiller wave function ansatz for the time-dependent Gutzwiller equation does not describes the the LM phase properly the Gutzwiller approach reveals completely different real-time dynamics. In the Gutzwiller approach the ansatz for the LM phase is defined by a vanishing $\langle D \rangle_{eq}$ for $U > U_c$. This is a strong shortcoming since $\langle D \rangle_{eq}$ is continuous across the QCP at U_c as equilibrium NRG calculations [25] have proven. While the NRG correctly contains the spatial extension of the decoupling effective local moment, the Gutzwiller state restricts this moment to the local impurity site. We conclude that the time-dependent Gutzwiller approach can only be applied to the strong coupling phase.

In Fig. 4.8 we show the effect on the real-time dynamics for a variation in the bandwidth D and for a variation in the bath exponent r. We use a set of different bandwidths $D/\Gamma_0 = 100, 125, 175, 200$ and a fixed $U_f/\Gamma_0 = 3$ in Fig. 4.8(a). The critical Coulomb repulsion $U_c(D/\Gamma_0 = 100)/\Gamma_0 = 0.3358$ is the largest for $D/\Gamma_0 = 100$ and decreases with increasing bandwidth. Hence, U_f exceeds U_c almost by one decade even for the largest U_c. With increasing bandwidth, we quench deeper into the LM phase. Therefore, the thermal double occupancy $\langle D \rangle_{eq}$, represented by an arrows at the right side of the graph, decreases with increasing D. For this strong interaction $U_f/\Gamma_0 = 3$ the spatial extension of the effective local moment is small and a damped oscillation due to strong local dynamics on the zeroth Wilson shell emerges. Furthermore, with increasing bandwidth D, the amplitude of the damped oscillation in $\langle D(t) \rangle$ is increased, due to the more strongly localised local moment, while the frequency is only proportional to U_f.

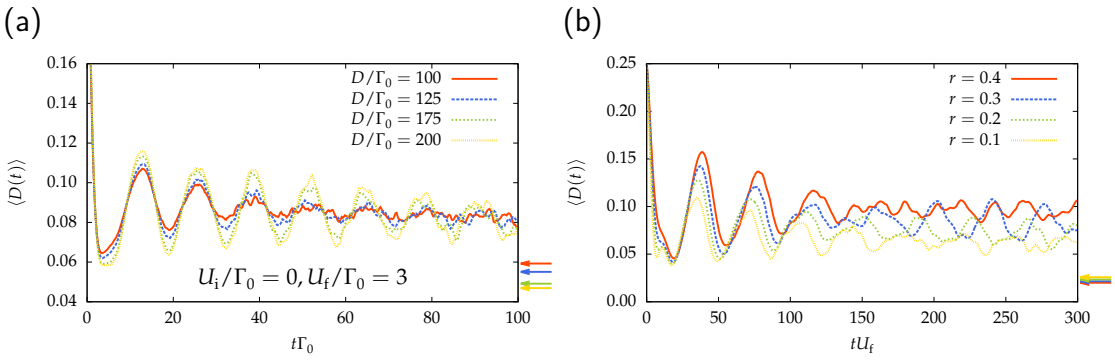

Figure 4.8: Double occupancy $\langle D(t)\rangle$ for quenches from the SSC FP into the LM phase. In (a): $\langle D(t)\rangle$ versus $t\Gamma_0$ for different bandwidths $D/\Gamma_0 = 100, 125, 175, 200$ with $r = 0.4$ and $U_f/\Gamma_0 = 3 > U_c$. In (b): $\langle D(t)\rangle$ versus tU_f for different exponents r with $D/\Gamma_0 = 100$ and $\langle D(U,r)\rangle_{eq} \simeq 0.02$ by $U_f(r = 0.4)/\Gamma_0 = 14.72$, $U_f(r = 0.3)/\Gamma_0 = 17.73$, $U_f(r = 0.2)/\Gamma_0 = 21.06$, and $U_f(r = 0.1)/\Gamma_0 = 24.79$. Taken from [117].

If we use a set of exponents $r = 0.1, 0.2, 0.3, 0.4$ with $D/\Gamma_0 = 100$, we have to adjust the Coulomb repulsion such that $\langle D(U_f)\rangle_{eq} \simeq 0.02$ remains nearly constant for all r as indicated by the arrows on the right side in Fig. 4.8(b). We plot in Fig. 4.8(b) $\langle D(t)\rangle$ versus tU_f to remove the leading frequency-dependent order of the oscillations for different Coulomb repulsions U_f. The remaining small frequency shift with increasing r is related to the different ratios U_f/Γ_0. As shown in Fig. 4.2(a), the double occupancy $\langle D\rangle_{eq}$ is stronger suppressed with increasing r for a constant U_f/Γ_0. For quenches from the SSC FP into the LM phase we have shown that $\langle D(t)\rangle$ overestimates for long times the thermal equilibrium value more strongly the stronger the effective local moment is localised, which is equivalent to a smaller $\langle D\rangle_{eq}$. Since we hold $\langle D\rangle_{eq}(r)$ constant in Fig. 4.8(b), the overestimation in $\langle D(t)\rangle$ increases with increasing r.

4.3.3 Quenches from the LM phase

Next we reverse the direction of the quenching and start within the LM phase with an initial $U_i > U_c$. The Coulomb repulsion is reduced to U_f, which is either $1 < U_f/U_c = 1.2, 1.5$ reflecting a quench within the LM phase, or $1 > U_f/U_c = 0.25, 0.5$ to quench over the QCP into the SSC phase. The initial double occupancy $\langle D(t = 0)\rangle$ decreases with increasing distance $U_i - U_c$ and vanishes in the limit $U_i \to \infty$.

We present $\langle D(t)\rangle$ for $U_i/U_c = 10$ in Fig. 4.9(a) and for $U_i/U_c = 100$ deeper in the LM phase in Fig. 4.9(b). The double occupancy $\langle D(t)\rangle$ increases U_f-independently with a slightly oscillatory behaviour. It reaches a U_f-dependent steady-state value at roughly $t\Gamma_0 \simeq 1$.

For quenches over the QCP into the SSC phase ($U_f/U_c < 1$), the steady-state value and corresponding thermal expectation value coincide independent of the initial prepara-

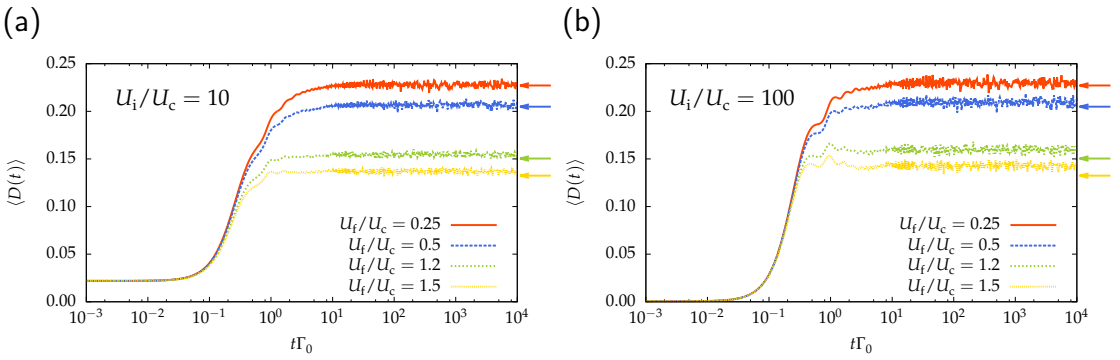

Figure 4.9: Double occupancy $\langle D(t)\rangle$ for quenches from the LM phase for the initial Coulomb repulsion $U_i/U_c = 10$ in (a) and $U_i/U_c = 100$ in (b). Either for quenching within the LM phase for $U_f/U_c = 1.2, 1.5$ or over the QCP into the SSC phase for $U_f/U_c = 0.25, 0.5$. Taken from [117].

tion. The thermal values are represented by the arrows on the right side of Fig. 4.9(a). We interpret this as indication for thermalisation. Whereas, for quenches within the LM phase ($U_f/U_c > 1$), the steady-state value and the thermal value differ about 7% in Fig. 4.9(a). Hence, we conclude that quenches within the LM phase do not thermalise. This statements also holds if the quench starts stronger in the LM phase, as in Fig. 4.9(b). The stronger the initial effective local moment is localised the more DOFs are prevented from relaxing to thermal equilibrium and, hence, the deviation for $U_f/U_c = 1.5$ in Fig. 4.9(b) increases up to 15%. Since we start with a strongly localised effective local moment in Fig. 4.9(b) also the quenches into the SSC phase show a slight deviation between the steady-state value and the thermal value. Nevertheless, we have recognised these quenches as thermalised.

4.3.4 Quenches with particle-hole asymmetry

We focus here on quenches with broken ph symmetry. The ASC FP features in equilibrium a complete screening of the impurity spin, independent of r as stated in Sec. 2.3.2. Furthermore, the equilibrium double occupancy $\langle D\rangle_{eq}$, which is $\langle D\rangle_{eq} = 1/4$ for ph symmetry, increases with increasing asymmetry $|U - 2\epsilon_d|$ or increasing exponent r [25].

In Fig. 4.10(a) the time-dependent double occupancy $\langle D(t)\rangle$ is shown for two different initial conditions: The solid curves describe the dynamics starting in the ASC phase using the parameters $U_i = 0$ and $\epsilon_{d,i}/\Gamma_0 = -0.1$, while the dashed curves depict the dynamics starting from the SSC FP with $U_i = \epsilon_{d,i} = 0$. The colours of the curves distinguish the different final parameters. Additionally, we present for these quenches the real-time level occupancy $\langle n_d(t)\rangle$ in Fig. 4.10(b) since the filling is also changing with time. All quenches equilibrate to a steady state. The thermal expectation values

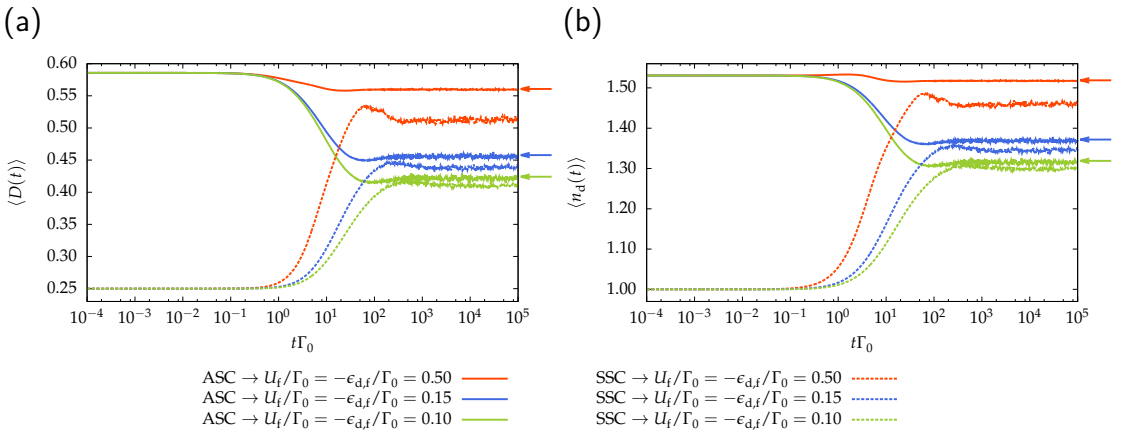

Figure 4.10: Double occupancy $\langle D(t)\rangle$ (a) and level occupancy $\langle n_d(t)\rangle$ (b) versus $t\Gamma_0$ for ph asymmetry. Quenching from the SSC FP ($U_i = \epsilon_{d,i} = 0$) or the ASC FP ($U_i = 0, \epsilon_{d,i}/\Gamma_0 = -0.1$) into or within the ASC phase with three different final configurations. All data has been obtained for $D/\Gamma_0 = 100$ and $r = 0.4$. Taken from [117].

are indicated by the arrows on the right side in Fig. 4.10. They reveal that only for quenching within the ph symmetry broken phase thermalisation occurs. Quenching into ph-symmetric final conditions leads to a deviation between the steady-state value and the thermal value. This is a known shortcoming of the TD-NRG [42, 120, 121] depending on the change in the degree of the ph asymmetry. This has recently been investigated in great detail in Ref. [124]. If we scale the data of Fig. 4.10(a) via Eq. (4.3) to $f(t)$, which is not shown here, the universal behaviour of $f(t)$ is lost and the shape of the function depends on the degree of the ph asymmetry.

4.4 Hybridisation quenches

For the second type of quenches, the hybridisation quenches, we change the hybridisation strength $\Gamma_0 \to \Gamma(t) = \Theta(-t)\Gamma_i + \Theta(t)\Gamma_f$ between the initial value Γ_i and the final value Γ_f at time $t = 0$. Since for this quench type the Coulomb repulsion is $U_i = U_f = U = const$ over time, the system is after quenching either characterised by the LM phase for $\Gamma_f < \Gamma_c(U)$ or by the SSC phase for $\Gamma_f > \Gamma_c(U)$. We set $\epsilon_{d,i} = \epsilon_{d,f} = -U/2$ to maintain ph symmetry. As reference point we use the LM FP by setting $\Gamma_i = 0$. Its ground state is U independent and features the double occupancy $\langle D(t=0)\rangle = 0$. Since we change $\Gamma(t)$, we use in the following the bandwidth D as unit of energy.

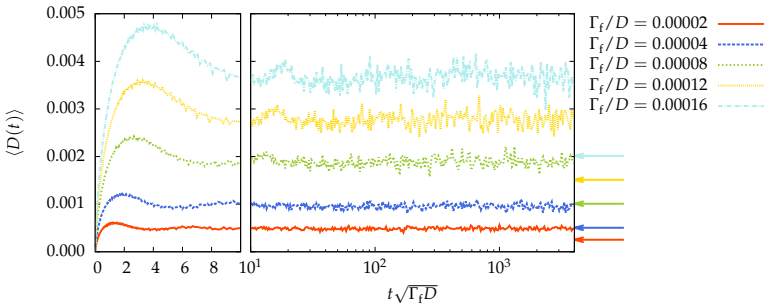

Figure 4.11: Quenches from the LM FP ($\Gamma_\mathrm{i} = 0$) at time $t = 0$ within the LM phase. The hybridisation is $\Gamma_\mathrm{f}/D = 0.00002, 0.00004, 0.00008, 0.00012, 0.00016 < \Gamma_\mathrm{c}/D \simeq 0.019$ with a constant Coulomb repulsion $U/D = U_\mathrm{i}/D = U_\mathrm{f}/D = 0.01$ and $r = 0.4$. We show the double occupancy $\langle D(t)\rangle$ linear for short and intermediate dimensionless times $t\sqrt{\Gamma_\mathrm{f} D}$ and on a log time scale for long times. As a guide to the eye $\langle D\rangle_\mathrm{eq}$ after quenching is indicated by arrows. After [117].

4.4.1 Quenches within the LM phase

In Fig. 4.11 we show weak quenches[19] within the LM phase, i.e. $\Gamma_\mathrm{f} \ll \Gamma_\mathrm{c}$, for a wide bandwidth $D/U = 100$. We show all data versus the dimensionless time $\tau = t\sqrt{\Gamma_\mathrm{f} D}$ revealing U-independent short-time dynamics which is only driven by the final hybridisation strength Γ_f. The time-dependent double occupancy $\langle D(t)\rangle$ is plotted linear in time for $t\sqrt{\Gamma_\mathrm{f} D} \leq 10$ and logarithmically for longer times. The hybridisation is switched on to very small values: $\Gamma_\mathrm{f}/D = 0.00002, 0.00004, 0.00008, 0.00012, 0.00016 \ll \Gamma_\mathrm{c}(U/D = 0.01)/D \simeq 0.019$.

Starting from the initial value $\langle D(t = 0)\rangle = 0$, the double occupancy $\langle D(t)\rangle$ rises quickly and exhibits a peak at intermediate dimensionless times $t\sqrt{\Gamma_\mathrm{f} D} \simeq 1$ before it falls off towards a steady-state value for long times. With increasing hybridisation Γ_f the peak height rises and its width increases. Although the system equilibrates for long times, the steady-state value deviates significantly from the thermal value which is depicted by an arrow on the right side in Fig. 4.11. The deviation increases with increasing hybridisation Γ_f. This indicates that the real-time dynamics is not governed by the FP properties but rather by the overlap of the initial wave function with the excited states of H^F. For $\Gamma_\mathrm{f} < \Gamma_\mathrm{c}$ the system approaches the LM FP with the twofold-degenerate ground state for low energies. Since an increasing Γ_f reduces the difference $|\Gamma_\mathrm{c} - \Gamma_\mathrm{f}|$, the characteristic energy scale $T^\star$ decreases, as well. In consequence, the effective local moment which decouples from the rest of the system becomes more extended. Therefore, a larger fraction of the impurity DOFs hybridises with the conduction band and $\langle D\rangle_\mathrm{eq}$ increases continuously. The spatially more extended the local

[19] In our publication [117] we produced a wrong Fig. 12 by mistake. The numerical value of the hybridisation there stated is given in units of Γ_f/U but wrongly named as in units of Γ_f/D. Furthermore, the scaling presented there went wrong by a factor of 10. All data is correctly scaled now and the captions are corrected. The following figures, which are based on the same data, are corrected as well.

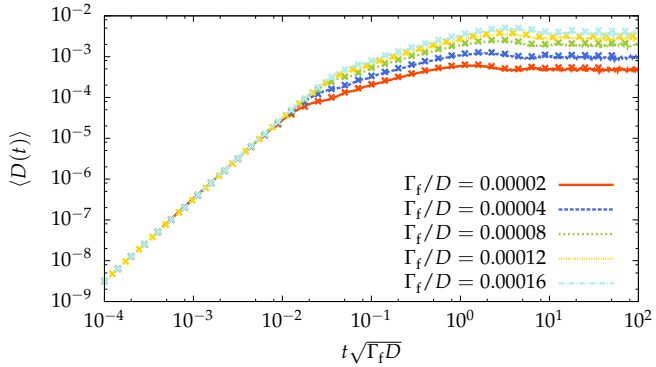

Figure 4.12: Double occupancy $\langle D(t)\rangle$ of Fig. 4.11 on a log-log scale augmented with the results of the second-order perturbation theory in Eq. (4.8) as crosses. After [117].

moment for $\Gamma_f > 0$ the more strongly differs it in the contributing states forming the local moment, compared to the initial ground state. Hence, the non-relaxing part increases and the steady-state differs significantly from the thermal state.

To augment our data obtained by the TD-NRG we analytically calculate the time-dependent double occupancy $\langle D(t)\rangle$ with perturbation theory for short times. Since for $\Gamma_i = 0$ we know all eigenstates and eigenenergies, we evolve the time-dependent density operator in powers of the hybridisation Γ_f and evaluate $\langle D(t)\rangle$ exactly up to second order. The detailed derivation can be looked up in Refs. [117, 149].
The short-time dynamics of the double occupancy is given by the analytic expression

$$\langle D(t)\rangle = \frac{\Gamma_f D}{\pi} t^2 + \frac{2\Gamma_f(1+r)}{\pi} \sum_{n=2}^{\infty} \frac{(-1)^{2n}}{(2n)!} \int_{-D}^{0} \left|\frac{\epsilon}{D}\right|^r \left((\epsilon - \epsilon_d - U)\, t\right)^{2n} \mathrm{d}\epsilon \tag{4.8}$$

which is asymptotically exact for $t \to 0$. We gain a quadratic increase of $\langle D(t)\rangle$ in leading order in t. The increase is proportional to the factor $\Gamma_f D/\pi$ and, hence, U independent. It verifies the dimensionless short-time time scale $\tau = t\sqrt{\Gamma_f D}$, which we used in Fig. 4.11. A U dependence enters only higher orders in t and yields a weak oscillation. To emphasise the universality in the short-time TD-NRG calculation, we present the data of Fig. 4.11 on a log-log scale in Fig. 4.12. We augment the analytical results of Eq. (4.8) for selected times as crosses in the same colour and see an excellent agreement between the numerical and analytical results up to $t\sqrt{\Gamma_f D} \simeq 10$. The analytical result does not only describe the leading time dependence correctly, it also accounts for the deviation from the parabola starting at $t\sqrt{\Gamma_f D} \simeq 10^{-2}$ and for the existence of a long-time steady state[20].

[20] Since we work with a perturbative approach, the deviation between the steady-state value of the TD-NRG and the steady-state value of the perturbation theory increases with increasing Γ_f.

4.4.2 Energy flow in the LM phase

For the double occupancy we showed, that there is a significant deviation $\Delta D = D^{\infty} - \langle D \rangle_{\mathrm{eq}}$ between the long-time steady-state value D^{∞} and the thermal expectation value $\langle D \rangle_{\mathrm{eq}}$. The question arises if this deviation is operator dependent. For an operator O the long-time value is given by [155, 156]

$$O^{\infty} = \lim_{T\to\infty} \frac{1}{T} \int_0^T \mathrm{d}t \, \langle O(t) \rangle = \sum_n^N \sum_{\substack{r,s \\ E_r = E_s}}^{\mathrm{trun}} O^n_{r,s} \rho^{\mathrm{red}}_{s,r}(n) \quad . \tag{4.9}$$

Together with the thermal expectation value $\langle O \rangle_{\mathrm{eq}}$ gained by an independent NRG calculation with the final Hamiltonian, we look at the deviation $\Delta O = O^{\infty} - \langle O \rangle_{\mathrm{eq}}$. If ΔO is operator dependent, different physical properties may show different behaviour regarding thermalisation for the same quench.
It has been conjectured [59] that a Wilson chain might not be able to serve as a heat reservoir for a larger change in the hybridisation energy and, therefore, unable to describe thermalisation correctly. However, Wilson's NRG, as well as the TD-NRG, target only the local dynamics. There is no physical meaning for any bath expectation value. A discretised finite bath, as used in any NRG calculation, has always only finite energy content, while the thermodynamic bath provides a reservoir with infinitely large energy. A quantum state can never thermalise by itself, since it evolves under the energy-conserving Schrödinger equation. Hence, one has to restrict such an investigation to quantum impurity expectation values [117]. From our point of view, it is a good way to reveal the thermalisation of a quantum impurity subsystem by a comparison of its long-time limit with a corresponding equilibrium NRG calculation with the same discretisation parameters.

To shed some light on the operator dependence of ΔO, we look at the local energy flow for quenches within the LM phase. The hybridisation energy[21] $E_{\mathrm{hyb}}(t) = \langle H_{\mathrm{hyb}}(t) \rangle$ with $H_{\mathrm{hyb}} = \sum_{k,\sigma} V_k (c^{\dagger}_{k,\sigma} d_{\sigma} + d^{\dagger}_{\sigma} c_{k,\sigma})$ is presented in Fig. 4.13 for the same parameters as in Fig. 4.11. For those parameters we have already shown that the double occupancy $\langle D(t) \rangle$ does not thermalise and $\Gamma_{\mathrm{f}} > 0$ leads to an overestimation of the double occupancy compared to the thermal expectation value. In Fig. 4.13(a) $E_{\mathrm{hyb}}(t)$ is shown versus the time scale $\tau = t\sqrt{\Gamma_{\mathrm{f}} D}$ for a constant $U/D = 0.01$. Clearly, the dynamics is not governed by the characteristic time scale of the double occupancy. As Fig. 4.13(a) reveals, the main contribution to the impurity energy is $E_{\mathrm{hyb}}(t)$, since it is huge compared to the contribution steaming from $U\langle D(t) \rangle$, cf. Fig. 4.11. Also the contribution $E_{\mathrm{d}} \langle n_{\mathrm{d}}(t) \rangle$ is negligible. $E_{\mathrm{d}} n_{\mathrm{d}}$ is discontinuous at $t = 0$ for ph symmetry, but after

[21] It is noted in Ref. [117] that the hybridisation energy $E_{\mathrm{hyb}}(t)$ involves in addition to the impurity operator only the local host DOFs on the first Wilson shell [20, 112, 113] and, therefore, is a local operator as required for the TD-NRG [42, 123].

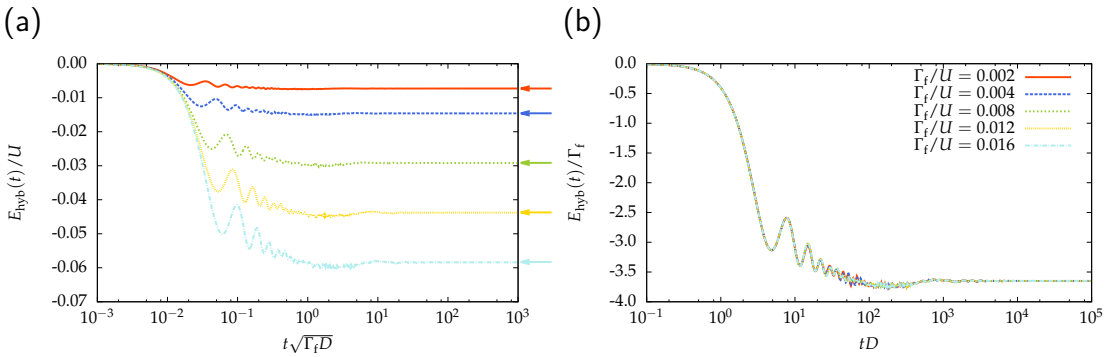

Figure 4.13: Hybridisation energy $E_{\mathrm{hyb}}(t)$ for hybridisation quenches within the LM phase using a constant Coulomb repulsion $U_{\mathrm{i}}/D = U_{\mathrm{f}}/D = U/D = 0.01$ and a set of hybridisation strengths $\Gamma_{\mathrm{f}}/U = 0.002, 0.004, 0.008, 0.0012, 0.0016 \ll \Gamma_{\mathrm{c}}/U \simeq 1.9$. In (a): $E_{\mathrm{hyb}}(t)/U$ versus the dimensionless time $\tau = t\sqrt{\Gamma_{\mathrm{f}}D}$ characterising the dynamics of $\langle D(t)\rangle$. In (b): $E_{\mathrm{hyb}}(t)/\Gamma_{\mathrm{f}}$ versus tD to reveal Γ_{f} dependence. For the TD-NRG calculations instead of Oliveira's averaging, a broadening with $\alpha = 0.4$ was used. Taken from [117].

quenching it remains constant for $t > 0$. We depict the thermal expectation value as arrow at the right side of the graph in Fig. 4.13(a). The long-time steady-state value and the thermal value coincide perfectly. In consequence, the hybridisation energy $E_{\mathrm{hyb}}(t)$ thermalises although the system stays in the LM phase with a non-thermalising double occupancy $\langle D(t)\rangle$.

Hybridisation energy E_{hyb} is proportional to $\sum_{k,\sigma} V_k \langle d_\sigma^\dagger c_{k,\sigma}\rangle \propto \Gamma_{\mathrm{f}}$. Hence, we divide out the leading factor Γ_{f} and plot $E_{\mathrm{hyb}}(t)/\Gamma_{\mathrm{f}}$ versus tD in Fig. 4.13(b). The dynamics of $E_{\mathrm{hyb}}(t)/\Gamma_{\mathrm{f}}$ appears to be universal and is driven by the bandwidth D. For $r = 0.4$, as in Fig. 4.13(b), the magnitude of E_{hyb} is determined by Γ_{f}, whereas for $r = 0$ it can be shown that $E_{\mathrm{hyb}}/\Gamma_{\mathrm{f}} \propto \ln(D/\Gamma_{\mathrm{f}})$ in equilibrium. It seems that with increasing r the hybridisation energy $E_{\mathrm{hyb}}/\Gamma_{\mathrm{f}}$ is weaker dependent on the ratio D/Γ_{f}. Furthermore, the hybridisation energy $E_{\mathrm{hyb}}(t)$ equilibrates very fast, one order of magnitude faster than the double occupancy. It seems that the hybridisation energy E_{hyb} is not influenced by the build-up of low-energy correlations for the LM FP since it has approached its steady-state value on a time scale where long-time correlations have not had a chance to develop.

Our findings indicate that indeed ΔO strongly depends on the operator O. This is reasonable since the double occupancy and the hybridisation energy are different in their physical content. The former operator provides a major contribution to the local moment formation, which decouples from the system in the LM phase. The latter operator instead probes the coupling to the full bath continuum. The number of bath DOFs contributing to the formation of the effective moment is of a measure zero in the integration over all k states. Therefore, the main error in $E_{\mathrm{hyb}}(t)$ is related to unavoidable TD-NRG discretisation errors.

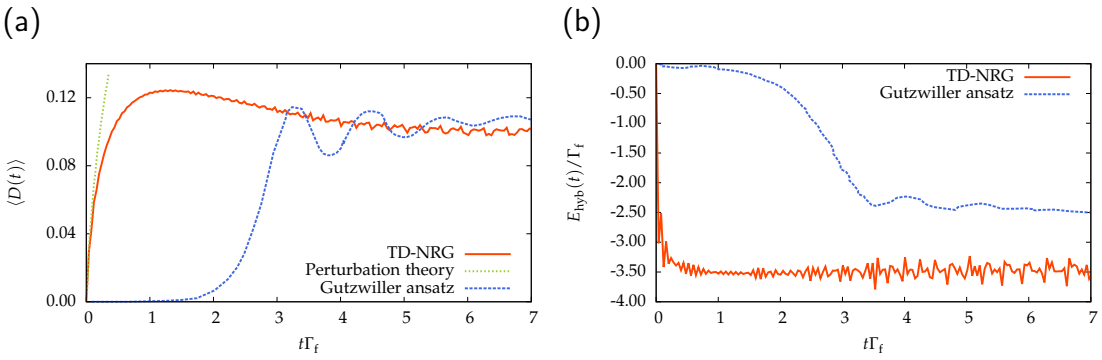

Figure 4.14: Comparison between the TD-NRG and time-dependent Gutzwiller ansatz for a hybridisation quench, $\Gamma_i = 0 \to \Gamma_f/D = 0.01$, and $r = 0.4$. The Gutzwiller data is taken from Ref. [60] and has been obtained for $U/\Gamma_f = 9$. The double occupancy $\langle D(t)\rangle$ in (a) and the hybridisation energy $E_{hyb}(t)$ in (b) have been calculated with the NRG parameters $U_i/\Gamma_f = U_f/\Gamma_f = 1.6$ and augmented with the Gutzwiller data. The NRG parameters have been chosen such that $D^{\infty}_{TD-NRG} \simeq D^{\infty}_{Gutz}$ for a quantitative comparison. Taken from [117].

4.4.3 Comparison with the Gutzwiller results

We have already discussed in Sec. 4.2 that the equilibrium properties calculated with the approximate Gutzwiller ansatz technique differ significantly from those of the accurate NRG. This discrepancy has been explained by the restriction of the Gutzwiller ansatz in which the effective local moment can only be formed on the impurity site. Whereas, the NRG features the extended nature of the local moment formation. Consequently, the Gutzwiller ansatz largely overestimates the critical U_c. For a comparison of real-time dynamics provided by both techniques, we adjust our NRG parameters such that the long-time double occupancy is approximately equal: $D^{\infty}_{TD-NRG} \simeq D^{\infty}_{Gutz}$. The Gutzwiller data is taken from Fig. 2 in Ref. [60] and describes a hybridisation quench ($\Gamma_i = 0 \to \Gamma_f/D = 0.01$) with $U/\Gamma_f = 9$, and $r = 0.4$. This quench mediates from the initial LM phase over the QCP into the SSC phase. If we used these parameters for U and r in the NRG, the final Hamiltonian would be situated deeply in the LM phase. Therefore, we have to reduce U to $U_c(\Gamma_i = 0)/\Gamma_f < U_i/\Gamma_f = 1.6 = U_f/\Gamma_f < U_c(\Gamma_f/D = 0.01)/\Gamma_f$ for the TD-NRG calculation to quench into the SSC phase.

In Fig. 4.14(a) we compare the dynamics of the double occupancy $\langle D(t)\rangle$ obtained by the TD-NRG and by the Gutzwiller approach. The latter predicts for $0 < t\Gamma_f < 1$ a very long silent phase which is followed by a steep rise of $\langle D(t)\rangle$ for $1 < t\Gamma_f$ until it exploits a damped oscillation and reaches its steady-state value for long times. In strong contrast to that, the TD-NRG data perfectly agrees with the analytical prediction of Eq. (4.8) for short times. We augment our comparison with the results for the time-dependent hybridisation energy $E_{hyb}(t)$ in Fig. 4.14(b). Not only that for long times the energies differ for both techniques, but also the different characteristics of the short-

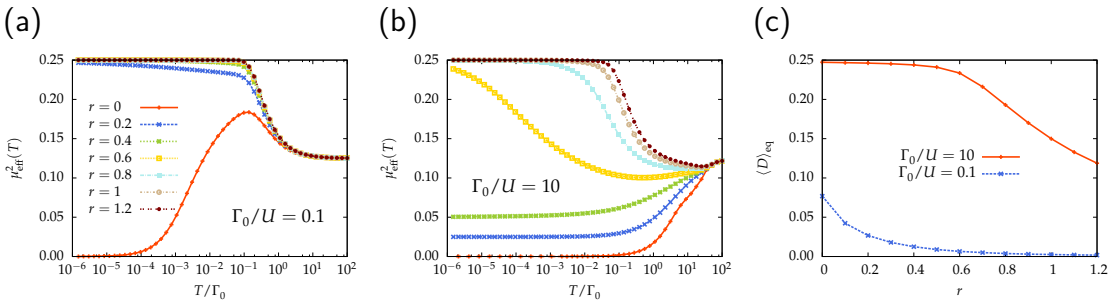

Figure 4.15: Equilibrium properties of the SIAM in dependence of the bath exponent r for fixed $D/\Gamma_0 = 100$. Effective local moment $\mu^2_{\rm eff}(T)$ (a) in a strongly correlated regime $\Gamma_0/U = 0.1$, and (b) in a weakly correlated regime $\Gamma_0/U = 10$. In (c): The equilibrium double occupancy $\langle D\rangle_{\rm eq}$ for both regimes in the limit $T \to 0$. Taken from [117].

time dynamics are even stronger pronounced for $E_{\rm hyb}(t)$ due to the ultrafast behaviour of $E_{\rm hyb}(t)$ for the TD-NRG.
The long silent phases for the double occupancy, as well as for the hybridisation energy, in the Gutzwiller approach are due to strong analytical restrictions. These strong restrictions in the parameter space for the equation of motion can be looked up in the Supplement Material of Ref. [60].

4.4.4 Quenches for exponents $r > 1/2$

While for the exponent $0 < r < 1/2$ and ph symmetry the SIAM exhibits a QCP for $U > 0$, the LM FP is the only stable FP for $1/2 < r$ independent of U [25]. In Fig. 4.15 we show the equilibrium properties in dependence of r for a strongly correlated regime $\Gamma_0/U = 0.1$ and a weakly correlated regime $\Gamma_0/U = 10$. The effective local moment $\mu^2_{\rm eff}(T)$ is plotted versus the temperature for the strongly correlated regime in Fig. 4.15(a) and for the weakly correlated regime in Fig. 4.15(b). For $r = 0$ the system always approaches the SC FP with $\mu^2_{\rm eff}(0) = \lim_{T\to 0}\mu^2_{\rm eff}(T) = 0$ while for $0.2 \leq r < 1/2$, the SSC FP with $\mu^2_{\rm eff}(0) = r/8$ for $\Gamma_0/U = 10$, and the LM FP with $\mu^2_{\rm eff}(0) = 1/4$ for $\Gamma_0/U = 0.1$ is reached. For $1/2 < r$, the system always flows to the LM FP, and the crossover scale $T^\star$ increases with increasing r. We augment the equilibrium properties by the equilibrium double occupancy $\langle D\rangle_{\rm eq}$ plotted versus r in Fig. 4.15(c). In the weakly correlated regime ($\Gamma_0/U = 10$) the double occupancy $\langle D\rangle_{\rm eq}$ remains close to the uncorrelated value of 0.25. Its slow decrease with increasing $0 < r < 1/2$ is related to a reduced screening of the residual effective local moment $\mu^2_{\rm eff}(0)$ in Fig. 4.15(b). For $1/2 < r$ the double occupancy $\langle D\rangle_{\rm eq}$ declines much faster with increasing r since the system approaches the LM FP in the limit $T \to 0$. For the strongly correlated regime ($\Gamma_0/U = 0.1$) the double occupancy $\langle D\rangle_{\rm eq}$ is already strongly suppressed for small r, since for $r \geq 0.1$ the system is in the LM phase.

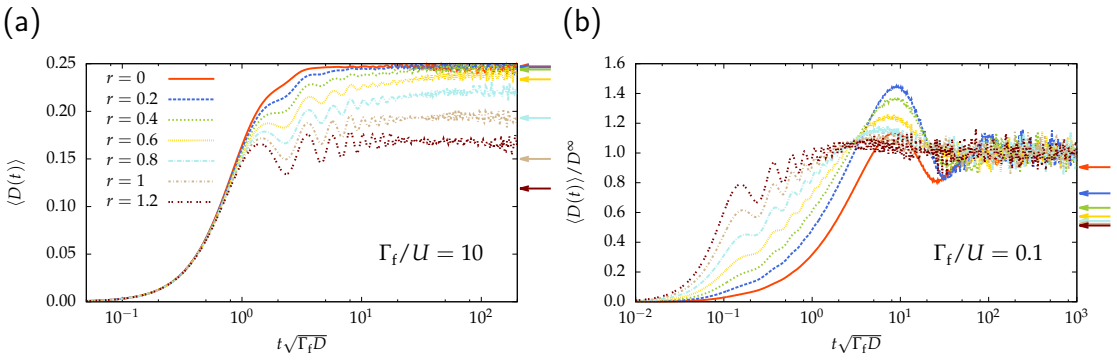

Figure 4.16: Double occupancy $\langle D(t)\rangle$ for hybridisation quenches from the LM FP ($\Gamma_i = 0$) into a weakly correlated regime $\Gamma_f/U = 10$ in (a) and into a strongly correlated regime $\Gamma_f/U = 0.1$ in (b) with $D/U = 100$ and $U = U_i = U_f = const.$ In (b) we divided $\langle D(t)\rangle$ by D^∞ to enlighten the oscillatory behaviour independently of the absolute value of $\langle D(t)\rangle$. Arrows indicate the thermal $\langle D\rangle_{eq}$. Taken from [117].

In Fig. 4.16 we present the time-dependent double occupancy $\langle D(t)\rangle$ for hybridisation quenches with different bath exponents $r = 0, 0.2, 0.4, 0.6, 0.8, 1.0, 1.2$. For the weakly correlated regime in Fig. 4.16(a) we find, as expected, thermalisation only for quenches into the SSC phase. For $1/2 < r$ the quench is within the LM phase and the steady-state value of $\langle D(t)\rangle$ is reduced with increasing r. The value deviates increasingly from thermal equilibrium due to quenching deeper in the LM phase with increasing r. Using the time scale $\tau = t\sqrt{\Gamma_f D}$ clearly reveals the universal r-independent time scale of the short-time dynamics, which has been predicted by the perturbation theory. For quenches remaining in the LM phase, we observe oscillations proportional to U at intermediate times, which are weaker damped with increasing r.

For the strongly correlated regime in Fig. 4.16(b) we quench for $r > 0$ within the LM phase. The double occupancy $\langle D(t)\rangle$ rises from its initial value towards its steady-state value which differs significantly from thermal equilibrium. By dividing out the steady-state value and showing $\langle D(t)\rangle/D^\infty$ in Fig. 4.16(b) we illustrate the short-time oscillatory behaviour independently of the absolute value of $\langle D(t)\rangle$. Due to this rescaling, the time scale $\tau = 1/\sqrt{\Gamma_f D}$ governing the dynamics is not directly discernible as in Fig. 4.16(a). For intermediate times, we observe a damped oscillatory behaviour for small r. These oscillations are stronger pronounced with increasing r due to a more concentrated effective local moment around the impurity. This leads to a more emphasised local dynamics between the impurity and the zeroth Wilson chain site, hence, in the first Wilson shell. Due to the increasingly localised local moment the deviation of the steady-state value from the thermal equilibrium value, which is indicated by the arrow on the right of the graph, increases with increasing r.

4.5 Conclusion

In this chapter we have analysed the local dynamics in the SIAM. We have used three different methods, the TD-NRG, the perturbation theory and a time-dependent Gutzwiller approach, and compared their different outcomes. In addition to the known equilibrium properties of the SIAM, we discussed the restrictions of the Gutzwiller ansatz in equilibrium in Sec. 4.2: Only in the LM phase it allows a decoupling of an effective local moment which is located on the impurity site, whereas the NRG accurately generates a ground state describing a spatially extended effective local moment.

For the dynamics we have either changed the Coulomb repulsion in time for the interaction quenches in Sec. 4.3 or the hybridisation strength for the hybridisation quenches in Sec. 4.4. For interaction quenches within the SSC phase the double occupancy $\langle D(t)\rangle$ reveals for a scaling function $f(t)$ an in leading order U_f-independent universal behaviour. The main dependence of $f(t/t_\mathrm{co})$ on the bandwidth D and the bath exponent r can be expressed by a crossover time scale t_co. For interaction quenches into the LM phase, we have extracted the crossover energy scale $T^\star$ tracking the build-up of the effective local moment from the temperature-dependent effective local moment $\mu^2_\mathrm{eff}(T)$. $T^\star$ depends on the distance $U - U_\mathrm{c}$ and vanishes for $U \to U_\mathrm{c}^+$. Since $T^\star$ reflects the approach to the LM FP, $1/T^\star$ can be interpreted as a characteristic length scale of the effective local moment formation. With increasing $T^\star$ the effective local moment, which decouples from the system, is more strongly localised at the impurity. Interestingly, the deviation between the long-time steady-state value D^∞ and the thermodynamic value $\langle D\rangle_\mathrm{eq}$ only depends on $T^\star$. It is unimportant if $T^\star$ is altered by a variation of U_f at fixed D or by a variation of D for fixed U_f. Furthermore, the spatial extension of this decoupling effective local moment can only be accounted by the NRG. In the Gutzwiller approach the restriction to a local moment formation on the impurity site yields a different dynamics.
For the hybridisation quenches, we have done a perturbation theory calculation in second order in the hybridisation and have verified our TD-NRG results for small hybridisation strengths. Hence, we confirmed that the short-time dynamics is governed by the time scale $1/\sqrt{\Gamma_\mathrm{f} D}$ which is independent of the Coulomb interaction. By comparison of our data to the recent Gutzwiller results we have demonstrated that these results are limited due to the strong locality of the ansatz. The dynamics of the variational Gutzwiller ansatz already deviates strongly from the asymptotically exact perturbation theory result for short times.
For quenches within or into the SSC phase, independent of the quench type, the double occupancy thermalises, meaning that the long-time steady-state value agrees with the thermal equilibrium value of an independent NRG calculation for H^F within the errors of the TD-NRG. Whereas, for quenches within or into the LM phase we have

demonstrated non-thermalisation for the double occupancy due to the extended nature of the decoupling effective local moment. Furthermore, we have revealed that the hybridisation energy, which tracks to the whole bath continuum, thermalises fast for hybridisation quenches, even within the LM phase. Hence, the question of thermalisation is dependent on the operator of interest.

Chapter 5

Influence of bosonic DOFs on the real-time dynamics in the BFAM

Since we have focused on the real-time dynamics of purely fermionic quantum impurity systems (QISs), in particular of the single-impurity Anderson model (SIAM) in the previous chapter, we will extend our investigation to BF-QISs. We work with the Bose-Fermi Anderson model (BFAM) here which is driven by a competition between the fermion-induced charge fluctuations with an energy-dependent scattering rate $\Gamma(\epsilon) \propto |\epsilon|^r$ and a friction induced by the continuum of bosonic DOFs with the bath spectral function $J(\omega) \propto \omega^s$. This yields a complex set of fixed points (FPs) which we have already presented in Sec. 2.4. Interestingly, the Bose-Fermi critical (BFCR) FP shows three different types of quantum criticality in equilibrium depending on the combination of bath exponents (r, s). We will analyse the influence of the bosonic DOFs on the real-time dynamics and show that for the F-type bath exponents the dynamics of the BFAM can be completely reproduced by the purely fermionic SIAM with a renormalised Coulomb interaction U_{ren}. Whereas for the B-type bath exponents a one-to-one correspondence fails.

We would like to note that parts of this chapter will be published [157] elsewhere. We will begin with a more general introduction in Sec. 5.1 and summarise the relevant known equilibrium properties in Sec. 5.2. There we will enlighten that the bosonic DOFs produce an effective renormalisation of the Coulomb repulsion even to an attractive interaction leading to a charge-Kondo (cK) and a localised (L) phase. Furthermore, we will propose a way to gain appropriate parameters for the SIAM which corresponds to the BFAM with a given bosonic coupling g.
Our study of the dynamics, especially on the local double occupancy $\langle D(t) \rangle$, considers F-type bath exponents in Sec. 5.3 and B-type exponents in Sec. 5.4. There, we will analyse different quench types, e.g. within one phase and over one or two quantum critical points (QCPs), and use a scaling function $f(t/t_{\text{co}})$ in combination with a crossover time scale t_{co} to reveal the leading order influences of the dynamics. For all

these quenches we will augment our data with corresponding dynamics of the SIAM to demonstrate that only for the F-type bath exponents the dynamics is in leading order driven by the fermionic DOFs.
We will close our investigation in Sec. 5.5 with dynamics of the level occupancy $\langle n_{\mathrm{d}}(t)\rangle$ for quenches out of a particle-hole (ph) symmetry-broken state into ph symmetric final conditions showing a friction-induced retardation of the dynamics. A brief conclusion in Sec. 5.6 summarises our main findings.

5.1 Introduction

To gain a better understanding in nanoscale devices, such as semi-conductor QDs, or qubits for quantum computation [158], a lot of work has been done to investigate QISs [20]. Since the 1980s fermionic QISs [19, 25, 83, 112, 113] have been analysed extensively. In the last decade bosonic DOFs [36] instead of [37, 90] or in addition [55–57, 81, 100, 122, 159–161] to the fermionic ones became accessible by the NRG and extended some earlier work [162–164].

The spin-1/2 impurity BFKM [55] and its extension to the charge sector, the BFAM [56, 57], are the most intensively examined models. They may serve as effective site in the EDMFT [101, 102] to address the occurrence of magnetic QPTs in heavy fermions [165, 166] and in the KLM [24, 103]. The fluctuating magnetic order parameter field, which is generated by the other f moments, is represented by the bosonic continuum in the BFAM. In the KLM the magnetic ordering induced by the RKKY interaction [76–79] competes with the screening of the f-shell moments due to the Kondo effect [22, 80]. The model has been applied to the equilibrium properties of a noisy QD system [54, 167] where the fluctuations of the gate voltage are modeled by the bosonic DOFs. The following investigation of the non-equilibrium dynamics for these BF-QIS is important for the understanding of relaxation and dissipation for such nano devices.

To investigate the real-time dynamics and the steady state of these BF-QISs one can use rate equations and Born-Markov approaches [168, 169], but these methods can only be applied for weak couplings and are not applicable close to the QPT. Therefore, we will use the non-equilibrium extension of Wilson's NRG approach [19, 20], the TD-NRG [42, 123] to access both, the weak coupling and the strong coupling regime. While the TD-NRG has already been used to access the real-time dynamics in QISs with purely fermionic or bosonic baths [42, 43, 117, 123, 124, 133, 170] or steady-state currents through nano-devices [99, 134, 171], we have extended the recently introduced BF-NRG [55] to non-equilibrium for combined BF-QIS using the TD-NRG.

The BFAM [56, 57] reveals in equilibrium a QPT with hyperscaling behaviour in the regimes $0 < r < 1/2$ and $1/2 < s < 1$. The specific combination of the bath exponents

(r,s) has not only a profound impact on the equilibrium properties of the QPT, but also divides different regimes in the real-time dynamics. We will show that for a final Hamiltonian whose low-energy FP is mainly governed by the fermionic bath properties (F-type), the non-equilibrium dynamics of the BFAM can be exactly reproduced by a purely fermionic SIAM replacing the bare U by an U_{ren} which includes the attractive electron-electron interaction mediated by the bosonic bath. For exponents where the FP is governed by the bosonic bath (B-type) [57], the real-time dynamics shows distinctive differences to a SIAM: In this case U_{ren} is dynamically generated leading to a characteristic slowdown of the decay time.
For quenches of the gate voltage, we will find different steady-state values for the impurity charge filling for identical bath couplings depending on the choice of the initial conditions since the FP of the final Hamiltonian is in the localised phase. Furthermore, we will demonstrate thermalisation within the numerical accuracy of the method for Hamiltonians approaching the SSC FP.

5.2 Equilibrium properties

In the previous chapter we have specified the energy-dependent power-law coupling function $\Gamma(\epsilon)$ in Eq. (4.1). This definition has been chosen in accordance to the time-dependent Gutzwiller results of Ref. [60] and features a r-independent coupling V_0 between the impurity and the zeroth Wilson chain site. For a better comparison of the known equilibrium properties of BF-QISs we change the coupling function to

$$\Gamma(\epsilon) = \Gamma_0 \left|\frac{\epsilon}{D}\right|^r \Theta(D - |\epsilon|) \quad , \tag{5.1}$$

as it has been used in the literature [57]. Therefore, the integral over the coupling function, $\pi V_0^2 = \int \mathrm{d}\epsilon\, \Gamma(\epsilon) = 2\Gamma_0 D/(r+1)$, is dependent on the bath exponent $r \geq 0$: With increasing r the hybridisation V_0 decreases. The parameter Γ_0, which we will use as energy scale in the following, is related to Γ_0^{SIAM} of the previous chapter by $\Gamma_0 = \Gamma_0^{\text{SIAM}}/(r+1)$. The bosonic spectral function $J(\omega)$ has been introduced in Sec. 1.3 in the context of the SBM and is approximated by the power-law form [36]

$$J(\omega) = 2\pi g \omega_c^{1-s} \omega^s \, \Theta(\omega_c - \omega) \quad . \tag{5.2}$$

The cut-off ω_c defines the high-energy scale while the overall coupling strength between the impurity and the bosonic bath is denoted by the dimensionless coupling g. Since the exponent s separates different bath types, $0 \leq s \leq 1$ for a sub-ohmic bath [90], $s = 1$ for ohmic bath [36] and $s \geq 1$ for a super-ohmic bath [91], we restrict ourselves to bosonic exponents $1/2 \leq s$ in this chapter due to so far unresolved problems applying the NRG [172] for the sub-ohmic SBM with $0 \leq s < 1/2$.

For simplicity, we set both bath cut-offs equal: $D/\omega_c = 1$. This assumption introduced by Glossop *et al.* [55] is well justified when targeting the low-energy physics and QPTs. Since for a greater fermionic bandwidth $D_0 \gg D$ it is possible to gain a reduction in the bandwidth to $D_0 \to D_{\text{eff}} \simeq \omega_c$ via a perturbative RG treatment leading to an effective impurity model with also renormalised parameters for ϵ_d, U and $\Gamma(\epsilon)$. Nevertheless, this renormalisation only effects the high-energy regime and has no impact on the low-energy physics.

The equilibrium properties of the BFAM are well understood by several publications [25, 56, 57, 83, 111, 116, 118, 119, 122, 139]. The phase diagram of the BFAM and the different NRG FP properties have been discussed in Sec. 2.4 in detail. Depending on the combination (r, s) of the bath exponents three types of quantum criticality have been identified in the model, cf. Ref. [57] and Sec. 2.4.3. For small r, the bosonic bath properties govern the critical exponents in equilibrium defining a B-type regime with a boundary $0.5 \leq s = 1 - 2r \leq 1$. For large r and s the critical exponents are given by the fermionic bath properties, hence defining the F-type regime with a non-linear boundary. Between the two regimes there is a mixed (M) type regime where the critical exponents do not decompose in fermionic and bosonic parts.
Independently of the specific type of (r, s), the BFAM features three stable phases for ph symmetry and two QCPs between them. For $U > U_c$ and $\Gamma_0 > 0$, all phases can be addressed by varying over the bosonic coupling g. As the phase diagram of the BFAM in Fig. 2.8 reveals, for $U > U_c$, $\Gamma_0 > 0$ and $g = 0$ the system is characterised by the LM FP describing a decoupled effective local moment. As we will show in the next section, the main effect of the bosonic bath is the renormalisation of the Coulomb repulsion $U > 0$ to a smaller or even attractive Coulomb interaction. Hence, an increase in g corresponds to a decrease in U. For $g^\star < g < g_c$ the absolute value of the renormalised Coulomb repulsion is smaller than the critical value $|U_{\text{ren}}| < U_c$ and forces the system in the SSC FP with a partially screened effective local moment. With an even stronger coupling $g_c < g$, the system is driven into the L phase where the effective local moment vanishes and an effective charge moment is built up. The critical coupling $g^\star$ refers to the BFCR* FP and g_c to the BFCR FP, as introduced in Sec. 2.4.1.

5.2.1 Renormalisation of the Coulomb repulsion

To enlighten the main effect of the bosonic bath, we neglect the conduction band and its coupling to the impurity for a moment. Then, the resulting Hamiltonian is given by

$$\begin{aligned} H'_{\text{BFAM}} = &\sum_\sigma \epsilon_d d_\sigma^\dagger d_\sigma + U d_\uparrow^\dagger d_\uparrow d_\downarrow^\dagger d_\downarrow + \sum_q \omega_q \phi_q^\dagger \phi_q \\ &+ \left(\sum_\sigma d_\sigma^\dagger d_\sigma - 1\right)\left(\sum_q \lambda_q \left(\phi_q^\dagger + \phi_q\right)\right) \quad . \end{aligned} \tag{5.3}$$

In presence of the bosonic bath, the Coulomb repulsion U undergoes a reduction due to a boson-induced effective electron-electron interaction. This was first shown for the Holstein model [164, 173–175]. The Hamiltonian in Eq. (5.3) is bi-linear in the bosonic operators. Thus, it can be diagonalised on the operator level by displaced bosonic operators $\tilde{\phi}_q^\dagger = \phi_q^\dagger + \theta_q$ with the displacement θ_q. The electronic subspace of the impurity is spanned by the impurity occupation states $|0\rangle$, $|\uparrow\rangle$, $|\downarrow\rangle$ and $|\uparrow\downarrow\rangle$. For $|\uparrow\rangle$ and $|\downarrow\rangle$ the bosonic bath plays no role because the coupling term is zero for half-filling. The effective bath Hamiltonians are

$$\langle 0|H|0\rangle = \sum_q \omega_q \tilde{\phi}_q^\dagger \tilde{\phi}_q - \sum_q \frac{\lambda_q^2}{\omega_q} \qquad \text{and} \tag{5.4}$$

$$\langle \uparrow\downarrow |H| \uparrow\downarrow\rangle = 2\epsilon_\mathrm{d} + U + \sum_q \omega_q \tilde{\phi}_q^\dagger \tilde{\phi}_q - \sum_q \frac{\lambda_q^2}{\omega_q} \quad . \tag{5.5}$$

To achieve this diagonal form in the bosonic operator $\tilde{\phi}_q^{(\dagger)}$, the displacement has to be $\theta_q = \lambda_q/\omega_q$. We re-define the energy shift into the Coulomb repulsion and gain the renormalised Coulomb repulsion

$$\begin{aligned} U_\mathrm{ren} &= U - \sum_q \frac{\lambda_q^2}{\omega_q} = U - \int_0^{\omega_\mathrm{c}} \frac{\mathrm{d}\omega}{\pi} \frac{J(\omega)}{\omega} \\ &= U - g\frac{2\omega_\mathrm{c}}{s} \quad , \end{aligned} \tag{5.6}$$

for which we have used the bosonic coupling function $J(\omega)$ of Eq. (5.2). Hence, a repulsive Coulomb repulsion $U > 0$ is reduced by the bosonic bath. It can even change sign and become attractive for $g > Us/(2\omega_\mathrm{c})$. Consequently, we define the coupling

$$g' = \frac{Us}{2\omega_\mathrm{c}} \tag{5.7}$$

where the renormalised Coulomb repulsion U_ren is zero. Due to this sign change at g', there is a simple level crossing from a spin-doublet ground state consisting of $|\uparrow\rangle$ and $|\downarrow\rangle$ for $g < g'$ to a charge-doublet ground state consisting of the two charged states $|0\rangle$ and $|\uparrow\downarrow\rangle$ for $g' < g$ [56].

5.2.2 Equilibrium double occupancy

So far, we have demonstrated that the coupled bosonic bath renormalises the Coulomb repulsion $U \to U_\mathrm{ren}$. If we additionally couple the impurity to the fermionic bath, the bare Coulomb repulsion U, the fermionic coupling strength Γ_0 and the bosonic coupling g influence the equilibrium properties. To estimate the renormalised Coulomb repulsion we take a closer look on the equilibrium double occupancy $\langle D\rangle_\mathrm{eq} = \langle d_\uparrow^\dagger d_\uparrow d_\downarrow^\dagger d_\downarrow\rangle$

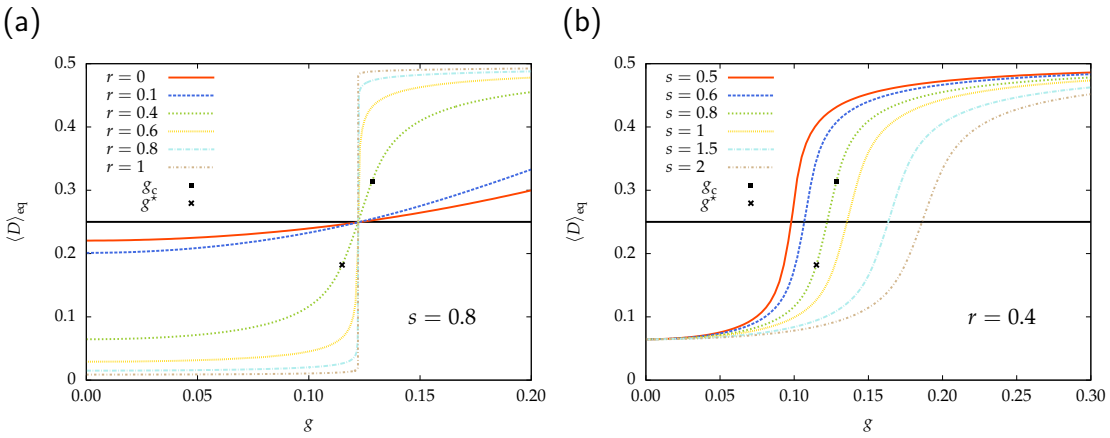

Figure 5.1: Equilibrium double occupancy $\langle D \rangle_{eq}$ of the BFAM versus the bosonic coupling g for fixed $U/\Gamma_0 = 1$, $\Gamma_0/D = 0.01$ and ph symmetry. In (a) the fermionic exponent is varied for fixed $s = 0.8$ while in (b) the bosonic exponent is varied for fixed $r = 0.4$. For the curve representing ($r = 0.4$, $s = 0.8$) the critical couplings $g^\star$ and g_c are complemented. The NRG parameters are $\Lambda = 6$, $N_S = 1000$, $N_B = 10$, $N = 40$ and $N_z = 1$. All data is obtained at the temperature $T \simeq 1.4 \cdot 10^{-16}$. Taken from [157].

at the impurity. We will show that the local equilibrium double occupancy $\langle D \rangle_{eq}$ is continuous over the QCPs. This is similar to the purely fermionic SIAM, for which the continuity of $\langle D \rangle_{eq}$ over a QPT has been stated in Refs. [25, 117]. Whereas, the zero-temperature values of the effective moments μ^2_{eff} and Q^2_{eff} are discontinuous over the QCPs and indicate the QPTs as depicted in Fig. 2.7. Hence, the effective moments combine both local DOFs and conduction band DOFs.

In Fig. 5.1 we present the equilibrium double occupancy $\langle D \rangle_{eq}$ in dependence of the bosonic coupling g for various combinations of bath exponents (r, s). We use a set of fermionic exponents r and a fixed $s = 0.8$ in Fig. 5.1(a), and a set of bosonic exponents s and a fixed $r = 0.4$ in Fig. 5.1(b). The equilibrium double occupancy is always greater than zero because the fermionic coupling $\Gamma_0 > 0$ is finite.
The equilibrium double occupancy $\langle D \rangle_{eq}$ at the vertical axis ($g = 0$) in Fig. 5.1(a) decreases with increasing $0 < r < 1/2$ because for $\Gamma_0 = const$ the low-energy contributions according to Eq. (5.1) are weaker due to the change of the exponent r and also the r-dependent hybridisation V_0 is smaller. Since for $1/2 < r$ the SSC FP is absent, the ground state in equilibrium is either characterised by the LM FP with $\langle D \rangle_{eq} \to 0$ for a positive Coulomb interaction U_{ren} ($g < g'$) or by the L FP with $\langle D \rangle_{eq} \to 0.5$ for a negative U_{ren} ($g' < g$). Therefore, the double occupancy $\langle D \rangle_{eq}$ shows a step-like behaviour at the coupling g' reflecting the level crossing of the two ground states.
If the Coulomb repulsion is renormalised to zero, all four impurity states contribute equally and the equilibrium double occupancy is consequently $\langle D \rangle_{eq} = 1/4$. We add a horizontal line for this value in Fig. 5.1. In the previous section, we have calculated

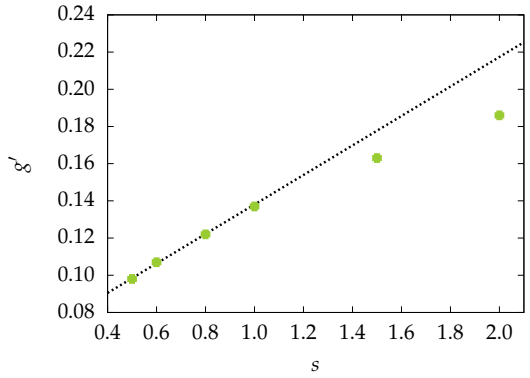

Figure 5.2: Dependence of the coupling g' on the bosonic bath exponent s. Data for g' is taken from Fig. 5.1(b). The dashed line is a linear regression for the points in the sub-ohmic regime $0 < s < 1$.

the analytical expression for g' in Eq. (5.7) for a decoupled fermionic bath revealing a vanishing Coulomb repulsion in the range $10^{-3} < g' < 10^{-2}$ for the parameters stated in Fig. 5.1(b). In presence of the finite fermionic coupling $\Gamma_0/D = 0.01$, as in Fig. 5.1(b), the coupling to the bosonic bath has to be much greater to reduce the Coulomb repulsion to zero. The bosonic coupling g' is much greater since (i) the fermionic coupling $\Gamma_0 > 0$ induces correlations between the impurity and the fermionic bath and (ii) the renormalisation due to the bosonic bath acts only locally on the impurity. Therefore, for the full model, we re-define the coupling g' by the empirical definition

$$\langle D \rangle_{\mathrm{eq}}(g') = \frac{1}{4} \quad . \tag{5.8}$$

All curves in Fig. 5.1(a) intersect at this point. Hence, the fermionic bath exponent r influences the slope of the renormalisation but not its strength and $U_{\mathrm{ren}}(g', s) = 0$ is independent of r. Furthermore, the influence of the Coulomb repulsion is non-linear: For a ten-times-greater Coulomb repulsion with $(r, s) = (0.4, 0.8)$ and $\Gamma_0/D = 0.01$, the bosonic coupling g' only increases from $g'(U/\Gamma_0 = 1) = 0.122$ to $g'(U/\Gamma_0 = 10) = 0.387$. As Fig. 5.1(b) reveals, the bosonic exponent s determines the strength of the renormalisation: With increasing exponent s a stronger coupling g' is needed to achieve $U_{\mathrm{ren}} = 0$. Surprisingly, it is unimportant if we stay in the sub-ohmic regime, or have ohmic or even super-ohmic dissipation. To reveal if g' depends linearly on the bosonic bath exponent s for the full model, as implied by Eq. (5.7) for zero hybridisation, we plot the coupling g' in Fig. 5.2 for the data of Fig. 5.1(b) versus s. In the sub-ohmic regime, the points and their linear regression curve agree very well. This verifies the linear dependence on s in the sub-ohmic regime. The ohmic dissipation also agrees fine with the regression curve. Only in the super-ohmic regime the dependence is weaker than linear.

Furthermore, if the renormalised Coulomb repulsion vanishes, the system is in the

phase	Coulomb repulsion	bosonic coupling
spin-Kondo	$0 < U$	$0 < g < g'$
charge-Kondo	$0 < U$	$g' < g < g_c$
	$-U_c < U < 0$	$0 < g < g_c$

Table 5.1: Phase boundaries of the sK and cK phases in accordance to Fig. 2.8 and to g' in Eq. (5.8).

SSC FP. Therefore, g' is not connected to one of the QCPs ($g^\star$ or g_c), which we complemented in Fig. 5.1. The critical coupling g_c ($g^\star$) is always greater (smaller) than g', reflecting that the build-up of the effective charge (local) moment needs a finite negative (positive) Coulomb interaction.

Spin-Kondo and charge-Kondo phases

Since the BFAM can be mapped to a KM containing either a spinful impurity spin or a chargeful pseudo impurity spin, see App. A.1, we refer to the former case as spin-Kondo (sK) phase and to the latter case as charge-Kondo (cK) phase. For ph symmetry, both cases lead to the SSC FP in equilibrium. Hence, the presented SSC phase in Fig. 2.8 can be subdivided into the sK phase and the cK phase. The level spectrum of the SSC FP is unique. It does not distinguish whether the system is in the sK or cK phase, nor are the effective moments μ^2_{eff} and Q^2_{eff} of help since they are identical for both phases. Nevertheless, we can use the renormalised Coulomb repulsion U_{ren} as indicator for the type of the phase. For $U_{\text{ren}} > 0$ the two single-occupied impurity states are favoured and form the spinful impurity, while for $U_{\text{ren}} < 0$ the zero- and double-occupied states are favoured and form a chargeful impurity. Hence, for $\langle D\rangle_{\text{eq}} \lesssim 1/4$ the system is in the sK phase and otherwise for $\langle D\rangle_{\text{eq}} \gtrsim 1/4$ in the cK phase. This leads to the phase boundaries stated in Tab. 5.1.

Effective parameters for a corresponding SIAM

Since the three stable phases of the BFAM can be reached as well for $g = 0$ by tuning U, the question arises what the influence of the additional bosonic bath is beyond a renormalisation $U \to U_{\text{ren}}(g)$ on the real-time dynamics compared to the SIAM. The equilibrium double occupancy $\langle D\rangle_{\text{eq}}$ monotonically increases with increasing g in the BFAM, and decreases with increasing U in the SIAM, as depicted in Fig. 5.3. While $\langle D\rangle_{\text{eq}}(U)$ in the SIAM is symmetric around $\langle D\rangle_{\text{eq}} = 1/4$, in the BFAM the increase of $\langle D\rangle_{\text{eq}}(g)$ shows no symmetric behaviour and its slope depends on the specific choice of (r, s). By the requirement

$$\langle D\rangle^{\text{BFAM}}_{\text{eq}}(g) = \langle D\rangle^{\text{SIAM}}_{\text{eq}}(U/\Gamma_0) \tag{5.9}$$

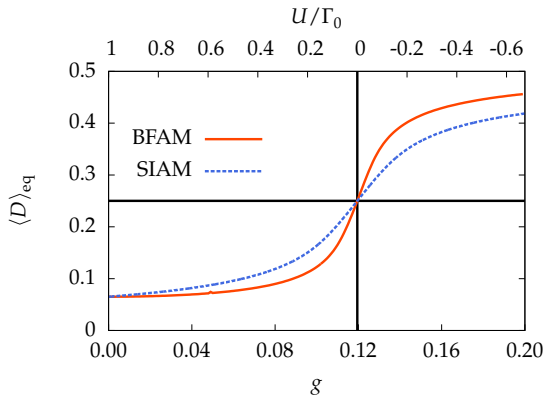

Figure 5.3: Equilibrium double occupancy $\langle D \rangle_{\rm eq}$ of the BFAM versus the bosonic coupling g for $U/\Gamma_0 = 1$, $\Gamma_0/D = 0.01$, $r = 0.4$ and $s = 0.8$ and of the SIAM versus the Coulomb repulsion U/Γ_0 for $\Gamma_0/D = 0.01$ and $r = 0.4$. All data is obtained in the limit $T \to 0$ and averaged over $N_z = 8$ realisations. Taken from [157].

we define an effective SIAM with the same r which has the same local fermionic equilibrium expectation values. Furthermore, we can estimate with this requirement the renormalised Coulomb interaction in the BFAM due to the bosonic coupling: $U_{\rm ren}(g) = U^{\rm SIAM}$ if Eq. (5.9) is fulfilled.

5.2.3 Preliminary remarks to the real-time dynamics

Since we can track all three phases by varying the bosonic coupling g for $U > U_c$, we switch $g_i \to g_f =: g$ at time $t = 0$ and hold all other parameters constant. We focus on the dynamics of the double occupancy $\langle D(t) \rangle$ for the F type in Sec. 5.3 and the B type in Sec. 5.4. All quenches are augmented with comparable quenches according to Eq. (5.9) with the SIAM to check if the real-time dynamics of the BFAM can be reproduced by the purely fermionic SIAM. For all these quenches we maintain ph symmetry leading to a level occupancy $\langle n_d(t) \rangle = 1$ for all times. In absence of a magnetic field, there are two pairs of locally degenerate states: the empty- and the double-occupied state $|0\rangle, |2\rangle$ and the two spin states $|\uparrow\rangle, |\downarrow\rangle$ which contain exactly one electron.
Furthermore, we address the dynamics of quenches out of a ph broken phase into the ph symmetric phases by switching the level energy $-U_i/2 \gg \epsilon_{d,i} \to \epsilon_{d,f} = -U_f/2$ at $t = 0$ with $U_i = U_f = U$. We restrict ourselves to $r = 0$. Since we know that for ph symmetry the level occupancy is given by $\langle n_d \rangle_{\rm eq} = 1$, we focus on the real-time dynamics of $\langle n_d(t) \rangle$ and investigate the deviation between the long-time expectation value and the thermal equilibrium in Sec. 5.5.

For the calculations of the BFAM we use $U/\Gamma_0 = 1$, $\Gamma_0/D = 0.01$ and vary over the bosonic coupling g. For the comparison with the SIAM, we also use $\Gamma_0/D = 0.01$ but vary over U/Γ_0 with the same bath exponent r. All our (TD-)NRG calculations are done with $\Lambda = 6$, and $N = 40$ NRG iterations. For the BFAM we use the NRG

Phase	$\langle D \rangle_{\mathrm{eq}}$	g	U/Γ_0
LM	**0.065119**	**0**	**1**
	0.069507	0.04	0.8917
	0.076314	0.06	0.7557
	0.089795	0.08	**0.5628**
	0.122573	0.1	0.3098
	0.195940	0.114	0.09381
	0.214397	0.116	0.06031
	0.234426	0.118	0.02601
SSC	**0.250000**	**0.119488**	**0**
	0.276720	0.122	-0.0449
	0.297465	0.124	-0.0816
	0.316741	0.126	-0.1188
	0.392307	0.14	-0.3999
	0.428959	0.16	-0.8580
	0.446127	0.18	-1.3860
L	**0.456499**	**0.2**	**-1.9872**

Table 5.2: Correspondence between the bosonic coupling g of the BFAM with $U/\Gamma_0 = 1$, $\Gamma_0/D = 0.01$, $r = 0.4$ and $s = 0.8$ and the Coulomb repulsion U/Γ_0 of the SIAM. The initial conditions are printed in bold. All data is obtained in the limit $T \to 0$.

parameters $N_{\mathrm{S}} = 1000$, $N_{\mathrm{B}} = 10$ and for the SIAM $N_{\mathrm{S}} = 2000$. We average over $N_{\mathrm{z}} = 8$ different bath realisations.

5.3 Quenches with F-type bath exponents

For the F-type bath exponents $(r, s) = (0.4, 0.8)$ we present different quenches in the BFAM with $U/\Gamma_0 = 1$, $\Gamma_0/D = 0.01$ and in the SIAM with $\Gamma_0/D = 0.01$. For the former model, we quench over the bosonic coupling $g_{\mathrm{i}} \to g_{\mathrm{f}} = g$, and for the latter model over the Coulomb repulsion $U_{\mathrm{i}} \to U_{\mathrm{f}}$. We use three representative initial values: (i) $g_{\mathrm{i}} = 0$ starting from the LM FP, (ii) $g^\star < g_{\mathrm{i}} = 0.119488 < g_{\mathrm{c}}$ starting from the SSC FP with $\langle D \rangle_{\mathrm{eq}}(g_{\mathrm{i}}) = 1/4$ ($U_{\mathrm{ren}} = 0$), as well as (iii) $g_{\mathrm{c}} < g_{\mathrm{i}} = 0.2$ starting from deep in the L phase. For $g_{\mathrm{f}} =: g$ we select a series of values within each phase. We will show that for the F-type bath exponents the real-time dynamics can be fully understood by mapping the BFAM onto a corresponding SIAM defined by the requirement in Eq. (5.9). The corresponding values of U/Γ_0 for the given g are stated in Tab. 5.2.

5.3.1 Quenches within one phase

In Fig. 5.4 we show the real-time dynamics of the double occupancy $\langle D(t) \rangle$ for quenches within each of the three stable phases. In addition to the dynamics in the BFAM we present the dynamics for the corresponding SIAM in black in the background. All

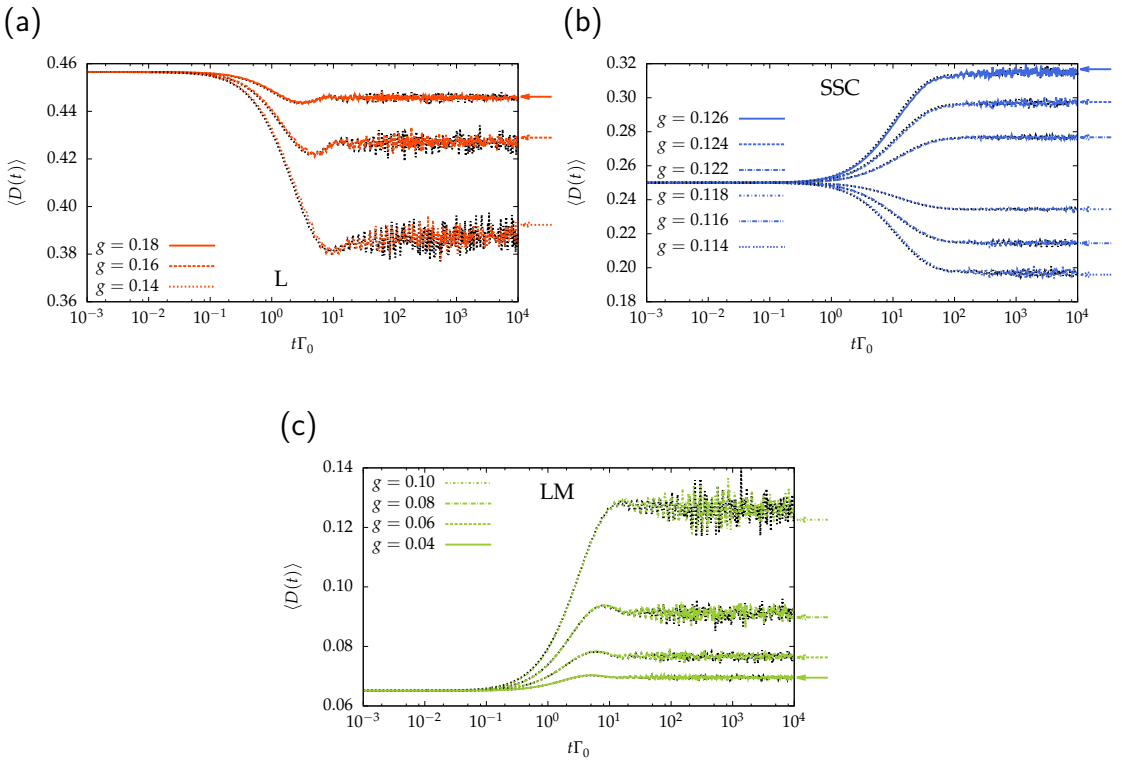

Figure 5.4: Real-time double occupancy $\langle D(t) \rangle$ (coloured curves) of the BFAM for bath exponents $r = 0.4$ and $s = 0.8$ with $U/\Gamma_0 = 1$ and $\Gamma_0/D = 0.01$. Black curves in the background are the corresponding double occupancy for the SIAM. We perform quenches within the (a) L phase, (b) SSC phase and (c) LM phase. Details on the chosen couplings g_i and g are given in Tab. 5.2. Taken from [157].

quenches equilibrate for long times but only the quenches within the SSC phase thermalise.

The quenches within the L phase are shown in Fig. 5.4(a) where we start with a double occupancy near $\langle D(t=0) \rangle \sim 0.5$ due to a large negative U_ren for $g_\mathrm{i} = 0.2$. Since $g < g_\mathrm{i}$, a reduction of $\langle D \rangle$ is expected. The double occupancy $\langle D(t) \rangle$ smoothly declines on a time scale roughly given by $1/\Gamma_0$ with some small g-dependent corrections.

In Fig. 5.4(b) the quenches start from the SSC FP ($g_\mathrm{i} = 0.119488$) where all local states are degenerated, hence $\langle D(t=0) \rangle = 1/4$ and $U_\mathrm{ren} = 0$. For $g > g_\mathrm{i}$, $\langle D(t) \rangle$ increases, while for $g < g_\mathrm{i}$ $\langle D(t) \rangle$ decreases in time. The corresponding thermal equilibrium values, indicated as arrows at the right side of the graph, demonstrate thermalisation in the long-time limit since the long-time expectation value agrees with the thermal one.

Starting from a decoupled bosonic bath ($g_\mathrm{i} = 0$) and quenching within the LM phase, we show the dynamics of $\langle D(t) \rangle$ for this case in Fig. 5.4(c). Similarly to the quenches in the L phase in Fig. 5.4(a) the long-time value of $\langle D(t) \rangle$ deviates from the thermodynamic equilibrium: With increasing g the deviation increases, although the deviations are very small. This expected behaviour is related to the decoupling effective local

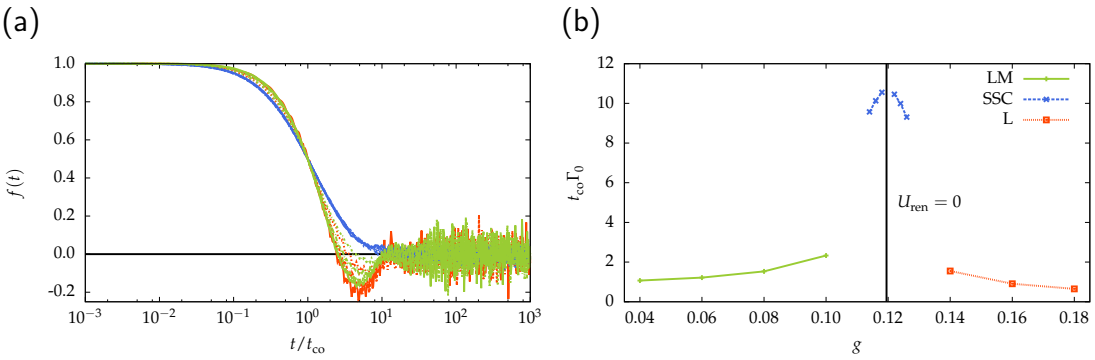

Figure 5.5: In (a): Scaled dynamics of all BFAM quenches of Fig. 5.4 according to Eq. (5.10) versus the crossover time scale t_{co}. In (b): Crossover time scale t_{co} versus g for all three quench types. Taken from [157].

moment in the LM phase, as already discussed in the previous chapter for the SIAM. In analogy, the deviation between the steady-state value and the thermal equilibrium value increases with decreasing g for the quenches within the L phase, since the overlap in the effective charge moment, which decouples in the L phase, between the initial and the final preparation decreases with decreasing g.
In addition, we have investigated the same type of quenches using a corresponding SIAM by setting $g_i = g_f = 0$ and switching between the corresponding U values that lead to identical $\langle D \rangle_{eq}$. The real-time dynamics of $\langle D(t) \rangle$ has been added as black curves to the graphs of Fig. 5.4. For all investigated cases, the corresponding SIAM results agree perfectly with those of the BFAM. Hence, for this F-type bath exponents the dynamics of the BFAM can fully be expressed by a corresponding SIAM determined by the requirement in Eq. (5.9) and the fermionic bath exponent r.

In analogy to our results of the SIAM in the previous chapter, we scale the dynamics by the function

$$f(t) = \frac{\langle D(t) \rangle - \langle D(\infty) \rangle}{\langle D(0) \rangle - \langle D(\infty) \rangle} \tag{5.10}$$

of Eq. (4.3) to eliminate the influence of the different long-time expectation values $\langle D(t \to \infty) \rangle$. We define the crossover time scale t_{co} by $f(t_{co}) = 1/2$ and scale all BFAM quenches of Fig. 5.4 as $f(t/t_{co})$ and show the resulting dynamics in Fig. 5.5(a). While the dynamics for quenches within the SSC phase (blue curves) show universal behaviour, this is not the case for quenches within the L or LM phase for times $t/t_{co} > 1$. Nevertheless, for the L and LM phase $f(t/t_{co})$ reveals comparable shapes which only slightly differ from the SSC case for $t/t_{co} < 1$.
The crossover time scales for the different quenches are depicted in Fig. 5.5(b). The vertical line marks the coupling $\langle D \rangle_{eq}(g' = 0.119488) = 1/4$ where the renormalised

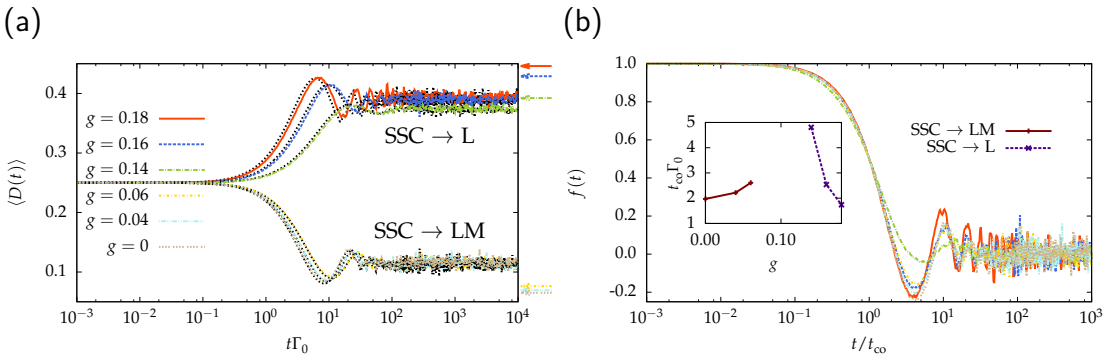

Figure 5.6: Real-time double occupancy $\langle D(t)\rangle$ (coloured curves) of the BFAM with the same parameters as in Fig. 5.4. Black curves in the background show the corresponding double occupancy for the SIAM. In (a): Quenching from the initial SSC FP ($g_i = 0.119488$) into the L and LM phase. In (b): Scaled data of BFAM quenches of (a) via Eq. (5.10) versus the time scale t_{co}. The inset shows the dependence of t_{co} on g. Taken from [157].

Coulomb repulsion vanishes. The crossover time scale[22] shows an ascending slope for $U_{ren} \to 0^+$ and a descending slope for an increasing attractive $U_{ren} \to -\infty$. This is independent of the quench type.

5.3.2 Quenches over QCPs

In Fig. 5.6 we quench over one QCP from the SSC FP ($g_i = 0.119488$) with $\langle D(0)\rangle = 1/4$ into the L and the LM phase. The used parameters for the BFAM and SIAM quenches are stated in Tab. 5.2. The time-dependent double occupancy $\langle D(t)\rangle$ performs a damped oscillation independent of the quench type, as Fig. 5.6(a) reveals. The oscillation frequency depends on the renormalised Coulomb repulsion $|U_{ren}|$. Those values can be estimated from the corresponding dynamics in the SIAM and, hence, $U_{ren} = U$ of the SIAM in Tab. 5.2. All quenches equilibrate to a steady-state value for long times. This steady-state value deviates significantly from the thermal equilibrium value which is indicated as arrow on the right side of the graph. With increasing difference $g^\star - g > 0$ or $g - g_c > 0$ respectively, the decoupling effective local moment or rather the effective charge moment is stronger localised to the impurity. Hence, the damping is reduced and the oscillation in $\langle D(t)\rangle$ is more strongly pronounced.

22 Since the dynamics of the BFAM can be completely reproduced here by a corresponding SIAM, we like to mention that the crossover time scale t_{co} for the SIAM here depends stronger on U_f compared to the presented results for the same quench types in Sec. 4.3. There, the variation of t_{co} for the quenches within the SSC phase is of the order of 2% and has been neglected. The stronger influence here originates in the larger $\Lambda = 6$ used for our calculations in this chapter and the fact that we do not include the discretisation correction factor A_Λ [112, 113]. Therefore, the hybridisation is effectively smaller for $\Lambda = 6$ leading to a smaller critical Coulomb repulsion U_c. Since the Coulomb repulsions U/Γ_0 used in Fig. 5.4 are an order of magnitude smaller compared the the same quenches in Sec. 4.3, the crossover time scales t_{co} are larger and their variation is greater.

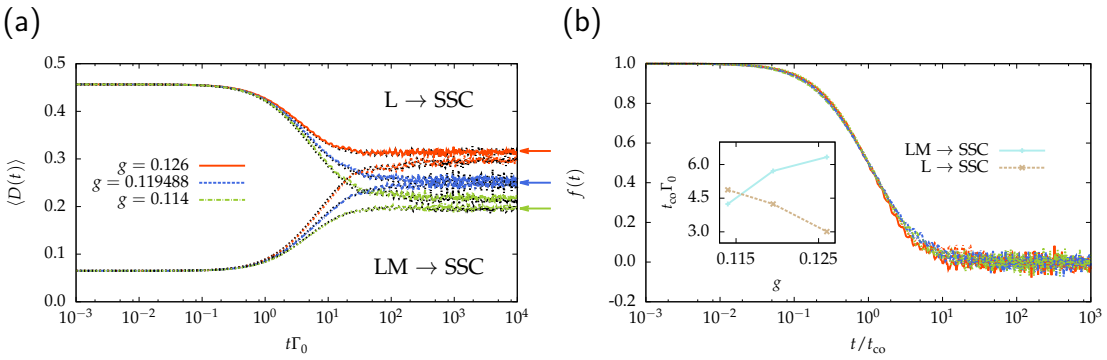

Figure 5.7: Real-time double occupancy $\langle D(t)\rangle$ (coloured curves) of the BFAM with the same parameters as in Fig. 5.4. Black curves in the background show the corresponding double occupancy of the SIAM. Quenches from the L and LM starting point into the SSC phase. In (a) we show $\langle D(t)\rangle$ versus $t\Gamma_0$ and the scaled data of the BFAM quenches via Eq. (5.10) versus t_{co} in (b). The inset in (b) depicts the dependence of t_{co} on g for these quenches. Taken from [157].

We extract the crossover time scale t_{co} and scale the data of Fig. 5.6(a) as $f(t)$ versus t/t_{co} in Fig. 5.6(b). There, the positions of the minima and maxima of the oscillations agree well. The inset of Fig. 5.6(b) shows the dependence of t_{co} on the bosonic coupling and is given approximately by $t_{\mathrm{co}} \simeq 2/|U_{\mathrm{ren}}|$.

For the reverse quench direction, we start from the LM or L FP and quench into the SSC phase. As presented in Fig. 5.7(a), the double occupancy $\langle D(t)\rangle$ equilibrates via a smooth crossover to a steady-state value for both quench types. Although the finial Hamiltonian H^{F} is identical for both quench types, their steady-state values differ slightly. However, the value for a quench starting from the L FP always exceeds the value for the quench starting from the LM FP. The deviation between the steady-state value and the thermal value is small and probably related to TD-NRG discretisation errors. Hence, we conclude that the quenches into the SSC phase thermalise in the continuum limit. Since Fig. 5.7(b) shows perfect universality of the dynamics scaled via $f(t/t_{\mathrm{co}})$, we conclude that the quenches from the L and LM FP are mirror images of each other.

Quenching over two QCPs, from the LM phase into the L phase or vice versa, is the extremest case. The dynamics of the double occupancy $\langle D(t)\rangle$ is shown in Fig. 5.8(a) and Fig. 5.8(b), respectively. Although the double occupancy equilibrates to a steady-state value, the deviation between this value and the thermal equilibrium is very strong and stronger compared to the previous case for quenches from the SSC FP over one QCP into the L or LM phase. Since for both the initial and the final preparation we have to deal with a decoupling effective local or charge moments, the overlap between the initial and final ground state is even smaller and, hence, the system does not relax completely to the thermal value. In Fig. 5.8(c) the data of Figs. 5.8(a) and 5.8(b) is scaled

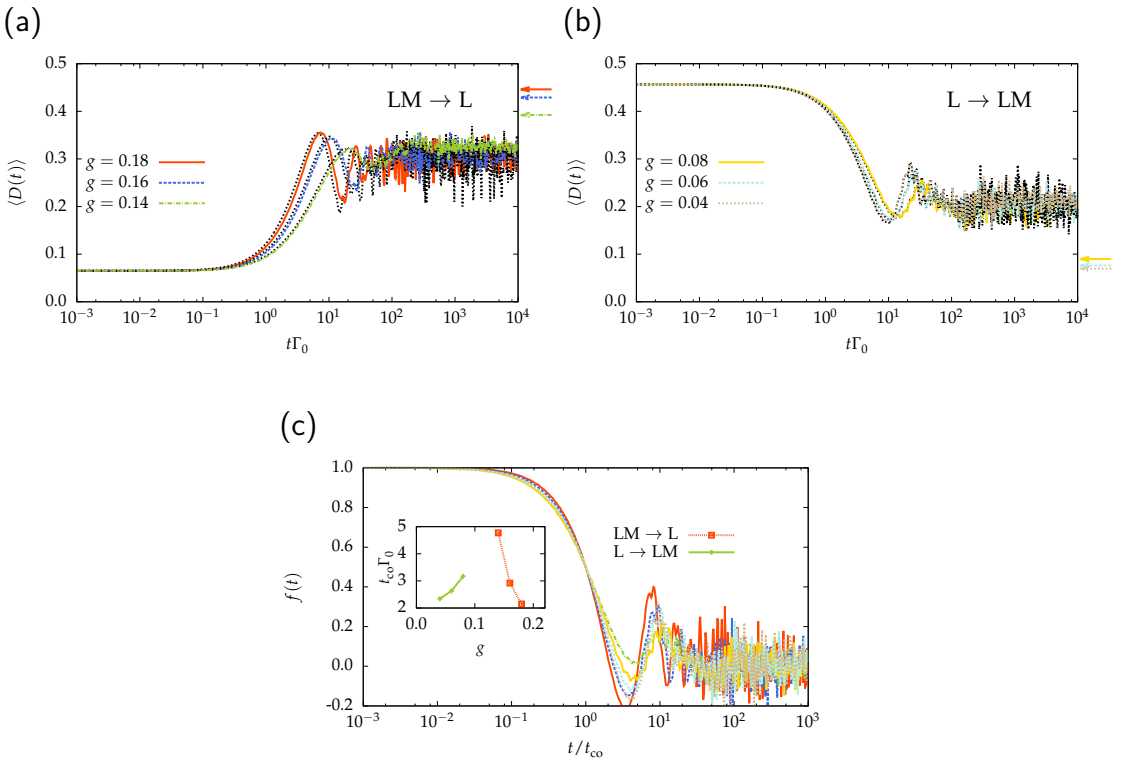

Figure 5.8: Real-time double occupancy $\langle D(t)\rangle$ (coloured curves) of the BFAM with the same parameters as in Fig. 5.4. Black curves in the background show the corresponding double occupancy of the SIAM. Quenches from the LM starting point into the L phase in (a) and vice versa in (b). The scaled dynamics of the BFAM quenches versus t_{co} are shown in (c) and the inset reveals the dependence of t_{co} on g. Taken from [157].

via Eq. (5.10) and plotted versus t/t_{co}. In this relative perspective the resemblance between the quenches into the LM and L phase is recognisable. For example, the quenches with $g = 0.02$ and $g = 0.17$ are very much alike. The inset in Fig. 5.8(c) shows t_{co}. The values are very similar in absolute value and in the functional dependence on g to the ones in Fig. 5.6 over one QCP.

5.4 Quenches with B-type bath exponents

In this section we switch to bath exponents of the B type and use exemplary $(r, s) = (0.1, 0.6)$ for the BFAM and the same r for the corresponding SIAM. The BFAM exhibits the same three phases, but the critical exponents are governed by the properties of the bosonic bath [57]. For the previously examined dynamics, for the F-type bath exponents, we have demonstrated that the real-time dynamics can be completely reproduced by an effective SIAM with the same fermionic exponent r, since the non-equilibrium dynamics are driven by the fermionic bath. Now, we address the question

Phase	$\langle D \rangle_{\mathrm{eq}}$	g	U/Γ_0
L	**0.468771**	**0.50**	**-12.335**
	0.464730	0.49	-10.904
	0.452747	0.47	-8.142
	0.428493	0.48	-5.455
SC	**0.250000**	**0.420422**	**0**
	0.088760	0.38	4.392
	0.053475	0.34	7.215
	0.040793	0.30	9.417

Table 5.3: Correspondence between the bosonic coupling g of the BFAM with $U/\Gamma_0 = 16$, $\Gamma_0/D = 0.01$, $r = 0.1$ and $s = 0.6$ and the Coulomb repulsion U/Γ_0 of the SIAM. The initial conditions are printed in bold. All data is obtained in the limit $T \to 0$.

whether the real-time dynamics of the BFAM is also governed by the details of the bosonic bath, which would lead to differences in the dynamics of the BFAM and the effective SIAM. We only look at quenches within the L and the SSC phase since the LM phase is a mirror image of the L phase. The initial conditions for the quenches are (i) $g_{\mathrm{i}} = 0.5$ for the L FP and (ii) $g_{\mathrm{i}} = 0.420422$ for the SSC FP at which $\langle D(g_{\mathrm{i}}) \rangle_{\mathrm{eq}} = 1/4$. The phases of the system for $t > 0$ are distinguished by their zero-temperature FPs and the final conditions are stated in Tab. 5.3.

In Fig. 5.9 we present the time-dependent double occupancy $\langle D(t) \rangle$ for the BFAM (coloured curves) and for the corresponding SIAM (black curves). For the quenches within the L phase in Fig. 5.9(a), as well as for the quenches within the SSC phase in Fig. 5.9(b), the dynamics between the BFAM and the SIAM differs significantly. Their agreement for short and long times is caused by the mapping of the model parameters. The dynamics in the SSC phase start in Fig. 5.9(b) from $\langle D(t = 0) \rangle = 1/4$ which corresponds to $U_{\mathrm{i}} = 0$ in the SIAM. Since we use $U/\Gamma_0 = 16$ in the BFAM, a small change in g translates into a strong variation of U, as stated in Tab. 5.3. The strong suppression of the double occupancy in the long-time limit yields damped oscillatory real-time dynamics. Again the damping in the BFAM exceeds the one in the effective SIAM and the oscillation frequency is reduced. Furthermore, the oscillations, which are present in the corresponding SIAM, are completely suppressed in the BFAM for quenches within the L phase, as shown in Fig. 5.9(a).
Similar to the quenches for the F-type bath exponents, the dynamics is slowed down with decreasing g for quenches within the L phase and with increasing g for quenches within the SSC phase. Hence, the crossover time scale t_{co}, not shown here, reveals the same functional dependence on g as for the F-type bath exponents. Furthermore, this is in accordance with our findings for the interaction quenches in the SIAM in Sec. 4.3, where the short-time dynamics is proportional to $\langle D(t) \rangle \propto 0.25(1 - \alpha(t/\sqrt{U_{\mathrm{f}} D})^2)$ leading here to an increasing slowdown with increasing U_{ren}.
If we compare the dynamics of $\langle D(t) \rangle$ in the BFAM to the corresponding black curve in

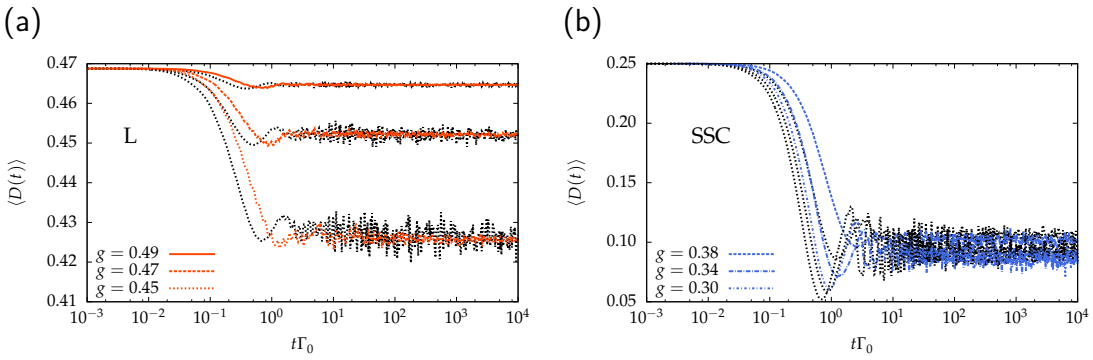

Figure 5.9: Real-time double occupancy $\langle D(t)\rangle$ (coloured curves) of the BFAM for B-type bath exponents $r = 0.1$ and $s = 0.6$ with $U/\Gamma_0 = 16$ and $\Gamma_0/D = 0.01$. Black curves in the background are the corresponding double occupancy of the SIAM with $\Gamma_0/D = 0.01$ and $r = 0.1$. We perform quenches within (a) the L phase and (b) the SSC phase.

the background, $\langle D(t)\rangle$ is more strongly slowed down with decreasing g in the L phase and with increasing g in the SSC phase. Consequently, the slowdown of $\langle D(t)\rangle$ in the BFAM compared the same quench in the SIAM increases with decreasing $|U_{\mathrm{ren}}|$. This is somehow counter-intuitive since one would expect that the renormalisation in U_{ren} is dynamically built up at lower energy scales and hence affects the dynamics at larger time scales, while the full U in the SIAM is already effective directly from the beginning. Hence, one would suggest an increasing deviation with increasing $|U_{\mathrm{ren}}|$. At this stage, this remains an open question and will be addressed in a following publication.

5.5 Quenches out of a particle-hole asymmetric phase

For a particle-hole (ph) symmetric broken model, the different asymmetric FPs for the SIAM have been introduced in Sec. 2.3.2. Since we change the level energy in time, we are interested in the dynamics of the level occupancy $\langle n_{\mathrm{d}}(t)\rangle$ for quenches out of a strongly ph-asymmetric state into ph-symmetric phases. We will commentate on the differences in the dynamics between the BFAM and an effective SIAM with the same equilibrium double occupancy $\langle D\rangle_{\mathrm{eq}}$. We show the dynamics for a constant DOS ($r = 0$) and $s = 0.6$. In equilibrium both, the BFAM and the SIAM, emerge the zero-temperature ASC FP if ph symmetry is broken and $|U/\Gamma_0| > 0$, $g \geq 0$. Similar to the SBM [36, 37] no QCP can occur in the asymmetric case.

To break the ph symmetry for $t < 0$, we set $|\epsilon_{\mathrm{d,i}}/\Gamma_0| \gg 1$. In the context of a QD this is essentially a large positive or negative gate voltage [58] which depletes or completely fills the local orbital. Since we hold $U_{\mathrm{i}} = U_{\mathrm{f}} = U = const$ for all times, we investigate the different dynamics whether (a) the bosonic bath is constantly coupled ($g_{\mathrm{i}} = g_{\mathrm{f}}$) for all times or (b) at $t = 0$ in addition switched from $g_{\mathrm{i}} = 0$ to $g_{\mathrm{f}} > 0$. The time evolution

$\langle D\rangle_{\mathrm{eq}}$	Phase	g_{f}	U/Γ_0
0.4558	L	$0.2 > g_{\mathrm{c}}$	-8
	L	$0.4 > g_{\mathrm{c}}$	6
	SC	(SIAM)	-13.144
0.3977	SC	$0.2 < g_{\mathrm{c}}$	-2
	L	$0.4 > g_{\mathrm{c}}$	11
	SC	(SIAM)	-6.223
0.2156	SC	$0.2 < g_{\mathrm{c}}$	4.6
	SC	$0.4 < g_{\mathrm{c}}$	15
	SC	(SIAM)	1.1753

Table 5.4: Set of final parameters for the quenches in Figs. 5.10 and 5.12 in presence of ph symmetry $-2\epsilon_{\mathrm{d,f}} = U_{\mathrm{f}} = U$.

is driven by a ph symmetric H^{F}, since we switch the level energy to $\epsilon_{\mathrm{d,f}} = -U/2$ at $t = 0$. The BFAM then features the SSC FP for $g_{\mathrm{f}} < g_{\mathrm{c}}$ and the L FP for $g_{\mathrm{f}} > g_{\mathrm{c}}$ in equilibrium.
We can adapt the bosonic coupling g and the Coulomb repulsion U such that there are two parameter pairs $(g_{\mathrm{f}}, U_{\mathrm{f}})_{1,2}$ which have the same equilibrium double occupancy $\langle D\rangle_{\mathrm{eq}} = const$. The two pairs can be adjusted such that they belong to (A) the L phase, (C) the SSC phase or (B) are located in two different phases with $g_{\mathrm{f},1} < g_{\mathrm{c}}$ and $g_{\mathrm{f},2} > g_{\mathrm{c}}$. The corresponding SIAM with the same $\langle D\rangle_{\mathrm{eq}}$ only reveals the SSC FP after quenching for ph symmetry. The fermionic bath is for all calculations time-independently coupled with $\Gamma_{\mathrm{i}}/D = \Gamma_{\mathrm{f}}/D = \Gamma_0/D = 0.01$.

We present the real-time dynamics of the level occupancy $\langle n_{\mathrm{d}}(t)\rangle$ for three representative $\langle D\rangle_{\mathrm{eq}} = const$ in Figs. 5.10(a) for (A), 5.10(b) for (B) and 5.12 for (C). Since we maintain ph symmetry after quenching, the thermal expectation value is $\langle n_{\mathrm{d}}\rangle_{\mathrm{eq}} = 1$ and the steady state of $\langle n_{\mathrm{d}}(t)\rangle$ is expected to reach this value for long times. For each case (A) – (C), we use the two coupling strengths $g_{\mathrm{f},1} = 0.2$ and $g_{\mathrm{f},2} = 0.4$. The corresponding values for U_{f} for the three cases are collected in Tab. 5.4. We augment our data of the BFAM with the dynamics of the corresponding SIAM with one black curve in the background.
We start with case (A) with the equilibrium double occupancy $\langle D\rangle_{\mathrm{eq}} \simeq 0.4558 > 1/4$ for all H^{F}, which corresponds to an attractive Coulomb interaction $U_{\mathrm{ren}} < 0$. Both final values $(g_{\mathrm{f},1}, g_{\mathrm{f},2}) = (0.2, 0.4)$ are located in the L phase. The resulting real-time dynamics of $\langle n_{\mathrm{d}}(t)\rangle$ is depicted in Fig. 5.10(a) and reveals characteristic differences. With increasing bosonic coupling the steady-state value

$$n_{\mathrm{d}}^{\infty} = \lim_{T\to\infty} \frac{1}{T} \int_0^T \mathrm{d}t \, \langle n_{\mathrm{d}}(t)\rangle \tag{5.11}$$

increases and in addition, if $g_{\mathrm{i}} = g_{\mathrm{f}} = const$, the bosonic system maintains its inertia and the relaxation on the thermal value is more strongly suppressed. Since in the

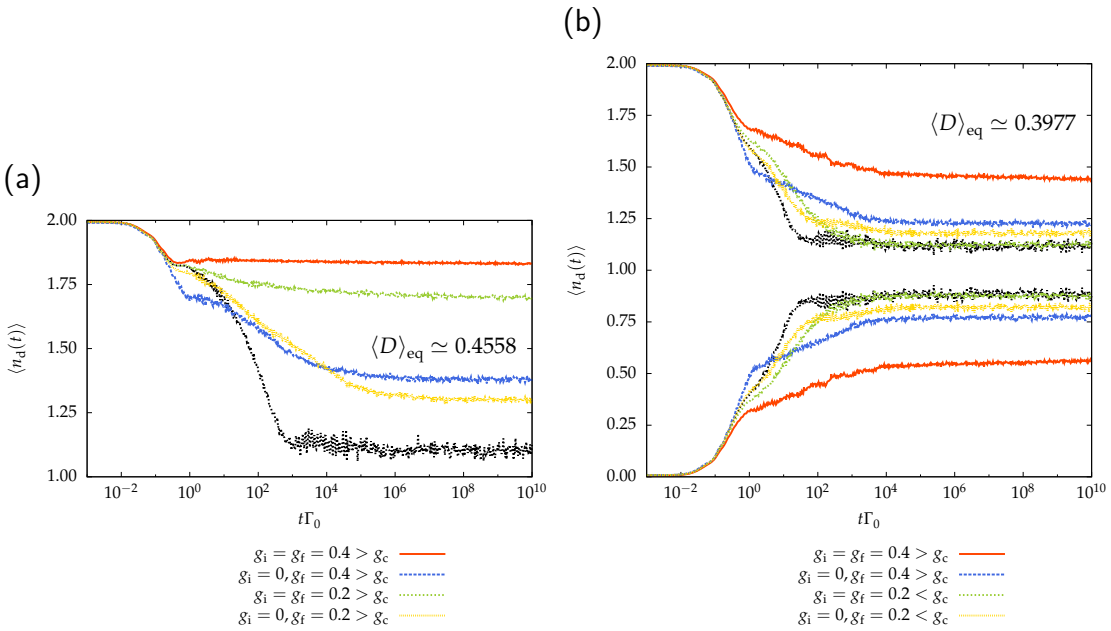

Figure 5.10: Dynamics of the level occupancy $\langle n_{\rm d}(t)\rangle$ of the BFAM with $r = 0$ and $s = 0.6$ for quenches from ph asymmetry to ph symmetry at finite temperature $T/D \sim 1.2 \cdot 10^{-7}$ with the equilibrium double occupancy (a) $\langle D\rangle_{\rm eq} \simeq 0.4558$ and (b) $\langle D\rangle_{\rm eq} \simeq 0.3977$. NRG parameters are $\Lambda = 6$, $N_{\rm S} = 800$, $N_{\rm B} = 8$, $N_{\rm z} = 8$ for the BFAM and changed to $N_{\rm S} = 2000$ for the SIAM. Taken from [157].

SIAM, the system is set in the SSC phase, the dynamics in $\langle n_{\rm d}(t)\rangle$ (black curve) clearly differs from those quenches approaching the L phase in the BFAM. Nevertheless, the dynamics is unique for $t\Gamma_0 < 1$ in all curves. This may indicate that the charge flow off the impurity is governed by the charge-fluctuation scale Γ_0. The black curve significantly deviates from the coloured ones for times $t\Gamma_0 > 1$, when the bosonic bath influences significantly the dynamics. A friction-induced slowdown can be observed. Since in the localised phase an effective charge DOF decouples from the rest of the bath, its overlap with the initial state prevents the system to approach its thermal equilibrium value. Our results agree with previous real-time investigations on the SBM [42, 43], where in the localised phase the spin polarisation is constant over a long stretch of time. However, $\langle n_{\rm d}(t)\rangle$ remains constant even for times $tT > 1$, for the finite temperature $T/D \sim 1.2 \cdot 10^{-7}$ of our calculations. This may indicate that thermal fluctuations do not influence the long-time behaviour of the level occupancy in contrary to the ohmic SBM, since here the total spin of the system is conserved. Nevertheless, the TD-NRG only provides reliable results for times $t < 1/T$.

In Fig. 5.10(b) the dynamics are shown for the case (B) $\langle D\rangle_{\rm eq} \simeq 0.3977$. There we use two parameter pairs $(g_{\rm f}, U_{\rm f})_{1,2}$ such that for $g_{\rm f,1} = 0.2 < g_{\rm c}$ the system approaches with $H^{\rm F}$ the SSC FP, while for $g_{\rm f,2} = 0.4 > g_{\rm c}$ the system is driven by the L FP. For all cases, the initial decay is governed by Γ_0 and for exponentially long times the sys-

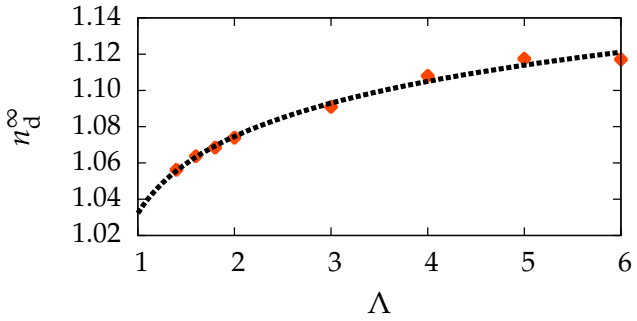

Figure 5.11: Dependence of n_d^∞ on Λ marked as rhombuses and calculated for the effective SIAM with $U/\Gamma_0 = -6.223$ as used in Fig. 5.10. The dashed line is an optimal fitting curve extrapolating n_d^∞ in the limit $\Lambda \to 1^+$. NRG parameters as in Fig. 5.10. Taken from [157].

tem equilibrates to a steady state. We present data for the two complementary cases, $\langle n_d(t=0)\rangle \simeq 0$ and $\langle n_d(t=0)\rangle \simeq 2$, to demonstrate the ph symmetry of these curves. For quenches in the L phase with $g_f > g_c$, the deviation of the steady-state value from the thermal equilibrium value $\langle n_d\rangle_{eq} = 1$ is strong for $g_i = g_f$ but smaller for $g_i = 0$. Since for $g_i = g_f$ the correlations with the bosonic bath are already present in the initial preparation, the deviation is stronger pronounced. Hence, for $g_i = g_f$ the relaxation is significantly suppressed, similar to case (A), while for $g_i = 0$ the build-up of correlations in the L phase needs some time and n_d^∞ is closer to the thermal value. For ($g_i = g_f = 0.2 < g_c$) the steady-state values agree perfectly with those obtained from the effective SIAM. The dynamics in the BFAM for ($g_i = g_f = 0.2 < g_c$) and ($g_i = 0$, $g_f = 0.2 < g_c$) are very similar those of the the corresponding SIAM. The decrease (or increase) in $\langle D(t)\rangle$ is slowed down due to the bosonic coupling but the slopes are identical to the dynamics in the SIAM, in contrast to the quenches into the L phase where the dynamics shows a different dependence on $t\Gamma_0$.

We see a clear discrepancy between the steady-state value n_d^∞ and the equilibrium value $\langle n_d\rangle_{eq} = 1$ even for quenches in the SSC FP where for all other quench types thermalisation has been confirmed. We assume that this deviation is related to discretisation artefacts of the TD-NRG [42, 120, 121] which occur for quenching over different degrees of ph asymmetry. Hence, we claim that the presented results for quenches into the SSC phase in Fig. 5.10(b) indeed show thermalisation. To confirm our argument, we perform non-equilibrium calculations for identical model parameters but different values of Λ and depict the results in Fig. 5.11. Using a fitting function, it becomes apparent that $\lim_{\Lambda\to 1^+} n_d^\infty(\Lambda) = 1$. The small difference to $n_d^\infty = 1$ is related to the finite number of states which has to be used for each calculation.

The dynamics for the last case (C) $\langle D\rangle_{eq} \simeq 0.2156$ with $g_{f,1}, g_{f,2} < g_c$ are presented in Fig. 5.12. Within the numerical accuracy thermalisation is found for all different parameters. Again, the initial decay is equal for all bosonic coupling constants and only governed by Γ_0 as before. The steady-state value is found up to $t\Gamma_0 = 1 \cdot 10^{10}$ although

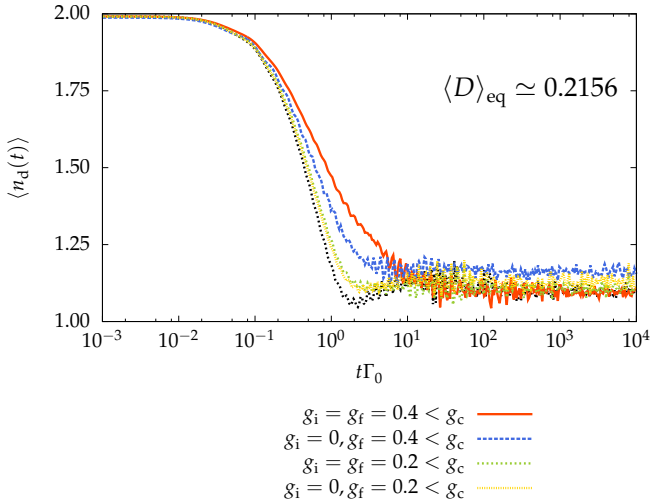

Figure 5.12: Dynamics of the level occupancy $\langle n_d(t)\rangle$ of the BFAM with $r = 0$ and $s = 0.6$ for quenches from ph asymmetry to ph symmetry at finite temperature $T/D \sim 1.2 \cdot 10^{-7}$ for $\langle D\rangle_{eq} \simeq 0.2156$. NRG parameters as in Fig. 5.10. Taken from [157].

only data up to $t\Gamma_0 = 1 \cdot 10^4$ is depicted in the figure. After a fast initial decay, we note a slowdown of the dynamics in the presence of a large coupling to the bosonic bath. The slowdown is stronger either by a larger g_f or by a time-independent bosonic coupling.

5.6 Conclusion

We have extended our investigation of local real-time dynamics on QIS which deal with fermionic and bosonic DOFs. For the equilibrium we revealed that the bosonic bath induces a renormalisation of the Coulomb repulsion to U_{ren} even to large attractive values enforcing the formation of an effective decoupling charge moment in the L phase. To estimate U_{ren} we equate the equilibrium double occupancy of the BFAM for a finite bosonic coupling and of the SIAM with the bare value of U. Then we conclude $U_{ren} = U^{SIAM}$. There is a one-to-one correspondence of the QPT between (i) the spin-Kondo effect and the local moment phase to (ii) the charge-Kondo effect and the localised phase. The spin-Kondo regime and the charge-Kondo regime are adiabatically connected, and there is one unique SSC FP with identical spin and charge moment, $\mu^2_{eff} = Q^2_{eff} = r/8$ depending on the fermionic exponent.
We have revealed that the real-time dynamics of the BFAM can be completely reproduced by a corresponding SIAM for ph symmetry, if the critical exponents are in leading order influenced by the low-energy properties of the fermionic bath, as it is the case for the F-type bath exponents. In addition, we have investigated quenches for B-type bath exponents showing that the coupling to the bosonic bath yields a retardation of the dynamics and a suppression of the oscillatory behaviour with increasing

bosonic coupling strength. Although the major effect of the bosonic bath can still be attributed to a renormalisation of U, the non-equilibrium dynamics of the full BFAM differs significantly from that of the effective SIAM. While the short-time dynamics is governed by the hybridisation strength Γ_0, the low-frequency bosonic modes cause a slowdown of the decay at intermediate time scales compared to the dynamics in the effective SIAM. The dynamics in the effective SIAM is significantly faster than the one in the full BFAM. However, the dynamics in the BFAM and in the SIAM differ for the same quench more strongly with decreasing $|U_{\mathrm{ren}}|$.

Although all quenches equilibrate for long times to a steady-state value, thermalisation is only found for quenches into the SSC phase or very close to the QCP where the characteristic low-energy scale vanishes. With increasing distance to the QCP, the low-energy LM or L FP is approached at higher temperatures in the NRG, indicating a smaller spatial extension [19, 117, 133, 150] of the decoupled effective moment. This leads to a greater overlap of the local operators with the decoupled effective moment and, hence, the deviation between the steady-state value and the thermal equilibrium increases.

For quenches out of a strongly ph asymmetric phase into ph symmetric phases, we investigated the dynamics of the level occupancy. Since we work only with $r = 0$, the BFAM features after quenching the SSC and the L phase in equilibrium, while the corresponding SIAM only exhibits the SSC FP. For all quenches, the level occupancy $\langle n_{\mathrm{d}}(t)\rangle$ equilibrates to a steady state. Nevertheless, quenching in the L phase ($g > g_{\mathrm{c}}$) leads to a strong deviation of the steady state from thermal equilibrium, which is obtained by an independent NRG calculation. This is related to a decoupling of an effective charge DOF preventing the system to relax to the thermal equilibrium. If the system is initially decoupled from the bosonic bath ($g_{\mathrm{i}} = 0$), the build-up of the decoupling charge DOF takes more time and, hence, the deviation is smaller. For quenches in the SSC phase ($g < g_{\mathrm{c}}$), the dynamics of $\langle n_{\mathrm{d}}(t)\rangle$ in the BFAM is alike to the dynamics in the SIAM, although the presence of the bosonic coupling yields a slowdown of the dynamics. Nevertheless, for all cases with $g < g_{\mathrm{c}}$ the system thermalises to the equilibrium value for long times within the accuracy of the TD-NRG, as we have shown in the continuum limit $\lim_{\Lambda\to 1^+} n_{\mathrm{d}}^{\infty}(\Lambda) = 1$.

Chapter 6

Spin relaxation influenced by bosonic and fermionic DOFs

In this chapter we are interested in the real-time dynamics of a spin-1/2 particle trapped in a noisy QD. The QD is coupled to a conduction band and additionally to a bosonic continuum, which mimics some noise within the QD. Therefore we use the BFKM of Sec. 1.4, which is an extension of the well-known Kondo model (KM).
In the BFKM, the impurity spin $\vec{S}$ couples with the coupling strength J to the spin density $\vec{s}$ of the surrounding conduction band electrons, whereas only its z component S_z couples with the coupling strength g to the bosonic bath. We assume a gapless Fermi system and use a constant density of states (DOS) which enables a Kondo screening of the impurity spin for any finite antiferromagnetic coupling $J > 0$, in absence of the bosonic bath. The bosonic continuum, which is described by the spectral function $J(\omega) \propto \omega^s$, leads to a localisation of the impurity spin for any finite $g > 0$, in absence of the fermionic bath. Since we couple the impurity to both baths, these effects compete with each other and yield a quantum phase transition (QPT) between the symmetric strong coupling (SSC) and localised (L) phase. We refer the reader to App. A.2 for further information on the quantum criticality in the BFKM.

We focus on the real-time decay in the spin polarisation $\langle S_z(t)\rangle$ of an initially polarised spin $|\langle S_z(t=0)\rangle| > 0$. The polarisation at $t = 0$ is achieved by applying a local magnetic field $\epsilon \gtrless 0$ in z direction. For times $t > 0$, we switch off the magnetic field and enable a decay of the polarisation through spin-flip processes with the conduction band electron spins by $J_f > 0$. For a sufficiently strong bosonic coupling the BFKM features in equilibrium the L phase, in which the Kondo screening of the impurity spin is suppressed. Therefore, we are interested in the effect of the bosonic coupling on the dynamics of $\langle S_z(t)\rangle$. We will show that an increasing coupling to the bosonic bath will yield a stronger slowdown in the dynamics of $\langle S_z(t)\rangle$. For quenches in the L phase a suppression of the decay will be revealed. The retardation, as well as the prevention of the decay in the L phase, are known effects, which also occur in the

spin-boson model (SBM) for an oscillating spin with a strong coupling to the bosonic bath. Furthermore, we will reveal that the dynamics of $\langle S_z(t)\rangle$ depends on the initial preparation of the system leading to strongly deviating steady states.

We will introduce the essential physics in the BFKM in Sec. 6.1 and summarise the relevant equilibrium properties in Sec. 6.2. In Sec. 6.3 we will present the real-time decay of the spin polarisation $\langle S_z(t)\rangle$ and close this brief investigation with a conclusion in Sec. 6.4.

6.1 Introduction

Different QISs [20] have been studied in the last decades to gain a detailed comprehension of effects as dissipation and decoherene in nanoscale devices. Basic models are the KM and the SBM consisting of an impurity spin which couples to a fermionic or a bosonic environment, respectively. Both models [18, 21, 36, 37, 90, 114] feature different phases in equilibrium and reveal QPTs with special properties. Also the real-time dynamics [42, 43, 132, 176] driven by the equilibrium phases has been of great interest.
In equilibrium the combined BFKM [55, 57, 100–102, 122, 167] shows a rich phase diagram and exhibits both fermion-induced Kondo screening and boson-induced localisation. The BFKM adresses, as well as the BFAM, the physics of dissipative mesoscopic qubit devices [54, 167], and of heavy-fermion systems [166]. Within the EDMFT [101, 102] the KLM is mapped to a BF-QIS in which the bosonic DOFs mimic these magnetic fluctuations. The additional quantum fluctuations provided by the bosonic DOFs yield a QPT [55, 177] due to a friction-induced localisation, as in the SBM, and therefore yield a breakdown of the Kondo physics.

Here we are interested in the real-time dynamics of the impurity spin polarisation $\langle S_z(t)\rangle$ and use our non-equilibrium extension of the BF-NRG. With this non-perturbative approach we can accurately track the breakdown of the Kondo phyics and perform quenches into both equilibrium phases, the SSC and the L phase. For our calculations, we assume a gapless fermionic environment with a constant DOS $\rho(\epsilon) = \rho_0\Theta(D - |\epsilon|)$ with $\rho_0 = 1/(2D)$. The bosonic environment is represented by the spectral bath function in its power-law form $J(\omega) = 2\pi g\omega_c^{1-s}\omega^s\Theta(\omega_c - \omega)$ as it has been introduced in Eq. (1.32) in the context of the SBM. The strength of the coupling between the impurity and the bosonic bath is given by g. We are interested in the sub-ohmic regime and select exemplified $s = 0.6$.

If not otherwise stated, we use the following NRG parameters for the calculations in this chapter: $\Lambda = 6$, $N_S = 800$, $N_B = 6$, $N_z = 8$.

6.2 Equilibrium properties

Since we apply a local magnetic field $\epsilon \gtrless 0$ only in z direction ($\Delta = 0$), we gain a full polarisation $|\langle S_z \rangle_{eq}| = 1/2$ for a decoupled spin in the zero-temperature limit. If we couple the spin to the fermionic bath with $J > 0$, a competition arises between the Kondo screening by the fermionic bath and the polarisation due to the magnetic field. In consequence, the equilibrium value is in the range $0 \leq |\langle S_z \rangle_{eq}| \leq 1/2$ revealing a partial Kondo screening of the impurity spin. The stronger the coupling to the fermionic bath $J/\epsilon \gg 1$, the stronger the polarisation is suppressed. In contrast, a strong magnetic field $\epsilon/J \gg 1$ favours a full polarisation of the spin and prevents the Kondo screening. If we, instead, couple the spin only to the bosonic bath, the system is set in the L phase for $\epsilon = 0$, independent of the bosonic coupling strength $g > 0$ and has a twofold-degenerated ground state. Whereas, for $\epsilon \gtrless 0$ a unique ground state is selected and, if the impurity spin is coupled to the fermionic bath leading to a polarisation in the range $0 \leq |\langle S_z \rangle_{eq}| \leq 1/2$, an additional coupling to the bosonic bath simply increases the polarisation $|\langle S_z \rangle_{eq}|$ with increasing g.

For both couplings $J > 0$ and $g > 0$ a competition between the Kondo screening and the localisation emerges in the full model. For no local magnetic field ($\epsilon = \Delta = 0$) and $J > 0$, the BFKM features a QPT between the Kondo-screened SSC phase and the L phase if we vary the bosonic coupling $g > 0$ [55]. The QCP at g_c can be identified by a change in the zero-temperature value of the effective local moment, which is defined in Sec. 2.2.1. The effective local moment has the zero-temperature value $\mu^2_{eff} = 0$ in the SSC FP and is unique for all $g < g_c$, whereas it is finite $0 < \mu^2_{eff}(g) \leq 1/4$ in the L FP and increases with increasing $g > g_c$. These two phases characterise the final Hamiltonian H^F in equilibrium and, hence, drive the dynamics.
In Fig. 6.1 we present the temperature-dependent effective local moment $\mu^2_{eff}(T)$ for a sub-ohmic ($s = 0.6$) bosonic bath in Fig. 6.1(a) and for an ohmic ($s = 1$) bosonic bath in Fig. 6.1(b). The coupling to the fermionic bath is $J\rho_0 = 0.05$ and we vary the bosonic coupling g.
We can define several crossover energy scales which will be helpful to characterise the dynamics of the spin polarisation $\langle S_z(t) \rangle$ later. The crossover to the SSC FP is tracked by the Kondo temperature T_K with the effective local moment value $\mu^2_{eff}(T_K) = 0.07$. In analogy, $T^\star$ tracks the crossover to the L FP: $T^\star$ marks at which temperature $\mu^2_{eff}(T)$ is reduced by 80% towards its zero-temperature value. Furthermore, the temperature T_L indicates the L FP: The effective local moment reaches its finite zero-temperature value $\mu^2_{eff}(T \leq T_L) = \mu^2_{eff} = const > 0$. For the presented coupling strengths in Fig. 6.1 the Kondo temperatures T_K are in the same range $10^{-8} < T_K/D < 10^{-6}$ for both bosonic exponents $s = 0.6, 1$. Whereas, the crossover temperatures T_L and $T^\star$, which are related to the L FP, are shifted by one to three magnitudes. Hence, for quenches in

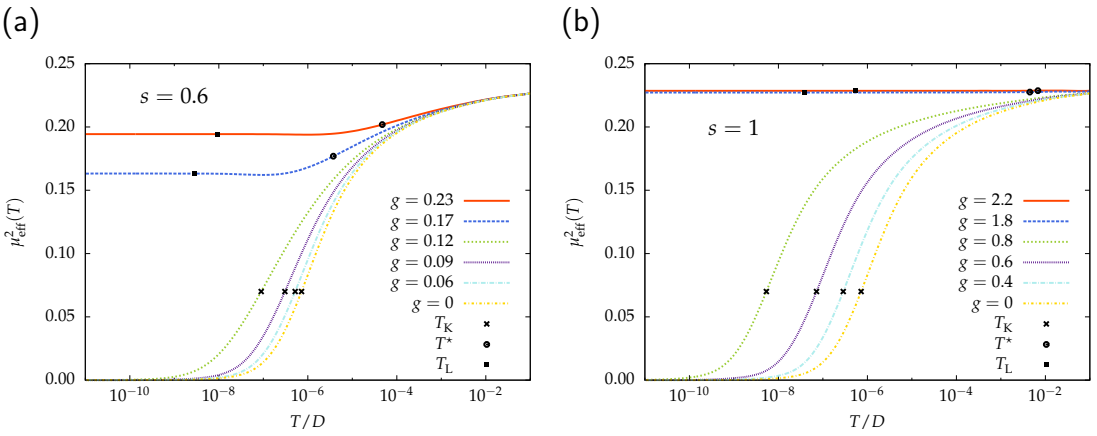

Figure 6.1: Effective local moment $\mu^2_{\rm eff}(T)$ for a sub-ohmic ($s = 0.6$) bosonic bath in (a) and for an ohmic ($s = 1$) bosonic bath in (b). The fermionic coupling is $J\rho_0 = 0.05$. The critical couplings are $g_{\rm c}(s = 0.6, J\rho_0 = 0.05) = 0.1311(8)$ and $g_{\rm c}(s = 1, J\rho_0 = 0.05) = 1.5(0)$.

the L phase, the dynamics will show significant differences regarding a sub-ohmic or an ohmic bath.

6.3 Real-time spin relaxation

A finite polarisation of the impurity spin for times $t < 0$ is achieved by setting the initial magnetic field to $\epsilon_{\rm i}\rho_0 = -0.5$ and $\Delta_{\rm i} = 0$. After the quench for $t > 0$ the magnetic field is switched off, and the spin polarisation decays to zero due to spin-flip scattering processes with the fermionic bath for an antiferromagnetic $J_{\rm f} > 0$. We will show that an additional coupling to the bosonic bath yields a retardation in the dynamics.

In Fig. 6.2 we show the decay of the spin polarisation $\langle S_{\rm z}(t)\rangle$ for a sub-ohmic bosonic bath ($s = 0.6$) with an antiferromagnetic coupling $J_{\rm f}\rho_0 = 0.05$. The coupling to the bosonic bath is constant over time in Fig. 6.2(a), while it is additionally switched on at $t = 0$ in Fig. 6.2(b). We vary over the bosonic coupling $g_{\rm f} \lessgtr g_{\rm c}(s = 0.6, J\rho_0 = 0.05) = 0.1311(8)$ to show a slowdown in the dynamics with increasing coupling to the bosonic bath, as well as a suppression of the decay for quenches in the L phase.
For $g_{\rm f} < g_{\rm c}$ the system is quenched in the SSC phase with a vanishing equilibrium polarisation. The decay of the polarisation in Fig. 6.2(a) equilibrates to a steady-state value for long times without reaching the thermal value, which is marked by the arrow at the right side of the graph. The deviation between the steady-state and the thermal value is significant but independent of the coupling $g_{\rm f}(< g_{\rm c})$. For stronger couplings $g_{\rm f} > g_{\rm c}$, the dynamics is driven by the L FP and both time scales $t^\star = 1/T^\star$

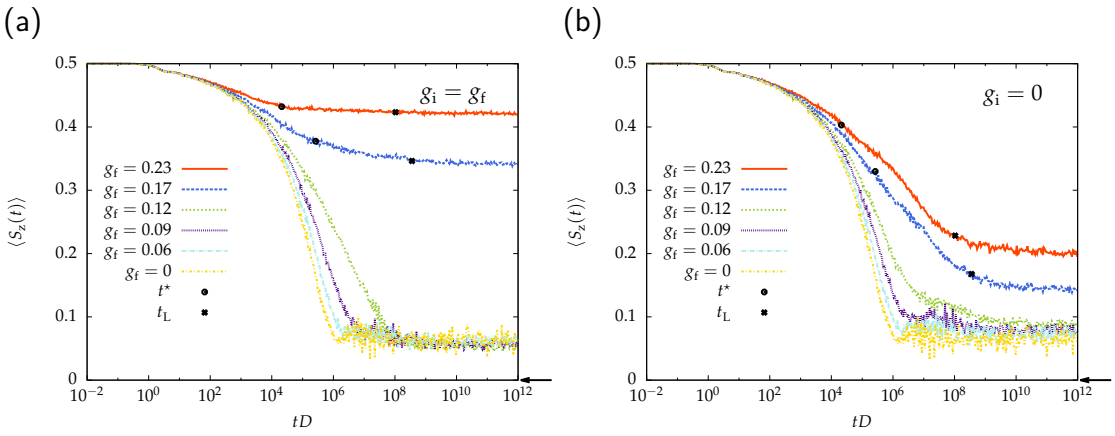

Figure 6.2: Real-time spin polarisation $\langle S_z(t)\rangle$ in z direction for a spin (a) constantly bosonic-coupled ($g_i = g_f$) and (b) initially decoupled. The initial polarisation is achieved by the magnetic field $\epsilon_i\rho_0 = -0.5$. For times $t > 0$ the magnetic field is switched off and the fermionic (and the bosonic) coupling is switched on: $J_f\rho_0 = 0.05$. The critical coupling is $g_c(s = 0.6, J_f\rho_0 = 0.05) = 0.1311(8)$. The data has been obtained for the finite temperature $T/D \sim 3 \cdot 10^{-16}$.

and $t_L = 1/T_L$ are marked in Fig. 6.2. The spin-flip processes ($J_f > 0$) drive the dynamics of the polarisation $\langle S_z(t)\rangle$ in leading order for times $tJ_f < 1$. The decay of $\langle S_z(t)\rangle$ is slowed down due to the bosonic friction. Therefore, at the crossover time scale $t^\star$ the polarisation $\langle S_z(t^\star)\rangle$ increases with increasing g_f. For times $t > t_L$, the decay is stopped. The greater g_f, the smaller both time scales $t^\star$ and t_L are and, hence, the decay stops at earlier times.

In Fig. 6.2(b) we additionally switch the bosonic coupling ($g_i = 0 \to g_f$), dealing with an initially decoupled, polarised impurity spin. In contrast to Fig. 6.2(a), here the decay of the polarisation $\langle S_z(t)\rangle$ for quenches in the L phase ($g_f > g_c$) takes place over a longer time interval leading to a smaller deviation of the steady-state value from the thermal value. The correlations forming the L FP have to be built up dynamically through the NRG and hence low-energy contributions affect the dynamics. Therefore, the time scales $t^\star$ (and t_L) reflect nicely in Fig. 6.2(b) the build-up of the correlations by a strong change in $\langle S_z(t)\rangle$ in the time interval $10^{-1} < t/t^\star < 10^1$. Whereas, in Fig. 6.2(a) these correlations are already present in the initial preparation and hence, the dynamics occurs on shorter time scales leading already to a stop of the decay for times $tT_L > 1$. For quenches in the SSC phase ($g_f < g_c$) in Fig. 6.2(b), the deviation of the steady-state value from the thermal value depends on the bosonic coupling g_f and increases slightly with increasing g_f. We suggest that this reflects the increasing mismatch in the bosonic DOFs between the initial and the final configuration. Whereas, for ($g_i = g_f$) in Fig. 6.2(a) the overlap in the bosonic DOFs stays constant over time and, hence, the deviation between the steady-state value and the thermal value is g_f-independent.

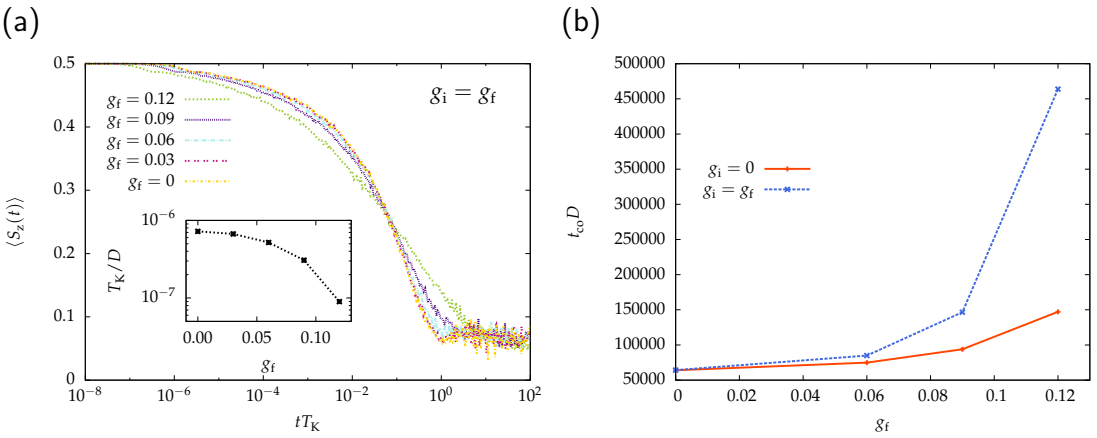

Figure 6.3: In (a): Scaled real-time dynamics of Fig. 6.2(a) versus the Kondo temperature T_K for quenches in the SSC phase with the Kondo temperatures given in the inset. In (b): Crossover time scale t_{co} versus the bosonic coupling g_f for the data of Fig. 6.2.

Furthermore, it is interesting to note that by comparing Figs. 6.2(a) and 6.2(b) for quenches in the L phase different initial preparations lead to different dynamics of the spin polarisation $\langle S_z(t)\rangle$ and to different steady states for the same final configuration.

To shed some more light on the characteristic time scales of the dynamics, we show in Fig. 6.3(a) the dynamics of $\langle S_z(t)\rangle$ scaled versus the Kondo temperature T_K for quenches in the SSC phase with the same parameters as in Fig. 6.2(a). The Kondo temperature T_K tracks the crossover to the SSC FP and decreases exponentially with increasing coupling $g_f \to {g_c}^-$, as shown in the inset in Fig. 6.3(a). Hence, due to the bosonic friction the fermionic bath screens the impurity spin for lower temperatures. The bosonic coupling induces a slowdown in the dynamics of $\langle S_z(t)\rangle$, although for small bosonic couplings $g_f/g_c \ll 1$ the curves are alike. The long-time effects are universal and are related to the low-energy Kondo temperature. The curves in Fig. 6.3(a) intersect at $\langle S_z(t)\rangle \simeq 0.25$. Consequently, the decay is faster before and slower after the intersection point with increasing g_f. Nevertheless, the Kondo temperature describes the universal behaviour for quenches in the SSC phase and reflects by itself the friction-induced retardation.

Furthermore, we use the data of Fig. 6.2 and scale it with the scaling function $f(t)$ of Eq. (4.3), which we have already used in the previous chapters. With the requirement $f(t_{co}) = 1/2$, we extract the crossover time scale t_{co} to illustrate the strength of the retardation induced by the bosonic bath. We present the crossover time scale t_{co} versus the bosonic coupling g_f in Fig. 6.3(b) for both initial conditions ($g_i = 0$) and ($g_i = g_f$). The faster the decay in $\langle S_z(t)\rangle$ reaches its steady-state value, the smaller the crossover time scale t_{co}, and hence, with increasing g_f the time scale t_{co} increases. The retardation by the bosonic bath leads to an exponentially increasing t_{co} for a linearly increasing $g_f(< g_c)$. For quenches in the SSC FP the crossover time t_{co} is smaller, if the spin is

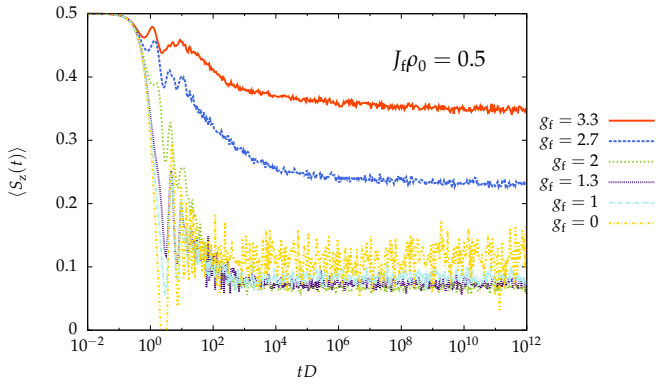

Figure 6.4: Real-time spin polarisation $\langle S_z(t)\rangle$ for a spin which is initially polarised due to $\epsilon_i\rho_0 = -0.5$ and is constantly bosonic-coupled ($g_i = g_f$). For times $t > 0$ the magnetic field is switched off and the fermionic coupling is switched on: $J_f\rho_0 = 0.5$. The critical coupling is $g_c(s = 0.6, J_f\rho_0 = 0.5) = 2.352(5)$. The data has been obtained for the finite temperature $T/D \sim 2 \cdot 10^{-8}$.

initially decoupled ($g_i = 0$). If the spin is constantly bosonic-coupled ($g_i = g_f$), the bosonic influence is present directly at the beginning and has to be compensated in addition, so that $\langle S_z(t)\rangle$ reaches the SSC FP value at larger times. Hence, the retardation and the crossover time scale t_{co} are greater in the latter case.

In Fig. 6.4 we present quenches in analogy to Fig. 6.2(a) with $g_i = g_f$ and $s = 0.6$ but for a stronger fermionic coupling $J_f\rho_0 = 0.5$. In this case the spin-flip processes due to J_f are very strong, and the local dynamics on the first Wilson shell — the interaction between the impurity and the zeroth Wilson chain site — yields a strong oscillation imposed on the decay with a frequency proportional to J_f. Due to the stronger J_f the critical coupling is shifted to $g_c(s = 0.6, J_f\rho_0 = 0.5) = 2.352(5)$. With increasing bosonic coupling g_f the oscillation is more strongly suppressed leading to a reduction in the amplitude. Each quench equilibrates to a steady-state value, which is g_f independent for quenches in the SSC FP. For the quench with $g_f = 0$, the steady-state value is different and is imposed by a strong oscillation. Since $g_f = 0$, the oscillation can not be damped through additional bosonic DOFs, but can be reduced if one increases the z averaging. The deviation of the steady-state value from its thermal value has, except for $g_f = 0$, roughly the same absolute value as in Fig. 6.2(a). The deviation may be related to finite-size artefacts in the TD-NRG and should decrease in the limit $\Lambda \to 1^+$; this is up to further investigation. For quenches in the L phase ($g_f > g_c$), the polarisation $\langle S_z(t)\rangle$ decreases very slowly over several decades to a steady-state value. The superimposed oscillation due to J_f is damped strongly by the strongly coupled bosonic bath. The long-time residual polarisation increases with increasing g_f, similar to Fig. 6.2(a).

In Fig. 6.5 we present the influence of different initial bosonic couplings g_i while the fermionic coupling $J(t)\rho_0 = 0.5$ is constant over time. Since J_i and ϵ_i are of the same

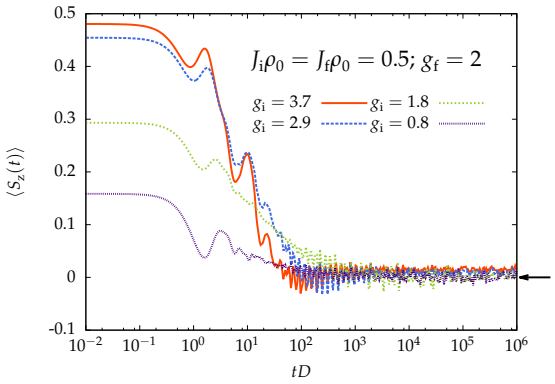

Figure 6.5: Real-time spin polarisation $\langle S_z(t)\rangle$ of an impurity spin constantly coupled to the fermionic bath and initially polarised with $\epsilon_i\rho_0 = -0.5$ for different initial bosonic couplings g_i. For times $t > 0$ the magnetic field is switched off and the bosonic coupling is changed to $g_f = 2$. The data has been obtained for the finite temperature $T/D \sim 2 \cdot 10^{-8}$.

order, the initial bosonic coupling has a strong influence on the initial polarisation $\langle S_z(t = 0)\rangle$. With increasing g_i the initial polarisation $\langle S_z(t = 0)\rangle$ is stronger. The decay of the polarisation is imposed by an oscillatory behaviour: The oscillation is induced by the strong fermionic coupling $J_f\rho_0 = 0.5$, reflecting the local dynamics on the first Wilson shell, and has a small amplitude due to the strong bosonic coupling $g_f = 2$. However, with increasing difference $|g_i - g_f|$ the polarisation reaches its steady-state value independently of the initial polarisation $\langle S_z(t = 0)\rangle$ at shorter times. Furthermore, the deviation of the steady-state value from its thermal value is significantly smaller, since we hold the fermionic coupling constant over time here. We suggest that this is due to a greater overlap in the fermionic DOFs between the initial and the final configuration for $J_i = J_f$. Whereas, the overlap is smaller for the presented quenches in Fig. 6.4 with $J_i = 0$, where in the initial preparation no correlations with the fermionic DOFs are present.

We now change the type of the bath and present the decay of the spin polarisation $\langle S_z(t)\rangle$ for an ohmic bath ($s = 1$) in Fig. 6.6. The figure is organised similar to Fig. 6.2 to make them more easily comparable. In Fig. 6.6(a) the impurity is time-independently bosonic coupled ($g_i = g_f$), whereas in Fig. 6.6(b) the spin is initially decoupled. The critical bosonic coupling is $g_c(s = 1, J_f\rho_0 = 0.05) = 1.5(0)$. As shown for the equilibrium properties in Fig. 6.1, the crossover energy scale $T^\star(g)$ is larger for $s = 1$ than for $s = 0.6$. We augment the corresponding time scale $t^\star$ in Fig. 6.6. Since the bosonic correlations are also present in the initial configuration in Fig. 6.6(a) and the bosonic coupling is large, the decay of the polarisation is nearly completely suppressed, if we quench in the L phase ($g_f > g_c$). Otherwise, if we quench in the SSC phase ($g_f < g_c$), the polarisation decays to a g_f-independent steady-state value. The decay is more strongly slowed down with increasing g_f. Furthermore, the change in the bath expo-

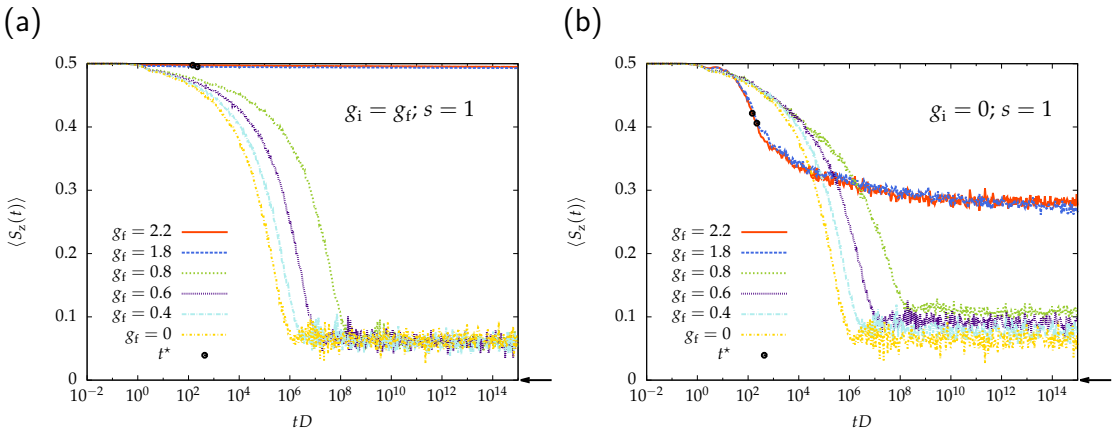

Figure 6.6: Real-time spin polarisation $\langle S_z(t)\rangle$ for an initially ($\epsilon_i\rho_0 = -0.5$) polarised spin for a ohmic bosonic bath ($s = 1$). In (a) the spin is constantly bosonic-coupled ($g_i = g_f$) and in (b) it is initially decoupled. For times $t > 0$ the magnetic field is switched off and the fermionic (and the bosonic) coupling is switched on: $J_f\rho_0 = 0.05$. The critical coupling is $g_c(s = 1, J_f\rho_0 = 0.05) = 1.5(0)$. The data has been obtained for the finite temperature $T/D \sim 3 \cdot 10^{-16}$.

nent s is balanced by an increased coupling strength g_f so that the Kondo temperatures, which drive the dynamics, are similar for the quenches presented here to those of the corresponding quenches in the sub-ohmic bath. On the other hand, for the initially decoupled impurity in Fig. 6.6(b), the correlations are built up dynamically and the time scale $t^\star$ indicates a time interval $10^{-1} < t/t^\star < 10^1$, in which the polarisation is decreased strongly. Since for the ohmic bath $t^\star \ll t_K = 1/T_K$, the decays for the quenches in the L phase are faster than those for the quenches in the SSC phase. For the former quenches the polarisation deviates more strongly from thermal equilibrium than for the latter ones, as already discussed for the sub-ohmic bath.

6.4 Conclusion

In this chapter we have analysed the relaxation of a polarised impurity spin due to spin-flip scattering processes with surrounding conduction band electrons under the additional influence of a bosonic bath. The decay of the polarisation $\langle S_z(t)\rangle$ undergoes an exponentially increasing slowdown with an increasing coupling g_f to the bosonic bath. All our data reveal a steady state for long times which deviates systematically from the thermal equilibrium, even for quenches in the SSC phase. This may be an artefact of the TD-NRG and remains an open question.

After the quench the system emerges two stable phases: the SSC phase with a crossover energy scale T_K and the L phase with the crossover energy scale $T^\star$. We have shown that for an initially decoupled impurity spin, the dynamical build-up of correlations

is tracked by these crossover temperatures and hence, we used them to reveal characteristic time scales. For quenches in the SSC phase, the dynamics for times $tT_K > 1$ is universal. The Kondo temperature reflects the boson-induced retardation leading to an intersection of different strong quenches at $\langle S_z(tT_K)\rangle = 1/4$. We have scaled these dynamics with $f(t/t_{co})$ and have extracted the crossover time scale t_{co}. For quenches in the SSC phase initial bosonic correlations ($g_i = g_f$) lead to larger crossover time scales t_{co} revealing a stronger retardation compared to an initially bosonic-decoupled impurity spin. Furthermore, with increasing bosonic coupling g_f the retardation and hence, t_{co} increases exponentially.

For quenches in the L phase, the polarisation changes most strongly in the time interval $10^{-1} < tT^\star < 10^1$, if the impurity spin is initially bosonic-decoupled. In contrast, for an initially bosonic-coupled ($g_i = g_f$) impurity spin, the relaxation of the polarisation occurs on shorter time scales, since the correlations with the bosonic DOFs are already present in the initial configuration at $t = 0$. The different initial preparations ($g_i = 0$ or $g_i = g_f$) yield different outcomes in the dynamics and in the steady state. The steady state deviates stronger from its thermal equilibrium if the bosonic coupling is already present in the initial preparation. Hence, for the same final conditions the initial preparation of the system has a profound impact on the dynamics and the long-time behaviour for quenches in the L phase. Whereas, for quenches in the SSC phase the dynamics is slowed down but the steady state is only slightly affected by the initial bosonic configuration: The steady-state value is independent of g_f for a time-independent bosonic coupling ($g_i = g_f$), whereas, it shows a slight g_f dependence for an initially bosonic-decoupled ($g_i = 0$) impurity spin, because the correlations are built up dynamically.

For an ohmic bosonic bath we have revealed the same functional dependences of the dynamics and the steady state on the bosonic coupling, as stated above for the sub-ohmic bath. Since for an ohmic bath, the crossover to the L FP occurs at higher temperatures, the dynamics for quenches in the L phase are faster because $t^\star(s = 1, g) \ll t^\star(s = 0.6, g)$.

Chapter 7

Summary

In this thesis we have investigated the real-time dynamics of QISs in which the impurity is coupled either only to a fermionic environment or in addition to a continuum of bosonic DOFs.

In Chap. 4 we have used the SIAM to analyse the dynamics which is only driven by the fermionic environment. In equilibrium the QPT between the SSC and LM phase is tuned by the ratio U/Γ_0. The formation of the effective local moment, which decouples from the rest of the system in the LM FP, is tracked by a crossover energy scale $T^\star$. This can be interpreted as a characteristic spatial extension $\xi^\star \propto 1/T^\star$ of the effective local moment. With increasing Coulomb repulsion the effective moment is more strongly localised to the impurity revealing a stronger suppression of the local double occupancy. The spatial extension is accurately described by the NRG leading to a continuous decrease of the double occupancy over the QCP. Whereas, the description of the LM phase by the Gutzwiller ansatz assumes a vanishing of the double occupancy at the QCP and, therefore, overestimates the critical $U_c(\Gamma_0)$. This corresponds to an effective local moment formation only on the impurity site.
We have performed different quenches within one phase and over the QCP and have presented the real-time dynamics of the local double occupancy $\langle D(t)\rangle$. For interaction quenches we have found a universal behaviour of the double occupancy for quenches within the SSC phase. Quenching from the SSC FP over the QCP into the LM phase leads to a damped oscillatory behaviour in $\langle D(t)\rangle$. Since the effective local moment decouples from the system, the relaxation of the double occupancy to its thermal equilibrium is more strongly suppressed with increasing localisation of the effective moment for interaction quenches. In absence of ph symmetry, the dynamics starting from the ASC FP thermalise nicely within the ASC phase, but not if the quench starts from the ph-symmetric SSC FP due to shortcomings in the TD-NRG.
For hybridisation quenches we start at $t = 0$ from a strongly localised effective moment, which gets spatially more extended with increasing hybridisation strength as

long as $\Gamma_f < \Gamma_c(U)$. The double occupancy does not thermalise for quenches within the LM phase. The deviation between its steady-state value and its thermal value increases with the more extended effective local moment because the overlap between the initial and the final ground state is reduced, leading to an increasing non-decaying fraction. While the double occupancy does not thermalise, the hybridisation energy, which couples to the whole bath continuum, thermalises fast even before long-time correlations can be formed. Furthermore, we have demonstrated that the time-dependent Gutzwiller approach is unsuitable for addressing the real-time dynamics in such a system: The approach can only describe the formation of a decoupling local moment on the impurity and, consequently, it overestimates the critical value of U, leading to a strongly oscillating dynamics in the LM phase. While the accurate TD-NRG reveals that the dynamics is driven by the charge-fluctuation scale Γ_f, in the time-dependent Gutzwiller approach the local dynamics evolves only for times $t > \Gamma_f$. Beside this, we have validated our results for the hybridisation quenches by a perturbation-theory calculation which becomes exact in the limit $t \to 0$ and we have revealed that the short-time behaviour is proportional to $1/\sqrt{\Gamma_f D}$ and independent of the Coulomb repulsion.

We have extended the BF-NRG to non-equilibrium using the TD-NRG and have studied the real-time dynamics in the BFAM in Chap. 5 for different quenches. In equilibrium the additional coupling to the bosonic bath leads to a renormalisation of the Coulomb repulsion $U \to U_{\text{ren}} < U$ and, consequently, to an increasing double occupancy. The renormalised Coulomb repulsion $U_{\text{ren}}(g)$ in the BFAM is estimated from an effective SIAM with the same r and Γ_0. In the SIAM we vary over U and on the condition that both models have the same equilibrium double occupancy, we identify $U_{\text{ren}}(g) = U$. The SSC FP is unique and the spin-Kondo (charge-Kondo) subspace can only be indirectly identified by the double occupancy $\langle D \rangle_{\text{eq}} \lesssim (\gtrsim) 1/4$. The QPT from the SSC phase to the LM phase is similar to the QPT from the SSC phase to the L phase leading to a decoupling effective local moment in the former case and an effective charge moment in the latter case. At the BFCR FP, which separates the SSC and L phase, the critical exponents show hyperscaling and three different types (F/M/B) of quantum criticality with respect to the bath exponent combination (r, s) are known.
For F-type bath exponents we have verified that the real-time dynamics of $\langle D(t) \rangle$ in the full BFAM can completely be reproduced in an effective SIAM with thoughtfully adjusted parameters for the same fermionic bath exponent r. The crossover time scale t_{co} for quenches within the LM and L phase decreases the stronger the decoupling effective moment is localised on the impurity. Also for quenches over one or both QCPs, the crossover time scale t_{co} shows the same functional dependence for the same final phase. Since in the LM and L phase an effective moment decouples from the system, no thermalisation occurs for quenches into these phases. The deviation between the steady-state value and the thermal value increases the more localised the decoupled moment is. Furthermore, we have emphasised that the LM and L phase are mirror

images of each other. Quenches from the SSC FP into both phases collapse under the scaling function $f(t)$ for the same $|U_{\mathrm{ren}}|$ on one curve. Also for quenches from both phases into the SSC phase the curves collapse supporting the mirror-image statement. For the B-type bath exponents the low-energy modes of the bosonic bath drive the dynamics, and at intermediate times the dynamics in the BFAM differ from those in the effective SIAM. The bosonic DOFs yield a retardation, since the renormalisation of U is built up through the NRG at lower energies, and hence, needs some time to influence the dynamics. Whereas, in the SIAM the Coulomb repulsion is effective directly with its full strength at $t = 0$.
Furthermore, we have examined the effect of a strongly ph-symmetric-broken initial condition on the real-time dynamics of the level occupancy. After quenching, the system evolves under the influence of the ph-symmetric SSC and L FP. While for short times $t\Gamma_0 < 1$ the dynamics is universal, the additionally coupled bosonic DOFs yield an increasing slowdown in the dynamics with an increasing coupling. We have demonstrated that the quenches into the SSC phase thermalise within the accuracy of the TD-NRG which we checked with the continuum limit $\Lambda \to 1^+$. Whereas, those into the L phase equilibrate to a steady-state value which deviates more strongly from the thermal value the more localised the decoupling charge moment is. If the system is initially decoupled from the bosonic bath ($g_{\mathrm{i}} = 0$), this deviation is smaller, since the correlations to the bosonic continuum are built up dynamically.

In context of the BFKM we have investigated the real-time polarisation $\langle S_z(t)\rangle$ of an initially polarised spin in Chap. 6. The decay in $\langle S_z(t)\rangle$ is driven by spin-flip processes with the surrounding conduction band electron spins. The decay is additionally slowed down by the coupled bosonic bath, leading to a suppression of the decay for quenches in the L phase. The crossover energy scales T_{K} and $T^\star$ reflect the build-up of correlations for the SSC and the L FP, respectively. If the dynamics is driven by the SSC FP, an increasing bosonic coupling yields an increasing retardation in the decay leading to an exponentially increasing crossover time scale t_{co}. Furthermore, the Kondo temperature T_{K} is g dependent and reflects the induced retardation, so that for times $tT_{\mathrm{K}} > 1$ the dynamics is universal. The initial preparation of the system affects the dynamics for quenches in the SSC phase: For an initially bosonic-decoupled ($g_{\mathrm{i}} = 0$) impurity spin $t_{\mathrm{co}}(g_{\mathrm{f}})$ is smaller than for an time-independently coupled ($g_{\mathrm{i}} = g_{\mathrm{f}}$) impurity spin, where the initially present bosonic correlations have to be reduced dynamically in addition. Under the influence of the L FP, the decay of an initially polarised, decoupled impurity spin is driven by the time scale $t^\star = 1/T^\star$. The polarisation changes most strongly in the time interval $10^{-1} < tT^\star < 10^1$. The initial preparation of the system, whether it is initially decoupled ($g_{\mathrm{i}} = 0$) or time-independently coupled ($g_{\mathrm{i}} = g_{\mathrm{f}}$), has a profound impact on the dynamics for quenches in the L phase, as well. In the latter case the bosonic correlations are already present at time $t = 0$ leading to an almost complete suppression of the decay. Furthermore, for an increasing bosonic bath expo-

nent s the dynamics in the L phase is speeded up and occurs at shorter time scales, i.e. $t^\star(s = 1, g) \ll t^\star(s = 0.6, g)$. Whereas under the influence of the SSC FP, the Kondo temperature T_K drives the dynamics and the change in s can be balanced by an adjusted bosonic coupling revealing the same T_K.

Appendix A

Notes on Kondo models

A.1 Relation between the SIAM and the KM

As mentioned in Sec. 2.3.1 the particle-hole (ph) symmetry in the SIAM is controlled by the impurity states. If $U = -2\epsilon_d$, ph symmetry is preserved and the full symmetry of the SIAM is $SU(2)_{spin} \times SU(2)_{charge}$. The two SU(2) symmetries are related to pseudo-spins consisting of the degenerated spin doublet $|\uparrow\rangle$, $|\downarrow\rangle$ and the degenerated charge doublet $|0\rangle$, $|\uparrow\downarrow\rangle$, respectively.
Different symmetry transformations to the model are applicable [118]. To exchange particles and holes we use the transformation

$$d_\sigma \to d_\sigma^\dagger \quad \text{and} \quad c_{\epsilon,\sigma} \to c_{\epsilon,\sigma}^\dagger \quad . \tag{A.1}$$

Therefore, the states $|\uparrow\rangle$ and $|\downarrow\rangle$ get interchanged, as well as the states $|0\rangle$ and $|\uparrow\downarrow\rangle$. Another way to achieve the same, is to simply change $\epsilon_d \to -(\epsilon_d + U)$ and $V_k \to -V_k$. More interesting is the interchange of the two SU(2) symmetries via

$$d_\uparrow \to d_\uparrow \quad , \quad d_\downarrow \to d_\downarrow^\dagger \quad , \quad c_{\epsilon,\uparrow} \to c_{\epsilon,\uparrow} \quad \text{and} \quad c_{\epsilon,\downarrow} \to c_{\epsilon,\downarrow}^\dagger \quad . \tag{A.2}$$

This transforms $|\uparrow\rangle \leftrightarrow |\uparrow\downarrow\rangle$ and $|\downarrow\rangle \leftrightarrow |0\rangle$. Consequently, the spin doublet and the charge doublet are interchanged.

The KM can now be understood as a limiting case of the SIAM. In the case that the single-occupied states are favoured over the zero- and double-occupied state, namely for

$$-\epsilon_d,\ U + \epsilon_d \ \gg \ \Gamma_0,\ k_B T \quad , \tag{A.3}$$

only a pure spin DOF remains on the impurity in the zero-temperature limit. This is essentially the KM. Via a SWT [67] the standard KM with its Hamiltonian in Eq. (1.3)

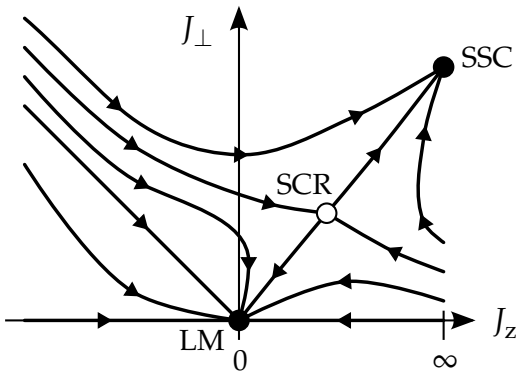

Figure A.1: Flow of the coupling constants J_z and $J_\perp$ for the ph-symmetric KM with the bath exponent $0 < r < 1/2$. (Un)Filled circles are (un)stable FPs. After [81].

can be obtained. The Kondo coupling J is related to the parameters of the SIAM through

$$J = 2V_0^2 \left(\frac{1}{|\epsilon_d|} + \frac{1}{|U + \epsilon_d|} \right) \quad . \tag{A.4}$$

Here, ph symmetry is maintained and we use a pg-DOS. If we express the KM by its anisotropic Hamiltonian in Eq. (1.6), with the spin polarisation term J_z and the spin-flip term $J_\perp$, we can make some comments on the RG flow concerning both parameters. For the metallic case ($r = 0$) we gain the flow which has already been presented in Fig. 1.2. For $0 < r < 1/2$ the KM exhibits a QPT between the LM and SC phase with the previously stated SCR FP in the context of the SIAM. In Fig. A.1 the RG flow for this case is shown.

For ph asymmetry an additional potential scattering term

$$H_{PS} = V \sum_{k,k',\sigma} c^\dagger_{k,\sigma} c_{k',\sigma} \tag{A.5}$$

is produced by the SWT with the coefficient

$$V = \frac{V_0^2}{2} \left(\frac{1}{|\epsilon_d|} - \frac{1}{|U + \epsilon_d|} \right) \quad . \tag{A.6}$$

With the help of the two parameters J and V we can describe the RG flow of the KM. As NRG calculations have established, the low-energy properties of the KM and the SIAM are identical [25]. Therefore, the FPs are the same and we can refer to their classification presented in Sec. 2.3.1. In Fig. A.2 we summarise the RG flow for the three regimes (a) $0 < r < r^*$, (b) $r^* \leq r < 1/2$ and (c) $1/2 \leq r$. We have already introduced these regimes in the context of the ph-asymmetric SIAM with $r^* \sim 0.375$. As the flow for the metallic case ($r = 0$) is simply towards the SSC FP for $V = 0$ and towards the ASC FP for $V > 0$, we forgo to draw an extra diagram here. In the regime

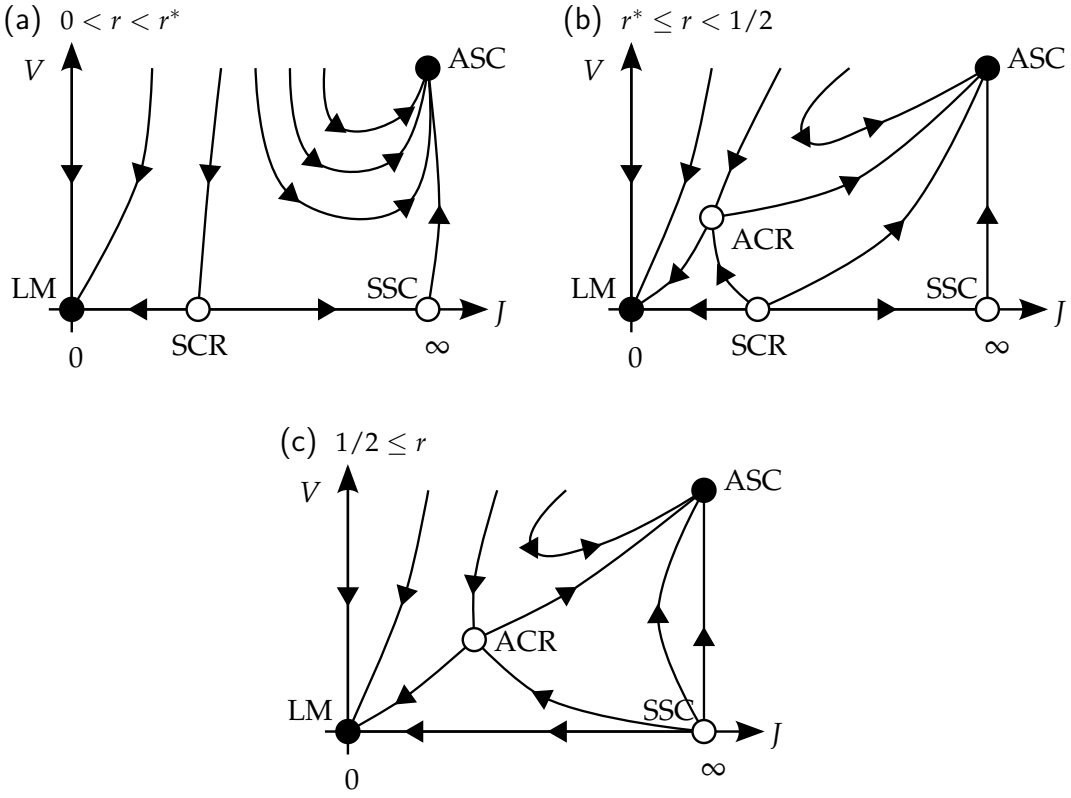

Figure A.2: RG flow for the KM with a pg-DOS. The plane is spanned by the Kondo coupling J and the potential scattering V. The figure is subdivided into three regimes: (a) $0 < r < r^*$, (b) $r^* \leq r < 1/2$ and (c) $1/2 \leq r$. (Un)Filled circles are (un)stable FPs. After [25].

$0 < r < r^*$, in Fig. A.2(a), and in presence of ph symmetry ($V = 0$) the unstable SCR FP separates the flow towards the LM FP from the flow towards the SSC FP. The former one describes a free impurity spin while for the latter one the impurity spin is screened by the conduction band. Due to the pg-DOS a residual spin moment $\mu_{\text{eff}}^2 = r/8$ remains unscreened. In presence of the potential scattering $V > 0$ the ph symmetry is broken and the flow is either towards the LM or towards the ASC FP. There is a dividing line for finite V which joins the SCR FP at $V = 0$. On the one side, for $J < J_c$, the flow is towards the LM FP, which is stable regarding ph asymmetry. On the other side, for $J_c < J$, the flow is towards the ASC FP. Consequently, the SSC FP is only reached for strict ph symmetry.

In the second regime $r^* \leq r < 1/2$, in Fig. A.2(b), above the specific r^* the ACR FP emerges in the plane at finite V. The ACR FP at the critical coupling $J_c' < J_c$ reflects that for $J_c' < J < J_c$ the ph symmetry cannot be restored by reaching the LM FP. Instead the flow is towards the ASC FP. Only for $J < J_c'$ the flow is towards the LM FP. For $r \to 1/2$ the SCR FP merges into the SSC FP. Hence, for the regime $1/2 \leq r$, in Fig. A.2(c), in presence of ph symmetry the flow is simply towards the LM FP, while

in absence of it the flow is towards the LM FP for $J < J_c{}'$ and towards the ASC FP for $J_c{}' < J$.

A.1.1 Charge-Kondo regime

By the condition in Eq. (A.3), we have related the SIAM to the KM with a SU(2) impurity spin which contains the spinful states of the SIAM. Therefore, the standard KM is a spin-type KM.

If we instead favour the zero- and double-occupied impurity state over the single-occupied states, e.g. by a strong attractive Coulomb interaction,

$$-U,\ -U-\epsilon_d \ \gg\ \Gamma_0,\ k_B T \quad , \tag{A.7}$$

only the chargeful impurity states remain in the zero-temperature limit. This leads to a KM consisting of a SU(2) impurity spin containing the chargeful zero- and double-occupied state. Hence, we call the model with a prime: KM′, the charge-type KM. For the KM′ the FP spectrum and the RG flow diagrams are identical to the ones of the KM presented above, if we replace the LM FP of the KM by the LM′ FP for the KM′ since the free moment consists of the two chargeful states.

A.2 Criticality in the BFKM

Since both limiting models of the BFKM, the SBM and the KM, exhibit a QPT under certain parameters, these QPTs have to occur in the combined model as well. In order to discuss the FPs and the RG flow of the BFKM we have to set some restrictions: (I) We omit the potential scattering term and, hence, maintain ph symmetry. Therefore, the limiting KM contains only the LM, SSC and SCR FP, depending on the specific choice of r. (II) We use a sub-ohmic bosonic bath exponent, $0 < s \leq 1$, so that a QPT due to localisation may take place. If no local magnetic field is applied ($\Delta = \epsilon = 0$), the limiting SBM is in the L FP for all $g > 0$.

The RG flow of the BFKM, under the restrictions stated above, is given in Fig. A.3. The horizontal axis represents the limiting SBM with the bosonic coupling g, whereas the vertical axis represents the limiting KM with the Kondo coupling J.
If we use a constant DOS, in Fig. A.3(a), the LM FP of the free impurity spin is unstable as $J, g > 0$. Either the flow is towards the SSC FP for $J > 0, g = 0$ or towards the L FP for $J = 0, g > 0$. If both couplings are switched on, there is a competition between the Kondo screening due to the fermionic bath and the localisation due to the bosonic bath. Indeed, between both stable FPs, a new unstable BFCR FP emerges and separates the flow towards both FPs.

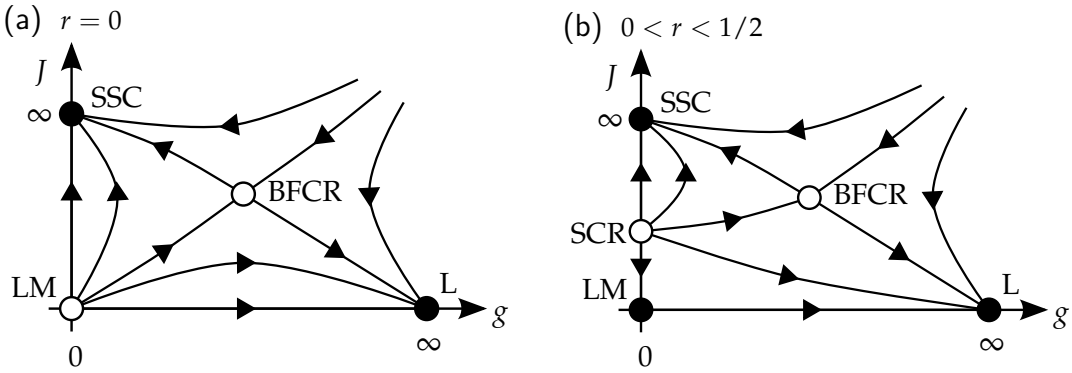

Figure A.3: RG flow for the ph-symmetric BFKM with a pg-DOS. The plane is spanned by the Kondo coupling J and bosonic coupling g. While the bosonic bath exponent is in the sub-ohmic range $0 < s < 1$, we distinguish the fermionic bath exponent in (a) $r = 0$ and (b) $0 < r < 1/2$. (Un)Filled circles are (un)stable FPs. After [55, 81, 159].

For a pg-DOS with $0 < r < 1/2$, in Fig. A.3(b), the LM FP becomes stable for $g = 0$ and the SCR FP emerges on the vertical axis at J_c. It separates the flow towards the LM and SSC FP, which we already know from the limiting KM. The SCR FP merges with the LM FP for $r \to 0^+$. Anyway, the LM FP is still unstable regarding the bosonic coupling. Therefore, for any $g > 0$ and $J < J_c$, the flow is towards the L FP. While the BFCR FP emerges due to the competition between the Kondo screening and the localisation, the critical coupling $J_{c,\mathrm{BFCR}} > J_{c,\mathrm{SCR}}$ of the BFCR FP has to be greater than the one of the SCR FP.

The energy spectrum of the FPs naturally contains purely fermionic energies, purely bosonic energies and linear combinations of them, cf. Sec. 3.2.2 and Ref. [55]. For the fermionic FPs, the LM and SSC FP, the bosonic coupling g is renormalised to zero and the bosonic energies are the energies of a free bosonic bath. For the L FP the bosonic energies are identical to the energies in the L FP in the SBM with the same exponent s. While the Kondo coupling term in Eq. (1.33) is SU(2) symmetric, the bosonic coupling term breaks the spin rotational invariance. Therefore, the fermionic energies correspond to an anisotropic KM with a renormalised $J_\perp$ to zero and a finite J_z for $g > g_c$. Furthermore, J_z diverges for $g \to {g_c}^+$: $J_z \propto (g - g_c)^{-\beta}$.

Appendix B

Critical exponents

Now we want to derive the critical exponents and the hyperscaling relations between them. For simplicity we only take into account a local magnetic field $H_{\mathrm{lf}} = \xi S_{z,d}$, but for a local electrical potential it is straight forward to derive the same behaviour.

We start with a scaling ansatz [61]

$$F_{\mathrm{imp}} = T\, f\left(tT^{-a}, \xi T^{-b}\right) \tag{B.1}$$

for the impurity contribution of the free energy. It depends on the local magnetic field ξ, the dimensionless measure $t = (r - r_{\mathrm{c}})/r_{\mathrm{c}}$ of the distance to criticality, $a = 1/\nu$ and $b = (1+x)/2$. Here, ν is the correlation-length exponent which describes the vanishing of the temperature scale $T^* \propto |t|^{\nu}$ bounding the quantum critical region in which the critical behaviour is observed. With the local magnetisation m_{loc} in Eq. (2.10) and the corresponding susceptibility $\chi_{\mathrm{s,loc}}$ in Eq. (2.11) the critical exponents are defined [61] by

$$m_{\mathrm{loc}}(t < 0, \xi \to 0, T = 0) \propto (-t)^{\beta} \quad , \tag{B.2a}$$

$$m_{\mathrm{loc}}(t = 0, T = 0) \propto |\xi|^{-\frac{1}{\delta}} \quad , \tag{B.2b}$$

$$\chi_{\mathrm{s,loc}}(t = 0, T) \propto T^{-x} \quad \text{and} \tag{B.2c}$$

$$\chi_{\mathrm{s,loc}}(t > 0, T = 0) \propto t^{-\gamma} \quad . \tag{B.2d}$$

To connect the critical exponents β, δ, x and γ to the scaling parameters a and b we have to work on the scaling ansatz. The free energy F is near the QCP a generalised homogeneous function in the temperature $T > 0$ and, therefore, the scaling function f can be re-written [178] to

$$f\left(tT^{-a}, \xi T^{-b}\right) = T^{-d} f(t, \xi) \tag{B.3}$$

with the dimension $d = 1$ for the Wilson chain concept. If we take the partial derivative with respect to ξ on both sides we gain

$$T^{-b}\frac{\partial}{\partial\xi}f\left(tT^{-a},\xi T^{-b}\right) = T^{-1}\frac{\partial}{\partial\xi}f(t,\xi) \quad . \tag{B.4}$$

Multiplying both sides with the temperature T and recognising $m_{\mathrm{loc}} = -T\frac{\partial f}{\partial\xi}$ leads to

$$T^{-b}m_{\mathrm{loc}}\left(tT^{-a},\xi T^{-b}\right) = T^{-1}m_{\mathrm{loc}}(t,\xi) \quad . \tag{B.5}$$

To reveal the scaling according to the exponent β, we set $\xi = 0$ and $T = (-t)^{1/a} > 0$, then,

$$(-t)^{-\frac{b}{a}}m_{\mathrm{loc}}(-1,0) = (-t)^{-\frac{1}{a}}m_{\mathrm{loc}}(-t,0) \tag{B.6}$$

$$\Leftrightarrow \qquad m_{\mathrm{loc}}(-t,0) = (-t)^{\frac{1-b}{a}}m_{\mathrm{loc}}(-1,0) \tag{B.7}$$

the scaling of m_{loc} with the exponent $\beta = (1-b)/a$ is revealed. Similarly, by setting $t = 0$ and $T = \xi^{1/b}$ we gain

$$m_{\mathrm{loc}}(0,\xi) = \xi^{\frac{1-b}{b}}m_{\mathrm{loc}}(0,1) \tag{B.8}$$

and reveal the exponent $\delta = b/(b-1)$. The other exponents are straight forward to calculate over the corresponding second derivative and lead to $x = 2b-1$ and $\gamma = (2b-1)/a$.

Inserting the exponent relations into each other we finally achieve the hyperscaling relations

$$\gamma = \nu x \quad , \quad \delta = \frac{1+x}{1-x} \quad \text{and} \quad \beta = \frac{\nu(1-x)}{2} \quad . \tag{B.9}$$

Such hyperscaling indicates that the QCP is interacting [61]. This is, for example, found for the QCP between the screened and the unscreened phase in the pg-KM [111]. If we use a local electrical potential ϕ, instead of the local magnetisation ξ, the QCP between the localised and the delocalised phase in the BFAM (with a constant fermionic DOS) is revealed to be interacting, as well. For this QCP the exponent x is equivalent to the bosonic bath exponent s [56].

B.1 Critical exponents in the KM and the SIAM

As NRG calculations have established, the low-energy properties of the KM and the SIAM are identical [25]. Therefore, the FPs are the same and we can refer here to the

simplier KM with a pg-DOS in the range $0 < r < 1$. The exponents of the SCR and ASC FP in the context of the KM are investigated with the NRG in Ref. [111].

For a local magnetic field h at the impurity site, the local magnetisation $m_{\mathrm{loc}} = \langle S_{\mathrm{z,d}} \rangle$ obeys via

$$m_{\mathrm{loc}}(J < J_{\mathrm{c}}, h = 0, T = 0) \propto (J - J_{\mathrm{c}})^{\beta} \quad \text{and} \tag{B.10}$$

$$m_{\mathrm{loc}}(J = J_{\mathrm{c}}, T = 0) \propto |h|^{-\frac{1}{\delta}} \tag{B.11}$$

to the exponents β and δ.

It is pointed out in Ref. [111] that in the full range $0 < r < 1$ for both FPs hyperscaling relations according to Eq. (B.9) are fulfilled. It is interesting to note, that in the range $r^* < r < 1/2$ the SCR and ACR FP have different exponents but for each FP the set of exponents obey separately the hyperscaling relations. Anyway, within this regime there is no easy dependence of the exponents β and δ on the bath exponent r. Furthermore, whereas for $r < 1$ the exponents take non-trivial r-dependent values and obey to hyperscaling, the exponents are trivial for $r > 1$ and hyperscaling is violated [25, 111]. These findings suggest to identify $r = 1$ as upper-critical dimension of the problem, whereas $r = 0$ plays the role of a lower-critical dimension [118].

B.2 Critical exponents in the SBM

In the SBM the QPT occurs between a D and L phase. To describe the properties of the QPT for the sub-ohmic regime $0 \leq s < 1$ in more detail, we exemplary look at the local magnetisation $m_{\mathrm{loc}} = \langle S_{\mathrm{z,d}} \rangle$. It is connected via

$$m_{\mathrm{loc}}(g > g_{\mathrm{c}}, \epsilon = 0, T = 0) \propto (g - g_{\mathrm{c}})^{\beta} \quad \text{and} \tag{B.12}$$

$$m_{\mathrm{loc}}(g = g_{\mathrm{c}}, T = 0) \propto |\epsilon|^{-\frac{1}{\delta}} \tag{B.13}$$

to the exponents β and δ.

In the last years there has been a discussion about the values these critical exponents take in the sub-ohmic regime. For the case $1/2 < s < 1$ all agreed that they obey hyperscaling relations. Nevertheless, for $0 < s < 1/2$ there are two competing opinions. One group claims that in this regime the exponents take mean-field values: $\beta = 1/2$ and $\delta = 3$. It is argued that by quantum-to-classical mapping [81] the SBM is mapped to the one-dimensional Ising model with long-range interactions $J_{i,j} = J/|i - j|^{1+s}$. While this Ising model obeys mean-field exponents [179–181], the SBM shell obey them as well. The other group claims that the hyperscaling relations of the exponents hold for the full sub-ohmic regime with $\beta = (1 - s)/(2s)$ and $\delta = (1 + s)/(1 - s)$ and that

mean-field behaviour is not observed. Consequently, the quantum-to-classical mapping fails in their point of view for $0 < s < 1/2$.
Although the first publication [182] which claimed hyperscaling relations of the exponents has been withdrawn [183] by the authors and detailed explanations why the NRG fails to reproduce the correct mean-field values has been presented in Refs. [172, 184], there are still claims that the NRG works correctly and quantum-to-classical mapping fails [185, 186]. Anyway, the consensus which is reached within the past years is that the critical exponents obey to mean-field behaviour for $0 < s < 1/2$ and show hyperscaling for $1/2 < s < 1$. This is also supported by quantum Monte Carlo (QMC) [187], exact diagonalisation (ED) [188] and DMRG [189] studies.
It is pointed out in Ref. [172] that two errors are responsible for the not reproduction of the quantum-to-classical mapping with the NRG: (i) the truncation of the bosonic Hilbert space [190, 191] and (ii) the mass-flow error [172, 184]. The interplay between those two independent errors leads to a hyperscaling of the critical exponents. Since we only treat the BF-QIS in the range $1/2 < s < 1$, we do not go into the details of these errors.

B.3 Critical exponents in the BFAM

The QPT at g_c, namely at the BFCR FP, is of great interest. While the limiting models of the BFAM enable QPTs with hyperscaling exponents, it is an interesting question what the fermionic and bosonic influence on the QPT is like.
In the following we focus on the exponent x belonging to the local spin susceptibility

$$\chi_{s,\mathrm{loc}}(g = g_c, T) \propto T^{-x} \quad . \tag{B.14}$$

For the limiting models of the BFAM, the critical exponents have been investigated in detail. With $x_F(r)$ we refer to the exponent x of the SIAM, where the SCR FP has been analysed. Numerical values for $x_F(r)$ in dependence of the fermionic bath exponent $0 < r < 1/2$ are given in Ref. [111]. With $x_B(s)$ we refer to the exponent x of the SBM [90]. For the QCP between the D and L FP the exponent x is identical to the bosonic bath exponent s: $x_B = s$ for $1/2 < s < 1$. Furthermore, for both limiting models the exponents obey to hyperscaling relations and, thus, indicate an interacting QCP.
For the BFAM the investigation of the BFCR FP at g_c has been done with continuous-time quantum Monte Carlo (CT-QMC) and NRG techniques in Ref. [57]. There, the authors identify three types of quantum criticality:

F For the fermionic type, the critical exponents are identical to those of the purely fermionic SIAM with the same r: $x(r,s) = x_F(r)$.

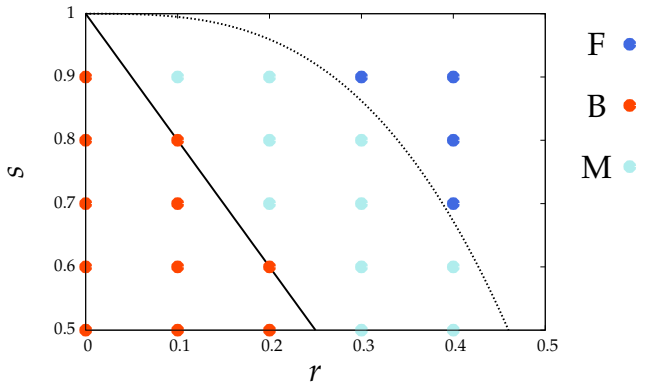

Figure B.1: Exponent types of the BFAM in dependence of the bath exponents r and s. Black boundaries are explained in the text. Taken from [57].

B For the bosonic type, the critical exponents are identical to those of the purely bosonic SBM with the same s: $x(r,s) = x_{\mathrm{B}}(s)$

M For the mixed type, the critical exponents satisfy $x(r,s) = x_{\mathrm{B}}$, but the order-parameter correlation-length exponent, cf. Sec. 2.1, lies between the values for the SBM and the SIAM: $\nu_{\mathrm{F}}^{-1}(r) < \nu^{-1}(r,s) < \nu_{\mathrm{B}}^{-1}(s)$.

If $x_{\mathrm{B}}(s) < x_{\mathrm{F}}(r)$ the bosonic bath should dominate the singular part of the spin response. Otherwise, for $x_{\mathrm{B}}(s) > x_{\mathrm{F}}(r)$ one should find fermion-dominated spin dynamics [55].

Astonishingly, the critical exponent x for the BFAM is simply the smaller of the exponents of the limiting models:

$$x(r,s) = \min(x_{\mathrm{F}}(r), x_{\mathrm{B}}(s)) \quad . \tag{B.15}$$

Furthermore, for all combinations (r,s) in $0 < r < 1/2$ and $1/2 < s < 1$ the critical exponents obey hyperscaling relations.

In Fig. B.1 we show the type of the quantum criticality for combinations (r,s) in the ranges $0 < r < 1/2$ and $1/2 < s < 1$. The three types are separated by two boundaries. The solid boundary, $s = 1 - 2r$, marks the line of equality of the frequency exponents of the bare bosonic propagator and the fermionic ph bubble [57]. The dashed boundary[23] is related to Eq. (B.15) and marks the line of equal exponents $x(r,s) = x_{\mathrm{B}}(s) = s = x_{\mathrm{F}}(r)$.

[23] To draw the dashed boundary in Fig. B.1 a regression function $f(x) = 1 - ax^b$ has been adjusted to the data of $x_{\mathrm{F}}(r)$ in Ref. [111].

Bibliography

[1] Stewart, G. R.: Heavy-fermion systems. In: *Rev. Mod. Phys.* 56 (1984), p. 755–787. doi: 10.1103/RevModPhys.56.755

[2] Cyrot, M. ; Pavuna, D.: *Introduction to Superconductivity and High-Tc Materials*. World Scientific, 1992. – ISBN 9789810201449

[3] Einstein, Albert: Quantentheorie des einatomigen idealen Gases – Zweite Abhandlung. In: *Sitzungsberichte der preussischen Akademie der Wissenschaften* Volume 1, 1925, p. 3–10. – http://www.lorentz.leidenuniv.nl/history/Einstein_archive/Einstein_1925_publication/index.html

[4] Pitaevskii, L.P. ; Stringari, S.: *Bose-Einstein Condensation*. Clarendon Press, 2003 (International Series of Monographs on Physics). – ISBN 9780198507192

[5] Onnes, H K.: Further experiments with liquid helium. In: *Proceedings of the KNAW* Volume 13, http://www.dwc.knaw.nl/DL/publications/PU00013343.pdf, 1911, p. 1910–1911

[6] Osheroff, D. D. ; Richardson, R. C. ; Lee, D. M.: Evidence for a New Phase of Solid He^3. In: *Phys. Rev. Lett.* 28 (1972), p. 885–888. doi: 10.1103/PhysRevLett.28.885

[7] Nozières, P. ; Schmitt-Rink, S.: Bose condensation in an attractive fermion gas: From weak to strong coupling superconductivity. In: *Journal of Low Temperature Physics* 59 (1985), No. 3-4, p. 195–211. doi: 10.1007/BF00683774. – ISSN 0022-2291

[8] Anderson, M. H. ; Ensher, J. R. ; Matthews, M. R. ; Wieman, C. E. ; Cornell, E. A.: Observation of Bose-Einstein Condensation in a Dilute Atomic Vapor. In: *Science* 269 (1995), No. 5221, p. 198–201. doi: 10.1126/science.269.5221.198

[9] Davis, K. B. ; Mewes, M. O. ; Andrews, M. R. ; Druten, N. J. van ; Durfee, D. S. ; Kurn, D. M. ; Ketterle, W.: Bose-Einstein Condensation in a Gas of Sodium Atoms. In: *Phys. Rev. Lett.* 75 (1995), p. 3969–3973. doi: 10.1103/PhysRevLett.75.3969

[10] Cornell, Eric A. ; Ketterle, Wolfgang ; Wieman, Carl E.: Bose-Einstein Condensation in Alkali Gases. In: *Advanced information on the Nobel Prize in Physics 2001*, http://www.nobelprize.org/nobel_prizes/physics/laureates/2001/advanced.html, 2001

[11] Bloch, Immanuel ; Dalibard, Jean ; Zwerger, Wilhelm: Many-body physics with ultracold gases. In: *Rev. Mod. Phys.* 80 (2008), p. 885–964. doi: 10.1103/RevModPhys.80.885

[12] Onnes, Heike K.: The disappearance of the resistivity of mercury. In: *Comm. Leiden* 122 (1911), p. 2

[13] Reynolds, C. A. ; Serin, B. ; Wright, W. H. ; Nesbitt, L. B.: Superconductivity of Isotopes of Mercury. In: *Phys. Rev.* 78 (1950), p. 487–487. doi: 10.1103/PhysRev.78.487

[14] Bardeen, J. ; Cooper, L. N. ; Schrieffer, J. R.: Theory of Superconductivity. In: *Phys. Rev.* 108 (1957), p. 1175–1204. doi: 10.1103/PhysRev.108.1175

[15] Si, Qimiao ; Steglich, Frank: Heavy Fermions and Quantum Phase Transitions. In: *Science* 329 (2010), No. 5996, p. 1161–1166. doi: 10.1126/science.1191195

[16] Anderson, P. W.: Localized Magnetic States in Metals. In: *Phys. Rev.* 124 (1961), p. 41–53. doi: 10.1103/PhysRev.124.41

[17] Andrei, N. ; Furuya, K. ; Lowenstein, J. H.: Solution of the Kondo problem. In: *Rev. Mod. Phys.* 55 (1983), p. 331–402. doi: 10.1103/RevModPhys.55.331

[18] Hewson, Alexander C.: *The Kondo Problem to Heavy Fermions*. Cambridge University Press, 1993. – ISBN 9780511470752

[19] Wilson, Kenneth G.: The renormalization group: Critical phenomena and the Kondo problem. In: *Rev. Mod. Phys.* 47 (1975), p. 773–840. doi: 10.1103/RevModPhys.47.773

[20] Bulla, Ralf ; Costi, Theo A. ; Pruschke, Thomas: Numerical renormalization group method for quantum impurity systems. In: *Rev. Mod. Phys.* 80 (2008), p. 395–450. doi: 10.1103/RevModPhys.80.395

[21] Withoff, David ; Fradkin, Eduardo: Phase transitions in gapless Fermi systems with magnetic impurities. In: *Phys. Rev. Lett.* 64 (1990), p. 1835–1838. doi: 10.1103/PhysRevLett.64.1835

[22] Kondo, Jun: Resistance Minimum in Dilute Magnetic Alloys. In: *Progress of Theoretical Physics* 32 (1964), No. 1, p. 37–49. doi: 10.1143/PTP.32.37

[23] Chen, Kan ; Jayaprakash, C.: Kondo effect in Fermi systems with a gap: A renormalization-group study. In: *Phys. Rev. B* 57 (1998), p. 5225–5234. doi: 10.1103/PhysRevB.57.5225

[24] Sigrist, Manfred ; Tsunetsuga, Hirokazu ; Ueda, Kazuo: Rigorous results for the one-electron Kondo-lattice model. In: *Phys. Rev. Lett.* 67 (1991), p. 2211–2214. doi: 10.1103/PhysRevLett.67.2211

[25] Gonzalez-Buxton, Carlos ; Ingersent, Kevin: Renormalization-group study of Anderson and Kondo impurities in gapless Fermi systems. In: *Phys. Rev. B* 57 (1998), p. 14254–14293. doi: 10.1103/PhysRevB.57.14254

[26] Castro Neto, A. H. ; Guinea, F. ; Peres, N. M. R. ; Novoselov, K. S. ; Geim, A. K.: The electronic properties of graphene. In: *Rev. Mod. Phys.* 81 (2009), p. 109–162. doi: 10.1103/RevModPhys.81.109

[27] Vojta, M. ; Fritz, L. ; Bulla, R.: Gate-controlled Kondo screening in graphene: Quantum criticality and electron-hole asymmetry. In: *EPL (Europhysics Letters)* 90 (2010), No. 2, p. 27006. http://stacks.iop.org/0295-5075/90/i=2/a=27006

[28] Ashcroft, N.W. ; Mermin, N.D.: *Solid State Physics*. Cengage Learning, 2011. – ISBN 9788131500521

[29] Haas, W.J. de ; Boer, J. de ; Berg, G.J. van dën: The electrical resistance of gold, copper and lead at low temperatures. In: *Physica* 1 (1934), No. 7–12, p. 1115 – 1124. doi: 10.1016/S0031-8914(34)80310-2. – ISSN 0031-8914

[30] MOTT, N. F.: Metal-Insulator Transition. In: *Rev. Mod. Phys.* 40 (1968), p. 677–683. doi: 10.1103/RevModPhys.40.677

[31] Gebhard, F.: *The Mott Metal-Insulator Transition: Models and Methods*. Springer Berlin Heidelberg, 2003 (Springer Tracts in Modern Physics). – ISBN 9783540148586

[32] Metzner, Walter ; Vollhardt, Dieter: Correlated Lattice Fermions in $d = \infty$ Dimensions. In: *Phys. Rev. Lett.* 62 (1989), p. 324–327. doi: 10.1103/PhysRevLett.62.324

[33] Georges, Antoine ; Kotliar, Gabriel ; Krauth, Werner ; Rozenberg, Marcelo J.: Dynamical mean-field theory of strongly correlated fermion systems and the limit of infinite dimensions. In: *Rev. Mod. Phys.* 68 (1996), p. 13–125. doi: 10.1103/RevModPhys.68.13

[34] Kotliar, G. ; Savrasov, S. Y. ; Haule, K. ; Oudovenko, V. S. ; Parcollet, O. ; Marianetti, C. A.: Electronic structure calculations with dynamical mean-field theory. In: *Rev. Mod. Phys.* 78 (2006), p. 865–951. doi: 10.1103/RevModPhys.78.865

[35] Georges, Antoine ; Kotliar, Gabriel: Hubbard model in infinite dimensions. In: *Phys. Rev. B* 45 (1992), p. 6479–6483. doi: 10.1103/PhysRevB.45.6479

[36] Leggett, A. J. ; Chakravarty, S. ; Dorsey, A. T. ; Fisher, Matthew P. A. ; Garg, Anupam ; Zwerger, W.: Dynamics of the dissipative two-state system. In: *Rev. Mod. Phys.* 59 (1987), p. 1–85. doi: 10.1103/RevModPhys.59.1

[37] Bulla, Ralf ; Tong, Ning-Hua ; Vojta, Matthias: Numerical Renormalization Group for Bosonic Systems and Application to the Sub-Ohmic Spin-Boson Model. In: *Phys. Rev. Lett.* 91 (2003), p. 170601. doi: 10.1103/PhysRevLett.91.170601

[38] Tornow, S. ; Tong, N.-H. ; Bulla, R.: Electron transfer in donor-acceptor systems: Many-particle effects and influence of electronic correlations. In: *EPL (Europhysics Letters)* 73 (2006), No. 6, p. 913. http://stacks.iop.org/0295-5075/73/i=6/a=913

[39] Tornow, Sabine ; Bulla, Ralf ; Anders, Frithjof B. ; Nitzan, Abraham: Dissipative two-electron transfer: A numerical renormalization group study. In: *Phys. Rev. B* 78 (2008), p. 035434. doi: 10.1103/PhysRevB.78.035434

[40] Tornow, Sabine ; Bulla, Ralf ; Anders, Frithjof B. ; Zwicknagl, Gertrud: Multiple-charge transfer and trapping in DNA dimers. In: *Phys. Rev. B* 82 (2010), p. 195106. doi: 10.1103/PhysRevB.82.195106

[41] Keil, Markus ; Schoeller, Herbert: Real-time renormalization-group analysis of the dynamics of the spin-boson model. In: *Phys. Rev. B* 63 (2001), p. 180302. doi: 10.1103/PhysRevB.63.180302

[42] Anders, Frithjof B. ; Schiller, Avraham: Spin precession and real-time dynamics in the Kondo model: Time-dependent numerical renormalization-group study. In: *Phys. Rev. B* 74 (2006), p. 245113. doi: 10.1103/PhysRevB.74.245113

[43] Anders, Frithjof B. ; Bulla, Ralf ; Vojta, Matthias: Equilibrium and Nonequilibrium Dynamics of the Sub-Ohmic Spin-Boson Model. In: *Phys. Rev. Lett.* 98 (2007), p. 210402. doi: 10.1103/PhysRevLett.98.210402

[44] Porras, D. ; Marquardt, F. ; Delft, J. von ; Cirac, J. I.: Mesoscopic spin-boson models of trapped ions. In: *Phys. Rev. A* 78 (2008), p. 010101. doi: 10.1103/PhysRevA.78.010101

[45] Costi, T. A. ; McKenzie, Ross H.: Entanglement between a qubit and the environment in the spin-boson model. In: *Phys. Rev. A* 68 (2003), p. 034301. doi: 10.1103/PhysRevA.68.034301

[46] Segal, Dvira ; Millis, Andrew J. ; Reichman, David R.: Numerically exact path-integral simulation of nonequilibrium quantum transport and dissipation. In: *Phys. Rev. B* 82 (2010), p. 205323. doi: 10.1103/PhysRevB.82.205323

[47] Albrecht, K. F. ; Martin-Rodero, A. ; Monreal, R. C. ; Mühlbacher, L. ; Levy Yeyati, A.: Long transient dynamics in the Anderson-Holstein model out of equilibrium. In: *Phys. Rev. B* 87 (2013), p. 085127. doi: 10.1103/PhysRevB.87.085127

[48] Perfetto, E. ; Stefanucci, G.: Image charge effects in the nonequilibrium Anderson-Holstein model. In: *Phys. Rev. B* 88 (2013), p. 245437. doi: 10.1103/PhysRevB.88.245437

[49] Reed, M. A. ; Randall, J. N. ; Aggarwal, R. J. ; Matyi, R. J. ; Moore, T. M. ; Wetsel, A. E.: Observation of discrete electronic states in a zero-dimensional semiconductor nanostructure. In: *Phys. Rev. Lett.* 60 (1988), p. 535–537. doi: 10.1103/PhysRevLett.60.535

[50] Kastner, M. A.: The single-electron transistor. In: *Rev. Mod. Phys.* 64 (1992), p. 849–858. doi: 10.1103/RevModPhys.64.849

[51] Gustavsson, S. ; Leturcq, R. ; Simovič, B. ; Schleser, R. ; Ihn, T. ; Studerus, P. ; Ensslin, K. ; Driscoll, D. C. ; Gossard, A. C.: Counting Statistics of Single Electron Transport in a Quantum Dot. In: *Phys. Rev. Lett.* 96 (2006), p. 076605. doi: 10.1103/PhysRevLett.96.076605

[52] Loss, Daniel ; DiVincenzo, David P.: Quantum computation with quantum dots. In: *Phys. Rev. A* 57 (1998), p. 120–126. doi: 10.1103/PhysRevA.57.120

[53] Stolze, J. ; Suter, D.: *Quantum Computing: A Short Course from Theory to Experiment*. Wiley, 2008. – ISBN 9783527617777

[54] Le Hur, Karyn: Coulomb Blockade of a Noisy Metallic Box: A Realization of Bose-Fermi Kondo Models. In: *Phys. Rev. Lett.* 92 (2004), p. 196804. doi: 10.1103/PhysRevLett.92.196804

[55] Glossop, Matthew T. ; Ingersent, Kevin: Kondo physics and dissipation: A numerical renormalization-group approach to Bose-Fermi Kondo models. In: *Phys. Rev. B* 75 (2007), p. 104410. doi: 10.1103/PhysRevB.75.104410

[56] Cheng, Mengxing ; Glossop, Matthew T. ; Ingersent, Kevin: Quantum phase transitions in a charge-coupled Bose-Fermi Anderson model. In: *Phys. Rev. B* 80 (2009), p. 165113. doi: 10.1103/PhysRevB.80.165113

[57] Pixley, J. H. ; Kirchner, Stefan ; Ingersent, Kevin ; Si, Qimiao: Quantum criticality in the pseudogap Bose-Fermi Anderson and Kondo models: Interplay between fermion- and boson-induced Kondo destruction. In: *Phys. Rev. B* 88 (2013), p. 245111. doi: 10.1103/PhysRevB.88.245111

[58] Elzerman, J. M. ; Hanson, R. ; Beveeren, L. H. W. van ; Witkamp, B. ; Vandersypen, L. M. K. ; Kouvenhoven, L. P.: Single-shot read-out of an individual electron spin in a quantum dot. In: *Nature* 430 (2004), p. 431. doi: 10.1038/nature02693

[59] Rosch, A.: Wilson chains are not thermal reservoirs. In: *The European Physical Journal B* 85 (2012), No. 1. doi: 10.1140/epjb/e2011-20880-7. – ISSN 1434-6028

[60] Schiró, Marco: Nonequilibrium dynamics across an impurity quantum critical point due to quantum quenches. In: *Phys. Rev. B* 86 (2012), p. 161101. doi: 10.1103/PhysRevB.86.161101

[61] Sachdev, S.: *Quantum Phase Transitions*. Cambridge University Press, 2011 (Troisième Cycle de la Physique). – ISBN 9781139500210

[62] Ōnuki, Y. ; Komatsubara, T.: Heavy fermion state in CeCu6. In: *Journal of Magnetism and Magnetic Materials* 63–64 (1987), No. 0, p. 281–288. doi: 10.1016/0304-8853(87)90587-7. – ISSN 0304-8853

[63] Costi, T. A. ; Bergqvist, L. ; Weichselbaum, A. ; Delft, J. von ; Micklitz, T. ; Rosch, A. ; Mavropoulos, P. ; Dederichs, P. H. ; Mallet, F. ; Saminadayar, L. ; Bäuerle, C.: Kondo Decoherence: Finding the Right Spin Model for Iron Impurities in Gold and Silver. In: *Phys. Rev. Lett.* 102 (2009), p. 056802. doi: 10.1103/PhysRevLett.102.056802

[64] Kouwenhoven, Leo ; Glazman, Leonid: Revival of the Kondo effect. In: *Physics World* 1 (2001), p. 33–38.
http://physicsworldarchive.iop.org/full/pwa-pdf/14/1/phwv14i1a28.pdf

[65] Anderson, P W.: A poor man's derivation of scaling laws for the Kondo problem. In: *Journal of Physics C: Solid State Physics* 3 (1970), No. 12, p. 2436.
http://stacks.iop.org/0022-3719/3/i=12/a=008

[66] Burkhardt, C.E. ; Leventhal, J.J.: *Foundations of Quantum Physics*. Springer New York, 2008. – ISBN 9780387776521

[67] Schrieffer, J. R. ; Wolff, P. A.: Relation between the Anderson and Kondo Hamiltonians. In: *Phys. Rev.* 149 (1966), p. 491–492. doi: 10.1103/PhysRev.149.491

[68] Nozières, Ph. ; Blandin, A.: Kondo effect in real metals. In: *J. Phys. France* 41 (1980), No. 3, p. 193–211. doi: 10.1051/jphys:01980004103019300

[69] Cragg, D.M. ; Lloyd, P. ; Nozières, Ph.: On the ground states of some s-d exchange Kondo Hamiltonians. In: *Journal of Physics C: Solid State Physics* 13 (1980), No. 5, p. 803.
http://stacks.iop.org/0022-3719/13/i=5/a=011

[70] Cox, D.L. ; Zawadowski, A.: Exotic Kondo effects in metals: Magnetic ions in a crystalline electric field and tunnelling centres. In: *Advances in Physics* 47 (1998), No. 5, p. 599–942. doi: 10.1080/000187398243500

[71] Cragg, D.M. ; Lloyd, P.: Kondo Hamiltonians with a non-zero ground-state spin. In: *Journal of Physics C: Solid State Physics* 12 (1979), No. 6, p. L215. http://stacks.iop.org/0022-3719/12/i=6/a=001

[72] Mehta, Pankaj ; Andrei, Natan ; Coleman, P. ; Borda, L. ; Zarand, Gergely: Regular and singular Fermi-liquid fixed points in quantum impurity models. In: *Phys. Rev. B* 72 (2005), p. 014430. doi: 10.1103/PhysRevB.72.014430

[73] Posazhennikova, A. ; Bayani, B. ; Coleman, P.: Conductance of a spin-1 quantum dot: The two-stage Kondo effect. In: *Phys. Rev. B* 75 (2007), p. 245329. doi: 10.1103/PhysRevB.75.245329

[74] Jones, B. A. ; Varma, C. M.: Study of two magnetic impurities in a Fermi gas. In: *Phys. Rev. Lett.* 58 (1987), p. 843–846. doi: 10.1103/PhysRevLett.58.843

[75] Jones, B. A. ; Varma, C. M. ; Wilkins, J. W.: Low-Temperature Properties of the Two-Impurity Kondo Hamiltonian. In: *Phys. Rev. Lett.* 61 (1988), p. 125–128. doi: 10.1103/PhysRevLett.61.125

[76] Ruderman, M. A. ; Kittel, C.: Indirect Exchange Coupling of Nuclear Magnetic Moments by Conduction Electrons. In: *Phys. Rev.* 96 (1954), p. 99–102. doi: 10.1103/PhysRev.96.99

[77] Kasuya, Tadao: A Theory of Metallic Ferro- and Antiferromagnetism on Zener's Model. In: *Progress of Theoretical Physics* 16 (1956), No. 1, p. 45–57. doi: 10.1143/PTP.16.45

[78] Yosida, Kei: Magnetic Properties of Cu-Mn Alloys. In: *Phys. Rev.* 106 (1957), p. 893–898. doi: 10.1103/PhysRev.106.893

[79] Fazekas, P.: *Lecture Notes on Electron Correlation and Magnetism*. World Scientific, 1999 (Series in modern condensed matter physics). – ISBN 9789810224745

[80] Doniach, S.: The Kondo lattice and weak antiferromagnetism. In: *Physica B+C* 91 (1977), No. 0, p. 231–234. doi: 10.1016/0378-4363(77)90190-5

[81] Vojta, Matthias: Impurity quantum phase transitions. In: *Philosophical Magazine* 86 (2006), No. 13-14, p. 1807–1846. doi: 10.1080/14786430500070396

[82] Kanao, Taro ; Matsuura, Hiroyasu ; Ogata, Masao: Theory of Defect-Induced Kondo Effect in Graphene: Numerical Renormalization Group Study. In: *Journal of the Physical Society of Japan* 81 (2012), No. 6, p. 063709. doi: 10.1143/JPSJ.81.063709

[83] Bulla, R ; Pruschke, Th ; Hewson, A C.: Anderson impurity in pseudo-gap Fermi systems. In: *Journal of Physics: Condensed Matter* 9 (1997), No. 47, p. 10463. http://stacks.iop.org/0953-8984/9/i=47/a=014

[84] Glossop, Matthew T. ; Logan, David E.: Local quantum phase transition in the pseudogap Anderson model: scales, scaling and quantum critical dynamics. In: *Journal of Physics: Condensed Matter* 15 (2003), No. 44, p. 7519. http://stacks.iop.org/0953-8984/15/i=44/a=007

[85] Takegahara, Katsuhiko ; Shimizu, Yukihiro ; Sakai, Osamu: Quantum Monte Carlo and Numerical Renormalization Group Studies of Magnetic Impurities in Nonmetallic Systems. In: *Journal of the Physical Society of Japan* 61 (1992), No. 10, p. 3443–3446. doi: 10.1143/JPSJ.61.3443

[86] Takegahara, Katsuhiko ; Shimizu, Yukihiro ; Goto, Naoya ; Sakai, Osamu: Magnetic impurity in nonmetallic systems. In: *Physica B: Condensed Matter* 186 (1993), p. 381–383. doi: 10.1016/0921-4526(93)90579-U

[87] Bulla, R.: Dynamical mean-field theory: from quantum impurity physics to lattice problems. In: *Philosophical Magazine* 86 (2006), No. 13-14, p. 1877–1889. doi: 10.1080/14786430500070313

[88] Caldeira, A.O ; Leggett, A.J: Quantum tunnelling in a dissipative system. In: *Annals of Physics* 149 (1983), No. 2, p. 374–456. doi: 10.1016/0003-4916(83)90202-6. – ISSN 0003-4916

[89] Leggett, A. J.: Quantum tunneling in the presence of an arbitrary linear dissipation mechanism. In: *Phys. Rev. B* 30 (1984), p. 1208–1218. doi: 10.1103/PhysRevB.30.1208

[90] Bulla, Ralf ; Lee, Hyun-Jung ; Tong, Ning-Hua ; Vojta, Matthias: Numerical renormalization group for quantum impurities in a bosonic bath. In: *Phys. Rev. B* 71 (2005), p. 045122. doi: 10.1103/PhysRevB.71.045122

[91] Weiss, U.: *Quantum Dissipative Systems*. World Scientific, 1993 (Series in modern condensed matter physics)

[92] Costi, T. A.: Scaling and Universality in the Anisotropic Kondo Model and the Dissipative Two-State System. In: *Phys. Rev. Lett.* 80 (1998), p. 1038–1041. doi: 10.1103/PhysRevLett.80.1038

[93] Kehrein, Stefan K. ; Mielke, Andreas: On the spin-boson model with a sub-ohmic bath. In: *Physics Letters A* 219 (1996), No. 5–6, p. 313–318. doi: http://dx.doi.org/10.1016/0375-9601(96)00475-6. – ISSN 0375–9601

[94] Tong, Ning-Hua ; Vojta, Matthias: Signatures of a Noise-Induced Quantum Phase Transition in a Mesoscopic Metal Ring. In: *Phys. Rev. Lett.* 97 (2006), p. 016802. doi: 10.1103/PhysRevLett.97.016802

[95] Ladd, T. D. ; Jelezko, F. ; Laflamme, R. ; Nakamura, Y. ; Monroe, C. ; O'Brien, J. L.: Quantum computers. In: *Nature* 464 (2010), No. 7285. doi: 10.1038/nature08812

[96] Hanson, R. ; Kouwenhoven, L. P. ; Petta, J. R. ; Tarucha, S. ; Vandersypen, L. M. K.: Spins in few-electron quantum dots. In: *Rev. Mod. Phys.* 79 (2007), p. 1217–1265. doi: 10.1103/RevModPhys.79.1217

[97] Palma, G. M. ; Suominen, Kalle-Antti ; Ekert, Artur K.: Quantum Computers and Dissipation. In: *Proceedings of the Royal Society of London A: Mathematical, Physical and Engineering Sciences* 452 (1996), No. 1946, p. 567–584. doi: 10.1098/rspa.1996.0029. – ISBN 1471-2946

[98] Meyer, D. ; Hewson, A. C. ; Bulla, R.: Gap Formation and Soft Phonon Mode in the Holstein Model. In: *Phys. Rev. Lett.* 89 (2002), p. 196401. doi: 10.1103/PhysRevLett.89.196401

[99] Jovchev, Andre ; Anders, Frithjof B.: Influence of vibrational modes on quantum transport through a nanodevice. In: *Phys. Rev. B* 87 (2013), p. 195112. doi: 10.1103/PhysRevB.87.195112

[100] Glossop, Matthew T. ; Ingersent, Kevin: Numerical Renormalization-Group Study of the Bose-Fermi Kondo Model. In: *Phys. Rev. Lett.* 95 (2005), p. 067202. doi: 10.1103/PhysRevLett.95.067202

[101] Si, Qimiao ; Rabello, Silvio ; Ingersent, Kevin ; Smith, J. L.: Locally critical quantum phase transitions in strongly correlated metals. In: *Nature* 413 (2001), p. 804–808. doi: 10.1038/35101507

[102] Si, Qimiao ; Rabello, Silvio ; Ingersent, Kevin ; Smith, J. L.: Local fluctuations in quantum critical metals. In: *Phys. Rev. B* 68 (2003), p. 115103. doi: 10.1103/PhysRevB.68.115103

[103] Coleman, P.: Theories of non-Fermi liquid behavior in heavy fermions. In: *Physica B: Condensed Matter* 259–261 (1999), p. 353–358. doi: 10.1016/S0921-4526(98)00795-9

[104] Coleman, P. ; Pépin, C. ; Si, Qimiao ; Ramazashvili, R.: How do Fermi liquids get heavy and die? In: *Journal of Physics: Condensed Matter* 13 (2001), No. 35, p. R723. http://stacks.iop.org/0953-8984/13/i=35/a=202

[105] Anderson, P. W. ; Yuval, G. ; Hamann, D. R.: Exact Results in the Kondo Problem. II. Scaling Theory, Qualitatively Correct Solution, and Some New Results on One-Dimensional Classical Statistical Models. In: *Phys. Rev. B* 1 (1970), p. 4464–4473. doi: 10.1103/PhysRevB.1.4464

[106] Furuya, K. ; Lowenstein, J. H.: Bethe-ansatz approach to the Kondo model with arbitrary impurity spin. In: *Phys. Rev. B* 25 (1982), p. 5935–5952. doi: 10.1103/PhysRevB.25.5935

[107] Schlottmann, P.: Bethe- *Ansatz* Solution of the Anderson Model of a Magnetic Impurity with Orbital Degeneracy. In: *Phys. Rev. Lett.* 50 (1983), p. 1697–1700. doi: 10.1103/PhysRevLett.50.1697

[108] Affleck, Ian ; Ludwig, Andreas W.: Critical theory of overscreened Kondo fixed points. In: *Nuclear Physics B* 360 (1991), No. 2–3, p. 641–696. doi: 10.1016/0550-3213(91)90419-X

[109] Affleck, Ian ; Ludwig, Andreas W. W.: Exact conformal-field-theory results on the multichannel Kondo effect: Single-fermion Green's function, self-energy, and resistivity. In: *Phys. Rev. B* 48 (1993), p. 7297–7321. doi: 10.1103/PhysRevB.48.7297

[110] Affleck, Ian ; Ludwig, Andreas W. W. ; Jones, Barbara A.: Conformal-field-theory approach to the two-impurity Kondo problem: Comparison with numerical renormalization-group results. In: *Phys. Rev. B* 52 (1995), p. 9528–9546. doi: 10.1103/PhysRevB.52.9528

[111] Ingersent, Kevin ; Si, Qimiao: Critical Local-Moment Fluctuations, Anomalous Exponents, and ω/T Scaling in the Kondo Problem with a Pseudogap. In: *Phys. Rev. Lett.* 89 (2002), p. 076403. doi: 10.1103/PhysRevLett.89.076403

[112] Krishna-murthy, H. R. ; Wilkins, J. W. ; Wilson, K. G.: Renormalization-group approach to the Anderson model of dilute magnetic alloys. I. Static properties for the symmetric case. In: *Phys. Rev. B* 21 (1980), p. 1003–1043. doi: 10.1103/PhysRevB.21.1003

[113] Krishna-murthy, H. R. ; Wilkins, J. W. ; Wilson, K. G.: Renormalization-group approach to the Anderson model of dilute magnetic alloys. II. Static properties for the asymmetric case. In: *Phys. Rev. B* 21 (1980), p. 1044–1083. doi: 10.1103/PhysRevB.21.1044

[114] Chen, Kan ; Jayaprakash, C: The Kondo effect in pseudo-gap Fermi systems: a renormalization group study. In: *Journal of Physics: Condensed Matter* 7 (1995), No. 37, p. L491. http://stacks.iop.org/0953-8984/7/i=37/a=003

[115] Ingersent, Kevin: Behavior of magnetic impurities in gapless Fermi systems. In: *Phys. Rev. B* 54 (1996), p. 11936–11939. doi: 10.1103/PhysRevB.54.11936

[116] Bulla, Ralf ; Glossop, Matthew T. ; Logan, David E. ; Pruschke, Thomas: The soft-gap Anderson model: comparison of renormalization group and local moment approaches. In: *Journal of Physics: Condensed Matter* 12 (2000), No. 23, p. 4899. http://stacks.iop.org/0953-8984/12/i=23/a=302

[117] Kleine, Christian ; Musshoff, Julian ; Anders, Frithjof B.: Real-time dynamics induced by quenches across the quantum critical points in gapless Fermi systems with a magnetic impurity. In: *Phys. Rev. B* 90 (2014), p. 235145. doi: 10.1103/PhysRevB.90.235145

[118] Fritz, Lars ; Vojta, Matthias: Phase transitions in the pseudogap Anderson and Kondo models: Critical dimensions, renormalization group, and local-moment criticality. In: *Phys. Rev. B* 70 (2004), p. 214427. doi: 10.1103/PhysRevB.70.214427

[119] Fritz, Lars ; Vojta, Matthias: The physics of Kondo impurities in graphene. In: *Reports on Progress in Physics* 76 (2013), No. 3, p. 032501. http://stacks.iop.org/0034-4885/76/i=3/a=032501

[120] Eidelstein, Eitan ; Schiller, Avraham ; Güttge, Fabian ; Anders, Frithjof B.: Coherent control of correlated nanodevices: A hybrid time-dependent numerical renormalization-group approach to periodic switching. In: *Phys. Rev. B* 85 (2012), p. 075118. doi: 10.1103/PhysRevB.85.075118

[121] Güttge, Fabian ; Anders, Frithjof B. ; Schollwöck, Ulrich ; Eidelstein, Eitan ; Schiller, Avraham: Hybrid NRG-DMRG approach to real-time dynamics of quantum impurity systems. In: *Phys. Rev. B* 87 (2013), p. 115115. doi: 10.1103/PhysRevB.87.115115

[122] Glossop, M.T. ; Khoshkhou, N. ; Ingersent, K.: Kondo physics in a dissipative environment. In: *Physica B: Condensed Matter* 403 (2008), No. 5–9, p. 1303 – 1305. doi: http://dx.doi.org/10.1016/j.physb.2007.10.132. – Proceedings of the International Conference on Strongly Correlated Electron Systems. – ISSN 0921-4526

[123] Anders, Frithjof B. ; Schiller, Avraham: Real-Time Dynamics in Quantum-Impurity Systems: A Time-Dependent Numerical Renormalization-Group Approach. In: *Phys. Rev. Lett.* 95 (2005), p. 196801. doi: 10.1103/PhysRevLett.95.196801

[124] Nghiem, H. T. M. ; Costi, T. A.: Generalization of the time-dependent numerical renormalization group method to finite temperatures and general pulses. In: *Phys. Rev. B* 89 (2014), p. 075118. doi: 10.1103/PhysRevB.89.075118

[125] Chin, Alex W. ; Rivas, Ángel ; Huelga, Susana F. ; Plenio, Martin B.: Exact mapping between system-reservoir quantum models and semi-infinite discrete chains using orthogonal polynomials. In: *Journal of Mathematical Physics* 51 (2010), No. 9. doi: http://dx.doi.org/10.1063/1.3490188

[126] Campo, Vivaldo L. ; Oliveira, Luiz N.: Alternative discretization in the numerical renormalization-group method. In: *Phys. Rev. B* 72 (2005), p. 104432. doi: 10.1103/PhysRevB.72.104432

[127] Frota, H. O. ; Oliveira, L. N.: Photoemission spectroscopy for the spin-degenerate Anderson model. In: *Phys. Rev. B* 33 (1986), p. 7871–7874. doi: 10.1103/PhysRevB.33.7871

[128] Yoshida, M. ; Whitaker, M. A. ; Oliveira, L. N.: Renormalization-group calculation of excitation properties for impurity models. In: *Phys. Rev. B* 41 (1990), p. 9403–9414. doi: 10.1103/PhysRevB.41.9403

[129] Oliveira, Wanda C. ; Oliveira, Luiz N.: Generalized numerical renormalization-group method to calculate the thermodynamical properties of impurities in metals. In: *Phys. Rev. B* 49 (1994), p. 11986–11994. doi: 10.1103/PhysRevB.49.11986

[130] Galperin, Michael ; Ratner, Mark A. ; Nitzan, Abraham: Molecular transport junctions: vibrational effects. In: *Journal of Physics: Condensed Matter* 19 (2007), No. 10, p. 103201. http://stacks.iop.org/0953-8984/19/i=10/a=103201

[131] Bera, S. ; Florens, S. ; H., Baranger ; Roch, N. ; Nazir, A. ; Chin, A.: Unveiling environmental entanglement in strongly dissipative qubits. In: *ArXiv e-prints* (2013). http://arxiv.org/abs/1301.7430

[132] Hackl, Andreas ; Roosen, David ; Kehrein, Stefan ; Hofstetter, Walter: Nonequilibrium Spin Dynamics in the Ferromagnetic Kondo Model. In: *Phys. Rev. Lett.* 102 (2009), p. 196601. doi: 10.1103/PhysRevLett.102.196601

[133] Lechtenberg, Benedikt ; Anders, Frithjof B.: Spatial and temporal propagation of Kondo correlations. In: *Phys. Rev. B* 90 (2014), p. 045117. doi: 10.1103/PhysRevB.90.045117

[134] Anders, Frithjof B.: Steady-State Currents through Nanodevices: A Scattering-States Numerical Renormalization-Group Approach to Open Quantum Systems. In: *Phys. Rev. Lett.* 101 (2008), p. 066804. doi: 10.1103/PhysRevLett.101.066804

[135] Costi, T A. ; Hewson, A C. ; Zlatic, V: Transport coefficients of the Anderson model via the numerical renormalization group. In: *Journal of Physics: Condensed Matter* 6 (1994), No. 13, p. 2519. http://stacks.iop.org/0953-8984/6/i=13/a=013

[136] Peters, Robert ; Pruschke, Thomas ; Anders, Frithjof B.: Numerical renormalization group approach to Green's functions for quantum impurity models. In: *Phys. Rev. B* 74 (2006), p. 245114. doi: 10.1103/PhysRevB.74.245114

[137] Weichselbaum, Andreas ; Delft, Jan von: Sum-Rule Conserving Spectral Functions from the Numerical Renormalization Group. In: *Phys. Rev. Lett.* 99 (2007), p. 076402. doi: 10.1103/PhysRevLett.99.076402

[138] Lo, Po-Wei ; Guo, Guang-Yu ; Anders, Frithjof B.: Gate-tunable Kondo resistivity and dephasing rate in graphene studied by numerical renormalization group calculations. In: *Phys. Rev. B* 89 (2014), p. 195424. doi: 10.1103/PhysRevB.89.195424

[139] Vojta, Matthias ; Fritz, Lars: Upper critical dimension in a quantum impurity model: Critical theory of the asymmetric pseudogap Kondo problem. In: *Phys. Rev. B* 70 (2004), p. 094502. doi: 10.1103/PhysRevB.70.094502

[140] Schneider, Imke ; Fritz, Lars ; Anders, Frithjof B. ; Benlagra, Adel ; Vojta, Matthias: Two-channel pseudogap Kondo and Anderson models: Quantum phase transitions and non-Fermi liquids. In: *Phys. Rev. B* 84 (2011), p. 125139. doi: 10.1103/PhysRevB.84.125139

[141] Seibold, G. ; Lorenzana, J.: Time-Dependent Gutzwiller Approximation for the Hubbard Model. In: *Phys. Rev. Lett.* 86 (2001), p. 2605–2608. doi: 10.1103/PhysRevLett.86.2605

[142] Lanatà, Nicola ; Strand, Hugo U. R.: Time-dependent and steady-state Gutzwiller approach for nonequilibrium transport in nanostructures. In: *Phys. Rev. B* 86 (2012), p. 115310. doi: 10.1103/PhysRevB.86.115310

[143] Gutzwiller, Martin C.: Correlation of Electrons in a Narrow *s* Band. In: *Phys. Rev.* 137 (1965), p. A1726–A1735. doi: 10.1103/PhysRev.137.A1726

[144] Schickling, Tobias ; Gebhard, Florian ; Bünemann, Jörg ; Boeri, Lilia ; Andersen, Ole K. ; Weber, Werner: Gutzwiller Theory of Band Magnetism in LaOFeAs. In: *Phys. Rev. Lett.* 108 (2012), p. 036406. doi: 10.1103/PhysRevLett.108.036406

[145] Mazur, P.: Non-ergodicity of phase functions in certain systems. In: *Physica* 43 (1969), No. 4, p. 533–545. doi: 10.1016/0031-8914(69)90185-2. – ISSN 0031-8914

[146] Suzuki, M.: Ergodicity, constants of motion, and bounds for susceptibilities. In: *Physica* 51 (1971), No. 2, p. 277–291. doi: 10.1016/0031-8914(71)90226-6. – ISSN 0031-8914

[147] Uhrig, Götz S. ; Hackmann, Johannes ; Stanek, Daniel ; Stolze, Joachim ; Anders, Frithjof B.: Conservation laws protect dynamic spin correlations from decay: Limited role of integrability in the central spin model. In: *Phys. Rev. B* 90 (2014), p. 060301. doi: 10.1103/PhysRevB.90.060301

[148] Lanatà, Nicola: Variational approach to transport in quantum dots. In: *Phys. Rev. B* 82 (2010), p. 195326. doi: 10.1103/PhysRevB.82.195326

[149] Musshoff, Julian: *Nonequilibrium dynamics of the pseudegap single impurity Anderson model*. Germany, Technische Universität Dortmund, Master thesis, 2014

[150] Barzykin, Victor ; Affleck, Ian: The Kondo Screening Cloud: What Can We Learn from Perturbation Theory? In: *Phys. Rev. Lett.* 76 (1996), p. 4959–4962. doi: 10.1103/PhysRevLett.76.4959

[151] Barzykin, Victor ; Affleck, Ian: Screening cloud in the *k*-channel Kondo model: Perturbative and large-*k* results. In: *Phys. Rev. B* 57 (1998), p. 432–448. doi: 10.1103/PhysRevB.57.432

[152] Affleck, Ian ; Simon, Pascal: Detecting the Kondo Screening Cloud Around a Quantum Dot. In: *Phys. Rev. Lett.* 86 (2001), p. 2854–2857. doi: 10.1103/PhysRevLett.86.2854

[153] Sørensen, Erik S. ; Affleck, Ian: Kondo Screening Cloud Around a Quantum Dot: Large-Scale Numerical Results. In: *Phys. Rev. Lett.* 94 (2005), p. 086601. doi: 10.1103/PhysRevLett.94.086601

[154] Affleck, Ian ; Borda, László ; Saleur, Hubert: Friedel oscillations and the Kondo screening cloud. In: *Phys. Rev. B* 77 (2008), p. 180404. doi: 10.1103/PhysRevB.77.180404

[155] Reimann, Peter: Foundation of Statistical Mechanics under Experimentally Realistic Conditions. In: *Phys. Rev. Lett.* 101 (2008), p. 190403. doi: 10.1103/PhysRevLett.101.190403

[156] Rigol, Marcos ; Srednicki, Mark: Alternatives to Eigenstate Thermalization. In: *Phys. Rev. Lett.* 108 (2012), p. 110601. doi: 10.1103/PhysRevLett.108.110601

[157] Kleine, Christian ; Anders, Frithjof B.: Influence of a bosonic environment onto the real-time dynamics of local electronic states in a quantum impurity system close to a quantum phase transition. In: *ArXiv e-prints* (2015).
http://arxiv.org/abs/1512.06221

[158] Nielsen, M.A. ; Chuang, I.L.: *Quantum Computation and Quantum Information: 10th Anniversary Edition*. Cambridge University Press, 2010. – ISBN 9781139495486

[159] Kirćan, Marijana ; Vojta, Matthias: Critical properties of the Fermi-Bose Kondo and pseudogap Kondo models: Renormalized perturbation theory. In: *Phys. Rev. B* 69 (2004), p. 174421. doi: 10.1103/PhysRevB.69.174421

[160] Chung, Chung-Hou ; Glossop, Matthew T. ; Fritz, Lars ; Kirćan, Marijana ; Ingersent, Kevin ; Vojta, Matthias: Quantum phase transitions in a resonant-level model with dissipation: Renormalization-group studies. In: *Phys. Rev. B* 76 (2007), p. 235103. doi: 10.1103/PhysRevB.76.235103

[161] Nica, Emilian M. ; Ingersent, Kevin ; Zhu, Jian-Xin ; Si, Qimiao: Quantum critical Kondo destruction in the Bose-Fermi Kondo model with a local transverse field. In: *Phys. Rev. B* 88 (2013), p. 014414. doi: 10.1103/PhysRevB.88.014414

[162] Haldane, F. D. M.: Hartree-Fock study of the Anderson model coupled to a boson field; mixed valence states. In: *Phys. Rev. B* 15 (1977), p. 281–289. doi: 10.1103/PhysRevB.15.281

[163] Haldane, F. D. M.: New model for the mixed-valence phenomenon in rare-earth materials. In: *Phys. Rev. B* 15 (1977), p. 2477–2484. doi: 10.1103/PhysRevB.15.2477

[164] Freericks, J. K.: Strong-coupling expansions for the attractive Holstein and Hubbard models. In: *Phys. Rev. B* 48 (1993), p. 3881–3891. doi: 10.1103/PhysRevB.48.3881

[165] Grewe, N. ; Steglich, F.: Heavy Fermions. In: Gschneidner, Jr., K. A. (Editor) ; Eyring, L. (Editor): *Handbook on the Physics and Chemistry of Rare Earths* Volume 14. Amsterdam : North-Holland, 1991, p. 343

[166] Stewart, G. R.: Non-Fermi-liquid behavior in d- and f-electron metals. In: *Rev. Mod. Phys.* 73 (2001), p. 797–855. doi: 10.1103/RevModPhys.73.797

[167] Li, Mei-Rong ; Le Hur, Karyn ; Hofstetter, Walter: Hidden Caldeira-Leggett Dissipation in a Bose-Fermi Kondo Model. In: *Phys. Rev. Lett.* 95 (2005), p. 086406. doi: 10.1103/PhysRevLett.95.086406

[168] May, V. ; Kühn, O.: *Charge and Energy Transfer Dynamics in Molecular Systems*. Wiley, 2011. – ISBN 9783527633814

[169] Welack, Sven ; Schreiber, Michael ; Kleinekathöfer, Ulrich: The influence of ultrafast laser pulses on electron transfer in molecular wires studied by a non-Markovian density-matrix approach. In: *The Journal of Chemical Physics* 124 (2006), No. 4. doi: 10.1063/1.2162537

[170] Roosen, David ; Wegewijs, Maarten R. ; Hofstetter, Walter: Nonequilibrium Dynamics of Anisotropic Large Spins in the Kondo Regime: Time-Dependent Numerical Renormalization Group Analysis. In: *Phys. Rev. Lett.* 100 (2008), p. 087201. doi: 10.1103/PhysRevLett.100.087201

[171] Schmitt, Sebastian ; Anders, Frithjof B.: Nonequilibrium Zeeman Splitting in Quantum Transport through Nanoscale Junctions. In: *Phys. Rev. Lett.* 107 (2011), p. 056801. doi: 10.1103/PhysRevLett.107.056801

[172] Vojta, Matthias ; Bulla, Ralf ; Güttge, Fabian ; Anders, Frithjof: Mass-flow error in the numerical renormalization-group method and the critical behavior of the sub-Ohmic spin-boson model. In: *Phys. Rev. B* 81 (2010), p. 075122. doi: 10.1103/PhysRevB.81.075122

[173] Freericks, J. K. ; Jarrell, M. ; Scalapino, D. J.: Holstein model in infinite dimensions. In: *Phys. Rev. B* 48 (1993), p. 6302–6314. doi: 10.1103/PhysRevB.48.6302

[174] Hewson, A. C. ; Meyer, D.: Numerical renormalization group study of the Anderson-Holstein impurity model. In: *Journal of Physics: Condensed Matter* 14 (2002), No. 3, p. 427. http://stacks.iop.org/0953-8984/14/i=3/a=312

[175] Koller, W. ; Meyer, D. ; Ōno, Y. ; Hewson, A. C.: First- and second-order phase transitions in the Holstein-Hubbard model. In: *EPL (Europhysics Letters)* 66 (2004), No. 4, p. 559. http://stacks.iop.org/0295-5075/66/i=4/a=559

[176] Anders, Frithjof B.: Dynamics of large anisotropic spin in a sub-ohmic dissipative environment close to a quantum-phase transition. In: *New Journal of Physics* 10 (2008), No. 11, p. 115007. http://stacks.iop.org/1367-2630/10/i=11/a=115007

[177] Zaránd, Gergely ; Demler, Eugene: Quantum phase transitions in the Bose-Fermi Kondo model. In: *Phys. Rev. B* 66 (2002), p. 024427. doi: 10.1103/PhysRevB.66.024427

[178] Stanley, H. E.: Scaling, universality, and renormalization: Three pillars of modern critical phenomena. In: *Rev. Mod. Phys.* 71 (1999), p. S358–S366. doi: 10.1103/RevModPhys.71.S358

[179] Fisher, Michael E. ; Ma, Shang-keng ; Nickel, B. G.: Critical Exponents for Long-Range Interactions. In: *Phys. Rev. Lett.* 29 (1972), p. 917–920. doi: 10.1103/PhysRevLett.29.917

[180] Luijten, Erik ; Blöte, Henk W. J.: Classical critical behavior of spin models with long-range interactions. In: *Phys. Rev. B* 56 (1997), p. 8945–8958. doi: 10.1103/PhysRevB.56.8945

[181] Fischer, Kurt: Quantum Phase Transition and Universality Class for a Boson-Impurity Model: Implications for the Spin-Boson Model. In: *Journal of the Physical Society of Japan* 82 (2013), No. 7, p. 073001. doi: 10.7566/JPSJ.82.073001

[182] Vojta, Matthias ; Tong, Ning-Hua ; Bulla, Ralf: Quantum Phase Transitions in the Sub-Ohmic Spin-Boson Model: Failure of the Quantum-Classical Mapping. In: *Phys. Rev. Lett.* 94 (2005), p. 070604. doi: 10.1103/PhysRevLett.94.070604

[183] Vojta, Matthias ; Tong, Ning-Hua ; Bulla, Ralf: Erratum: Quantum Phase Transitions in the Sub-Ohmic Spin-Boson Model: Failure of the Quantum-Classical Mapping [Phys. Rev. Lett. **94** , 070604 (2005)]. In: *Phys. Rev. Lett.* 102 (2009), p. 249904. doi: 10.1103/PhysRevLett.102.249904

[184] Vojta, Matthias: Numerical renormalization group for the sub-Ohmic spin-boson model: A conspiracy of errors. In: *Phys. Rev. B* 85 (2012), p. 115113. doi: 10.1103/PhysRevB.85.115113

[185] Kirchner, Stefan: Spin Path Integrals, Berry Phase, and the Quantum Phase Transition in the Sub-Ohmic Spin-Boson Model. In: *Journal of Low Temperature Physics* 161 (2010), No. 1-2, p. 282–298. doi: 10.1007/s10909-010-0193-4. – ISSN 0022-2291

[186] Kirchner, Stefan ; Ingersent, Kevin ; Si, Qimiao: Quantum criticality of the sub-Ohmic spin-boson model. In: *Phys. Rev. B* 85 (2012), p. 075113. doi: 10.1103/PhysRevB.85.075113

[187] Winter, André ; Rieger, Heiko ; Vojta, Matthias ; Bulla, Ralf: Quantum Phase Transition in the Sub-Ohmic Spin-Boson Model: Quantum Monte Carlo Study with a Continuous Imaginary Time Cluster Algorithm. In: *Phys. Rev. Lett.* 102 (2009), p. 030601. doi: 10.1103/PhysRevLett.102.030601

[188] Alvermann, A. ; Fehske, H.: Sparse Polynomial Space Approach to Dissipative Quantum Systems: Application to the Sub-Ohmic Spin-Boson Model. In: *Phys. Rev. Lett.* 102 (2009), p. 150601. doi: 10.1103/PhysRevLett.102.150601

[189] Guo, Cheng ; Weichselbaum, Andreas ; Delft, Jan von ; Vojta, Matthias: Critical and Strong-Coupling Phases in One- and Two-Bath Spin-Boson Models. In: *Phys. Rev. Lett.* 108 (2012), p. 160401. doi: 10.1103/PhysRevLett.108.160401

[190] Hou, Y.-H. ; Tong, N.-H.: Criticality of the mean-field spin-boson model: boson state truncation and its scaling analysis. In: *The European Physical Journal B* 78 (2010), No. 1, p. 127–135. doi: 10.1140/epjb/e2010-10426-0. – ISSN 1434-6028

[191] Tong, Ning-Hua ; Hou, Yan-Hua: Scaling analysis in the numerical renormalization group study of the sub-Ohmic spin-boson model. In: *Phys. Rev. B* 85 (2012), p. 144425. doi: 10.1103/PhysRevB.85.144425

Publication list

During the course of the work for this thesis parts of this thesis have been published or are going to be published and have been cited in the main body.

- Kleine, C. ; Mußhoff, J. ; Anders, F. B.: *Real-time dynamics induced by quenches across the quantum critical points in gapless Fermi systems with a magnetic impurity*. In: Phys. Rev. B **90** (2014), p. 235145.
- Kleine, C. ; Anders, F. B.: *Influence of a bosonic environment onto the real-time dynamics of local electronic states in a quantum impurity system close to a quantum phase transition*. arXiv:1512.06221

Acknowledgements

This thesis is dedicated to the memory of my beloved father, Detlef.

In the first place, I would like to thank my adviser Prof. Dr. Frithjof Anders for giving me the opportunity to work in his group and making this PhD thesis possible. Numerous discussions as well as helpful advice have provided the guidelines for my research.

Prof. Dr. Joachim Stolze kindly agreed to co-report this thesis.

I want to thank Dr. Fabian Güttge for his effort in developing the BF-NRG code and its extension to non-equilibrium. It was a pleasure to collaborate with him on the development.

Our master student Julian Mußhoff kindly provided the perturbation theory calculations for the dynamics in the SIAM.

I want to thank my colleagues Benedikt and Johannes for their enduring support and a lot of funny moments in the office and on a private level.

Special thanks are dedicated to my boy-friend Stefan and my mother Brigitte for being there for me, always.